DISSERTATION

DYNAMICS OF PROTEIN INTERACTIONS WITH NEW BIOMIMETIC INTERFACES: TOWARD BLOOD-COMPATIBLE BIOMATERIALS

Submitted by

Mohammadhasan Hedayati

Department of Chemical and Biological Engineering

In partial fulfillment of the requirements

For the Degree of Doctor of Philosophy

Colorado State University

Fort Collins, Colorado

Fall 2019

Doctoral Committee:

Advisor: Matt J. Kipper

Diego Krapf
Melissa Reynolds
Travis Bailey

ABSTRACT

DYNAMICS OF PROTEIN INTERACTIONS WITH NEW BIOMIMETIC INTERFACES: TOWARD BLOOD-COMPATIBLE BIOMATERIALS

Nonspecific blood protein adsorption on the surfaces is the first event that occurs within seconds when a biomaterial comes into contact with blood. This phenomenon may ultimately lead to significant adverse biological responses. Therefore, preventing blood protein adsorption on biomaterial surfaces is a prerequisite towards designing blood-compatible artificial surfaces.

This project aims to address this problem by engineering surfaces that mimic the inside surface of blood vessels, which is the only known material that is completely blood-compatible. The inside surface of blood vessels presents a carbohydrate-rich, gel-like, dynamic surface layer called the endothelial glycocalyx. The polysaccharides in the glycocalyx include polyanionic glycosaminoglycans (GAGs). This polysaccharide-rich surface has excellent and unique blood compatibility. We developed a technique for preparing and characterizing dense GAG surfaces that can serve as models of the vascular endothelial glycocalyx. The glycocalyx-mimetic surfaces were prepared by adsorbing heparin- or chondroitin sulfate-containing polyelectrolyte complex nanoparticles (PCNs) to chitosan-hyaluronan polyelectrolyte multilayers (PEMs).

We then studied in detail the interactions of two important blood proteins (albumin and fibrinogen) with these glycocalyx mimics. Surface plasmon resonance (SPR) is a common ensemble averaging technique for detection of biomolecular interactions. SPR was used to quantify the amount of protein adsorption on these surfaces. Moreover, single-molecule microscopy along with advanced particle tracking were used to directly study the interaction of single molecule proteins with synthetic surfaces. Finally, we developed a groundwork for a kinetic model of long-term protein adsorption on biomaterial surfaces.

In the first chapter, we thoroughly summarize the important blood-material interactions that regulate blood compatibility, organize recent developments in this field from a materials perspective, and recommend areas for future research. In the second chapter, we report preparation and characterization of dense GAG surfaces that can serve as models of the vascular endothelial glycocalyx. In the third chapter, we investigate how combining surface plasmon resonance, X-ray spectroscopy, atomic force microscopy, and single-molecule total internal reflection fluorescence microscopy provides a more complete picture of protein adsorption on ultralow fouling polyelectrolyte multilayer and polymer brush surfaces, over different regimes of protein concentration. In the fourth chapter, the interactions of two important proteins from blood (albumin and fibrinogen) with glycocalyx-mimetic surfaces are revealed in detail using surface plasmon resonance and single-molecule microscopy. Finally in the fifth chapter, the long-term protein interactions with different biomaterial surfaces are studied with single-molecule microscopy and

ACKNOWLEDGMENTS

I would like to express my sincere gratitude to all amazing scientists, students, staff, and coworkers during my Ph.D. First, I would like to recognize my advisor Dr. Matt J. Kipper for his exceptional role as a mentor and friend who never stopped me from working in different fields. Matt’s passion for science has inspired and given me the motivation and strength to follow my goals and overcome challenges. His endless patience and dedication to listen and improve my ideas helped me learn many valuable skills. Thank you for mentoring me and making my experience as your research assistant fun, enriching, and fulfilling.

Second, I would like to thank my committee members, Dr. Diego Krapf, Dr. Melissa Reynolds, and Dr. Travis Bailey for their support and helpful insights. I am extremely grateful for having had the opportunity to work with these exceptional scientists. Diego, thank you being wonderful co-advisor and collaborator, for always making time for meetings and designing my TIRFM experiments. Melissa, thank you for your input and advice for designing surfaces. Travis, thank you for the great time that we had during polymers science and engineering course which I learnt a lot.

Third, I thank my research colleagues past and present who assisted with the research or gave feedback on research presentations including Drs. Raimundo Romero, Xinran Xu, Jessi Vlcek, Tara Wigmosta, and Dafu Wang. I would especially like to thank undergraduate students Sarah Igli, Anugrah Mathew, and Natalie Rapp who worked patiently in the lab to prepare my samples.

Fourth, I thank several CSU faculty and staff for their discussions, administrative assistance, equipment training, and use which were invaluable in this work. These include: Drs.

Pat McCurdy and Karolien Denef from the Central Instrument Facility in the Department of Chemistry; Dr. Arun Kota from the Department of Mechanical Engineering; Dr. Ellen Brennan-Pierce, Tim Gonzalez, Claire Lavelle, and Denise Morgan from the Department of Chemical and Biological Engineering.

Fifth, I must thank my funding sources which supported me during my time in graduate school which included the National Science Foundation, NTU foundation, and CSU Vice President for Research.

The special acknowledgements go to my parents who always have taught me about science and instilled in me an appreciation for the education and opportunities I have received in my life. It has been very tough to be far away from them, but I know they are now very happy that their son is a scientist.

Finally, I would like to thank my wife, for being there for me when I needed her, for her patience, for her positive energy, and for making every experience we live together.

DEDICATION

To my family

TABLE OF CONTENTS

CHAPTER 1: THE QUEST FOR BLOOD-COMPATIBLE MATERIALS: RECENT ADVANCES AND FUTURE TECHNOLOGIES[1]

Overview

The development of blood-compatible materials represents a grand challenge in biomaterials science. Blood is a complex fluid containing many types of living cells, functional proteins, and other signaling molecules, which work together to protect the circulatory system from injury, pathogens, and foreign materials. Blood-contacting biomaterials include the components of cardiovascular implants (such as stents, shunts, and valves) and extracorporeal circuit components (such as tubing, membranes, and pumps). The engineered materials used in these applications are distinctly unlike the biological tissues that make up the cardiovascular system in their physical, chemical, and biological properties, leading to undesirable—and sometimes catastrophic—blood-material interactions. The pursuit of blood-compatible materials challenges nearly every aspect of materials design, including composition, mechanical properties, structure across multiple length scales, tribology, surface physical-chemistry, and biochemical functionalization. Materials have been designed to bind or reject specific blood proteins, interact favorably with specific cell types, or to interact with particular biochemical pathways in blood. This review summarizes the important blood-material interactions that regulate blood compatibility, organizes recent developments in this field from a materials perspective.

---

[1] This work was published in *Materials Science & Engineering R* and is reproduced in modified form here with permission [1]. M. Hedayati was responsible for the most of the literature review, data collection, organization, writing, and editing. M. Neufeld provided commentary on NO section, writing, reviewing, and editing. M. Reynolds and M.J. Kipper conceived of the review, advised and oversaw the work, and edited the manuscript.

1.1. Introduction

1.1.1 The blood-material interface in medical devices

Worldwide, millions of blood-contacting medical devices are used annually [2]. These include implants, such as stents and heart valves, components of extracorporeal life support systems (i.e., catheters, tubing, and membranes used in blood oxygenators) and materials used for blood collection, storage and sensing. Some of these applications require only momentary or incidental blood contact while other applications involve long-term blood contact (days to years). For implanted cardiovascular devices and components of life-support systems, undesirable blood-material interactions such as blood clotting (thrombosis) and inflammation can lead to catastrophic failure. The success of all of these life-saving technologies is therefore critically dependent upon the ability to manage and prevent these complications.

There is a widespread recognition that preventing thrombosis and inflammation on the surfaces of biomaterials is an important challenge. The clinical literature testifies that managing thrombosis and inflammation risks through pharmaceuticals is essential for the treatment of patients with cardiovascular implants and extracorporeal circuits. For the cardiovascular interventionist, these risks are often worth taking: trading a potentially life-threatening or debilitating condition (such as a blocked artery or congenital valve disorder) for a risk that can be mediated pharmaceutically represents a cost-benefit trade off. Anticoagulant therapy causes other risks and side effects, requires patient compliance, and is not 100% effective. While the systemic treatment of anticoagulants and antiplatelet therapies may reduce the thrombosis risk, an alternative *localized* approach that prevents clotting on synthetic surfaces without systemic effects is ideal for future iterations of blood-contacting devices. The clinical literature also recognizes that there is a huge unmet need for blood-contacting medical devices that reduce the need for continuous systemic anticoagulant therapy. To identify strategies and develop rational designs for materials with enhanced blood compatibility, it is essential to understand why these outcomes occur when synthetic materials are in contact with blood and why these outcomes do not occur in the healthy vasculature.

Materials scientists and engineers working in the field of blood-contacting materials tend to view this challenge differently than clinicians. The questions “what is blood doing to my material?” and “what is this material doing to my patient’s blood?” result in two very different approaches for solving this problem. Materials scientists have the opportunity to address the perennial challenge of blood-compatible materials from a materials design paradigm which optimizes the features and functions of the material to suit both the long-term performance criteria and the multiple environmental challenges that the material will encounter. Materials scientists can also design functional and responsive materials that dynamically interact with the biological environment.

Blood is a particularly complex biological fluid, containing as many as 4,500 different proteins and peptides, as well as cells that participate in complex and dynamic biological phenomena, including blood clotting and inflammation responses. In healthy blood vessels, hemostasis is the process by which bleeding is stopped through the formation of a blood clot. Hemostasis is essential for maintaining the health of the cardiovascular system by preventing blood loss and by initiating repair of damaged blood vessels. Inflammation is an essential response of the innate immune system, enabling the blood to respond quickly to harmful foreign objects and pathogens. These two remarkably robust processes, blood clotting and inflammation, present enduring grand challenges to the development of blood-compatible materials.

1.1.2 Materials at the blood-material interface

Early attempts to develop blood-compatible materials date to at least the middle ages, centuries before the molecular and cellular mechanisms of clotting and inflammation were understood [3,4]. As early as the 1800s, Freund and Haycraft independently discovered that a surface coated with paraffin wax lengthens blood coagulation time compared to glass [5–7]. They discovered that blood failed to clot upon removal and placement in a tube coated with paraffin wax or when directly added to a solution of paraffin oil [5–7]. However, if the blood contacted a surface that lacked the oily coating, coagulation was induced. These rudimentary observations of blood-material incompatibility by Freund and Haycraft were caused by the same factors which result in blood-device incompatibilities in current clinical practice.

Today, the materials used in blood-contacting applications include a wide variety of organic and inorganic materials, metals, polymers, and ceramics. These materials have a wide variety of composition, surface chemistry and structure. Table 1.1 summarizes cardiovascular and blood-contacting devices and their common materials of construction.

Table 1.1. Common materials used in blood-contacting medical devices.

catheters	hydrophilic and hydrophobic polyurethanes (PU), silicone rubber, polyethylene
tubing	PU, Tygon™, silicone rubber
vascular grafts	polytetrafluoroethylene (PTFE), Dacron®
stents	stainless steel, nitinol
oxygenator fibers	silicone, polymethyl pentene, polypropylene
artificial heart valves	pyrolytic carbon, stainless steel, titanium, Dacron®, PTFE

Despite decades of modern research in blood-contacting materials (preceded by centuries of early failures), we know of no material that is completely blood-compatible for long-term contact with flowing whole blood, other than the inside surfaces of healthy blood vessels [8]. All blood-contacting materials used in medical devices initiate undesirable blood-material interactions, such as thrombosis and inflammation [9,10]. Even supposedly 'inert' or 'passive' surfaces will initiate these responses when in contact with whole blood [11–13]. A key limitation of synthetic materials is that they lack the ability to dynamically integrate with and respond to the biological system through molecular signals, to regulate blood-material interactions. Development of blood compatible-materials will require that the biomaterials scientist acknowledge these limitations, and where possible, mitigate them through new materials technologies. The next sections review some of the key biological responses.

1.2. Thrombosis and inflammation

Thrombosis and inflammation are initiated by the adsorption of proteins onto biomaterials surfaces. Protein adsorption modifies the surface chemistry, often creating a biologically active surface that can specifically interact with blood cells, including platelets and leukocytes. These cells are key initiators of negative blood-material interactions. Platelets are involved thrombosis and leukocytes are primarily responsible for inflammation. While these processes occur on different time scales, they are related as shown in Figure 1.1 and discussed below. The mechanisms of inflammation and blood clotting are not completely independent of one another, leading some authors to consider them as a combined phenomenon [14], or as distinct phases in an overall foreign body reaction [15]; regardless of how they are described, these two mechanisms interact through multiple signals.

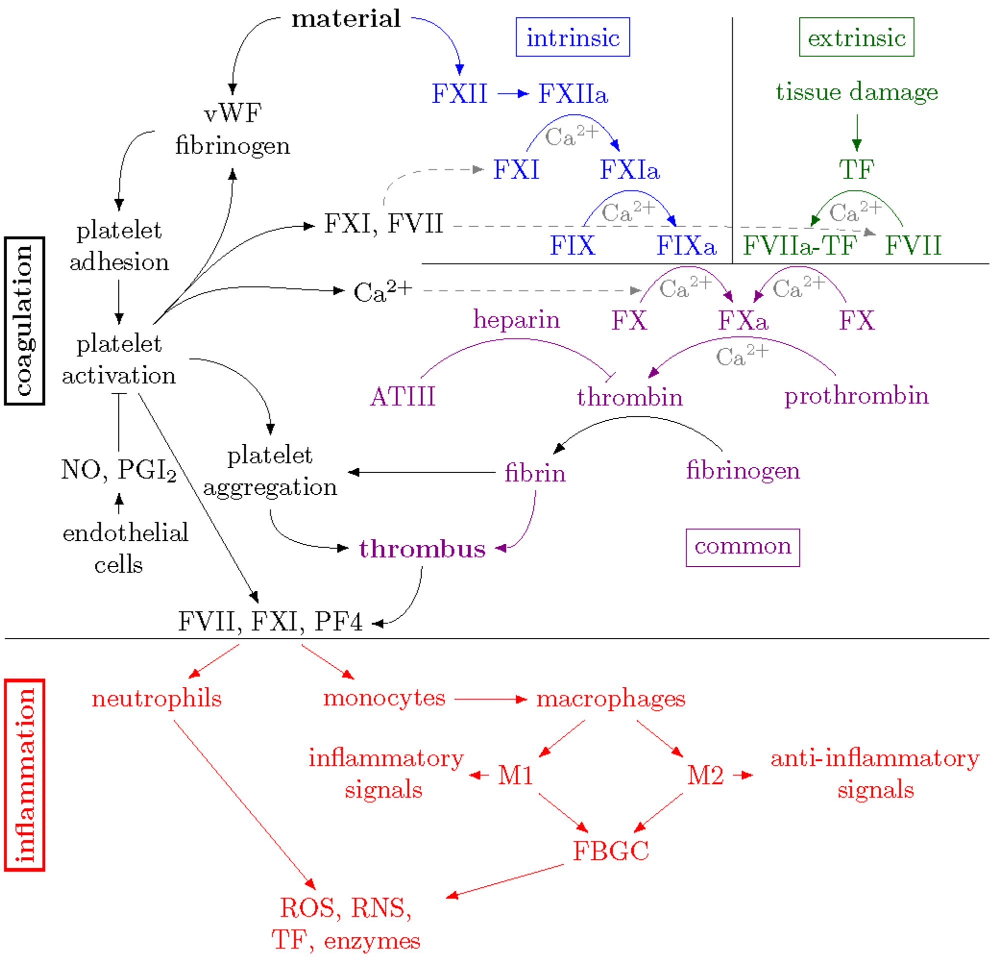

Figure 1.1. Relationships in the coagulation cascade (top) and inflammation (bottom). The coagulation cascade is made up of intrinsic (blue), extrinsic (green), and common (violet) pathways. Inflammation processes are shown at the bottom (red). Attachment, activation and aggregation of platelets, and their associated contributions to thrombus formation are shown in black. The material is shown here as initiating the intrinsic pathway, which is the way this is commonly understood in the biomaterials literature. Nonetheless, the presence of a foreign material can also initiate the extrinsic pathway, for example by inflammatory responses leading to TF production [16].

1.2.1 Costs, consequences, and complicated management of thrombosis

Thrombosis, or the formation of blood clot, is a common mode of failure for cardiovascular implants and extracorporeal circuits. The adverse clinical effects of thrombosis include thrombotic occlusion in grafts, obstruction of stents, embolic complications, and may necessitate the life-long use of anticoagulants [17,18]. A thrombus that dislodges from a biomaterial surface and enters the circulation can occlude blood flow by forming an embolism. Particularly for stents and heart valves, thrombosis and embolism represent high risks for stroke, heart attack, and mortality, and frequently necessitate repeating the procedure or replacing the implant altogether [19,20]. For this reason patients with cardiovascular implants must take anticoagulants and/or antiplatelet drugs indefinitely, leading to complications such as bleeding disorders [21].

Extracorporeal circuits are used in hemodialysis and blood oxygenation. Frequently, these are used in life support systems for critically ill and injured patients that are facing immanent respiratory and/or cardiac failure [22]. Managing thrombosis and bleeding complications for patients on extracorporeal life support adds an additional layer of complexity to the treatment of patients who are already suffering from severe injury or illness [8]. In a retrospective study of adult patients on extracorporeal life support, over 50% of patients had a serious bleeding-related event, with 13.6% being a thrombosis complication [23]. In another retrospective analysis of over 2000 pediatric patients receiving extracorporeal life support, thrombosis occurred in over 30% of cases correlating to a substantial decrease (33%) in survival [24].

Despite these risks, in the past four decades the use of cardiovascular implants and extracorporeal life support has grown dramatically. This growth has been accompanied by continuous improvements in device design and in surgical and managerial procedures that improve outcomes and reduce risks of complications. Notably, this growth has also been facilitated by the development of strategies to manage the risk of thrombosis. The early use of stents was accompanied by high doses of anticoagulant therapeutics, but still resulted in very high rates of thrombosis (~25%), as well as bleeding complications (~9%) [19]. While these rates have been reduced through improvements in stent design, the risk of thrombosis still necessitates long-term systemic anticoagulant and/or antiplatelet therapy. For patients who are in a hospital setting, anticoagulants such as intravenous heparin are administered for the management of thrombosis in procedures involving blood-contacting devices [25]. While anticoagulants can provide symptomatic relief, their associated complications make them undesirable as a permanent solution. As an example, the use of heparin can lead to low platelet counts (thrombocytopenia) and produce internal hemorrhaging that requires platelet transfusions to maintain patient vitality [23,25–27]. For patients on extracorporeal life support due to other injury or illness, bleeding complications can be particularly threatening, were found to be even more common than thrombosis in pediatric patients (38%), and were also associated with a 40% decrease in survival [24]. These studies demonstrate that there is a need to balance the materials interactions with the blood and the goal of patient survival or desired outcomes.

1.2.2 Biological mechanisms of blood clotting

Thrombosis is a multistep sequence of events, illustrated in Figure 1.2, resulting in the formation of a blood clot (thrombus) [16,28]. The typical sequence of events that results in thrombus formation upon device implantation proceeds as follows: (1) protein adsorption, (2) platelet adhesion and activation, (3) coagulation cascade activation and (4) thrombus formation [29]. Upon implantation of a blood-contacting biomaterial, two distinct pathways can act in parallel or separately to trigger clot formation (Figure 1.1) [2,29,30]. These include platelet adhesion and activation and activation of the coagulation cascade which together forms the overall thrombus. The specific interactions of cells and proteins with surfaces and their roles in thrombus formation are described in the remaining subsections of 1.2.2.

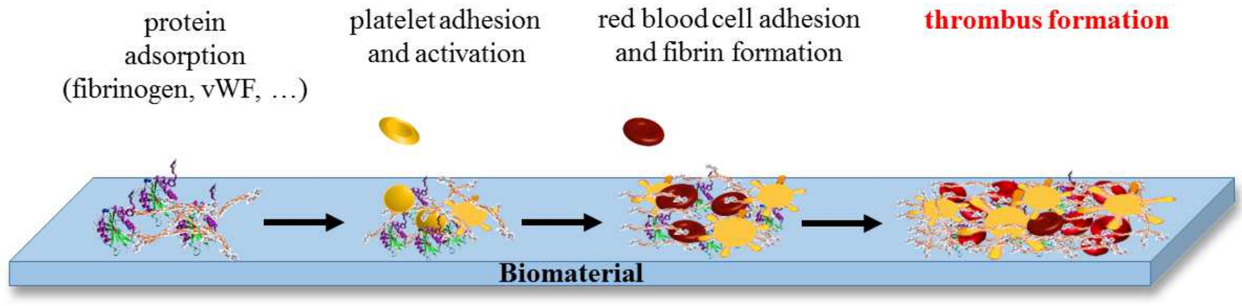

Figure 1.2. Simplified representation of the sequence of events leading to thrombus formation on the surface of blood-contacting biomaterials.

1.2.2.1 Platelets

Platelets are anuclear, disc-shaped cells circulating with a concentration of about 250,000 cells μl^{-1} [31]. Their primary role is hemostasis—preventing blood loss following a blood vessel injury. Prevention of blood loss is accomplished through the formation of a thrombus or blood clot, when blood is in contact with surfaces and tissues other than a healthy luminal wall of a blood vessel. In addition to stopping blood loss, the thrombus also serves as a provisional matrix for subsequent tissue repair. The special role of platelets in thrombosis is why platelets are sometimes referred to as "thrombocytes".

Platelets ordinarily circulate in a quiescent state, suspended in blood, where they co-exist with dissolved blood proteins, such as fibrinogen and von Willebrand factor (vWF) [32]. Platelet quiescence is maintained in part by the action of signals in the blood produced by endothelial cells lining the blood vessel, including prostaglandin I_2 (PGI_2) and nitric oxide (NO) [33,34]. Because platelets have no nucleus, they cannot alter gene expression in response to soluble or surface-bound signals. Nonetheless, platelets are preprogrammed to respond quickly to surface-bound and soluble protein signals presented on a surface, initiating a sequence of events essential to blood clotting. Platelet activation can occur in fractions of a second, leading to the formation of a blood clot in less than five minutes [21]. Surface-induced platelet activation occurs when platelets adhere to surface-adsorbed plasma proteins, such as vWF or fibrinogen, or tissue-specific proteins [31]. Activation is accompanied by platelets rapidly changing their shape, through cytoskeletal rearrangement [31]. Platelet activation is characterized by a morphological change from discoidal (inactivated) to spherical with the appearance of appendages, known as pseudopods, which promote platelet contact and adhesion [35]. Partially activated platelets exhibit multiple short (shorter than the cell body) dendrites or long dendrites (longer than the cell body). Fully activated platelets are flattened and spread on the surface of a biomaterial [36,37]. Examples of platelet adhered to biomaterials in various stages of activation are shown in (Figure 1.3).

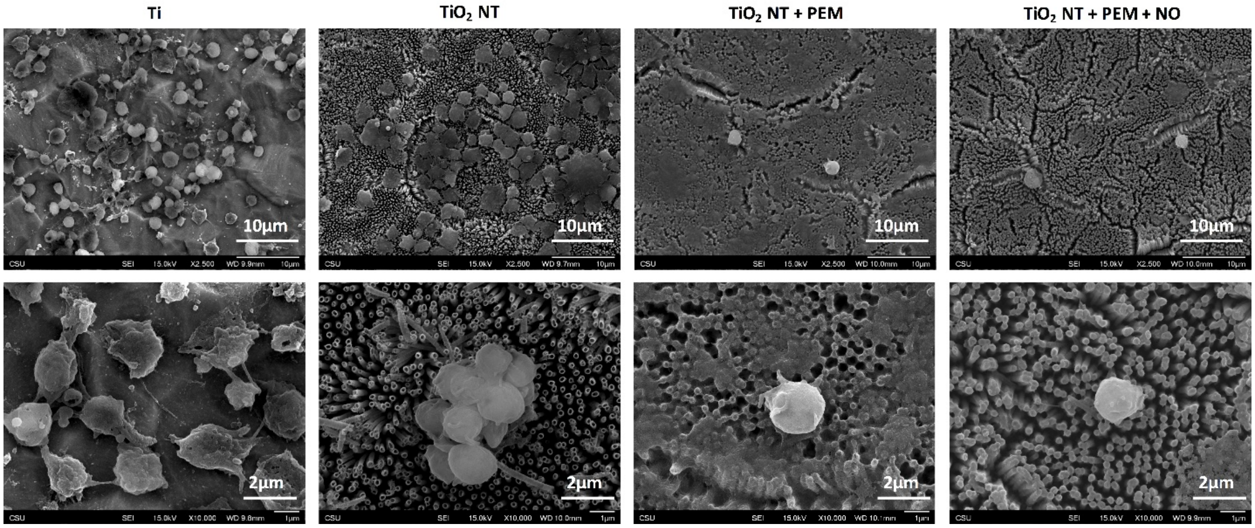

Figure 1.3. Examples of human platelets in various stages of activation, after a 2 hour incubation of human platelets in plasma on titanium and modified substrates. From left to right, platelets on a titanium substrate are spread and fully activated. Platelets on titanium anodized to present titania nanotubes (TiO_2NT) are aggregated, but not fully activated. Platelets on TiO_2NT coated with heparin-containing polyelectrolyte multilayers (TiO_2NT+PEM) are round with few short extensions, and are not aggregated. On a similar surface containing an NO-donor chemistry (TiO_2NT+PEM+NO), very few platelets attach. Attached platelets remain round and do not advance to a further stage of activation. *Reproduced with permission from* [37]*, copyright 2016, American Chemical Society.*

Although platelets circulate in an inactive state, they constantly surveil the endothelium for sites of damage or injury. Platelet interactions with surfaces are mediated by cell surface glycoproteins (GP) [31]. Initial platelet binding to a surface can be mediated by GPIb (often in the GPIb-IX or GPIb-IX-V complexes) interacting with vWF [38]. Elongated vWF on surfaces displays exposed, positively charged vWF-A1 domains which bind to a negatively charged ligand binding domain on GP1b [32]. The GP1b-vWF bond has a shear-dependent bond strength that results in transient binding, enabling platelets to "roll" on vWF-activated surfaces [39,40]. GP1b binding to vWF-A1 and shear-induced rolling produces tensile forces that unfold GP1b, thereby mechanically transducing a signal, which ultimately results inactivation of GPIIb-IIIa [32].

GPIIb-IIIa is an integrin (integrin $\alpha_{IIb}\beta_3$) and is the most abundant receptor on platelet surfaces [38]. It undergoes a conformational change upon platelet activation, enabling it to bind to the arginine-glycine-aspartic acid peptide sequence (RGD), found in proteins such as adsorbed fibrin(ogen) [41,42]. Additional adhesion ligands GPIa-IIa (integrin $\alpha_{II}\beta_1$), and GPVI enable rolling platelets to form strong adhesive contacts with collagen on surfaces [32,38]. GPIIb-IIIa binding to fibrin(ogen) and to vWF is important for platelet adhesion to surfaces, and also enables fibrin(ogen) to link platelets to one another within platelet aggregates [16,41,42]. Mechanical signal transduction also occurs through GPIIb-IIIa, initiating signaling that causes rearrangement of the cytoskeleton, enabling filopodia and lamellipodia formation, and promoting granule secretion [32]. This interaction has been shown to be stronger on stiff substrates than on more compliant substrates. The resulting shape changes of the platelet are identifiable markers of platelet activation.

The interaction between the GP receptors and their ligands induces activation through the release of phospholipase C, leading to an increase in platelet cytoplasmic Ca^{2+} concentration. An increase in the cytoplasmic Ca^{2+} concentration leads to secretions of the granular contents (dense, alpha, and lysosomal granules) and subsequent shape change of the platelet [2,29,30,35]. The secreted granules contain both adhesion molecules, and cytokines. The secreted granules then release their contents, which include Ca^{2+}, platelet factor (PF), fibrinogen, vWF and coagulation factors (F) FXI and FVII. Fibrinogen and vWF provide positive feedback by further activating additional platelets and inducing platelet aggregation [2]. Activated platelets also release additional pro-thrombotic signals, including PF3 and PF4. These interactions are shown on the left side of Figure 1.1.

Platelet adhesion and activation can be influenced significantly by surface topographic features. This requires a rational design approach that considers the feature geometry and inter-feature spacing, and not just an average surface roughness. When the adhesion area (the area accessible to a cell) is smaller than a critical value, platelets may not be able to attach, spread, or activate on a micro- and/or nanostructured surfaces. For example, Koh *et al.* utilized poly(lactic-co-glycolic acid) pillars of various dimensions and proposed that interspacing, width and height significantly influence platelet adhesion and activation. Their proposed optimal range of topographical dimensions of the pillars is: height = 300–800 nm, width =100–200 nm, interspacing < 200 nm [43]. Platelet adhesion and activation on arrays of groove and pillar patterns with various dimensions on TiO_2 surfaces has also been investigated [44]. In this work, groove patterns resulted in much higher levels of platelet adhesion and activation than pillar patterns. In addition, platelets can bridge over spacing between adjacent patterns when inter-feature spacing is smaller than 1.5 μm. Moreover, when inter-feature spacing is larger than 3 μm, platelets cannot bridge but fully contact the entire surface, including the bottom, top, and side-walls of the pattern. Therefore the optimal spacing range for reducing platelet adhesion is between 1.5 μm and 3 μm.

1.2.2.2 The coagulation cascade

In addition to the activation of platelets, thrombus formation involves the blood coagulation cascade which leads to the formation of a fibrin clot [2,29,30,45]. The coagulation cascade consists of a series of proenzyme activations where one activated factor then activates another inactive precursor factor. The coagulation cascade is initiated by either the “intrinsic pathway” or the “extrinsic pathway”. As illustrated in (Figure 1.1), these two pathways converge at the activation of factor X (FX) to the active form, FXa. The conversion of FX to FXa and the subsequent steps make up the “common pathway”.

Traditionally biomaterials scientists have considered the intrinsic pathway to be the most important mechanism because the intrinsic pathway is initiated by FXII activation (to FXIIa) upon adsorption to a material surface. The extrinsic pathway, on the other hand, is activated by damage to tissues, leading to expression of tissue factor (TF) on the surfaces of cells. However, tissue damage can also result directly from the deployment of a cardiovascular implant. Furthermore, TF can also be initiated by a biomaterial that induces inflammatory responses, as TF is a product of inflammation (shown at the bottom of Figure 1.1) [16]. Therefore, both the intrinsic and the extrinsic pathway are important initiators of coagulation in response to blood-contacting materials [16].

In the intrinsic pathway, FXII adsorbs to a surface and becomes activated. This activation can be enhanced by immunoglobulin and albumin [46]. FXIIa, along with other cofactors, activates FXI to FXIa, which subsequently activates FIX to FIXa [2,29,30,45,47]. FIXa then initiates the common pathway by activation of FX to FXa. In the extrinsic pathway, damaged cells express TF which forms a complex on the surfaces of cells with activated FVII (FVIIa). This FVIIa-TF complex can also activate FX to FXa, also initiating the common pathway [2,29,30,45,47].

In the common pathway, prothrombin is converted to thrombin, which cleaves the small fibrinopeptides A and B from the *N*-termini of the Aα and Bβ chains in fibrinogen, as discussed below, to form the polymerizable fibrin [48,49]. Fibrin then polymerizes into fibrin fibers which form a crosslinked network, making up the primary structure of the blood clot. The fibrin(ogen) network also promotes platelet aggregation by providing adhesive links between platelets. Thrombin also provides positive feedback to both the intrinsic and common pathways; thrombin promotes the activation of FXIa and another coagulation factor not shown in Figure 1.1—FVIII [16]. FVIII binds to FIXa and FX, promoting FX activation [16,50]. Thrombin also promotes the activation of FV to FVa which accelerates FXa-mediated conversion of prothrombin to thrombin [16]. The central role of thrombin in activating fibrinogen and in providing positive feedback to the coagulation cascade make thrombin inhibition an important strategy for reducing blood clotting.

Under normal conditions, the vascular endothelium prevents thrombus formation and maintains homeostasis through a variety of factors. These include platelet inhibitors such as PGI_2, adenosine diphosphatase (ADPase), matrix metalloproteinases, and the free radical molecule NO [47]. Heparan sulfate is a glycosaminoglycan (GAG) presented on the surfaces of endothelial cells lining the blood vessel wall. Heparan sulfate binds and activates an important anticoagulant, antithrombin III (ATIII), which inhibits thrombin, FXa, and FIXa [51]. Heparin is structurally similar to heparan sulfate, and has similar activity, making heparin a useful anticoagulant.

1.2.3 Inflammation

Leukocytes or white blood cells are far less abundant in blood, than platelets, at a concentration of about 4000 cells μl^{-1}. This leukocyte fraction includes several important cell types that mediate blood-material interactions, notably neutrophils and monocytes. The monocytes can differentiate into macrophages, which are important mediators of inflammation. Neutrophils and macrophages are both phagocytes, which specialize in eliminating damaged tissue, foreign materials, and pathogens, both by phagocytosis (ingestion) and by secretion of various antimicrobial, digestive, and reactive species. The interactions of these cell types with materials in contact with blood can ultimately lead to a negative response known as the foreign body reaction.

Neutrophil adhesion to biomaterials may be promoted by adsorbed fibrinogen [52]. Upon surface adhesion, neutrophils change the environment by releasing proteolytic enzymes, reactive oxygen species (ROS), and TF [52]. ROS can chemically modify biomaterials surfaces and cause local tissue damage [53]. Neutrophils also secrete pro-inflammatory cytokines such as the interleukin (IL) IL-8, macrophage chemoattractant protein, and macrophage inflammatory protein-1β [15]. The activity of neutrophils at a site of a foreign body response is identified as the acute inflammation phase which typically lasts just a few days.

Neutrophils and macrophages may be recruited to the site of a biomaterial by activated platelets' release of FVII and FXI and by PF4 (Figure 1.1) [15]. Leukocytes use membrane-associated proteins called pattern recognition receptors to identify pathogens and damaged tissue. Biomaterials implanted in the cardiovascular system, such as stents, shunts, catheters and heart valves can all cause injury to surrounding tissue, leading to activation of pattern recognition receptors. There is some evidence that some pattern recognition receptors, such as toll-like receptor-4 (TLR-4) can also be stimulated directly by synthetic biomaterials [54]. TLR-4 has been implicated in determining the response of monocytes/macrophages to materials both *in vivo* and *in vitro* [55,56].

Monocytes circulate in the blood and are recruited to sites of tissue injury and inflammation [57]. Their homing to sites of injury is achieved through chemoattractant signals such as the macrophage chemoattractant proteins and macrophage inflammatory proteins [15]. Monocytes/macrophages express integrins that enable their attachment to both vWF and fibrin(ogen) in the thrombus or provisional matrix [15]. They also express integrins that bind to the complement C3b fragment, and to immunoglobulin that may be adsorbed to biomaterials surfaces [58]. Their activity at the site of biomaterials is associated with the chronic phase of the foreign body reaction which can last weeks to months. Monocytes differentiate into macrophages whereupon they may either promote inflammation, or contribute to its resolution depending upon the local microenvironmental cues (Figure 1.1) [57]. The M1 or pro-inflammatory response is characterized by secretion of pro-inflammatory cytokine signals, such as IL-1, IL-6, IL-8, and tumor necrosis factor-α (TNF-α) [15]. The M2 phenotype is generally considered to be anti-inflammatory, and is characterized by anti-inflammatory cytokine production (e.g. IL-4 and IL-10) [59]. The M2 phenotype is complex, and several subsets of macrophages have been identified, including those which participate in wound healing and remodeling [60]. The adoption of either the M1 or the M2 phenotype is classically referred to as macrophage polarization, though there is recent evidence that macrophages can exhibit both pro- and anti-inflammatory activity simultaneously [59].

Macrophage phenotype has been implicated as an important predictor of tissue healing around implants [61]. Macrophages will attempt to phagocytose foreign materials including implanted biomaterials. For implanted devices with dimensions much larger than the cell body, this phagocytosis is not possible, leading to a state called "frustrated phagocytosis" [58]. Frustrated phagocytosis is thought to be the primary initiator of macrophage fusion, leading the formation multinucleated foreign body giant cells (FBGC), characteristic of the foreign body reaction. Regardless of their polarization, both M1 and M2 macrophages can contribute to FBGC formation

[59]. These cells then produce enzymes, ROS (including superoxide anion, hydrogen peroxide, hydroxyl radicals and singlet oxygen) and reactive nitrogen species (RNS) that can degrade biomaterials, and otherwise alter their surface chemistry [15,59,62,63].

Recent work has hypothesized that materials can be designed with features to guide macrophage polarization. For example, based on the observation that the M1 macrophages are rounded, while M2 macrophages are elongated, McWhorter *et al.* used micropatterned presentation of the adhesion ligand fibronectin, to induce macrophage elongation, leading to modulation of polarization (Figure 1.4) [64]. More recently, surface treatments on titanium have generated significant interest [65–67]. Macrophage phenotype on titanium is of particular interest in the field of orthopedic materials, as macrophage signaling has impacts on bone cell differentiation and matrix deposition. The foreign body reaction to orthopedic implants can lead to poor apposition of implants to host bone, implant loosening, and other complications. The interactions of macrophages with titanium can also be important for cardiovascular implants, as stents and heart valve components are also made from titanium or titanium alloys (Table 1.1). In one study, titanium surfaces that were smooth or were treated to present micron-scale surface roughness exhibited a pro-inflammatory phenotype, unless the surface was treated to be hydrophilic, in which case an anti-inflammatory phenotype was induced [65]. Other studies have shown that nanotexturing on titanium produced by anodization or other techniques can induced M2 polarization [66] or reduce pro-inflammatory phenotypes compared to smooth titanium [67]. These studies demonstrate that better understanding of the mechanisms whereby surface properties influence macrophage polarization will lead to improved control over inflammatory responses. One working hypothesis is that surface chemistry can be used to alter the composition of adsorbed protein layers, which in turn could modify the integrins with which macrophages interact with the surface leading to differential signaling [68].

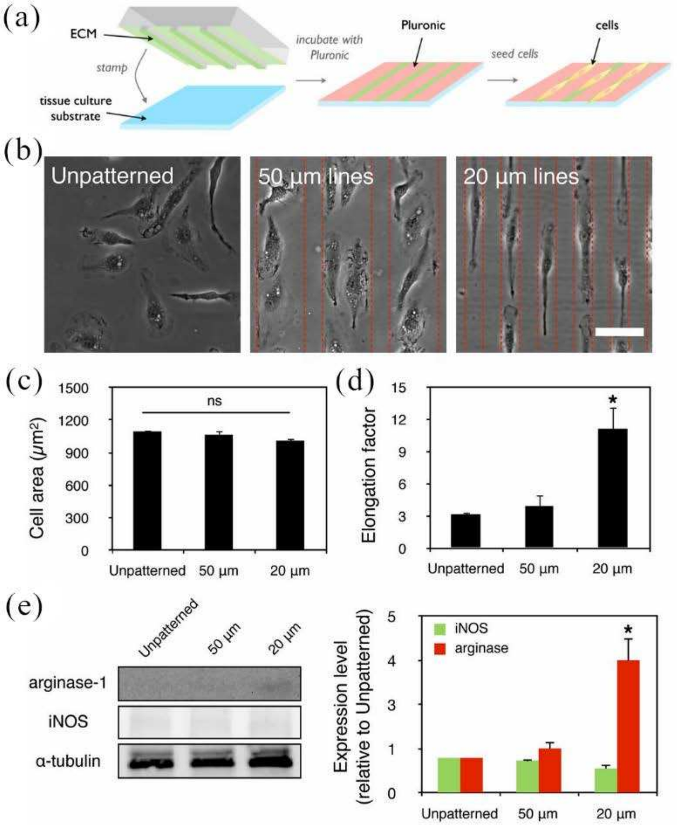

Figure 1.4. Elongation of cells by micropatterning drives macrophage polarization. (a) Schematic of method used to micropattern cells by microcontact printing of arrays of fibronectin lines of various widths. (b) Phase contrast images of unpatterned cells and cells patterned on 50-μm and 20-μm wide lines. (Scale bar: 50 μm.) (c) Quantification of cell area of unpatterned cells and cells patterned on 50-μm and 20-μm wide lines. (d) Quantification of elongation factor of unpatterned cells and cells patterned on 50-μm and 20-μm wide lines. (e) Representative Western blot of iNOS (a marker of inflammatory phenotype), arginase-1 (a marker of anti-inflammatory phenotype), and α-tubulin of unpatterned and patterned cells and quantification across three separate experiments. Error bars indicate the SEM for three separate experiments. *$p < 0.05$ compared with unpatterned cells as determined by the Student's *t*-test. ns, not significantly different. *Reproduced with permission from* [64], *copyright 2013, Proceedings of the National Academy of Sciences.*

1.2.4. Red blood cells and hemolysis

Red blood cells, or erythrocytes, are the most abundant cells in blood, with 4 to 6 × 10^6 cells μl^{-1} [62]. Therefore, understanding their interactions with blood-contacting biomaterials is essential. Unlike the other cell types described above, red blood cells do not typically directly attach and spread on biomaterials. Blood contact with materials, however, can induce hemolysis or the rupture of red blood cells. Hemolysis is often associated with the shear forces induced by abnormal blood flow [69]. Abnormal flow conditions can occur in blood-contacting device components, such as the centrifugal and roller pumps used in extracorporeal blood circuits, but they also occur in and around cardiovascular implants, such as heart valves and stents [69,70].

Hemolysis results in the contents of erythrocytes being released into the blood stream and abnormally high plasma hemoglobin levels (hemoglobinemia). Severe cases can lead to anemia [71]. Hemoglobinemia can be diagnostic of problems with cardiovascular implants and extracorporeal circuits, and has been associated with mortality and other complications [72,73]. Device design geometry, placement, and other complicating health conditions, but not the materials per se, are typically the root causes of severe cases. Nonetheless, materials surface structure and physical chemistry can also have a strong influence on promoting or reducing hemolysis [70,74]. Taken together, the biomaterials scientist must be aware of the materials-related causes and consequences of hemolysis.

1.3. Protein interactions with biomaterials

When a biomaterial comes into contact with blood, nonspecific blood protein adsorption on the surface occurs within seconds. These proteins have a wide range of size, concentration, biological function, and chemical activity that determine their mode of adsorption and their rates of transport to the surface [75]. The initial adsorption is assumed to be reversible. Reversible adsorption can occur through interactions resulting in low affinity with the surface. Over time, irreversible adsorption may occur due to multiple cooperative protein-surface interactions, protein-protein intermolecular interactions, or protein unfolding. As a result, small proteins with higher concentration and low surface affinity, such as albumin, adsorb quickly and reversibly and may be later displaced by larger proteins with high surface affinity, like fibrinogen, leading to a change in the nature of the adsorbed proteins over time [41,76]. This competitive phenomenon is known as the Vroman effect, and leads to protein adsorption exchange on the surface over time [77,78]. Blood clotting on the surface of biomaterials is mainly affected by the type of proteins adsorbed and their structural changes (folded versus unfolded) rather than the total amount of adsorbed protein. As a result, the blood compatibility of biomaterials is frequently evaluated by resistance to nonspecific protein adsorption. Albumin, fibrinogen, vWF, fibronectin, and vitronectin are among the most important blood proteins that mediate blood clotting on biomaterials [41].

Proteins mainly interact with the surface of biomaterials through electrostatic interactions, van der Waals forces, hydrogen bonds, and hydrophobic dehydration. These interactions can lead to reversible or irreversible adsorption. Reversibly adsorbed proteins do not undergo large conformational changes and therefore do not permanently modify the physical chemistry of the surface. Irreversible adsorption often results in the unfolding of the protein (changes in the secondary and tertiary structure) which affect the protein's biological functions and permanently modify the surface physical chemistry. Often the unfolded protein exposes functional protein domains that lead to activation of coagulation or of an immune or inflammatory response [79]. As such, protein denaturation on artificial surfaces is generally considered unfavorable. The irreversibly adsorbed proteins enable the subsequent adsorption of circulating platelets and monocytes, which can then attach and activate [80–82]. Platelets can bind to the specific peptide regions within adsorbed proteins via cell membrane receptors and induce platelet adhesion and aggregation, as described above [83]. This activation results in blood clot formation. The monocytes differentiate into macrophages, which initiate the inflammatory response and foreign body response. These important cell-mediated biological responses are ultimately regulated by the adsorbed proteins. Understanding the behavior of protein interactions with biomaterials is an essential prerequisite to developing rational strategies for blood compatible materials.

1.3.1 Fibrinogen

Fibrinogen is a 340 kD, rod-shaped, dimeric glycoprotein, approximately 47 nm long and 6 nm in diameter, with a plasma concentration of 2-4 mg ml^{-1}. Each dimer of fibrinogen is composed of three distinct chains, designated as the Aα, Bβ and γ chains [84]. Fibrinogen has two important roles in blood clotting: 1) mediating platelet adhesion and 2) providing a structural component to blood clots. Fibrinogen adsorption is a key mediator of cell-surface interactions, promoting both platelet and monocyte adhesion [85]. At low shear rates fibrinogen serves as a major surface-adsorbed protein mediating platelet adhesion, activation, and aggregation, while its role is less significant at high shear rates [86,87]. Adsorption-induced unfolding of fibrinogen exposes platelet binding motifs that are otherwise not accessible to platelet receptors in the folded state of this protein [88]. The degree of adsorption-induced conformational change of fibrinogen can have a greater effect on platelet adhesion than the amount of adsorbed fibrinogen [89]. Non-activated platelets bind through an integrin receptor $\alpha_{IIb}\beta_3$ (GPIIb/IIIa) to receptor recognition sites (RGD) on adsorbed fibrinogen [85,90,91]. The second important role of fibrinogen is in forming crosslinked fibrin fiber networks. When the coagulation cascade is activated, fibrinogen is converted to fibrin monomers through thrombin-mediated cleavage of small fibrinopeptides A and

B from the *N*-termini of the Aα and Bβ chains [48,49]. The fibrin monomers then polymerize and cross-link to form the network of fibrin fibers. This fibrous mesh on the surface of biomaterials provides a scaffold for cell adhesion during blood coagulation, trapping platelets and red blood cells to form thrombus [92–94].

1.3.2 Albumin

Albumin is a 66 kD globular protein with dimensions approximately 14 nm × 4 nm. It is the most abundant protein in plasma at a concentration of approximately 40 mg ml^{-1}. Additionally, albumin is an amphiphilic protein with high surface activity. Since albumin lacks specific sequences for binding platelet receptors, platelets adhere minimally to adsorbed albumin on surfaces. Its high surface activity also makes albumin widely used for blocking other blood proteins, such as fibrinogen, from adsorbing to the surfaces of biomaterials [95–98]. However, some studies have suggested that platelets may bind to adsorbed albumin through a non-canonical interaction, whereby RGD-specific receptors bind to R residues on denatured albumin [99–101]. This binding increases with increasing degree of albumin unfolding on the surface. Beyond a critical level of albumin unfolding platelet adhesion occurs very similar to the mechanism of platelet adhesion on adsorbed fibrinogen [99]. As such, using albumin to block adsorption of other serum proteins may not be sufficient to reduce or prevent platelet adhesion and activation. Preadsorption of albumin must be done in a manner that preserves the folded protein state. Moreover, fully-folded albumin may be only weakly adsorbed. To overcome the Vroman effect in displacing albumin with other proteins, albumin should be covalently bound to the surface when used for surface compatibilization [95].

1.3.3 vWF

vWF is a large multimeric glycoprotein consisting of monomers ranging in size from 500 to 10,000 kD with a plasma concentration of approximately 10 µg ml^{-1}. vWF plays a central role in platelet adhesion and aggregation especially under high shear rates [102–104]. vWF plays a role as a carrier protein for FVIII, protecting FVIII from degradation [105,106]. In circulating blood, vWF multimers remain non-adhesive and adopt a globular conformation [107,108]. In the globular conformation, platelet GPIb binding sites in the vWF A1 domain are shielded [107,108]. Above a critical shear rate ($\dot{\gamma} > 5000\ s^{-1}$) vWF undergoes an abrupt transition from the collapsed to a stretched conformation (Figure 1.5) [109–112]. The stretched conformation has a length of approximately 15 µm that aggregates to form a protein network [109–112]. The shear-induced transition to the stretched conformation enables stretched vWF to recruit platelets by revealing the binding sites for the GPIb. High shear rates occur at sites of vascular injury or atherosclerotic stenoses [113]. High shear rates can also occur at the surfaces of cardiovascular implants and extracorporeal blood circuit components such as centrifugal pumps and extracorporeal oxygenation membranes [113,114]. The wall shear rates in the human circulatory system can range from 20 s^{-1} in large veins to $10^5\ s^{-1}$ in stenotic vessels [115].

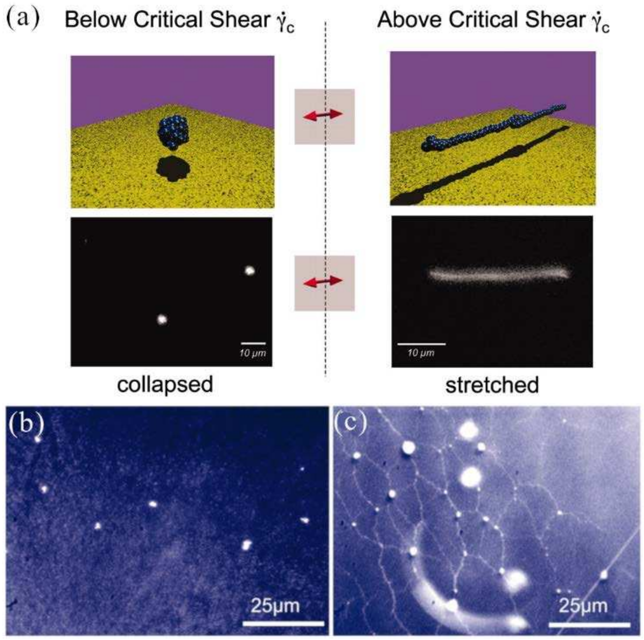

Figure 1.5. Dynamic conformational change of vWF under shear. (a) Cartoon (Upper) and selected fluorescence (Lower) images of a video sequence of vWF below and above the critical shear rate of a few thousand s^{-1}. Above $\dot{\gamma}_{crit}$, the protein is in an elongated conformation. The little yellow spots on the protein are meant to represent a variety of known binding sites. Adhesion of vWF (b) Below the critical shear rate $\dot{\gamma}_{crit}$, only few vWF coils adhere to the collagen coated surface. (c) vWF adhered at high shear rates forms a spider web like network, which represents a very adhesive substrate for blood platelets. *Reproduced with permission from* [109], *copyright 2007, National Academy of Sciences.*

The platelet-vWF interaction is stabilized by activation of platelet integrin $\alpha_{IIb}\beta_3$ leading to platelet aggregation [110,111,116]. Designing surfaces that prevent vWF adsorption is a necessary prerequisite for materials that have contact with blood at high shear rate, since evidence suggests that at high shear rates platelet adhesion is more highly correlated to vWF adsorption than to fibrinogen adsorption on some model surfaces [117–119]. While many studies report fibrinogen and albumin adsorption on biomaterials surfaces, we know of no studies aimed at developing specifically vWF-resistant surfaces. The central role of this blood protein under flow in regulating blood clotting necessitates studies to elucidate design principles for vWF-resistant surfaces.

1.3.4 Complement

The complement system is comprised of more than 50 proteins that interact with immune cells in blood to help them identify and clear pathogens [14]. Complement activation is a series of reactions that leads to the promotion of inflammatory responses of immune cells [120,121]. Complement activation can occur via three different pathways [14]. When antibodies bind to antigens in the blood, the "classical" pathway is initiated. Lectin proteins binding to pathogen-associated mannose glycans activate complement through the "lectin" pathway. The "alternative" pathway is initiated by the spontaneous hydrolysis of a complement protein C3 into two fragments. One of these fragments, C3b, accumulates on pathogenic cells, signaling complement activation. While it is well-known that biomaterials in contact with blood can activate complement, leading to inflammatory responses, the mechanisms of biomaterials-associated complement activation are not entirely clear [16,120]. Direct binding of complement proteins, the nonspecific adsorption of antibodies (leading to the classical activation mechanism) and the accumulation of C3b (leading to the alternative activation mechanism) have all been proposed as possible initiators of complement activation by biomaterials surfaces [15]. Though some experiments suggest that hydrophobic surfaces are more reactive with respect to activating the complement system, both hydrophobic and hydrophilic surfaces (containing either negatively charged or nucleophilic groups) can contribute to complement activation [15,62]. The interactions of blood-contacting biomaterials with elements of the complement system is a less frequently investigated phenomenon but is an important blood-material interaction.

1.3.5 Driving forces of protein adsorption and denaturation

Both nonspecific protein adsorption and protein denaturation play key roles in thrombosis, inflammation and complement activation on the surfaces of materials. A vast amount of the literature on blood-compatible materials is focused on the first of these challenges—reducing protein adsorption. A surface that adsorbs less than 5 ng cm^{-2} of protein in a controlled experiment is said to be "ultra low-fouling" [122]. Surface modification is an efficient approach to make the biomaterials "stealthy" with regard to nonspecific protein adsorption [123]. However, even a small amount of adsorbed proteins on a surface can initiate changes in the surface chemistry and ultimately lead to significant adverse biological responses [124,125]. Comparatively few studies have investigated how surfaces can be designed to address the second of these challenges—preventing protein denaturation. To set the stage for understanding recent advances in the design of blood-compatible materials, this sub-section reviews the driving forces for protein adsorption and denaturation.

Irreversible protein adsorption is often modeled as a series of multiple steps, following a path towards lower Gibbs free energy (G). The minimum in G can be achieved by a decrease in the enthalpy (H) and/or an increase in the entropy (S) at constant temperature.

$$\Delta G = \Delta H - T\Delta S \tag{1}$$

Proteins in solution are stabilized by interactions between peptide residues that include hydrogen bonds, ionic bonds, and internal hydrophobic-hydrophobic interfaces. Their solvent-exposed surfaces are typically hydrophilic, and may also have bound water molecules and associated small counterions (Figure 1.6). Similarly, the surfaces to which proteins adsorb may also have bound water and counterions. Protein adsorption to a surface liberates these bound small counterions and water molecules from both the protein and the surface in a region near the protein-surface interaction, resulting in an increase in entropy. As a protein subsequently denatures, its internal stabilizing interactions must be broken, often leading to the exposure of hydrophobic regions to the solvent. These processes are endothermic (resulting in a positive ΔH and a positive contribution to ΔG) [75,126]. These may be accompanied by the formation of new bonds between the protein and the surface, which are exothermic, but the net enthalpy change of protein adsorption is typically still positive. However, the liberation of counterions and water molecules as well as conformational changes in the protein result in a positive ΔS [127]. Protein denaturation on a surface is therefore assumed to be entropically driven, with the increase in entropy being more than sufficient to overcome unfavorable enthalpy of adsorption, resulting in a net decrease in Gibbs free energy [128].

Protein adsorption depends upon both the dynamics and equilibrium of the entire system, and protein adsorption at solid liquid interfaces is governed by properties of both the solution and the interface. In the liquid phase, protein properties, buffer composition, pH, ionic strength and temperature affect the processes of protein adsorption. At the solid interface, surface chemistry, surface energy, and surface topography impact the protein-surface interaction.

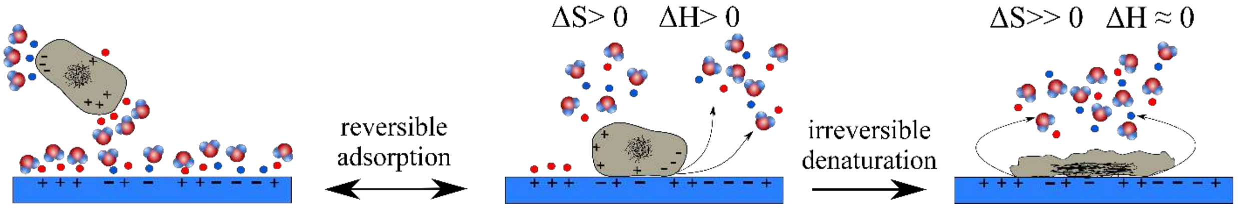

Figure 1.6. Schematic of the thermodynamics of protein adsorption on a biomaterial surface. Both the protein and the surface may have formally charged groups on their surfaces, and may have bound counterions (anions shown in red, and cations shown in blue), as well as bound water. Hydrophobic interactions that stabilize the protein structure are shown as black lines in the interior of the protein. The initial reversible interaction of the protein with the surface may have a positive ΔS (due to release of bound water and ions from the protein and surface interfaces), and a positive ΔH (due to rearrangement of the protein structure). Irreversible denaturation and binding of the protein to the surface is characterized by a large positive ΔS (due to many water molecules and counterions desorbing into solution, and due to rearrangement of the protein secondary and tertiary structure) and a relatively small (close to 0) ΔH as intermolecular protein interactions are exchanged for new interactions within the protein or between the protein and the surface.

1.3.5.1 Protein characteristics influencing adsorption

The unique structure of each protein influences its adsorption behavior on surfaces. Important structural features include size, solvent-accessible surface area, structural stability, net charge, configuration, and amino acid composition. Proteins are high molecular weight macromolecules composed of 20 naturally occurring amino acids. The folded protein surfaces consist of different local patches characterized by positively charged, negatively charged, hydrophobic, and hydrophilic moieties that are dictated by the primary, secondary, and tertiary protein structure [129]. Proteins are broadly classified as “soft” if they readily unfold upon adsorption on surfaces, or “hard” if they are more stable and mobile. Important blood proteins such as albumin, fibrinogen, and immunoglobulin G (IgG) are considered soft, whereas hard proteins include small enzymes, such as lysozyme.

1.3.5.2 Solution characteristics influencing protein adsorption

The solution pH is another parameter that controls protein adsorption through two different mechanisms. Proteins contain weak ionic groups (amines and carboxylic acids) which are sensitive to pH. The isoelectric point is the pH at which the surface net charge of the protein is zero. At pH > pI the proteins are negatively charged in solution and at pH < pI they are positively charged. Proteins exhibit higher adsorption at their isoelectric point (when pH = pI) due to minimized protein-protein repulsions. Electrostatic interactions are another major contributor to protein adsorption on biomaterials controlled by pH [130]. Formal charges of opposite sign on the surface and the protein create electrostatic attractions, increasing transport rates to the surface, and can form ionic bonds that stabilize surface-adsorbed proteins.

The amount of adsorbed proteins on surfaces generally increases at higher temperature due to both thermodynamic and kinetic effects. From a thermodynamics perspective, increased temperature increases both conformational and configurational entropy in the bulk solution

[98,131–133] and increases the liberation of water molecules and ions from solid-liquid and protein-liquid interfaces [126]. Kinetically, at higher temperatures, protein diffusion is accelerated leading to higher protein transport to the surface [75].

Buffer composition and ionic strength can strongly affect protein adsorption behavior on solid surfaces by altering protein solubility [134,135]. The effects of specific ions can be understood by their classification according to the Hofmeiseter series [136]. Kosmotropes (e.g., HPO_4^{2-}, Mg^{2+}, SO_4^{2-}) are highly hydrated and bind water more tightly, reducing the solubility of non-polar groups, and thereby accelerating protein precipitation [137]. On the other hand, chaotropes (e.g., NH_4^+, I^-, NO_3^-) are weakly hydrated and decelerate protein precipitation [137]. Phosphate buffered saline (PBS) at physiological pH is the most commonly used buffer for protein adsorption studies on solid surfaces. PBS usually contains NaCl, KCl, KH_2PO_4, and NaH_2PO_4.

1.3.5.3 Surface characteristics influencing protein adsorption

Surface properties also play a decisive role in the protein-surface interactions. The chemistry [138], topography [139], and surface energy [140] all influence the extent of protein adsorption and possible conformational changes. Researchers have developed materials that to some degree are resistant to nonspecific protein adsorption to enhance blood compatibility of surfaces. Since there is still no biomaterial with absolute resistance to protein adsorption, new materials and surface treatments that eliminate nonspecific protein adsorption for various applications including blood-compatible materials are currently under development.

For nearly 20 years the rules articulated by Whitesides and co-workers [141] have guided much of the research on preventing protein adsorption through surface chemistry. By surveying structure-property relationships of well-defined self-assembled monolayers (SAMs), this group discerned four surface properties that can reduce protein adsorption: (1) hydrophilicity of the surface (polar functional groups); (2) the presence of hydrogen-bond acceptors; (3) the absence of hydrogen-bond donors and (4) neutral overall electrical charge of the surface. The first three of these properties are all related to retaining bound water on the surface. Hydrophilicity is generally quantified by water contact angle measurements (θ_{CA}). Hydrophilic surfaces ($\theta_{CA} < 90°$) are hypothesized to resist protein adsorption since hydrogen bonding to water is so strong that protein cannot displace water from the interface. Hydrophobic surfaces ($\theta_{CA} > 90°$) have low surface energy and more readily release water molecules, inducing protein adsorption. Subsequent protein denaturation can result in inner hydrophobic protein domains interacting with the surface, while their outer hydrophilic domains are exposed to the solution, further stabilizing the adsorbed state. The fourth property—net charge neutrality—can reduce both kinetic and thermodynamic effects leading to protein adsorption. Charge neutrality reduces electrostatic attractions that facilitate protein attraction to the interface. Charge neutrality also may reduce the number of counterions that can be released upon protein adsorption thereby reducing the overall ΔS of adsorption. Taken together, these "rules" suggest that hydrophilic uncharged chemistries probably are among the best candidates for designing protein-resistant surfaces. The question still remains, however, as to whether protein-resistant surfaces provide long-term blood compatibility.

Surface topography is another important factor that influences protein adsorption and subsequent cell behaviors [142–145]. Texture, at the microscale and nanoscale, including features with both vertical and lateral topographical dimensions, increases specific surface area and alters surface energy [146]. These changes may affect the amount of protein adsorption and the conformation of adsorbed protein. Nanoscale topographical features may be more important than features at larger length scales for influencing the interactions of individual protein molecules with surfaces as they are measured at the same length scale as protein dimensions. While several studies reviewed below characterize the effects of surface topography on protein adsorption, there is still no universal set of rules that describe how these features should be chosen to optimize performance.

Studies of protein adsorption on nanostructured model surfaces including titanium, TiO_2, tantalum, and platinum have been reported with the goal of discerning the effects of nanostructure on protein-surface interactions. Fibrinogen adsorption to tantalum and albumin adsorption to platinum are both increased with increasing nanoscale roughness [147,148] while albumin adsorption to tantalum is less affected by surface roughness [147]. One report of albumin and fibrinogen adsorption on titanium found that nanoscale features in the range from about 20 to 200 nm have no effect on the amount of adsorbed protein [149]. The conformation of adsorbed proteins is also potentially affected by nanoscale surface features. For example, fibrinogen adsorbs with an altered conformation on nanopatterned diamond-like carbon and TiO_2 compared to planar surfaces of the same chemistry [143]. It is apparent that the local features on nanostructured surfaces may influence the surface properties such as surface chemistry and surface energy [150] but the overall effects of these surface properties on the extent, orientation, and conformation of adsorbed proteins is not completely understood.

1.4. Strategies for improving blood compatibility of biomaterials

Over the last three decades, research thrusts in biomaterials and surface science have aimed to address the interactions of biomaterials surfaces with blood components, reviewed above. This has led to advances in our understanding of thrombosis and inflammation on biomaterials and the connections between thrombosis and inflammatory responses. Understanding how the physical chemistry of surfaces influences blood-surface interactions is leading to new advances in blood-compatible materials. To combat thrombus formation on artificial blood-contacting surfaces, research has focused on several different materials and surface modification approaches. Various strategies such as incorporation of hydrophilic polymers, bioactive components, bioinspired surfaces, surface endothelialization, and NO release have been proposed. These strategies can be optimized to reduce protein adsorption, control coagulation, and mitigate platelet adhesion and activation, and inflammation. Strategies to reduce protein adsorption have received the greatest amount of attention in this field; studies aimed at understanding how surface properties affect blood cells is also leading to exciting new materials design opportunities. This section highlights the current state of these strategies to improve blood compatibility through materials design.

1.4.1 Polymer brushes

Polymer brushes on solid interfaces represent a unique surface architecture with features that can be engineered to control protein-surface and cell-surface interactions [151–154]. Polymer brushes present a thin film that modifies surface properties such as chemistry, nanotopography, and wettability. These surface properties in turn can be tuned to reduce protein adsorption and cell attachment under physiological conditions. Covalently attached polymer brushes can be prepared by either a “grafting to” or a “grafting from” method [152]. In general “grafting to” (attaching pre-formed polymer chains to a surface) results in lower grafting density than “grafting from” (initiating the polymerization from the surface). However, “grafting to” decouples the polymerization from the brush formation step, affording the opportunity for better control over the polymerization, for example, to achieve lower polydispersity.

1.4.1.1 Physical structure and chemistries of polymer brushes

The physical structure of surface-anchored polymer brushes can be characterized by grafting density and brush thickness [155]. The conformations of the polymer chains attached to a surface are broadly classified as "pancake," "mushroom," "brush," and "highly stretched brush" (Figure 1.7). These conformations are defined based on the reduced tethered density, $\Sigma = \sigma \pi R_g^2$, that determines three regimes. Where R_g is radius of gyration of a tethered chain at specific experimental conditions of solvent and temperature, and the brush grafting density (σ) is determined by $\sigma = (h \rho N_A)/M_n$. ($h$ is dry brush thickness, ρ is bulk density of the polymer, N_A is Avogadro's number, and M_n is the number average molecular weight). The transition from the low grafting density "mushroom" regime to the "brush" regime occurs when $\Sigma > 1$ and the "highly stretched brush" regime is characterized by $\Sigma > 5$ (Figure 1.7) [151,156]. Many researchers have demonstrated polymer brushes that suppress nonspecific protein adsorption [157].

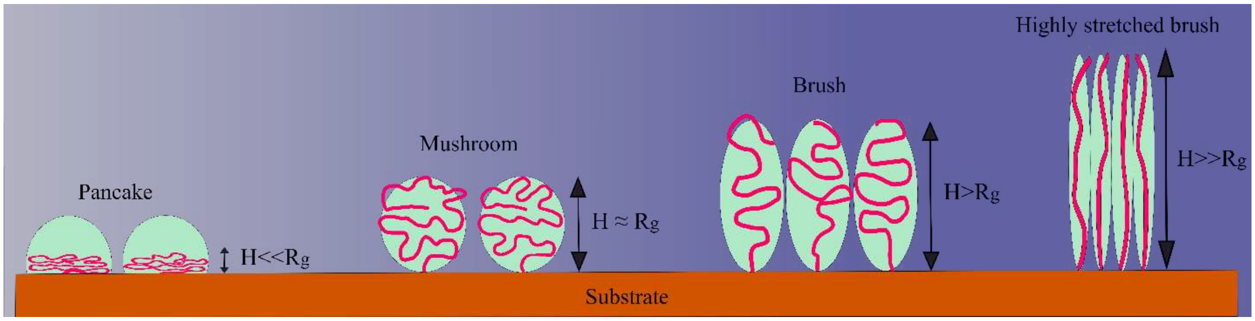

Figure 1.7. Schematic of the conformations that polymer chains tethered to a surface may adopt, as classified based on the polymer chain configuration in relation to the surface and as constrained by the polymer graft density.

Poly(ethylene glycol) (PEG)/poly(ethylene oxide) (PEO) brushes are widely used to create a steric barrier, shielding the surface from fouling by nonspecific protein adsorption. PEG or PEO brushes are often used as a standard for comparison of new surface chemistries and new polymer architectures. Other materials used for preparing protein-resistant and blood-compatible polymer brushes include modified poly(methacrylates) [158], modified poly(acrylamides) [159,160], and poly(2-oxazoline)s (POX) [161,162]. When new materials are developed, the initial studies are usually done to demonstrate how the brush properties affect protein adsorption. Functional biological responses, such as cell and bacterial adhesion, platelet activation, and thrombus formation are assumed to be regulated by initial protein adsorption. However, comparatively few studies investigate these important downstream biological responses in detail. The literature reviewed in this section focuses on results that are particularly relevant for blood-contacting materials, beginning with protein resistance of PEG/PEO brushes.

1.4.1.2 Mechanisms of protein resistance

The ability of nontoxic and non-immunogenic PEG/PEO brushes to suppress protein adsorption has been attributed to ‘‘steric’’ repulsion from high mobility of polymer chains, hydrogen bonding with water to form a hydration shells, and very low electrostatic interactions between protein and the PEG/PEO layer [163–165]. In the highly-stretched brush conformation, protein adsorption is prevented primarily by a kinetic barrier; the brush slows protein diffusion to the underlying surface, and confinement retards local brush mobility [166,167]. Tethered polymer chains that interact favorably with the surface may also prevent protein adsorption thermodynamically, via site-blocking, by competing for the surface [166,168]. The differences between these kinetic and thermodynamic barrier mechanisms is difficult to verify experimentally. Nonetheless, the relative effects of these two mechanisms is important for the long-term performance of protein resistance. Surfaces that resist protein adsorption primarily through kinetic barriers will not perform well in long-term applications. However, for short-term applications, they may perform more favorably. Therefore, the time scale for the application of the surface in contact with blood should be considered when designing protein-resistant and blood-compatible polymer brushes.

1.4.1.3 Tuning PEG/PEO brushes to optimize protein and cell resistance

Many studies have shown grafting density, brush thickness, and polymer molecular weight have essential impact on extent, orientation, and overall rate of protein adsorption as well as affinity for unfolded proteins [169–172]. Polymer brush hydrophobicity also can be tuned to optimize protein resistance. Hydrophobicity of the brush can be modified by selection of the terminal functional group on a PEG/PEO chain, and by selection of polymer chain and substituent functional groups. Important recent findings also show that hydrophobicity of PEG/PEO brushes is dictated by their structural properties.

Grafting density can modulate the hydrophobicity of the brush. Therefore, resistance to protein adsorption and stabilization of protein conformation are not necessarily improved monotonically by increasing grafting density. The optimum grafting density and brush thickness depends upon the PEG/PEO molecular weight [170,171]. The correlation between the protein adsorption and the amount of water contained within different polymer brushes was investigated recently. The water content inside the polymer brushes strongly impacts the extent of protein adsorption; brushes having the highest water content more efficiently resist protein adsorption [173]. Molecular dynamics simulations have revealed that hydration of PEO brushes depends on the accessibility of water inside the grafted layer. Therefore at lower grafting densities PEO is well-hydrated ($\sigma < 1.5$ chains nm^{-2}) with the exception of the close vicinity of the substrate [174]. By increasing the grafting density (with highest $\sigma = 4.18$ chains nm^{-2}), however, the polymer volume fraction increases and the PEO grafted layer becomes dehydrated [174]. The relative degree of hydration may impact the local hydrophobicity of the brush. Recently, it has been shown that by increasing PEG grafting density (from 0.16 to 0.34 chains nm^{-2}) the rate of fibronectin adsorption decreases, but adsorbed fibronectin unfolds more readily and the unfolded fibronectin remains on the surface for longer residence times relative to folded molecules (Figure 1.8) [171]. The same authors later showed that PEG brushes are spatially heterogeneous, presenting nanoscale hydrophobic niches on the surface, and that these hydrophobic niches increase with the surface grafting density of the polymer chains (Figure 1.8) [175]. This phenomenon may explain denaturation of surface-adsorbed proteins at high grafting density. Interestingly, static contact angle of both low and high grafting density PEG surfaces was identical despite the existence of nanoscale hydrophobic niches, indicating the inability of conventional macroscopic measurements to elucidate such differences [175].

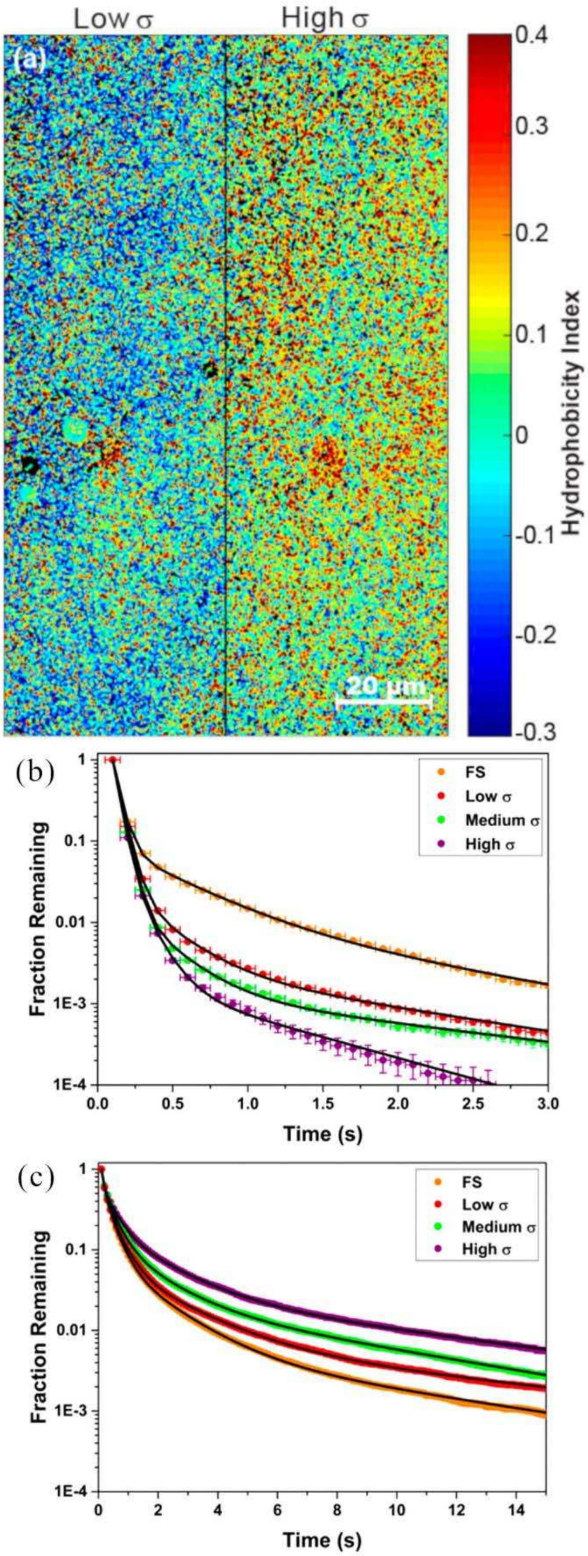

Figure 1.8. (a) Single-molecule observations provide detailed local information about nanoscale hydrophobicity in PEG brushes. Super-resolution maps generated from accumulated NBD-X trajectories for both high and low grafting density PEG brush surfaces (6×10^5 and 1×10^6 trajectories, respectively). The color scale indicates the differences in local hydrophobicity based

on the parameter HI. (b) and (c) The apparent surface residence time of unfolded molecules increased with grafting density, confirming that the apparent increase of unfolded molecules at high grafting densities was due to an increase in surface residence time. Complementary cumulative surface residence time distributions for molecules that were (b) always folded and (c) always unfolded on bare fused silica and various PEG brushes, as annotated. Each distribution was fit to an exponential mixture model (black lines). *Reproduced with permission from* [171,175], *copyright 2016 and 2018, American Chemical Society.*

Many researchers have studied how the brush thickness, molecular weight, and chain terminus chemistry of PEG/PEO brushes affect nonspecific blood protein adsorption. PEG/PEO brushes have also been used to reduce adsorption of a wide variety of proteins, bacteria, platelets and cells [176–181]. Emilsson *et al.* [182] presented a new grafting-to method that uses Na_2SO_4 in the solvent, allowing for high grafting density to be achieved. They grafted different molecular weights of both methoxy- and hydroxyl-terminated PEG and investigated irreversible binding of 10× diluted serum. Surface plasmon resonance (SPR) data clearly showed that 2, 5, and 10 kDa methoxy-terminated PEG brushes, with thicknesses between 6 and 25 nm provide good serum resistance that exceeds the performance of oligo(ethylene glycol) (OEG) monolayers. A trend of reduced protein adsorption with increasing brush height was observed from 2 kDa to 10 kDa PEG brushes. For higher molecular weight (20 kDa and 30 kDa) the protein resistance is reduced, and these PEG brushes do not out perform OEG monolayers. The best performance was achieved for hydroxyl-terminated 10 kDa PEG, which corresponded to 4 ng cm^{-2} adsorbed proteins. They concluded that their strongly stretched PEG brushes provide a kinetic barrier to blood protein adsorption rather than an equilibrium barrier. In a similar study, grafting densities from 0.26 to 1.60 chains nm^{-2} were obtained in different concentrations of Na_2SO_4 from 5 kDa methoxy-terminated PEG [183]. This study found that increasing PEG graft density reduced BSA adsorption to below the detection limit using quartz crystal microbalance measurements [183].

Riedel *et al.* also prepared different brushes using a grafting-from method, to identify proteins responsible for blood plasma fouling on PEG- and OEG-based surfaces [158]. In their work, mixed alkane thiol SAMs were compared to PEG brushes (-COOH, -OH, and -OCH_3 terminated) and to brushes made from methacrylate polymers with grafted OEG side chains (-OH and -OCH_3 terminated). The poly(methacrylate-*g*-OEG) graft copolymer brushes are much thicker than the PEG brushes, and result in less deposited blood proteins compared to PEG brushes. The authors concluded that closely packed brush structure prevents the penetration of the fibrinogen, human serum albumin (HSA), and IgG into the brush layers regardless of the hydrophilic or hydrophobic end groups on the graft copolymer brushes. On PEG-OH and PEG-COOH polymer brushes, however, HSA, and IgG proteins were detected. SPR data also confirmed that the mass of plasma deposited on the surfaces decreased in the order SAM > PEG > poly(methacrylate-*g*-OEG) brushes.

An important outstanding issue with PEG-/PEO-based brushes is the durability of their antifouling properties in physiological and oxidative environments [184,185]. PEG/PEO may be oxidized by exposure to air and physiological environments, over hours to days, altering the chemistry and structure of the brush [186–188]. When in long-term contact with biological systems, enzymes, ROS and RNS may alter the chemistry of biomaterials, including PEG/PEO, reducing their ability to resist protein adhesion [189]. Development of alternative chemical structures with improved durability is an important direction for future research.

1.4.1.4 POXs and poly(2-oxazine)s

POXs provide access to a different polymer chemistry and have become a prominent PEG/PEO alternative, because of their biocompatibility [161,162]. These hydrophilic polymers contain hydrogen bond acceptors and bear no formally charged groups, consistent with the

Whitesides criteria, described in section 3.5.3. Furthermore, the hydrophilicity and mechanical properties can be tuned by simply changing the side chain of the monomer, and their antifouling properties can be retained for longer periods than PEG/PEO [162,184]. The longer term stability of their antifouling properties may be related to higher resistance to oxidation compared to PEG/PEO [190]. Poly(2-alkyl-2-oxazoline)s (PAOXAs), in particular the poly(2-methyl-2-oxazoline) (PMOXA) and poly(2-ethyl-2-oxazoline) (PEOXA), have been emerging as very promising candidates to modulate the interfacial, chemical, and mechanical properties for enhancing antifouling properties [191–194]. Several studies have reported the grafting of PAOXAs to PU (PU-*g*-PEOXA)s [195], poly(methylacrylic acid) (PMAA-*g*-PMOXA) [196], poly(ethylenimine) (PEI-*g*-PMOXA) [197], poly(L-lysine) (PLL-*g*-PMOXA) [198] as well as brush copolymers of 4-vinylpyridine (PMOXA-*r*-4VP) [199] that to some extent showed resistance to protein adsorption, platelet attachment, and other cell attachment.

A recent study by Tang *et al.* investigated a series of poly[oligo(2-alkyl-2-oxazoline)methacrylate] (POAOXMAs) brushes by grafting from the surface of SPR chips [200]. They characterized the amount of protein adsorption using bovine serum albumin (BSA), fibronectin, and fetal bovine serum (FBS) on POX-based brushes and PEG-thiol monolayers. They investigated the effects of surface hydrophilicity/hydrophobicity and brush thickness on protein adsorption. All brush films performed significantly better compared to the PEG monolayer. The poly[oligo(ethylene glycol)methacrylate] (POEGMA) (13 nm thick, water contact angle = 53°), and poly[oligo(2-ethyl-2-oxazoline)methacrylates] (POEOXMA-Me, 21 nm thick, water contact angle = 58°) showed only very little adsorption from all protein solutions studied. However, when the POEOXMA-Me thickness is reduced to 12 nm, more BSA and serum were adsorbed [200]. This result could be because of the slightly increased hydrophobicity of POEOXMA-Me, compared to POEGMA. For poly[oligo(2-methyl-2-oxazoline)methacrylates] (POMOXMA-Me, water contact angle = 28°) with 12 nm thickness, adsorption was low for BSA and fibronectin. FBS adsorption for POMOXMA-Me had intermediate values of protein adsorption compared to POEGMA and POEOXMA-Me. The authors concluded that adsorption of small molecules from serum is based on diffusion into spaces between polymer brushes rather than brush hydrophilicity [200].

In another recent study, Morgese *et al.* generated poly(2-methyl-2-ozazine) (PMOZI) grafted to PLL (PLL-*g*-PMOZI) on SiO_2 surfaces and compared the interfacial physicochemical properties of brushes with PLL-g-PEG, PLL-g-PMOXA, and PLL-g-PEOXA (Figure 1.9) [201]. PMOXA and PMOZI brushes showed the most hydrophilic character. They tested the protein resistant of PLL-g-X films, exposing them to 10% human serum (HS) and FBS for 1 hour. All the brushes significantly reduced protein adsorption compared to the bare SiO_2 surface. PMOZI and PEOXA brushes were the most, and the least antifouling films form HS and FBS despite the fact that the hydrophilicity of PMOZI and PMOXA are very similar. The authors believed that the differences in antifouling activity stem from the higher flexibility of PMOZI chains that generates an efficient entropic barrier with respect to PAOXA counterparts (additional methylene group). PMOZI brushes also presented a very strong barrier towards cell (chondrocyte) attachment. After a 24 h incubation there was no cell attachment (Figure 1.9). The percentage of cell attachment on surfaces decreased in the order SiO_2 > PLL-*g*-PEOXA > PLL-*g*-PEG> PLL-*g*-PMOXA brushes. The authors concluded that the combination of high hydration and enhanced chain flexibility generates a significant barrier against protein and cell attachment.

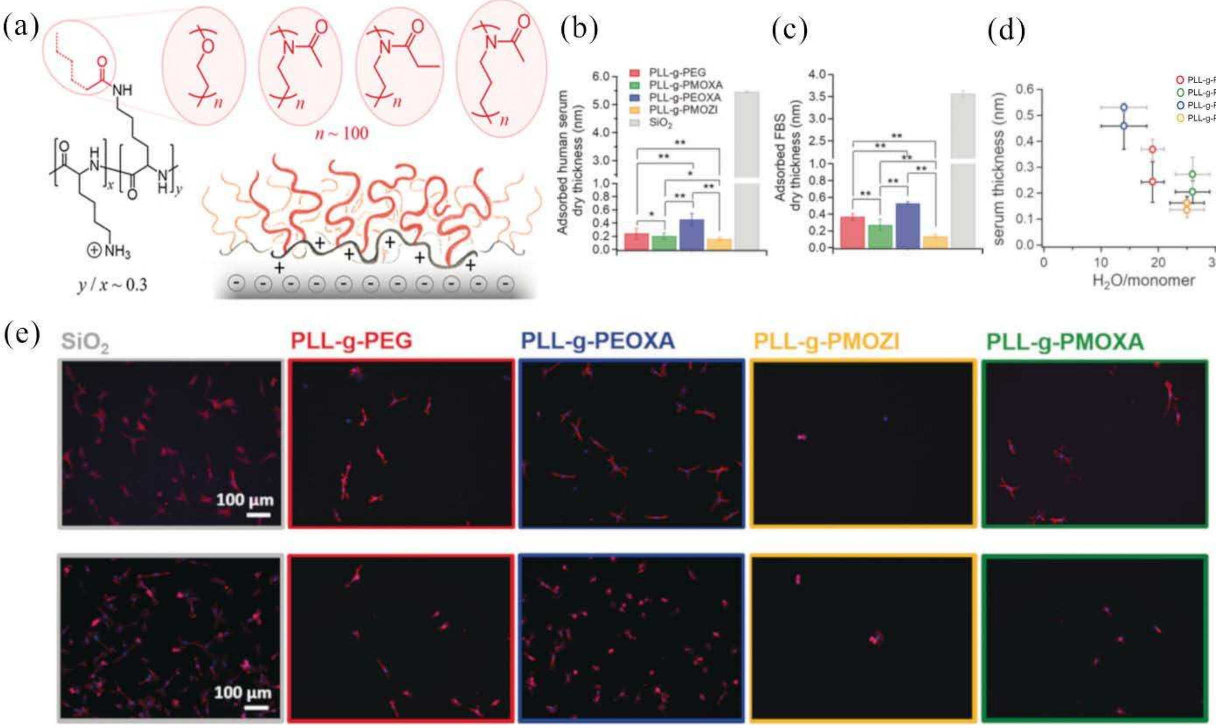

Figure 1.9. (a) Surface functionalization with brush-forming graft copolymers of different side-chain compositions. All of the brushes significantly reduced the amount of adsorbed protein both from HS and FBS compared to the bare SiO_2 surface. Protein adsorption from (b) 10% HS and (c) 10% FBS on PLLg-X films measured by variable angle spectroscopic ellipsometry after 1 h of exposure. (d) Amount of adsorbed proteins as a function of polymer brush hydration (H_2O/ monomer). (e) Representative immunofluorescence micrographs highlighting chondrocytes adhered on the different films are reported in (first row) (without 10% FBS) and (second row) (with 10% FBS). *Reproduced with permission from* [201], *copyright 2018, John Wiley and Sons.*

1.4.1.5 Other synthetic approaches

Other synthetic approaches are also widely used to prepare polymer brushes that reduce nonspecific protein adsorption and subsequent thrombus formation. Polymer brushes from poly(amides), poly(thiophenes), poly(acrylamides), and poly(methacrylates) can also be tuned to reduce adsorption of a single protein, proteins from human blood serum or plasma, and/or bacteria adhesion and/or cell attachment [202–208]. Poly[*N*-(2-hydroxypropyl) methacrylamide] (poly(HPMA)) and poly(carboxybetaine acrylamide) (poly(CBAA)) brushes grafted from gold surfaces exhibit very low protein adsorption, reduce the adhesion of leukocytes, erythrocytes, and reduce thrombosis formation in short-term (< 1 h) studies [159,160]. When these polymer brushes are translated to polycarbonate (PC) substrates, they drastically reduce fouling from full human blood plasma compared to the bare PC for short contact time (10 min) under flow [209]. In another study from this group, uniform polymer brushes of poly(2-hydroxyethyl methacrylate) (PHEMA) and poly(methacrylate-*g*-OEG) were grafted from chitosan hydrogel surfaces to produce coatings for implantable biosensing devices [210]. The polymer brushes exhibited better resistance to protein fouling from single protein solutions and from diluted human blood plasma in a short-term study compared with bare chitosan hydrogel. They also prevent the adhesion and activation of platelets and leukocytes after 60 min contact.

This body of work affirms that the underlying mechanisms whereby polymer brushes reduce protein adsorption on materials surfaces can be elucidated, and that these mechanisms can be linked to tunable brush properties, such as brush density, hydrophobicity/hydrophilicity, and molecular weight. Many of the fundamental studies on polymer brushes have been conducted on model surfaces optimized for interrogation by particular high-resolution analytical techniques (e.g. gold surfaces used for SPR). The translation of these polymer brushes to materials already used in blood-contacting applications, with control over brush properties is a technological challenge for some material types. While polymer brushes provide promising surface types for resisting protein adsorption, their stability for long-term blood-contacting applications remains an important open question. Future studies should continue to develop rational design principles for blood-compatible polymer brushes and should anticipate the need for long-term stability, particularly in a potentially oxidative environment created by a local inflammatory or foreign body response. To that end the interactions of promising polymer brush surfaces with specific cell types involved in blood clotting and inflammation should also be further investigated.

1.4.2 Zwitterionic interfaces

Although polymer brushes reviewed above can be tuned to suppress nonspecific protein adsorption and subsequent fouling from whole blood, chemical stability decreases in the presence of metal ions and oxygen which significantly reduces their antifouling properties. Zwitterionic interfaces are an attractive alternative to polymer brushes for preventing protein adsorption. Zwitterionic materials possess both anionic and cationic groups with overall neutral charge. Two primary classes of zwitterionic materials have been most widely studied: (1) betaines that carry both cationic and anionic groups on the same monomer unit such as carboxybetaines and sulfobetaines and (2) polyampholytes which are copolymers, carrying a 1:1 ratio of positively and negatively charged groups on two different monomer units [211].

1.4.2.1 Mechanism of protein resistance

Surface modification of biomaterials with zwitterions to inhibit fouling can be achieved either by adsorbing as a two-dimensional monolayer (2-D) or by creating three-dimensional polymer brushes (3-D). Both 2-D and 3-D zwitterionic surfaces prevent protein adsorption by enthalpic and entropic mechanisms. The antifouling ability of both types of coatings is mainly attributed to formation of a hydration shell via ion-dipole interactions with water, which are much stronger than hydrogen bonds, creating a stronger enthalpic resistance to protein adsorption than similar PEG/PEO surfaces or other types of polymer brushes [212]. Moreover, since zwitterion surfaces contain paired positively and negatively charged groups covalently attached to each other, there is no release of small counterions to provide an entropic driving force for protein adsorption (compare Figure 1.6) [213]. Zwitterionic polymer brushes (3-D), have the benefit of an excluded volume effect that works as an additional entropy penalty preventing proteins from approaching the surface [211].

1.4.2.2 Tuning zwitterionic surfaces to optimize blood compatibility

Zwitterionic biomaterials have gained special attention for designing blood-compatible surfaces because of their resistance to nonspecific protein adsorption, platelet adhesion and activation, cell attachment, and thrombus formation [214–224]. Yang *et al.* reported that protein adsorption from undiluted HS and plasma on poly(carboxybetaine) brushes is undetectable at both 25 °C and 37 °C by SPR for approximately 1 h exposure [225]. This group also grafted zwitterionic copolymers containing anionic and zwitterionic blocks of poly(11-mercaptoundecyl sulfonic acid)-*b*-poly(sulfobetaine methacrylate) (PSA-*b*-PSBMA) onto a positively charged surface with controlled surface density [226]. The resulting zwitterionic copolymer brushes reduce protein adsorption to approximately 0 ng cm^{-2} using fibrinogen solution, and < 10 ng cm^{-2} in 100% HS and plasma. They also reported zero blood platelet adhesion and blood cell attachment in a short-term experiment.

PU materials are widely used in medical devices that have contact with blood despite their poor blood compatibility. Several studies report reduced biofouling on zwitterion-modified PU surfaces compared to commercially available PU [227–229]. In particular PU modified with zwitterionic chemistries can reduce biofouling from blood. In a recent study, PU was modified with three types of zwitterionic brushes to improve biofouling properties [230]. All three types of zwitterionic brushes reduced the blood protein adsorption, platelet adhesion, and cell attachment on the PU surface. One of the few studies demonstrating long-term blood-compatibility used poly(sulfobetaine) to modify the inner and outer surfaces of PU-based peripherally inserted central catheters (PICCs) (Figure 1.10) [231]. Modified catheters significantly reduce thrombus accumulation after 60 days of exposure to serum compared to unmodified and commercial catheters that were used less than one day in serum. This demonstrates the long-term protection against thrombus formation (Figure 1.10). Significant reductions of protein, mammalian cell, and microbial cell attachment *in vitro* and *in vivo* were also observed on modified PICCs compared to commercial PICCs.

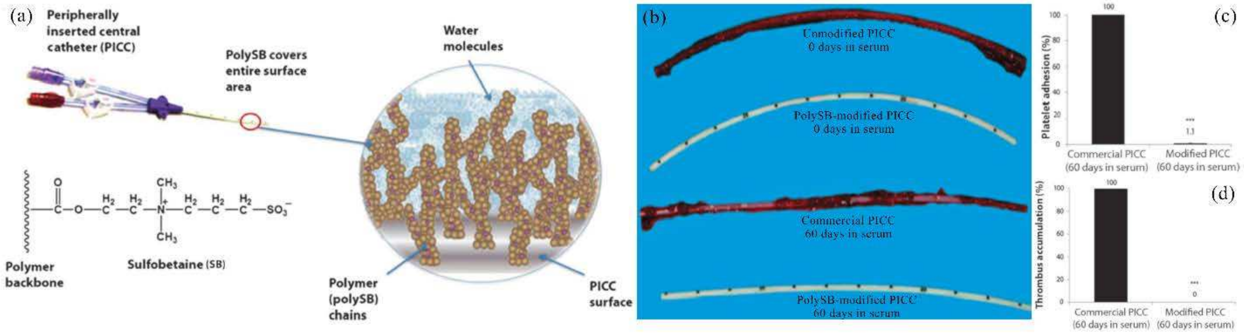

Figure 1.10. (a) PolySB modification of PICC (peripherally inserted central catheters) surface. PolySB is bound to the surface of the PICC to form a conformal polymer surface. The zwitterionic polySB modification coordinates both free and bound water molecules to create a hydrophilic surface. (b) PolySB-modified PICC has reduced thrombus accumulation. Catheters were exposed to bovine blood in a flow loop system. Image shows variations in thrombus accumulation with different PICCs. (c) PolySB-modified and commercial PICCs were exposed to serum for 60 days. Adherent platelet data from serum-exposed polySB-modified PICCs were normalized to serum-exposed commercial PICCs. (d) Accumulated thrombus was removed from serum-exposed polySB-modified and commercial PICCs and weighted. Weight data were normalized to the commercial PICCs (60 days in serum). For (c) and (d) actual average percentage of values are indicated above each bar. *Reproduced with permission from* [231], *copyright 2012, The American Association for the Advancement of Science.*

Improvements in hemocompatibility of membrane oxygenators have facilitated the increased use of extracorporeal membrane oxygenation in recent years [232]. Several studies have demonstrated reduced blood protein adsorption, platelet adhesion, and/or cell attachment on membranes modified with zwitterionic materials [233–238]. Wang *et al.* coated the surfaces of a polypropylene hollow fiber membrane oxygenator and its connecting tubes with a zwitterionic copolymer bearing hydrophobic *N*-butyl and crosslinkable trimethoxysilyl side chains (PMBT) [239]. This modification significantly reduces fibrinogen adsorption, platelet adhesion and activation, and blood cell attachment. Moreover, thrombus formation is significantly reduced on the modified membrane, compared to the unmodified membrane using whole canine blood circulated for 2 hours (Figure 1.11).

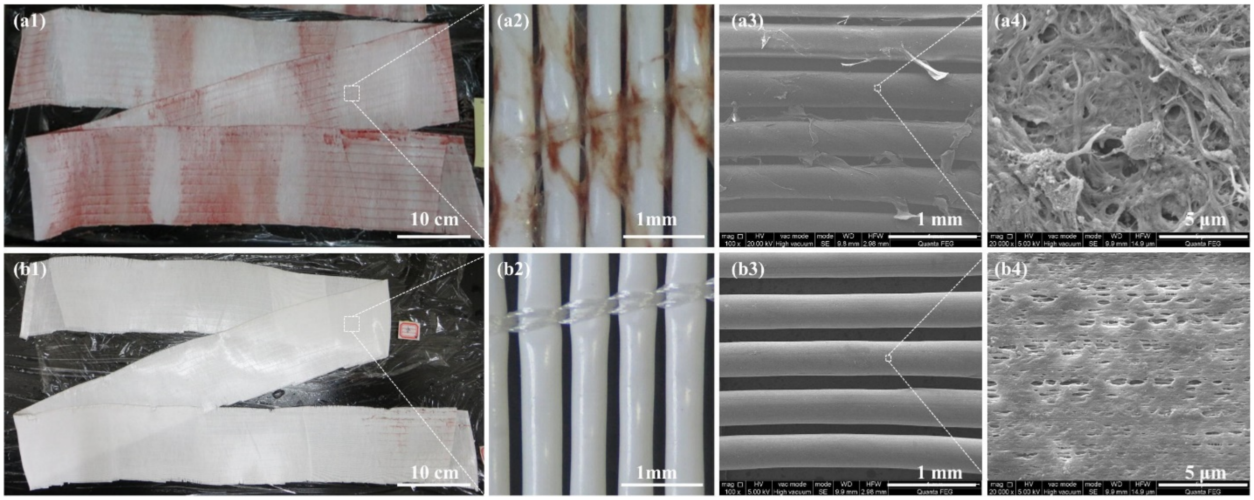

Figure 1.11. Zwitterionic copolymer PMBT coated oxygenator membrane has reduced thrombus accumulation. Optical microscope and SEM images of the bare (a1, a2 and a3, a4) and PMBT copolymer coated (b1, b2 and b3, b4) polypropylene hollow-fiber membranes after circulation with dog blood for 2 h. *Reproduced with permission from* [239], *copyright 2016, Elsevier.*

Modification of surfaces with zwitterionic chemistries is a promising strategy for improving blood compatibility of blood-contacting materials. While a relatively small number of zwitterionic chemistries have been studied in detail, these model chemistries have demonstrated that reduced protein adsorption can be correlated to improved performance in both long-term and whole blood studies, as shown above. The general strategy of using zwitterions could be expanded to other chemistries that are scalable and manufacturable to improve the prospects of these types of surfaces.

1.4.3 Bioactive surfaces

Surface immobilization of bioactive molecules or biopolymers including polysaccharides, peptides, enzymes, and antibodies has attracted considerable attention for designing antifouling surfaces. This section discusses heparinized surfaces, surfaces modified with direct thrombin inhibitors and immunomodulators, and surfaces modified with other biopolymers.

1.4.3.1 Heparin and heparin mimics

Heparin coatings to improve blood compatibility of surfaces have been in clinical application for over 30 years. For example, the CBAS (which stands for Carmeda bioactive surface) of Carmeda AB® was developed from early work of Larm *et al.* [240], in which heparin is covalently bonded to the substrate. This surface has been used in a variety of blood-contacting applications including extracorporeal circulation devices (Medtronic plc), ventricular assist devices (Berlin Heart GmbH), vascular stents, stent grafts, and vascular grafts (W.L. Gore & Associates, Inc.) [241].

Heparin is a naturally occurring GAG that possess structural similarity to heparan sulfate. Heparan sulfate is a key component of the glycocalyx presented by the endothelial cells lining the inside surfaces of blood vessels. Heparin inhibits FXIa, FIXa, FXa, and thrombin, thereby inhibiting blood clot formation [8]. For long-term blood compatibility of heparinized biomaterials, heparin can be immobilized by surface conjugation. The immobilized which binds ATIII through an active pentasaccharide sequence [242]. For example, heparin was bound to aminated poly(1,8-octanediol-*co*-citrate) (POC) onto POC-modified ePTFE vascular grafts material and remained bioactive up to 28 days [243]. The modified grafts were shown to significantly reduce platelet adhesion and clot formation during that period. Several studies have also reported that heparin immobilization to poly(lactic acid) (PLA) membrane surfaces improves hemocompatibility of dialysis membranes [244,245]. In another study, small-diameter nanofibrous vascular grafts using a thermoplastic polycarbonate-urethane (PCU) were electrospun and fabricated [246]. The surface was modified via plasma treatment and subsequent covalent conjugation with heparin (Figure

1.12). The patency of heparin-conjugated PCU grafts was investigated by implanting grafts with an inner diameter of 1 mm and approximate length of 1.0 cm in the left common carotid artery of rats. Compared to untreated grafts, much more surrounding tissue around the heparin-modified grafts was observed with visible microvessels indicative of vascularization after 4 weeks (Figure 1.12). Moreover, anti-thrombogenic activity of the immobilized heparin prevented occlusion as a consequence of thrombosis in the synthetic grafts. Cross-section staining for CD163, which is a marker of M2 (anti-inflammatory) macrophages, showed some positive cells in the tissue surrounding both the plasma-control and plasma-heparin grafts after 4 weeks *in vivo*, indicating some anti-inflammatory macrophage phenotype (Figure 1.12).

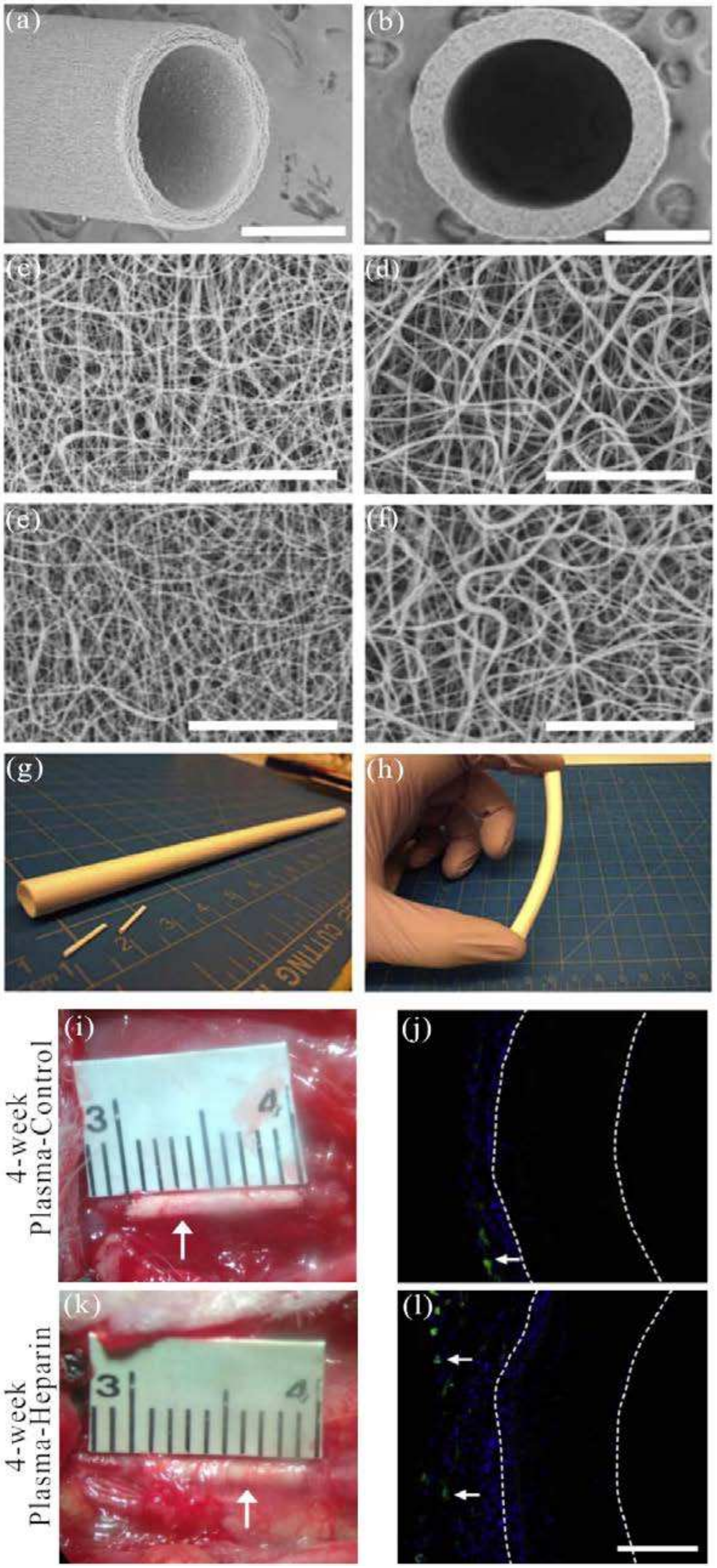
(a)
(b)
(c)
(d)
(e)
(f)
(g)
(h)
(i)
(j)
4-week
Plasma-Control
(k)
(l)
4-week
Plasma-Heparin
3
4

Figure 1.12. Structural characterization of nanofibrous PCU vascular graft, explantation of the grafts, and inflammatory response of PCU plasma-control and plasma-heparin grafts after 4 weeks *in vivo*. SEM images taken from (a) side and (b) top view of an electrospun PCU vascular graft. Structure of nanofibers in the (c) inner (luminal) and (d) outer surface of the vascular graft before the plasma treatment; structure of nanofibers in the (e) inner and (f) outer surface of the vascular graft after the plasma treatment. (g) Nanofibrous PCU vascular grafts of various inner diameters (i.e. 1-mm and 6-mm) were fabricated to demonstrate the versatility of the electrospinning method. (h) Bending of a 6 mm-diameter PCU graft to confirm desired mechanical property. Scale bar = 500 μm in a, b; scale bar = 30 μm in c, d, e, f. (i) 4-week plasma-control graft *in situ* taken immediately prior to explantation. (k) 4-week plasma-heparin graft *in situ* taken immediately prior to explantation. White arrows indicate noticeable microvessels and vascularization in the surrounding tissue of the grafts. Immunostaining for CD163 (j and l) of the cross-sections obtained from the vascular graft of the plasma-control and plasma-heparin grafts after 4 weeks *in vivo* was performed. White arrows indicate cells positive for CD163, within the graft wall. White dashed lines delineate the border of the graft wall. Cell nuclei were stained using DAPI (blue). Scale bar = 100 μm. *Reproduced with permission from* [246], *copyright 2017, Elsevier.*

Heparin immobilization with other biomolecules on the surface of biomaterials to inhibit thrombus formation and accelerate endothelialization is another promising method for developing blood-compatible materials. Co-immobilization of heparin and fibronectin on the surface of titanium reduces fibrinogen denaturation, platelet activation and aggregation, improves blood compatibility, and increases ATIII binding density compared to unmodified titanium [247,248]. Modified surfaces also exhibit improved endothelial cell compatibility compared to Ti surfaces. Recently, RGD and heparin were grafted onto PTFE surfaces coated with dopamine (PTFE-DA) via a thin layer of PEI to promote endothelial cell affinity and to improve blood-compatibility of PTFE (Figure 1.13) [249]. While RGD-modified PTFE-DA increased platelet adhesion, the addition of heparin co-immobilization dramatically decreased platelet adhesion and improved human umbilical vein endothelial cell (HUVEC) affinity (Figure 1.13).

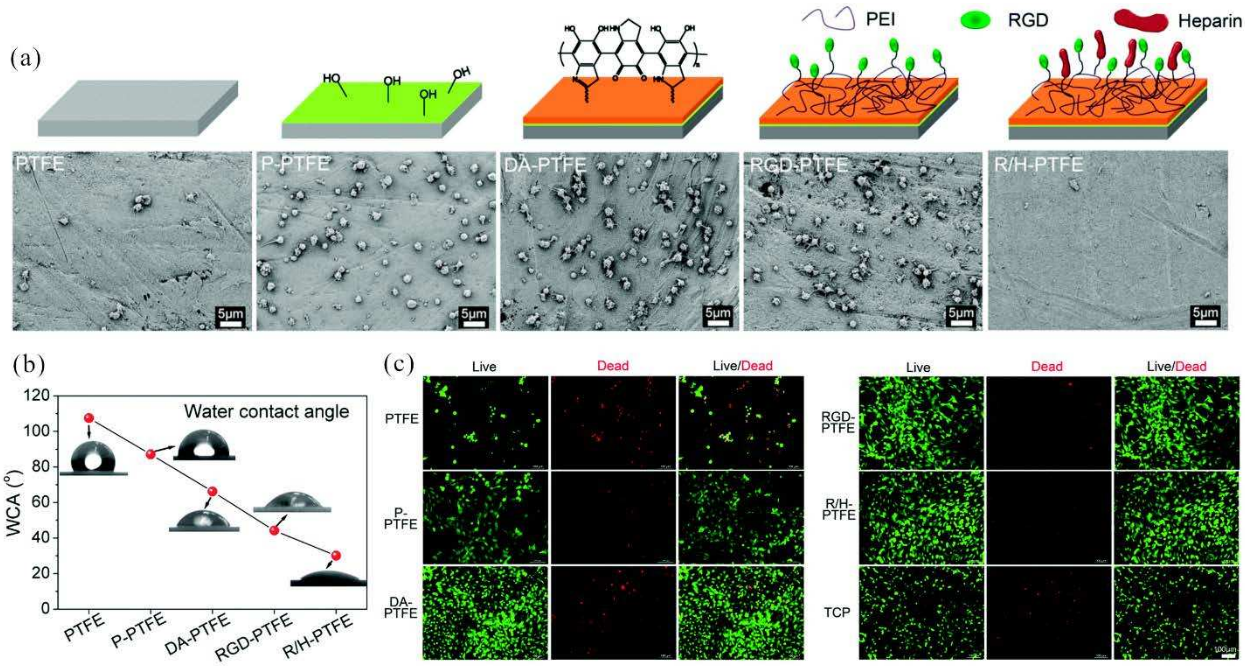

Figure 1.13. (a) SEM images of platelets attached to PTFE, P-PTFE (plasma-treated PTFE), DA-PTFE (Dopamine-coated P-PTFE), RGD-PTFE (RGD-grafted PTFE), and R/H-PTFE (RGD/heparin-grafted PTFE). (b) Water contact angle results of different PTFE samples. (c) Fluorescence images of HUVECs cultured on different PTFE substrates for 7 days. Live cells were stained with calcein-AM (green) and dead cells were stained with EthD-1 (red). *Reproduced with permission from* [249]*, copyright 2018, The Royal Society of Chemistry.*

Since the ability of immobilized heparin to preserve ATIII is a key attribute to retain its anticoagulant activity, chemical conjugation should retain this important functional activity [250,241]. However, heparin coating on the surface of biomaterials has a number of limitations. Heparin is known to bind to many plasma proteins other than ATIII, including fibrinogen, which reduces heparin efficacy over time and which may increase protein adsorption [251]. More importantly, at least one specific anticoagulant function of heparin is dependent on a pentasaccharide sequence to activate ATIII, but only one-third of commercial heparin molecules contains this sequence [241]. As an alternative to heparin coating, immobilization of an antithrombin-heparin covalent complex (ATH), which restricts access for the binding of other plasma proteins and has at least one pentasaccharide sequence, was proposed to increase anticoagulant activity [252,253]. Immobilized ATH on gold surfaces reduces fibrinogen adsorption and binds significantly higher amounts of ATIII from plasma compared to heparinized surfaces [253]. Moreover, this group also showed that ATH immobilization on poly(dimethyl siloxane) (PDMS) modified with polydopamine (PDA) (PDMS–PDA–ATH) has the ability to inactivate FXa well beyond the surface without ATH (PDMS–PDA), suggesting that the activity on this surface is mainly due to the specific inhibition of FXa by the heparin moiety of the ATH [254].

Another alternative to heparin is synthetic and semi-synthetic heparin-mimicking polymers. These are attractive alternatives for preparing blood-compatible surfaces. Compared to heparin, they have better defined chemical structures, higher purity, and greater stability, with comparable anticoagulant activity [255]. Heparin mimics are designed to contain sulfate, sulfamide, and carboxylate groups. For biomedical membranes, for example, modification with heparin-mimics is of tremendous interest, enabling reduced blood protein adsorption, platelet adhesion and aggregation, and improved blood compatibility [256–259]. Modification with heparin mimics is also used to modify other blood-contacting materials. In a study by Chen *et al.* vinyl-functionalized PU was modified with copolymers of 2-methacrylamido glucopyranose and sodium 4-vinylbenzenesulfonate, to include both saccharide and sulfonate groups (Figure 1.14) [260]. The optimum of 2:1 ratio of sulfonate to saccharide surface resulted in reduced fibrinogen and HSA adsorption from human plasma, suppressed platelet and human umbilical vein smooth muscle cell (HUVMSC) density, and increased HUVEC density (Figure 1.14). This optimum ratio also resulted in the longest plasma clotting time compared to bare PU and other fabricated surfaces. The authors concluded that by regulating the content of sulfonate and saccharide, a multifunctional surface with anticoagulant properties and the ability to endothelialize and inhibit intimal hyperplasia could be achieved.

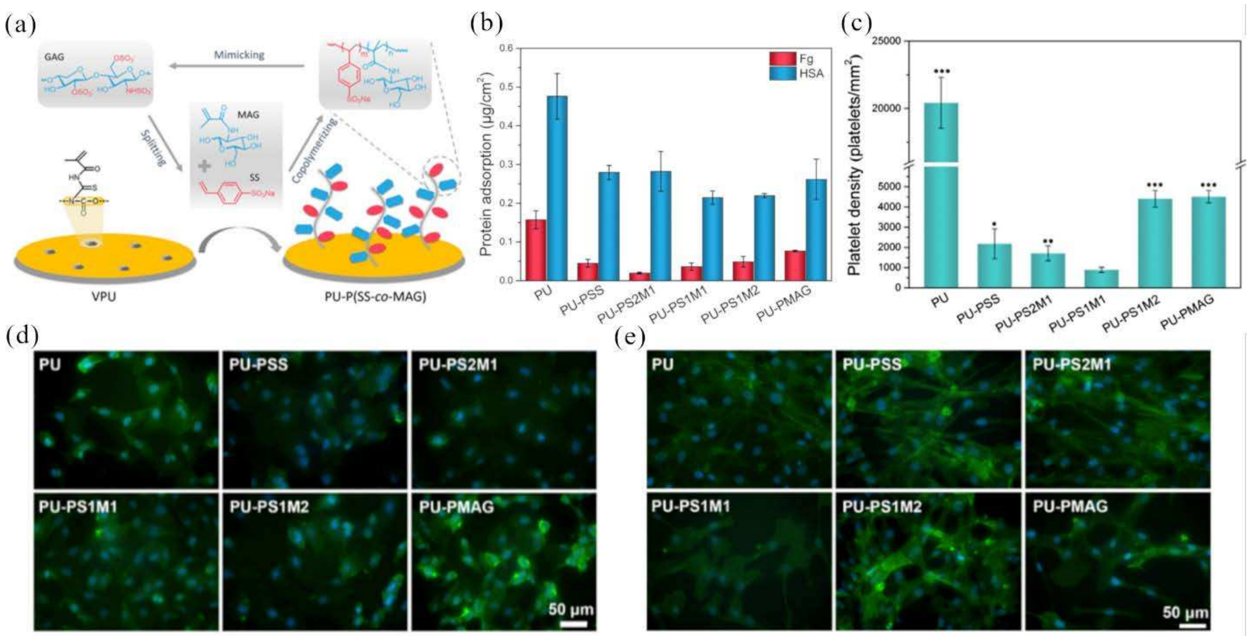

Figure 1.14. (a) Schematic depicting procedure for the preparation of PU-P(SS-*co*-MAG) surfaces. (b) Adsorption of Fg (fibrinogen) and HSA (human serum albumin) from human plasma to unmodified PU and PU surfaces grafted with PSS (sodium 4-vinylbenzenesulfonate), PMAG (2-methacrylamido glucopyranose), and P(SS-*co*-MAG). (c) Density of adherent platelets. (d) Fluorescence images of HUVECs on surfaces after 48 h culture. (e) Fluorescence images of HUVSMCs on the surfaces after 48 h culture. The cells were co-stained for nuclei (DAPI; blue) and F-actin (Phalloidin-FITC; green). *Reproduced with permission from* [260]*, copyright 2018, American Chemical Society.*

1.4.3.2 Direct thrombin inhibitors and immunomodulators

Unlike heparin, direct thrombin inhibitors including hirudin, hirudin derivatives, argatroban, and other peptides directly block the thrombin active site. Hirudin is a small protein and is the most potent known natural direct thrombin blocker [261]. It has been used as a biomolecule for modification of some biomaterials [262,263]. For example, hirudin immobilization reduces clotting on the surface of PLA membranes [264]. A major limitation of hirudin modification over heparin immobilization is that hirudin acts through a one-to-one stoichiometry, with each hirudin molecule on a surface irreversibly inhibiting only one thrombin molecule. This stoichiometric limitation results in short-term anticoagulant activity of hirudin-modified surfaces [265]. Hirudin alternatives such as bivalirudin have been developed that, unlike hirudin, bind thrombin reversibly. Bivalirudin was covalently conjugated on polymerized allylamine coated 316L stainless steel to develop blood-compatible surfaces [265]. The resulting surfaces extend clotting times, inhibit platelet adhesion and activation, reduce fibrinogen adsorption, and significantly enhance endothelial cell adhesion, proliferation, and migration.

Argatroban is a synthetic direct thrombin inhibitor that reversibly binds to both free and clot-associated thrombin. Furthermore, argatroban is able to inhibit several procoagulant factors (FV, FVIII, FXIII) and platelet aggregation [266]. Argatroban chemically immobilized on the surface of polyurethane–silicone polymer (CarboSil®) was applied as a surface coating to the inner lumen of poly(vinyl chloride) (PVC) extracorporeal circuit tubing [267]. Thrombosis was evaluated using a 4 h rabbit extracorporeal circuit model and demonstrated significantly less thrombus formation compared to the control CarboSil®, as measured by the thrombosis area.

Immobilization of immunomodulatory molecules such as CD47 and CD200 on the surface of biomaterials is a strategy to reduce inflammation. These proteins are recognizable by immune cells via specific inhibitory receptors. When these immunomodulatory molecules bind to their cognate receptor, they function as a molecular marker of self that reduces the material-induced inflammatory response [268]. Immunomodulation with CD47, a ubiquitously expressed cell membrane protein, has become a promising approach to develop blood-compatible, immune evasive biomaterials. Stachelek and coworkers have shown immobilization of recombinant CD47 on PVC and PU surfaces reduces inflammation, human neutrophil activation, and platelet adhesion and activation, compared to unmodified surfaces [269,270]. In a follow-up study from this group, immobilization of CD47 on metallic stent surfaces was shown to significantly reduce inflammatory cell attachment without impeding endothelial cell retention and expansion [271]. Moreover, stents functionalized with an active peptide from the extracellular domain of CD47 prevented thrombus deposition and reduced restenosis by 30% in a rat model. In a recent study, multi-immobilization of heparin, stromal cell-derived factor-1α (SDF-1α), and CD47 on the surface of PTFE was performed to improve blood-compatibility, endothelialization and anti-inflammatory properties of vascular grafts [272]. The multi-functionalized PTFE exhibited reduced blood clotting (heparin impact), increased the recruitment of endothelial progenitor cells (SDF-1α impact), and reduced the inflammatory immune responses of monocytes-macrophages (CD47 impact) compared to the bare PTFE.

1.4.3.3 Drug release

The release of small-molecule drugs or other therapeutics is another way to impart specific biological functions to materials. Antithrombogenic drugs can be incorporated into blood-contacting materials to inhibit thrombosis for the duration of the drug release [273,274]. To improve blood compatibility of materials via controlled drug release, this approach has been primarily implemented by combining antithrombogenic agents with the erosion of a biodegradable polymer. Antithrombotic agents include biopolymers, such as heparin, peptides, such as bivalirudin, and small molecules, such as dipyridamole (DPA) and aspirin [275–278]. For example, covalent incorporation of the DPA into biodegradable polycaprolactone-based PU has been investigated, for use in heart valves [279]. In vitro characterization indicates that DPA is homogeneously distributed in the materials and is released slowly throughout the polymer degradation process for 130 days. After incubation of the synthetic materials in platelet rich plasma for 2 h, significantly reduced levels of platelet adhesion and activation were observed compared to the control surfaces without drug. Moreover, the modified PUs support cell adhesion and proliferation for two types of human vascular cells: HUVEC and HUVSMC. In another similar and consistent study, a series of randomly crosslinked PU (PU-DPA) were prepared using polycaprolactone (PCL), hexamethylene diisocyanate (HDI) and DPA through a one-step/one-pot synthesis method (Figure 1.15) [280]. DPA content was tuned by varying the molar ratio of DPA to PCL to achieve various PU-DPA ratios. The results obtained for hemolysis showed that all of the surfaces were observed to cause less than 2% of hemolysis and there existed a trend of reduced hemolysis with the increase in DPA amount in the PU. Furthermore, increasing amounts of DPA incorporated into the PU resulted in reduced platelet adhesion; substantially reduced platelet adhesion was observed only for PU-DPA (70:30) compared to unmodified PU, which is in agreement with the amounts of lactate dehydrogenase (LDH) released by the adhered platelets (Figure 1.15). Furthermore, a platelet study was conducted after 14 days of enzymatic degradation of PU-DPA materials. Significantly reduced platelet adhesion was reported on the enzyme-degraded PU-DPA (70:30) compared to degraded PU-DPA (100:0) and glass.

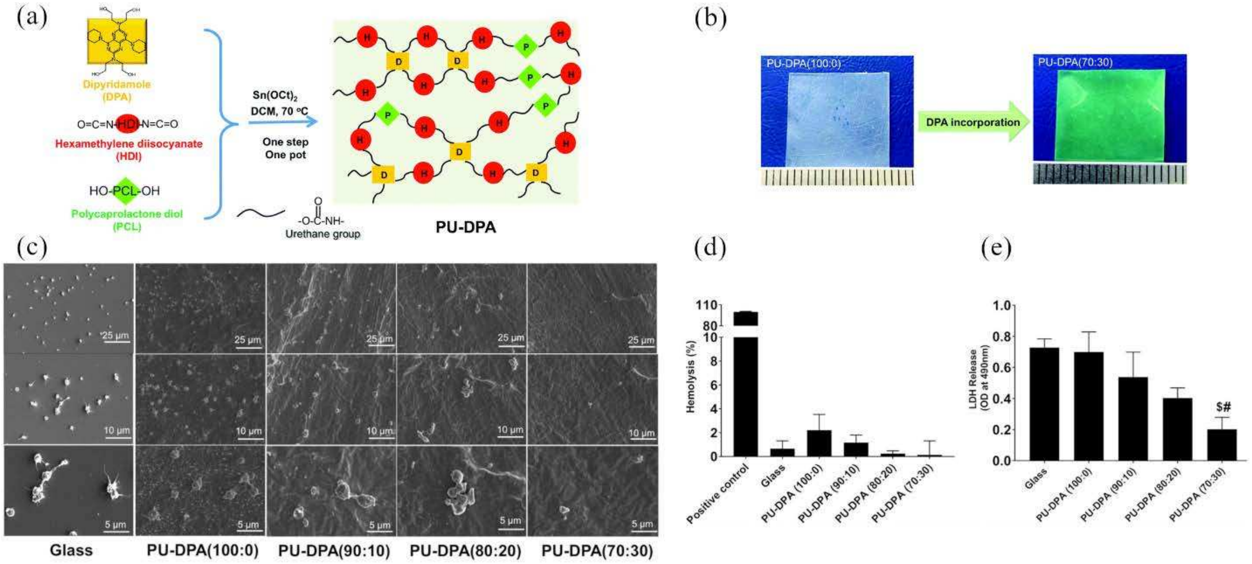

Figure 1.15. PU-DPA synthesis and hemocompatibility assessment of PU-DPA films. (a) Synthesis scheme of PU-DPA from polycaprolactone (PCL) diol, hexamethylene diisocyanate (HDI) and an antithrombogenic drug, dipyridamole (DPA). (b) Digital images to show the color change with PU-DPA films after DPA incorporation. (c) SEM images to show platelet deposition and morphology on PU-DPA films. (d) Percentage of red blood cell lysis after 2 hour exposure of whole blood with PU-DPA films (n = 4). DI water- and saline-diluted blood served as positive and negative controls, respectively. Glass is used for a comparison for blood testing studies. (e) amount of LDH released by triton-treated platelets after adhering on to PU-DPA films in 1 hour incubation at 37 °C. *Reproduced with permission from* [280], *copyright 2018, The Royal Society of Chemistry.*

To create longer and more effective antithrombotic agent release, several bio-responsive polymer hydrogels have been developed based on a controlled and on-demand release system [281–285]. Hydrogels have the ability to be used as smart materials that respond to changes in the physiological environment [286]. The signal feedback-controlled system can be designed to be responsive to the levels of thrombin triggering antithrombotic agent release in a thrombin-responsive mode which further quenches the blood coagulation cascade. For example, a hydrogel system with thrombin-sensitive peptide sequences has been developed to prevent clotting [283]. A high level of blood thrombin causes cleavage of the gel, leading to heparin release to inactivate thrombin, reducing blood clotting. Heparin release also prevents additional thrombin-cleavage of the gel, making the system capable of on-demand delivery. The synthetic bio-responsive hydrogel was exposed to freshly drawn whole blood without any soluble anticoagulant. Blood was protected from clotting for a 1 h time period. Whereas blood in contact with the non-responsive gels and clinically applied PTFE vascular graft materials with and without immobilized heparin completely coagulated in the same time period. In another feedback-controlled anticoagulation system, a thrombin-responsive patch that can be inserted in the skin was designed to prevent undesired blood clot formation [284]. In this hydrogel, a thrombin cleavable peptide acts as a linker during the conjugation of heparin to the main chain of hyaluronic acid (HA). The heparin release profile is sensitive to thrombin concentration. The *in vivo* studies in a mouse model demonstrated effective protection from acute thrombosis.

1.4.3.4 Other biopolymers

Natural biopolymers have attracted considerable interest due to their similarity to human tissues, and their diverse repertoire of inherent biological functions. The use of biopolymers can take advantage of potential biocompatibility and biodegradability. Furthermore, there are many existing strategies whereby biopolymers can be biologically or synthetically modified to introduce new chemical and biological functions. The functionality and diversity of biopolymers therefore make them attractive candidates for antifouling and blood-compatible materials.

Polysaccharide-based materials have been used extensively to suppress bacterial adhesion, blood protein adsorption, platelet adhesion and activation, and blood coagulation [287]. A variety of methods including surface conjugation, physical adsorption, and layer-by-layer (LbL) assembly have been investigated for developing antifouling surfaces.

HA, a linear polysaccharide with multiple biological functions, is one of the prominent polysaccharides that has been used for designing antifouling surfaces. HA is a major component of the extracellular matrix of many tissues, and is a primary GAG found in the endothelial surface layer (ESL) that lines blood vessels [51]. HA can be immobilized by modifying surfaces with PDA to provide HA binding sites. Such HA-PDA modified surfaces can reduce platelet activation and aggregation, thrombosis, and inflammation [288,289]. HA-PDA modification improves blood compatibility of PDMS-based implants [290]. An appropriate ratio of HA to PDA has been shown to considerably reduce platelet adhesion and activation on modified PDMS substrates, indicating an enhanced hemocompatibility compared to native PDMS, and to PDMS coated with HA or PDA alone [290]. Moreover, the surface modification inhibits inflammation, and reduces cytotoxicity compared to unmodified PDMS.

HA and other biopolymers can also be deposited into thin films using LbL assembly. LbL of natural biopolymers has become a popular technique to modify and functionalize the surface of biomaterials. LbL assembly is performed by sequentially adsorbing polymers that have complementary interacting groups onto a substrate to produce a thin film [291,292]. Often these are polyanion-polycation pair. The polyelectrolytes may be polysaccharides, synthetic polymers, nanoparticles, proteins, lipids, or DNA. In addition to ionic complementarity, the intermolecular interactions stabilizing each bilayer can also include covalent bonding, hydrogen bonding, host-guest interactions, and hydrophobic interactions, depending upon the chemistries of the materials chosen [293,294]. This method is attractive for its simplicity and scalability. The LbL method can be implemented by exposing a surface to alternating solutions containing the complementary chemistries, by spraying, dip-coating or other methods. The diversity of candidate materials enables a wide variety of biological functions to be introduced into the film, such as endothelialization [295], fibrinolytic activity [296], antimicrobial activity [297–299], antiplatelet activity [300] , and antifouling [301].

The antifouling activity of the multilayered films is dictated by the nature of the polymers, assembly conditions, homogeneous or heterogeneous topography, and number of layers as well as electrostatic charge of the terminal layer. LbL films formed from strong polycation-polyanion pairs usually fail to prevent protein adsorption, since they display a net charge on their surface, which can accelerate the migration of protein towards the surface. Charged surfaces may also bind small counterions which can be released, providing an entropic driving force for protein adsorption (compare Figure 1.6). Therefore, multilayered films should be designed in a way that neutralize the surface net charge, to achieve fouling resistance [302].

In our lab, we have developed several different polyelectrolyte multilayers from biopolymers and shown that by adjusting the pH, molarity, number of layers, and chemistry of the terminal layer we are able to control the structure, thickness, and physical chemistry of polysaccharide-based surfaces at the nanometer length scale [303–306]. Other groups also use biopolymers to modify and functionalize surfaces via LbL techniques to design blood-compatible biomaterials, demonstrating promising ability to reduce protein adsorption and biofouling [302,307–313]. In a study by Meng *et al.* chitosan-heparin polyelectrolyte multilayers on coronary artery stents accelerated the re-endothelialization and improved blood-compatibility of stent surfaces tested both *in vitro* and *in vivo* [314]. Five-bilayer heparin-collagen LbL coatings on ePTFE in the presence or absence of anti-CD133 antibodies were able to accelerate endothelialization, reduce platelet activation and aggregation, and prolong the blood coagulation time [300].

Recently, LbL assembly has been used to fabricate self-healing antifouling surfaces [315]. Sun and coworkers fabricated antifouling coatings by LbL assembly of PEGylated poly(ethylene imine) (bPEI-PEG) and HA for 40.5 deposition cycles [316]. The bPEI–PEG/HA multilayer film was then crosslinked by PEG bis(carboxymethyl) to make it stable. The fabricated film exhibits highly effective antifouling ability for inhibiting long-term BSA adsorption and cell attachment. This ability of the film was attributed to the presence of the PEG-rich surface and the extremely soft nature of the film. Moreover, the films exhibit rapid self-healing in response to multiple damages, such as cuts and scratches. The self-healing property was attributed to mobility of bPEI–PEG and HA polyelectrolytes and their reversible electrostatic and hydrogen bonding interactions.

Biological activation of surfaces with naturally derived polymers, synthetic analogs, or drugs enables the introduction of specific and tunable biochemical functions. This can be an effective method for improving the blood-compatibility of materials, and has led to some clinical and commercial success. Biological activation with biopolymers may lead to the introduction of multiple biological functions, including susceptibility to biodegradation. Materials designed for controlled release of a drug must be judiciously designed to release the drug at a controlled rate, and with awareness that the bioactive drug reservoir will eventually be depleted, leading to loss of activity. This may only be an effective strategy for long-term applications in cases where the drug is intended to impact a temporary phenomenon, such as re-endothelialization or tissue healing. For the long-term application of blood-contacting materials, biological activation may be most effective when it is combined with other strategies to synergistically improve multiple aspects of blood-compatibility.

1.4.4 Bioinspired surfaces

Bioinspired superhydrophobic and lubricant-infused surfaces have been developed as an effective platform for designing anti-biofouling surfaces. The functionality of these surfaces is inspired by the complex hierarchical structures and chemical composition of natural materials, such as the lotus leaf and *Nepenthes* pitcher plants (Figure 1.16). Lotus leaf is well-known for its low adhesion, self-cleaning, and superhydrophobicity properties imparted by the cooperative influence of hierarchical microstructures and nanostructures and low-surface energy waxes [317,318]. Unlike lotus leaf, the *Nepenthes* pitcher plant surface locks in a layer of liquid water to create a low friction repellent surface that is able to prevent the attachment of insects [319,320]. Inspired by these biological surfaces, researchers have recently begun to design and fabricate biomimetic superhydrophobic and lubricant-infused surfaces with many kinds of synthetic materials, including polymers, ceramics, and metals to develop low biofouling, blood-repellent surfaces [321–324].

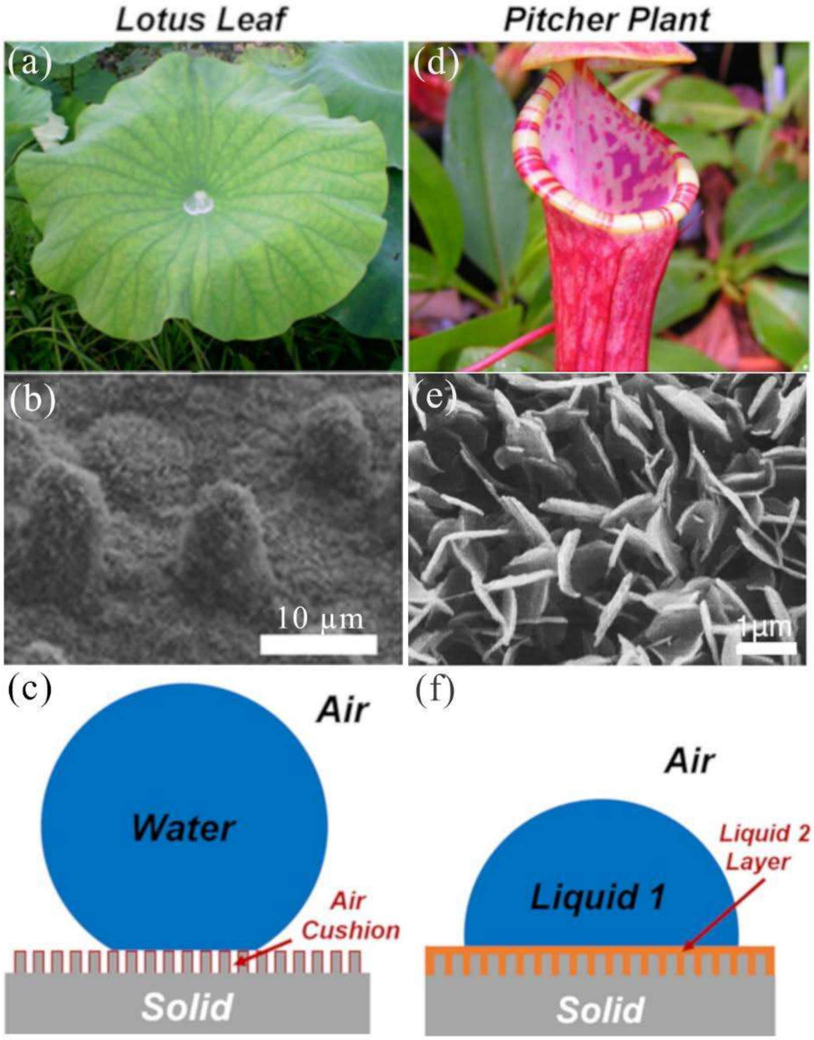

Figure 1.16. (a) Image of a lotus leaf in nature. (b) SEM image of the micro-structure of lotus leaf. (c) Illustration of design principal and contact modes of a superhydrophobic surface in air. (d) Image of a pitcher plant in nature. (e) SEM image of the platelet-shaped wax crystals of slippery surfaces in *Nepenthes alata*. (f) Illustration of design principal and contact modes of liquid-1-repellent surface based on the liquid-2 layer in air. *(a,c,d, and f) Reproduced with permission from* [325], *copyright 2015, American Chemical Society. (b) Reproduced with permission from* [326], *copyright 2016, Elsevier. (e) Reproduced with permission from* [327], *copyright 2010, The Company of Biologists Ltd.*

1.4.4.1 Superhydrophobic (SH) surfaces

SH surfaces are being explored in recent years for their potential use in blood-compatible materials since they have demonstrated self-cleaning, nonwetting, and anti-biofouling properties [328]. SH surfaces by definition have a water contact angle (θ_{CA}) exceeding 150° and contact angle hysteresis (the difference between the advancing and receding contact angle) less than 10° [329]. Superhydrophobicity is achieved by combination of appropriate surface roughness (nanoscale and/or microscale) with low-surface-energy materials (Figure 1.16). The theoretical models of wetting states on these textured surfaces can be explained by the Wenzel and Cassie-Baxter models [150]. Surface roughening leads to increasing the solid–liquid interfacial surface area. In the Wenzel state, liquid droplets fully wet the surface by entering into all cavities. As a result, based on the Wenzel equation, intrinsically hydrophilic materials ($\theta_{CA} < 90°$) become more hydrophilic, and intrinsically hydrophobic materials ($\theta_{CA} > 90°$) become more hydrophobic with increased surface roughness [330]. In the Cassie–Baxter state (or Cassie state), in contrast, the liquid droplets sit on top of rugosities and on air trapped inside surface features, resulting in smaller contact area between the liquid and the solid interface. Reduced effective area between blood and biomaterials caused by topographical features, in addition to their low surface energy can improve the design of SH blood-repellent surfaces.

SH surfaces reduce blood protein adsorption, platelet adhesion and platelet activation, and therefore reduce blood coagulation. In the SH Cassie state, as long as the entrapped air is maintained at the interface, it can limit the available liquid-biomaterial surface area and thereby decrease the total area available for protein binding. Air trapped within the interstices of TiO_2 nanotube-microtemplated surfaces exhibit suppression of BSA and FBS binding when air is present in the SH regions [331]. However, once air is displaced by sonication, proteins bind to the SH domains [331]. In another study, the air trapped within the interstices of the SH fibular ePTFE significantly reduced adsorption of HSA compared to commercially available ePTFE [332].

The stability of the Cassie state is a key factor for the protein resistance of SH surfaces. However, it has been shown that proteins are able to even adsorb to the small solid interfaces of SH surfaces and increase the surface energy of the biomaterial [333]. Increased surface energy promotes the penetration of water into interstices, causing a transition from the Cassie to the Wenzel state, and eventual displacement of the air-bubble layer. Moreover, when this transition occurs, the formerly SH surface is rendered non-superhydrophobic. The entire effective surface area is intrinsically hydrophobic, which promotes protein adsorption. Therefore, the Cassie-to-Wenzel transition increases effective surface area resulting in more protein adsorption compared to a flat surface of the same material [334]. As a result, maximizing underwater stability of the Cassie state of SH surfaces over long time scales is important when designing SH surfaces for long-term contact with blood.

SH surfaces can reduce platelet adhesion and activation [335,336], by a similar mechanism proposed for reduced protein binding. The Cassie state decreases the total area available for cell adhesion on SH surfaces. SH titania nanotubes reduce platelet adhesion and activation on 316L stainless steel [337], and are superior to other nontextured titania and nanoflower-textured titania surfaces [338]. SH titania surfaces can significantly reduce platelet adhesion and activation but only when the SH surfaces have a robust Cassie–Baxter state [338]. In another study laser ablation was used to alter the wettability of stainless steel with defined pattern geometry to investigate how surface morphology, surface roughness, and SH character of the surfaces affect platelet adhesion [339]. SH cauliflower-like surfaces with a stable Cassie–Baxter state (stable on immersion in water up to six days) were shown to be highly resistant to platelet adhesion compared to other SH surface patterns, including triple pattern topography that had a high contact angle but less stable Cassie–Baxter state.

Since SH surfaces demonstrate promising results in reducing blood protein adsorption and platelet adhesion and activation, they are being explored for their potential application in developing blood-compatible biomaterials. In recent years, several SH surfaces have been developed with a nanoscale topography and hydrophobic surface chemistry to demonstrate their short-term blood-repellency [338,340–342]. The potential use of a SH coating (a commercial Ultra-Ever Dry spray coating) on a Jude Medical Bileaflet mechanical heart valve (BMHV) was investigated by Bark and coworkers [343]. The SH coating with a receding contact angle of 160° was able to reduce blood cell adhesion in a static environment compared to pyrolytic carbon (receding contact angle of 47°), the base material for BMHVs. Recently, a sand-casting technique was used to prepare a SH blood-repellent surfaces (blood contact angle of 150° and roll-off angle of 10° for 10 µl porcine blood) composed of silicone and functionalized SiO_2 nanoparticles (Figure 1.17) [344]. The multi-scale micro-structure provided trapped air-bubble layer on the casted surface to maintain a robust Cassie–Baxter state. The fabricated surface reduces water drag force by up to 72% compared to PDMS and can withstand harsh durability tests, such as high-speed (9.7 m s^{-1}) water jetting and extensive high-pressure sandpaper abrasion. 10 µl of blood dispensed onto the casted sample rolls off quickly leaving no trace of blood on the surface, which is a sign of blood-repellency in a short-term experiment (Figure 1.17).

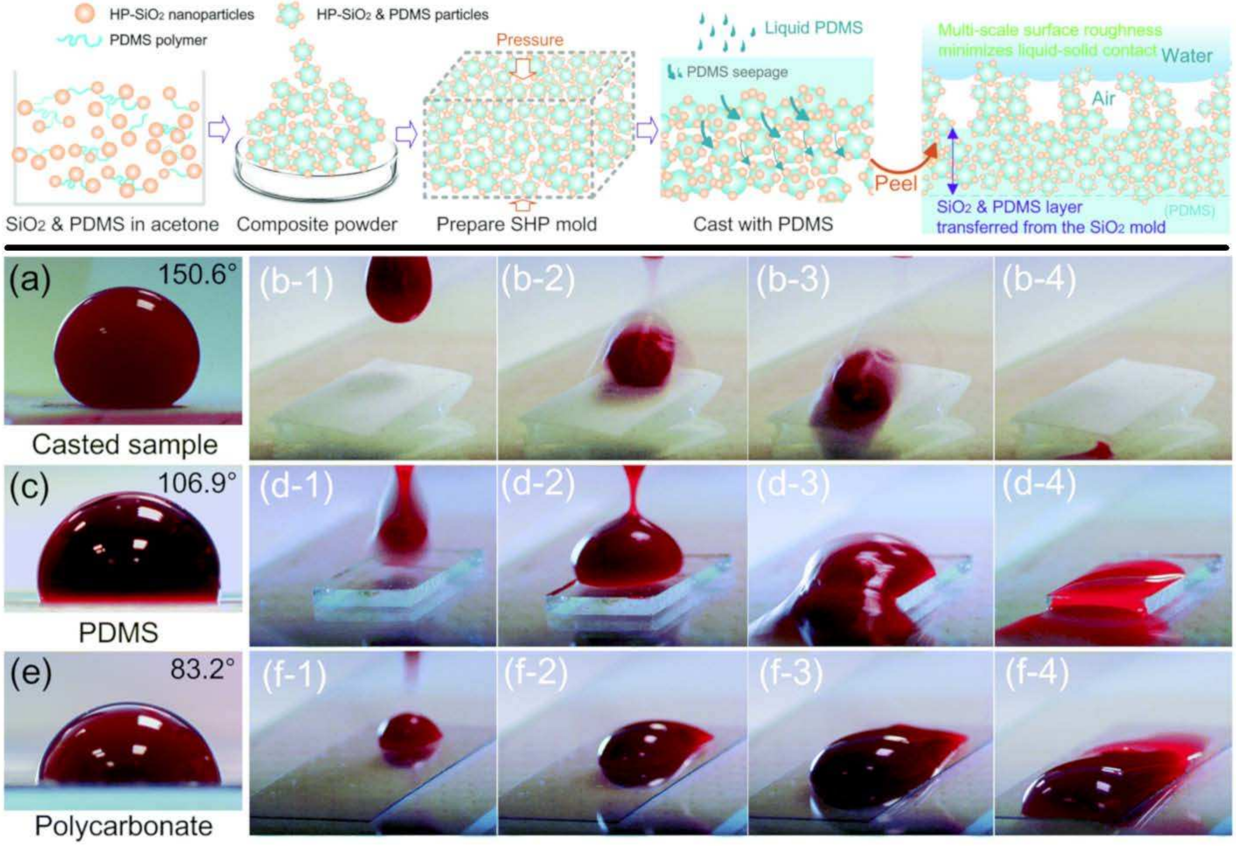

Figure 1.17. Top. Illustration of the sand-casting processes, showing particle aggregation and transfer of SiO_2 nanoparticles from the SiO_2 mold to the final casted item. Bottom. (a) Blood repelling properties of the sand-casted SHP sample compared with materials commonly used to make blood pumps, PDMS and polycarbonate. (a) Blood contact angle of the casted SHP sample, (b) blood rolling off the casted sample without leaving stains, (c) blood contact angle of PDMS, (d) blood flowing off the PDMS surface while leaving stains, (e) blood contact angle of polycarbonate, and (f) blood remains adhered to the polycarbonate surface. *Reproduced with permission from* [344]*, copyright 2018, The Royal Society of Chemistry.*

1.4.4.2 Lubricant-infused surfaces

Lubricant-infused surfaces are a new emerging class of bioinspired materials that create a stable dynamic surface which repel immiscible fluids and display ultralow adhesion to micro/nanoporous solid substrates (Figure 1.16). Aizenberg and co-workers reported the first type of these surfaces, which they named slippery liquid-infused porous surfaces (SLIPS) [345]. These materials are fabricated by infusion of viscous oils into porous surfaces, rendering the surface with low sliding angles for various complex liquids [346]. To fabricate a liquid-infused slippery surface several criteria for both solid substrate and infused liquid should be met [347]. The solid substrate must have the capacity for entrapment of a lubricating liquid within a micro/nanoporous structure to enable it to be firmly locked into the pores and mask the surface roughness. Several different materials in recent years such as polyamide-6 (PA6) [348], poly(ethylene terephthalate) (PET), poly(methyl methacrylate) (PMMA), PC [349], and titanium [350] have been used to design hierarchical micro/nanoporous structured substrates for lubricant-infused surfaces. In addition, the solid substrate must have a surface chemistry matching the chemical composition of the lubricating liquid to create an appropriate surface energy match between two phases. The stability of SLIPS also relies on a mobile lubricant layer which must wet the solid substrate and be immiscible with the repelled liquids. The long-term stability of the lubricating liquid is also essential since lubricant layer depletion leads to the loss of the slippery characteristics of these surfaces. Various lubricating liquids including silicone oils [349], perfluorodecalin [351], Krytox [352], and almond oil [353] have been used as infused liquid in several reports.

The ability of SLIPS to repel complex biological fluids such as blood for designing blood-repellent surfaces was introduced by the Aizenberg group (Figure 1.18, top). They showed that SLIPS composed of a tethered perfluorocarbon layer and a medical-grade liquid film of perfluorodecalin on different surfaces prevent fibrin attachment, reduce platelet adhesion and activation, and are stable under blood flow in vitro (Figure 1.18, top) [351,354]. Since the initial report of these surfaces, many different approaches have been used to design, fabricate, and utilize lubricant-infused surfaces as blood-repellent materials that reduce biofouling [353,355–357]. ePTFE-perfluorocarbon SLIPS, for example, prevent biofouling while preserving the viability and bactericidal function of macrophages in vitro [358]. SLIPS also show low innate immune responses and reduced inflammatory capsule formation *in vivo*, in a murine model [358]. SLIPS composed of hydrophobic silica nanoparticles infused with sesame oil showed blood repellent properties. These blood-repellent SLIPS can improve imaging when used as a covering for endoscope lenses in a mouse model [359].

To incorporate both aspects of blood compatibility and targeted cell binding, biofunctional lubricant-infused surfaces (BLIS) have been proposed. BLIS are proposed to yield surfaces that prevent nonspecific adhesion of biomolecules and cells, while capturing target species in complex fluids such as blood (Figure 1.18, bottom) [360]. BLIS were fabricated by creating SAMs of organosilanes with optimized ratios of aminopropyl triethoxysilane (APTES) and trichloro(1H,1H,2H,2H-perfluorooctyl)silane (TPFS). APTES provides amine groups for conjugating biomolecules, and TPFS serves as the substrate for immobilizing perfluoroperhydrophenanthrene lubricant on the surface. These BLIS prevent nonspecific fibrinogen adsorption and platelet adhesion to the same extent as 100% TPFS-treated samples (Figure 18, bottom). They also exhibit good blood repellency properties, evidenced by immediate sliding of a blood droplet. Moreover, a long-term cell adhesion study showed that BLIS promote endothelialization and cell growth, and that no significant difference was seen in the cell confluency and viability in BLIS compared with 100% APTES-treated samples after 5 days (Figure 1.18, bottom).

The development of new chemistries and structures for superhydrophobic and lubricant-infused surfaces is an exciting and active area of research that could lead to advances in blood-compatible materials. Methods for preparing superhydrophobic surfaces through texturing, in particular, can be readily scaled to enable manufacturing methods. Outstanding challenges include confirming the stability and safety of these surfaces for long-term blood-contacting applications.

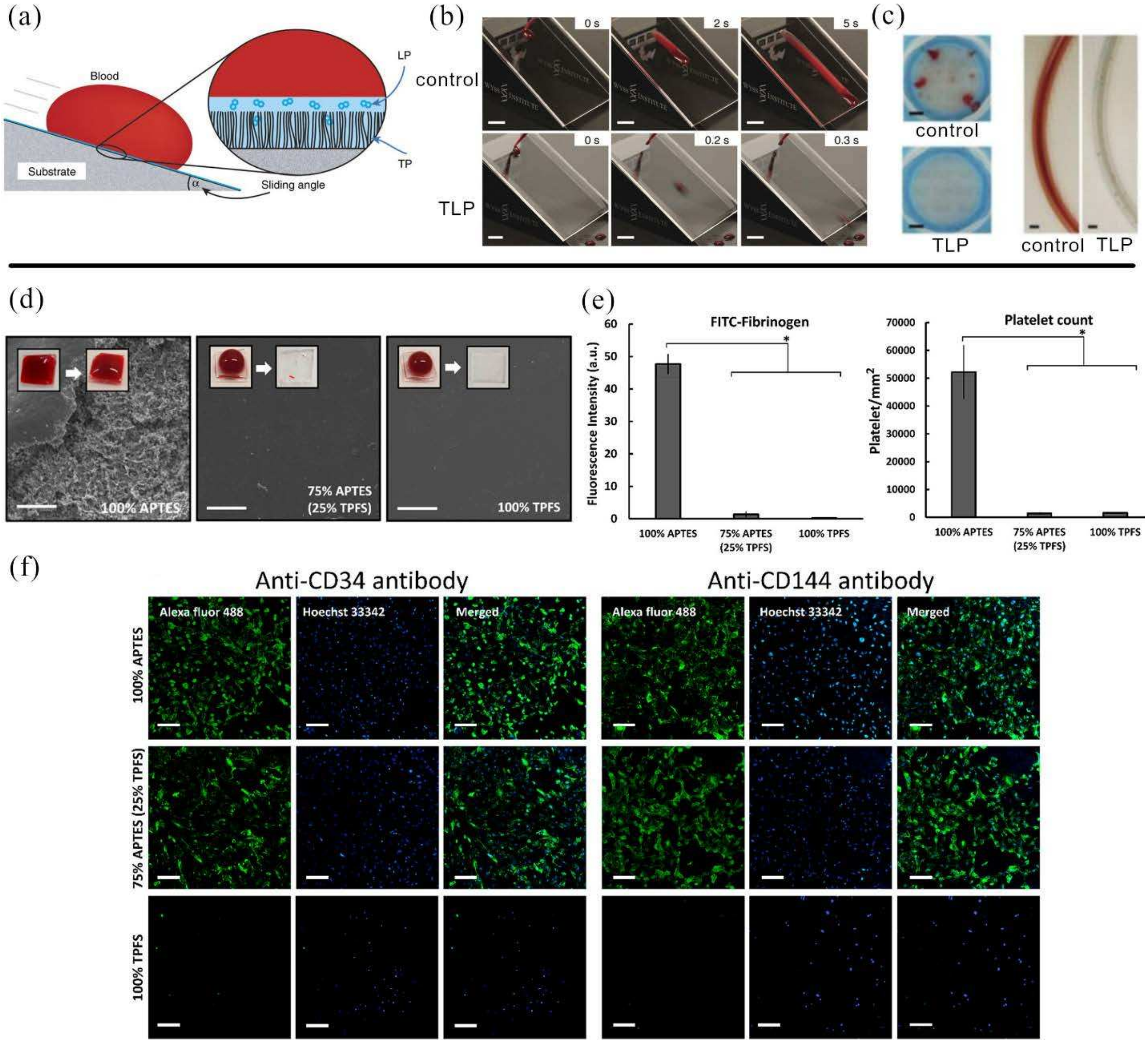

Figure 1.18. **Top**. TLP-coated (tethered-liquid perfluorocarbon) surfaces repel whole human blood. (a) Schematic of blood repellency on TLP surfaces showing the TP (tethered perfluorocarbon) bound to a substrate through plasma activation and silane treatment, which then allows a stable film of LP (perfluorodecalin) to adhere to the surface. (b) Surfaces without TP or LP (–TP/–LP; control) show adhesion of a blood droplet (50 µl, 3.2% sodium citrate) on the 30 degree angled surface, low velocity and residence over 5 s (upper panels). When TLP is applied to the surface, a blood droplet (50 µl, 3.2% sodium citrate) is immediately repelled and slides down the surface at an incline of 30 degrees within 0.3 s (lower panels). Scale bars, 1 cm. (c) Thrombogenicity of TLP surfaces. Photographs of filtered thrombi after blood was pumped in a closed loop at 3 L/h for 2 h in control (upper image) and TLP medical-grade PVC (lower image), and photographs of control (left) or TLP (right) cardioperfusion tubing sterilized with ethylene oxide after it had been exposed to porcine blood for 2 min. Scale bars, 5 mm. Reproduced with permission from [351], *copyright 2014, Springer Nature.*

Bottom. Investigating the blood, protein interaction, platelet and cell adhesion with optimized biofunctional lubricant-infused surfaces. (d) SEM images taken from samples incubated with human whole blood indicate that samples treated with mixed silanes or 100% TPFS have excellent blood repellency properties, and no clot or blood cell adhesion was observed on them. (e) Left. Fluorescence intensity of FITC−fibrinogen adhered to treated substrates. Right. Number of platelets/mm^2 adhered to surfaces. (f) Long-term cell experiments conducted on anti-CD34- and anti-CD144-treated samples and the investigation of cell phenotype and cytocompatibility of the treated surfaces. Samples were functionalized with (left) anti-CD34 and (right) anti-CD144 antibodies and incubated with HUVECs for 5 days. The positive immunofluorescence staining for Alexa Fluor 488-conjugated VE-cadherin confirms the HUVEC phenotype for adherent cells. Both endothelial cell-specific antibodies promoted cell adhesion and endothelialization. The 100% TPFS-lubricated samples inhibited the nonspecific binding of cells and had significantly less adherent cells after 5 days compared to other treated substrates. The scale bars are 100 µm. *Reproduced with permission from* [360]*, copyright 2018, American Chemical Society.*

1.4.5 Glycocalyx-mimetic surfaces

The inside surface of healthy blood vessels is the only known material that is completely blood-compatible when in long-term contact with flowing whole blood. By mimicking key features of the blood vessel wall, it may be possible to elucidate the structure-function relationships that could guide the development of new blood-compatible materials. In particular, mimicking the physical chemistry and topography of the luminal surface of healthy blood vessels has been proposed as a biomimetic strategy that could yield promising blood compatibility. The luminal surface of blood vessels is covered with a monolayer of endothelial cells. This endothelium surface is multifunctional, providing both blood-compatible properties and regulating the coagulation cascade once there is a vascular lesion [361]. The endothelial cells on the blood vessel wall present a carbohydrate-rich, gel-like, dynamic surface layer called the endothelial glycocalyx. The endothelial glycocalyx is connected to the endothelium mainly through proteoglycans, and to a lesser extent, through glycoproteins [51]. The ESL is composed of membrane-bound mesh of proteoglycans, GAGs, HA, glycoproteins, and plasma proteins [51,362,363]. Proteoglycans are composed of a core protein that carries one or more covalently attached GAG chains [364].

Heparan sulfate, chondroitin sulfate (CS), dermatan sulfate (DS), keratan sulfate, and HA are five types of GAGs. The most common GAG in the ESL is heparan sulfate (roughly 50–90%), followed by CS and DS [51]. With the exception of HA, all GAGs are covalently connected to the protein core of proteoglycans. The thickness of the ESL varies throughout the vasculature, with reported thicknesses ranging from 200 to 4000 nm [51].

Since the ESL is located between the endothelium and flowing blood, it has several fundamental functions that impart blood compatibility [51,365]. Specifically, the ESL plays a central role in preventing blood clotting on the inside surfaces of healthy blood vessels. The negatively charged surface of the ESL acts as a barrier that limits the access of certain components, such as leucocytes, platelets, and some proteins to the endothelium [51,366]. Moreover, this highly hydrated layer reduces nonspecific blood protein adsorption [367]. The ESL is also responsible for binding several serine protease inhibitors (serpins), enhancing its anticoagulant activity [368,369]. When coagulation is not necessary, ATIII, and heparin cofactor II (two important anticoagulant proteins) bind to the GAGs through specific binding sequences to inhibit thrombin and FXa [369]. Therefore, mimicking the endothelial glycocalyx on a biomaterial surface is a potential strategy for development of blood-compatible surfaces. To this end, GAGs have been used as surface modifications to improve the blood-compatibility of surfaces [370,371]. Fabrication of heparin coatings for improving blood compatibility is one of the well-known applications of GAGs in the realm of designing blood-compatible surfaces, which was discussed earlier. In this section we highlight the strategies used to mimic the ESL on biomaterials to improve antifouling and blood-compatibility of surfaces.

Several studies with different GAGs have been conducted to understand blood protein, platelet, and whole blood interactions with glycocalyx-like surfaces. Glycocalyx-like surfaces have been prepared by a variety of techniques to immobilize GAG-rich sulfated materials, including oligosaccharides and polysaccharides [367,372–376]. These studies reported reduced blood protein adsorption and/or platelet adhesion and activation, and in one case reduced the inflammatory responses compared to unmodified substrates. In a study by Ham *et al.* inspired by glycoproteins present in the ESL, glycopeptoids were grafted to TiO_2 substrate to make glycocalyx-mimetic peptoids [377]. The interfacial saccharide residues of glycopeptoids formed a biomimetic shielding layer that dramatically reduced nonspecific blood protein adsorption, fibroblast, and bacterial cell attachment compared to unmodified substrate. The fouling resistance of the fabricated layer was attributed to both a water barrier effect due to high number of hydrogen bonds with water molecules, as well as steric hindrance from the 20-mer *N*-methoxyethyl peptoid linker of the glycopeptoid. In another study, CS was covalently grafted to primary amine-rich plasma-polymerized films to compare antifouling ability and blood compatibility to PEG-grafted and carboxymethylated dextran-grafted (CMD-grafted) surfaces [378]. CS was shown to be as effective as PEG in reducing fibrinogen and BSA adsorption, although CMD reduced fibrinogen adsorption more than both of the other surfaces. PEG-, CMD-, and CS-grafted surfaces drastically decreased platelet adhesion and activation compared to unmodified PET surfaces in a study with whole blood for 15 min. Interestingly, CS-grafted surfaces exhibited much better endothelial cell adhesion and growth compared to PEG and CMD surfaces. In addition to interfering with blood coagulation, the CS-grafted surface could therefore promote the more complete restoration of a stable endothelium. In another study, PTFE vascular grafts were coated with perlecan (a major heparan sulfate-containing proteoglycan) and tested in an ovine carotid interposition model for a 6-week period [379]. Reduced thrombus formation was the result of both reduced platelet adhesion and aggregation and enhanced endothelialization compared to the uncoated surface. It was shown also that perlecan is resistant to platelet adhesion as long as it possesses heparan sulfate side chains. Once the GAGs were removed, platelet adhesion and aggregation were supported. This result shows the importance of GAGs in improving blood compatibility and promoting endothelial cell proliferation.

Most of the current research in glycocalyx-mimics has addressed mimicking the surface chemistry of the ESL on biomaterials to improve antifouling properties of surfaces and ultimately enhance blood-compatibility. However, in addition to the chemistry of the ESL, mechanical properties and topography of the ESL are also important to thoroughly mimic this layer. Hedayati *et al.* developed a technique to mimic bush-like structures found in the ESL based on the LbL assembly of polyelectrolyte multilayers (PEMs) and their subsequent modification with polyelectrolyte complex nanoparticles (PCNs), to make PEM+PCN surfaces [380]. The polyelectrolytes used are all polysaccharides, and include polyanionic GAGs, like those found in the glycocalyx. The PEMs provide a uniform surface for deposition of the GAG-rich PCNs, and the PCNs provide supermolecular assembly of the GAGs into bush-like structures similar, to those reported by Rostgaard and Qvortrup for the endothelial glycocalyx [381]. The fabricated glycocalyx-mimetic surfaces present dense GAG-rich regions that swell when hydrated, and have higher Young’s modulus than the underlying PEM with height features from 100 to 150 nm high (Figure 1.19). They later showed that these glycocalyx-mimetic nanostructures suppress nonspecific blood protein adsorption compared to unmodified glass and PEM surfaces [382]. More interestingly, once they added thrombin to the fibrinogen solution in the absence of ATIII, a network of fibrin fibers were formed on PEM surfaces terminated with either chitosan, CS or heparin. Therefore, coating the surface with GAGs such as heparin or CS does not suppress fibrin polymerization on the surface or fibrin fiber adsorption from solution onto the surface. Strikingly, in the cases of glycocalyx-mimetic nanostructures (PEM+PCNs) no fibrin fibers are observed on the surfaces (Figure 1.19). They concluded that both chemistry and surface topography of the glycocalyx-mimetic layer are required to inhibit fibrin fiber and fibrin network formation. In another study [37], titania nanotubes with high surface area were coated with heparin-chitosan PEMs to provide GAG functionalization. Then chitosan was modified with a NO-donor chemistry to provide an important antithrombotic small-molecule signal. Combination of surface nanotopography, GAG-based surfaces, with NO-donor chemistry demonstrated substantial reduction in platelet adhesion and activation compared to unmodified TiO_2 surfaces (Figure 1.3).

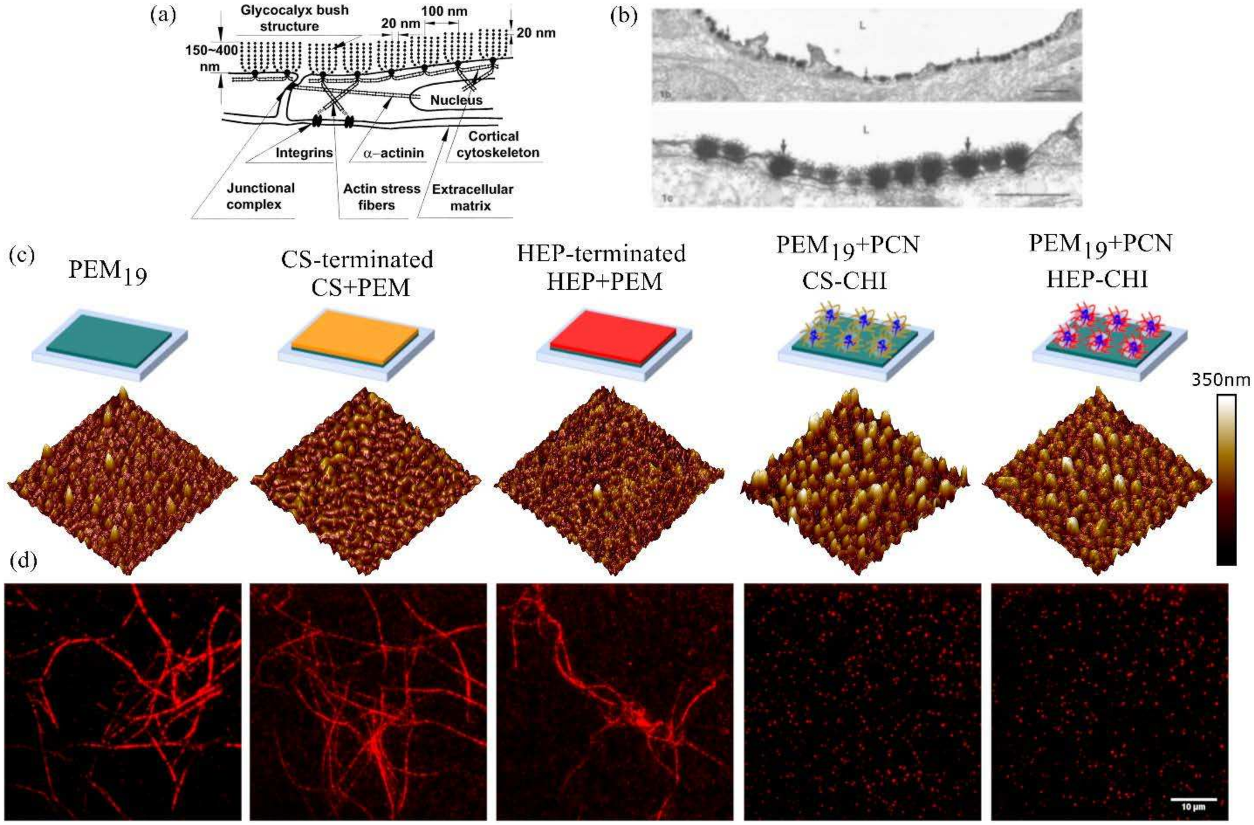

Figure 1.19. (a) Sketch of endothelial surface layer (not to scale) showing core protein arrangement and spacing of scattering centers along core proteins and their relationship to the actin cortical cytoskeleton. *Reproduced with permission from* [383], *copyright 2003, National Academy of Sciences.* (b) Electron micrographs of capillary from small intestine. Bush-like structures are indicated by the arrows. The capillary lumen is labeled “L”. Scale bars: (top) 1.0 μm; (bottom) 0.5 μm. *Reproduced with permission from Molecular Sieve Plugs in Capillary Fenestrae,*

copyright 1997, Elsevier. (c and d) Surface chemistries and structures of glycocalyx-mimetic surfaces (PEM_{19}+PCNs) inhibit both the surface-mediated polymerization of fibrin and the adsorption of fibrin fibers from solution. (c) Representative 5 μm × 5 μm AFM topographic images of PEM_{19} (19-layer chitosan/hyaluronan), PEM_{19} + CS (chondroitin sulfate-terminated PEM), PEM_{19} + HEP (heparin-terminated PEM) and PEM_{19} + PCN (CS-CHI and HEP-CHI) taken in liquid. (d) Total internal reflection fluorescence (TIRF) microscopy images of fluorescently labeled fibrin fibers, polymerized from physiologic concentration of fibrinogen (0.75 mg mL^{-1}), in the presence of thrombin (1 NIH U mL^{-1}) on PEMs. The structure of the glycocalyx-mimetic surfaces (PEM_{19}+PCNs) samples does not prevent the adsorption of fibrin(ogen) monomers, but it completely prevents adsorption of fibrin fibers and fibrin polymerization on the surface. *Reproduced with permission from* [382]*, copyright 2018, American Chemical Society.*

Since the inside surfaces of healthy blood vessels are the only surface known to be completely compatible with flowing whole blood for long-term contact, strategically mimicking key features of the endothelial glycocalyx is a rational approach to developing blood compatible materials. Although this emerging approach is still in its infancy, some studies have shown that such biomimetic surfaces suppress blood protein adsorption, platelet adhesion and activation, bacterial adhesion and ultimately improve blood compatibility in short-term experiments. These evidences indicate that surfaces that mimic the chemistry and structure of the ESL have the potential to be developed as a new class of improved blood-contacting biomaterials. One challenge to this approach is that the vascular endothelium is a multicomponent surface, with many biological functions. Further mechanistic studies should be aimed at elucidating which chemical and structural features of the ESL impart important biological functions critical to blood compatibility, and how these features can be tuned to optimize performance for specific applications. Another challenge to this biomimetic strategy is that both the blood and the blood vessel wall are alive. Endothelial cells lining the blood vessel wall can expend energy and consume nutrients to continuously alter the presentation of the glycocalyx, for example, in response to mechanical stimuli, and can repair damage to the glycocalyx. A durable and robust glycocalyx mimic must be designed to maintain its various functions in the challenging and dynamic environment represented by flowing whole blood.

While mimicking the nanoscale and macromolecular assembly of some components of the vascular endothelium is a promising strategy, these are not the only features that impart blood compatibility to blood vessel walls. Endothelial cells lining the blood vessel wall also produce an important antithrombotic signal, NO. NO delivery can also be exploited to improve the blood compatibility of surfaces, as discussed in the next section.

1.4.6 Delivery of the small molecule NO

Over 40 years ago Ferid Murad proposed that NO was a molecule responsible for activation of an enzyme, guanylate cyclase, involved in vasodilation [384,385]. Over the subsequent decade, Luis J. Ignarro and Robert F. Furchgott contributed to elucidating a biological source and modes of action of NO. Ignarro and others showed that NO activates the enzyme guanylate cyclase, which synthesizes 3',5'-cyclic guanosine monophosphate (cGMP) from guanosine triphosphate (GTP) [386]. The subsequent increase in cGMP levels triggers relaxation of the vascular smooth muscle cells, in addition to inhibiting platelet adhesion and activation that can lead to thrombosis [387]. Furchgott and others discovered that vasodilation was achieved through the action of a factor produced by endothelial cells [388,389]. Ignarro and co-workers later showed that the endothelial-derived molecule responsible was NO [390,391]. Consequently, Furchgott, Ignarro, and Murad received the 1998 Nobel Prize in Physiology or Medicine for their identification of NO as a signaling molecule in the cardiovascular system. Mechanisms of NO signaling are still being discovered [392]. Nonetheless, what is currently known about the potency of NO and its importance in signaling in the cardiovascular system have made NO delivery an important strategy for the development of blood-compatible materials.

1.4.6.1 NO in the cardiovascular system

NO is continuously produced by healthy endothelial cells at a basal level and in response to physiological stimuli. For example, Rubanyi *et al.* proposed, and others later confirmed, that NO release from endothelial cells is triggered by increased pulsatile flow [393–395]. Today, the bioactivity of NO is well established and encompasses cardiovascular regulation, neurotransmission, promotion of wound healing, and antibacterial effects [396–398]. Biologically, NO reacts with metal centers or other radicals, the latter resulting in the production of RNS. NO has direct effects due to chemical interactions between a receptor biomolecule and NO itself, such as the binding of NO to the Fe^{2+} of the heme moiety to form a metal nitrosyl adduct (Figure 1.20, top) [399]. Indirect effects involve the production of RNS such as peroxynitrite ($ONOO^-$), nitrate (NO_3^-), nitrite (NO_2^-), dinitrogen trioxide (N_2O_3) and dinitrogen tetroxide (N_2O_4), which form through the reactions of NO with oxygen [399,400]. These RNS species proceed to target specific functions without the direct participation of NO. Vasodilation, inhibition of platelet activation, and various wound healing functions are typically attributed to direct effects of NO, while indirect effects are primarily responsible for antimicrobial activity.

Direct

$$NO + HbFe(II) \longrightarrow HbFe(II)NO$$

Indirect

$$NO + O_2^- \longrightarrow ONOO^-$$

$$NO + O_2 \longrightarrow ONOO$$

$$NO + ONOO \rightleftharpoons ONOONO$$

$$ONOONO \longrightarrow 2\ NO_2$$

$$NO_2 + NO \rightleftharpoons N_2O_3$$

$$N_2O_3 + H_2O \longrightarrow 2\ NO_2^- + 2\ H^+$$

$$2\ NO_2 \rightleftharpoons N_2O_4$$

$$N_2O_4 + H_2O \longrightarrow NO_2^- + NO_3^- + 2\ H^+$$

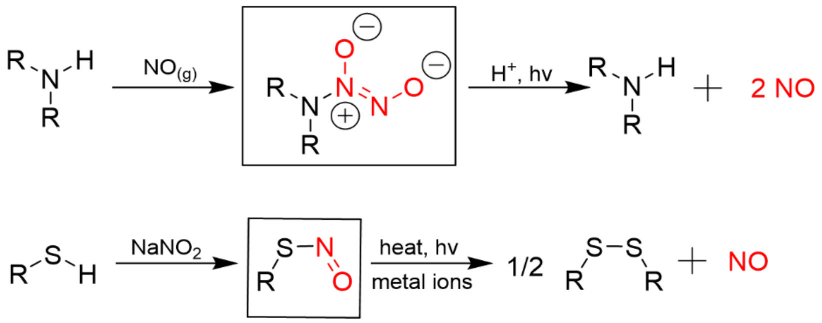

Figure 1.20. **Top**. Examples of the reactivity of NO to form RNS under physiological conditions. **Bottom**. Reactions to form diazeniumdiolates and *S*-nitrosothiols followed by the subsequent release of NO.

Three different isoforms of the NO synthase enzyme (NOS) are responsible for NO production in mammalian biology; these enzymes are neuronal NOS (NOS I or nNOS), inducible NOS (NOS II or iNOS) and endothelial NOS (NOS III or eNOS) [401]. NO generation can also occur in a NOS-independent manner in the nitrate-nitrite-NO pathway, which involves the reduction of nitrate or nitrite to NO [402]. The nitrate-nitrite-NO pathway activity increases under low oxygen conditions (hypoxia) when the classical oxygen-dependent mechanism of NO synthesis is inhibited. During this process, bacteria, hemoglobin, myoglobin, and certain enzymes such as xanthine oxidase can reduce nitrate and nitrite to NO. Notably this pathway can be fueled by exogenous nitrate and nitrite sources in our diet that can produce therapeutic effects particularly for the treatment of cardiovascular disease [403,404].

Plasma thiols are likely precursors for natural NO generation in the endothelium, and participate in the activation of nitrosovasodilators. Stamler *et al.* were the first to demonstrate that the majority of *S*-nitroso adducts occur as *S*-nitrosoalbumin (SNO-albumin) through nitrosation of the lone cysteine residue [405]. The balance was proposed to consist of *S*-nitrosothiols (RSNOs) derived from low-molecular weight thiols, such as *S*-nitrosoglutathione (GSNO). Scharfstein and colleagues later speculated that transnitrosation occurs *in vivo* between SNO-albumin and low-molecular weight thiols [406]. Subsequent studies have shown several mechanisms whereby SNO-albumin may serve as a biological reservoir from which low-molecular weight thiols are nitrosated, and other mechanisms of RSNO formation [407–410].

NO produced by endothelial cells has regulatory effects on the cardiovascular system, largely through NO-induced formation of cGMP and its influence on a variety of receptors. NO prevents platelet adhesion and aggregation along the endothelium by increasing the intracellular concentration of cGMP. The presence of cGMP then decreases the intracellular concentration of Ca^{2+}, a key regulatory promoter of platelet activation [394,395,411,412]. Another route through which NO prevents platelet adhesion and activation is via inhibition of thromboxane A_2 (TXA_2), a signaling molecule produced by activated platelets with prothrombotic properties. Previous research has shown that cGMP can directly inhibit TXA_2 activity, thereby reducing platelet adhesion and activation [110].

Understanding the relationship between NO concentration and biological activity has been the target of substantial research efforts. The effective therapeutic dose of NO for medical applications depends upon the desired effect (Table 1.2). At low concentrations (1-30 nM), NO exhibits regulation such as vasodilation and formation of new blood vessels (angiogenesis) [413]. An increased NO concentration of approximately 100 nM results in protective effects towards cell apoptosis (anti-inflammatory and wound healing), whereas concentrations above 400 nM induce cellular apoptosis [413]. Higher concentrations have proven to be beneficial for anticancer and antibacterial applications [414]. From a clinical perspective, the varied biological effects of NO illustrates the need for fine control over NO release kinetics when developing materials for NO delivery.

Table 1.2. Concentration ranges of NO and corresponding physiological activities [413].

	[NO]	physiological results
cell protection	1-30 nM	proliferative and protective effects (vasodilation, angiogenesis)
	30-60 nM	apoptosis protection (antioxidant)
	100 nM	tissue injury protection (anti-inflammatory, wound healing)
cell damage	400 nM	apoptosis induction (antibacterial and anticancer)
	1 µM	full cell cycle arrest (toxicity)

The healthy endothelium is estimated to release NO with a surface flux of $0.5\text{-}4.0 \times 10^{-10}$ mol NO cm^{-2} min^{-1}. Therefore, materials for blood-contacting applications should fall within this target range [415]. Due to its reactivity, localized surface delivery of NO is desirable for antithrombotic applications without the systemic effects, such as hemorrhaging, which may occur from use of anticoagulants. However, the applicability of therapeutic NO is limited by the overall reactivity of the molecule. Several factors can influence the consumption of NO within the body, including the availability of oxygen and hemoglobin. In aqueous solution, the rate of NO consumption with oxygen and hemoglobin is proportional to the square of NO concentration and follows second order kinetics [416]. The half-life of NO in extravascular tissue is reported to fall within the range of 0.09 s to > 2 s, depending on the concentration of oxygen present [417].

However, the half-life of NO in whole blood has been calculated to be much smaller (1.8×10^{-3} s) and is correlated to the concentration of red blood cells [418]. In blood, an additional route of NO consumption is through the reaction of NO with oxyhemoglobin or heme-bound iron of the heme proteins to yield iron(III)-peroxynitrite species [419]. This very short half-life of NO in blood necessitates strategies to stabilize NO. To increase the availability of NO materials have been developed that contain much more stable NO-donor chemistries. The next sections discuss materials that carry NO-donor chemistries or that can catalytically generate NO from endogenous NO precursors in the bloodstream.

1.4.6.2 Materials with NO-donating groups

Since NO inhibits platelet activity in the healthy endothelium, strategies incorporating an exogenous supply of NO for blood contacting devices have been widely explored as a method for inhibiting thrombus formation [420–422]. Given the fleeting nature of NO in the presence of the reactive components of blood, chemical functional groups that decompose to release NO have been proposed to function as NO carriers that can stabilize NO within a biomaterial or at a surface. Both RSNOs and *N*-diazeniumdiolates (NONOates) (Figure 1.20, bottom) have been proposed as NO-donor groups for the controlled delivery of NO from materials. NONOates are synthetic molecules formed through nitrosation of secondary and primary amines. NONOates exhibit spontaneous decomposition, generating two molecules of NO per NONOate molecule [420–422]. RSNOs, on the other hand, occur in both natural and synthetic forms, and can be prepared through nitrosation of the sulfur atom of the thiol (Figure 1.21) [420–422]. RSNOs decompose in response to heat, light, copper ions, and changes in pH, to release one molecule of NO per RSNO. Recently, Lutkze *et al.* demonstrated that other metal ions, such as indium, also facilitate the release of NO from RSNOs [423]. This discovery may lead to additional systems that can be engineered to produce NO from RSNOs. Some RSNOs are naturally occurring within the blood, and likely serve as the endogenous substrates for NO production by endothelial cells [424]. Both NONOates and RSNOs have demonstrated their ability as potent antiplatelet agents and vasodilators and are therefore very promising for blood-contacting applications [421]. While there are numerous reports related to small-molecule and polymeric NO donors, only a few will be discussed in this section.

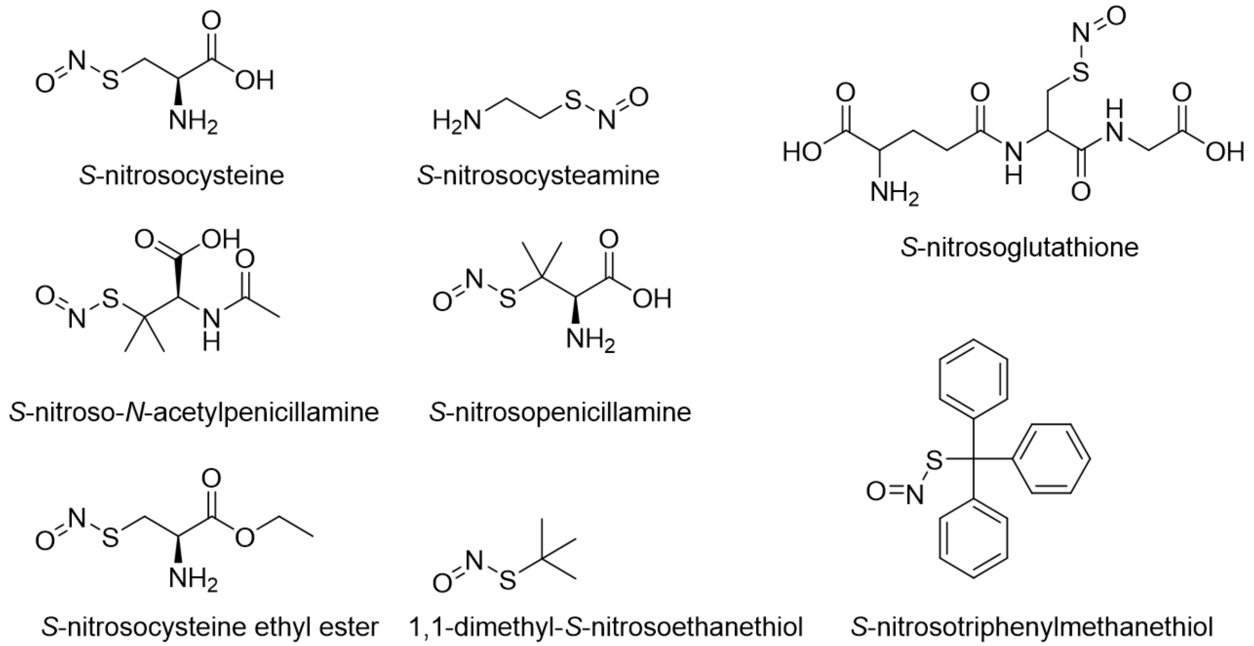

S-nitrosocysteine

S-nitrosocysteamine

S-nitrosoglutathione

S-nitroso-*N*-acetylpenicillamine

S-nitrosopenicillamine

S-nitrosocysteine ethyl ester

1,1-dimethyl-*S*-nitrosoethanethiol

S-nitrosotriphenylmethanethiol

Figure 1.21. Example *S*-nitrosothiols that serve as natural or synthetic NO donors.

An early report observed that *S*-nitroso-*N*-acetylcysteine can inhibit fibrinogen binding to activated platelets in a dose-dependent manner. Fibrinogen inhibition was correlated with a corresponding increase in platelet cGMP levels [425]. This fibrinogen inhibition is potentially related in part to cGMP inhibition of phosphoinositide 3-kinase (PI3-K) receptors, which activate the GPIIb-IIIa receptors on platelets that bind to fibrinogen. This mode of action could therefore be exploited to reduce platelet adhesion, activation, and aggregation, as these processes are promoted by fibrin(ogen)-GP binding, as described above. The influence of NO on fibrinogen has been further investigated by the Reynolds group. Here, it was observed that NO-releasing polymer films increase fibrinogen deposition onto surfaces once the critical flux of NO is achieved [426]. The fibrinogen adsorbed in the presence of NO, however, does not bind to platelets, thus demonstrating an alternative mechanism for NO to act as an anti-clotting agent [427].

To achieve targeted and controllable release, NO donors are often incorporated into a polymer scaffold. Two commonly used approaches include covalently bound NO-releasing polymers and direct blending of the NO donors through physical encapsulation in the polymer [420–422]. Towards this end, NO donors have been incorporated into PVC, hydrogels, PU, PEG, silicone rubbers, polymethacrylates, sol-gels, chitosan, polyphosphazenes, and PEO to name a few materials [420–422]. As an example, one of the first reports to incorporate NONOates into a blood-contacting polymer used vascular grafts coated with cross-linked PEI, containing covalently attached NONOates [428]. To determine the effect of the NO-releasing polymer on platelet function, the vascular grafts were implanted in segments of artery-vein shunts in baboons. When compared to the control (PEI-coated vascular grafts without the NONOate chemistry) the NO-releasing grafts had substantially less platelet deposition after 1 hour. The incorporation of NONOates into polymers has proven to be a versatile strategy; a variety of materials platforms have been fabricated to incorporate these NONOates including silica particles, sol-gels, xerogels, dendrimers, electrospun fibers and polymer blends [429–436]. However, the utilization of these materials may ultimately be hindered by the formation of carcinogenic products (nitrosamine).

The covalent attachment of RSNOs to polymer blends for blood-contacting surfaces has been investigated [437]. In this work, polynitrosated polyester/poly(methyl methacrylate) (PE/PMMA) blends were synthesized, which released NO at a rate of 1.8 ± 0.1 nmol g^{-1} h^{-1} for up to 24 h. Platelet adhesion experiments showed that the use of polynitrosated PE/PMMA blends resulted in complete inhibition of platelet deposition, demonstrating their potential as a blood-contacting surface with local antiplatelet activity. Despite the availability of alternative NO donor species such as NONOates, RSNOs exhibit significant advantages that include limited toxicity, and a diverse selection of environmental triggers.

Recently sustained NO release by covalently attaching *S*-nitrosoacetylpenicillamine (SNAP) to PDMS was achieved [438]. The NO donor chemistry resulted in a measurable NO surface flux in the range of 0.5 to 8.35×10^{-10} mol cm^{-2} min^{-1} for 38 days, with no leaching of the NO-donor. After that, the materials continued to release measurable amounts of NO for as long as 125 days, though at a level below the target minimum physiological flux (0.5×10^{-10} mol cm^{-2} min^{-1}). The materials were tested in blood flow circuits. In the control circuits, platelet concentrations were observed to drop below 55% of baseline levels. Comparatively, the NO-releasing circuits maintained platelet levels of 75% compared to baseline after 4 hours (Figure 1.22). Evaluation of the circuits both qualitatively and quantitatively, revealed that the SNAP-PDMS coated circuits displayed a 78% reduction in thrombus formation compared to control circuits (Figure 1.22). In an additional report, the same group evaluated controlling NO release from SNAP through covalent attachment to PVC (SNAP-PVC) [439]. Both photointiated and metal ion-induced NO release was demonstrated in this work.

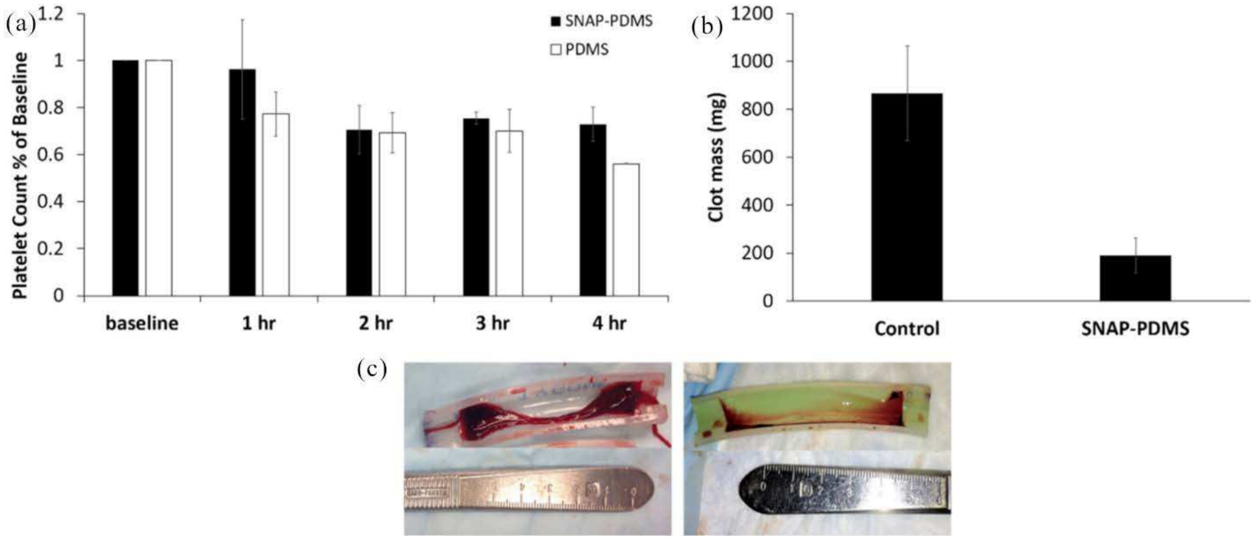

Figure 1.22. Hemocompatibility measurements of SNAP−PDMS-coated tubing for ECC testing. (A) Time-dependent effects of NO release from the ECC on platelet count over the course of the 4 h study ($n = 3$). (B) Quantification of clot mass obtained from the thrombogenicity chamber. (C) Visual representation of the clotting that occurred in PDMS-coated controls (left) and SNAP−PDMS-coated circuits (right). $p < 0.05$ was used for comparison. Error bars represent standard deviation. *Reproduced with permission from* [438], *copyright 2018, American Chemical Society*.

Xu *et al*. assessed SNAP-doped, textured PU as a dual-functional surface to mimic the inner surface of blood vessels for inhibiting platelet and bacterial adhesion (Figure 1.23, top) [440]. Plasma coagulation properties of SNAP-doped PU were evaluated by assessment of FXII activation to FXIIa. In comparison to textured films, smooth PU displayed the highest amount of FXIIa at a yield of 0.64 ± 0.08 ng mm^{-2}. SNAP loading (either 5 or 10%) further reduced FXIIa yields to one third of the amount produced on smooth PU (Figure 1.23, top). Furthermore evaluation of platelet adhesion and activation on the polymer surfaces by optical imaging suggested that SNAP-doped, textured PU significantly reduced both platelet adhesion and activation when compared to smooth PU (Figure 1.23, top).

In another report, catheters were fabricated from a SNAP-doped CarboSil system. The ability of the material to prevent thrombus formation was evaluated in an in vivo model by placing catheters into the external jugular veins of rabbits for 7 h [441]. After removal, digital images of the catheter surfaces demonstrated that thrombus formation was significantly reduced on the SNAP-doped CarboSil catheters compared to the control (Figure 1.23, bottom). Furthermore, evaluation of the NO release properties demonstrated that SNAP-doped CarboSil films can generate NO fluxes above 0.5×10^{-10} mol cm^{-2} min^{-1} (which is at the low end of the physiological range of the endothelial surface flux) for greater than three weeks (Figure 1.23, bottom).

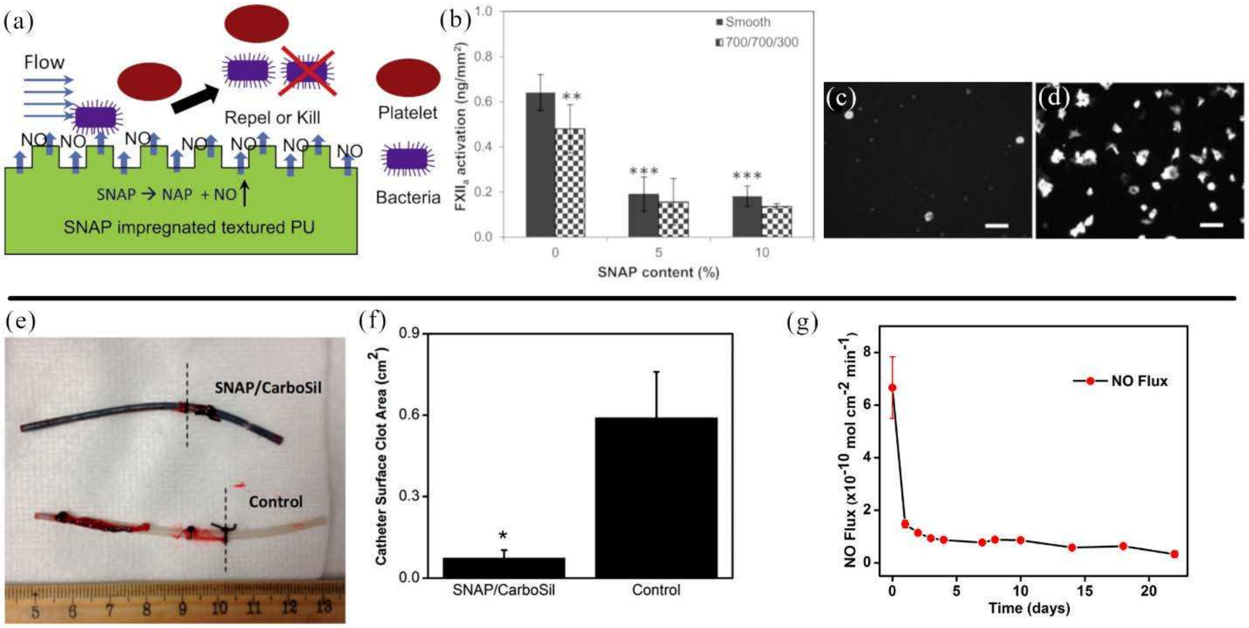

Figure 1.23. Top. (a) Textured polyurethane (PU) is impregnated with SNAP. The combination of surface texturing and NO release mimics the inner surface of blood vessels and inhibits platelet and bacterial adhesion. (b) FXII contact activation in contact with polymers for 60 min. Statistical analysis was performed to compare the smooth PU films without SNAP. (Statistical symbols, **: $p < 0.01$; ***: $p < 0.001$). Representative images of platelets adhered on surface of (c) 10% SNAP impregnated 700/700 nm and (d) smooth PU films without SNAP impregnation, showing different platelet morphologies. Scale bar = 10 µm. *Reproduced with permission from* [440], *copyright 2019, Elsevier.* **Bottom**. (e) Five cm of the catheters (left of the dash line) were inserted into the rabbit external jugular veins for 7 h. Representative pictures of thrombus formation on the SNAP/CarboSil and control catheters after removal from veins. (f) Two-dimensional representation of clot area (cm^2) on SNAP/CarboSil and control catheters in rabbit veins for 7 h, as quantitated using ImageJ software from NIH. Data are mean ± SEM ($n = 3$). * = $p < 0.05$, SNAP/CarboSil vs control catheters. (g) NO flux from 10 wt % SNAP-doped CarboSil films with SR topcoats in PBS at 37 °C for 22 days. Data are mean ± SEM ($n = 3$). *Reproduced with permission from* [441], *copyright 2015, American Chemical Society.*

For the long-term application of blood-contacting materials, NO-donor chemistries have a distinct disadvantage: the NO release decays with time, and is eventually depleted. One strategy to overcome this challenge is to develop materials that can catalyze the generation of NO directly from endogenous RSNOs. This strategy is discussed in the next section.

1.4.6.3 Catalytic generation of NO

The use of exogenous NO donors to produce NO-releasing medical implants for long-term applications is limited by a finite reservoir of the NO-donating group. Once the donor species is depleted of its NO release capability, the direct on-going therapeutic effects from the action of NO are arrested. In the majority of cases, this depletion occurs within hours, days, or weeks. To transcend this limitation, alternative routes have proposed the generation of NO directly from endogenous substrates. Materials that harness this concept have included polymer-immobilized organotellurium and selenium catalysts, as well as copper nanoparticles and complexes [442–453]. The Meyerhoff group has pioneered the generation of NO from RSNOs that occur naturally in blood. The use of catalysts developed from the Group 16 elements selenium and tellurium was inspired by a biomimetic approach that sought to reproduce the biological activity of glutathione peroxidase, a selenium-containing enzyme that generates NO from RSNOs through a catalytic reaction [454]. While selenide-based and telluride-based materials successfully generated NO from RSNOs such as GSNO and *S*-nitrosocystein (CysNO), the addition of thiol was necessary to maintain the catalytic cycle [443–446]. Other approaches have used copper species to induce the catalytic generation of NO from both RSNOs and nitrite [447–453,455]. However, many of these approaches proceed through the intentional generation and release of copper ions into solution, which depletes the activity of the material, and could cause potential toxicity [448–453].

The ability of 1,4,7,10-tetraazacyclododecane complexes [Cu(II)-cyclen] to generate NO from both GSNO and CysNO has been investigated, following covalent attachment to cross-linked PHEMA [452]. NO release experiments demonstrated that immersion of Cu(II)-cyclen/PHEMA films into solutions containing RSNOs could produce steady NO surface fluxes in the range of 2.5 $\times 10^{-10}$ mol cm^{-2} min^{-1}, a value that is within the range observed for NO release from healthy endothelial cells. Unfortunately, substantial copper leaching occurred (approximately 40%) after soaking the materials in PBS with GSNO/GSH over 15 days. Subsequent evaluation of catalytic activity showed a resulting decrease in NO generation by 25-50% [456].

In another report the catalytic properties of Cu(II)-cyclen complexes covalently attached to a hydrophillic PU were investigated [453]. While this material generated an NO flux between 1-3 $\times 10^{-10}$ mol cm^{-2} min^{-1}, the material lost 25% of the copper, due to leaching, within the first 24 h, with an additional 25% within a week. These subsequent findings of copper leaching demonstrate that the initial materials were not catalytic in function.

Major *et al.* incorporated 1, 5, and 10 wt.% copper nanoparticles into a hydrophilic PU to develop a material which mimicked the tubing of an extracorporeal circulation device [448]. This approach was based on the slow corrosion of Cu^0 to generate catalytically active Cu^{2+} ions. Addition of 1 μM GSNO resulted in NO flux measurements of 5, 10 and 12×10^{-10} mol cm^{-2} min^{-1}, using different weight percentages of copper nanoparticles. Experiments with blood showed that the plasma copper concentration increased by a factor of 1-1.3 after 4 hours, suggesting some copper leaching [448]. Meyerhoff and coworkers have also demonstrated the ability to electrochemically generate NO in the presence of nitrite through a Cu^+-mediated pathway. Generation of Cu^+ proceeded either through the reduction of a Cu^{2+} or through the oxidation of Cu^0 wire. The materials were able to generate NO in the range of $0.5\text{-}3.5\times10^{-10}$ mol cm^{-2} min^{-1}, corresponding to physiologically produced levels [457–459]. Catheters designed using this strategy resulted in substantial reductions in thrombus formation, when implanted into rabbit veins for 7 h, and they also exhibited substantial antibacterial activity against *S. aureus* and *E. coli* [458].

Other reports described the incorporation of a copper dibenzol [e,k]-2,3,8,9-tetraphenyl-1,4,7,10-tetraaza-cyclododeca-1,3,7,9-tetraene complex (CuDTTCT) into polymers for the catalytic generation of NO from nitrite [447,455]. By incorporating CuDTTCT species into PVC, NO could be produced from nitrite using ascorbic acid as the reducing agent. More recently, the same group reported on an iron-based complex which was capable of facilitating the redox cycle for catalytic generation of NO from nitrite in the presence of the copper species [455]. In both reports, less than 1% of the copper was leached after three days of incubation with nitrifying bacteria [455]. While these studies hold merit for medical applications, the ability to generate NO from nitrite becomes more relevant for antibacterial applications, because nitrite is an established product of bacterial metabolism [447,455].

While immobilized copper-based species generate NO from the decomposition of RSNOs, limitations arise with respect to long-term medical devices due to gradual loss of the catalytic materials and subsequent toxicity related to copper leaching. As such, research has progressed towards the development of a material in which the copper sites remain immobilized within the structural framework under physiological conditions, which is extremely desirable for medical applications. In particular, a promising alternative involves the use of metal–organic frameworks (MOFs) for NO generation. In MOFs, the immobilization of the metals within the extended framework can result in their enhanced stability over other copper complexes, reducing the copper leaching. Two copper-based MOFs have been investigated for their NO-generating activity in the presence of certain NO donors. These include the copper-carboxylate based MOF, copper benzene-1,3,5-tricarboxylate (CuBTC, Figure 1.24) and the copper triazoleate-based MOF, $H_3[Cu_4Cl)_3(BTTri)_8(H_2O)_{12}]\bullet 72H_2O$, where BTTri is 1,3,5-tris(1*H*-1,2,3-triazol-5-yl)benzene (CuBTTri, Figure 1.25) [460,461].

CuBTC forms face-centered cubic crystals composed of dimeric copper(II) ions at the vertices and four trimesate ligands, which form a paddle-wheel-type configuration (Figure 1.24) [462]. CuBTC has remained the subject of ongoing study and has been proposed for numerous applications. In particular, Harding *et al.* evaluated the ability of CuBTC to generate NO from the NO donor, CysNO. Experiments performed in reagent alcohol in the presence of CysNO and cysteine (CysH), showed that CuBTC recovered nearly 100% of theoretical NO upon the addition of 2, 10, and 15-fold excesses of CysNO relative to theoretical copper sites in CuBTC, with no evidence that copper species were uncomplexed or leached into solution [460].

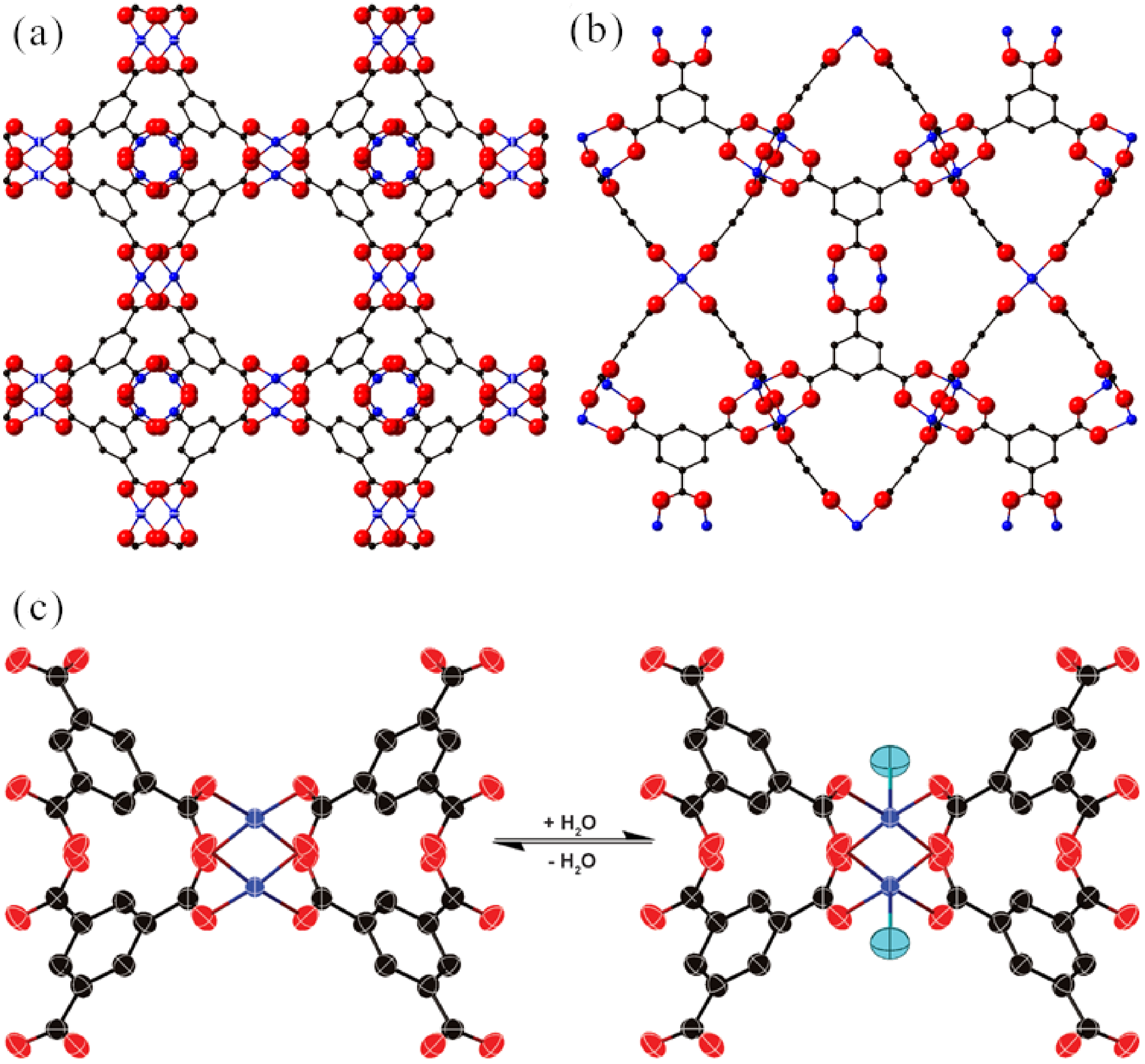

Figure 1.24. Structure of CuBTC (a) as viewed along the a-axis (b) viewed along the (110) plane (c) local environment around the copper centers which forms the SBUs. Image on the left illustrates the copper centers upon dehydration with two possible binding sites. Image on the right illustrates the hydrated version. Carbon atoms are represented in black, oxygen in red and copper in blue. Hydrogen atoms have been omitted for clarity.

The robust, cubic sodalite-type MOF, CuBTTri, featuring open Cu(II) coordination sites has been synthesized (Figure 1.25) [463]. CuBTTri has enhanced water stability compared to CuBTC [463]. The catalytic production of NO from *S*-nitrosocysteamine by both CuBTTri itself and a CuBTTri/polymer blend (PU) has been demonstrated [461]. The presence of CuBTTri resulted in enhanced NO generation when compared to the baseline decomposition of the RSNO. The inclusion of CuBTTri into a polymer gave an 8-fold reduction in the rate of NO generation, demonstrating that incorporation into a polymeric material can impact NO generation due to diffusion limitation of the RSNO [461].

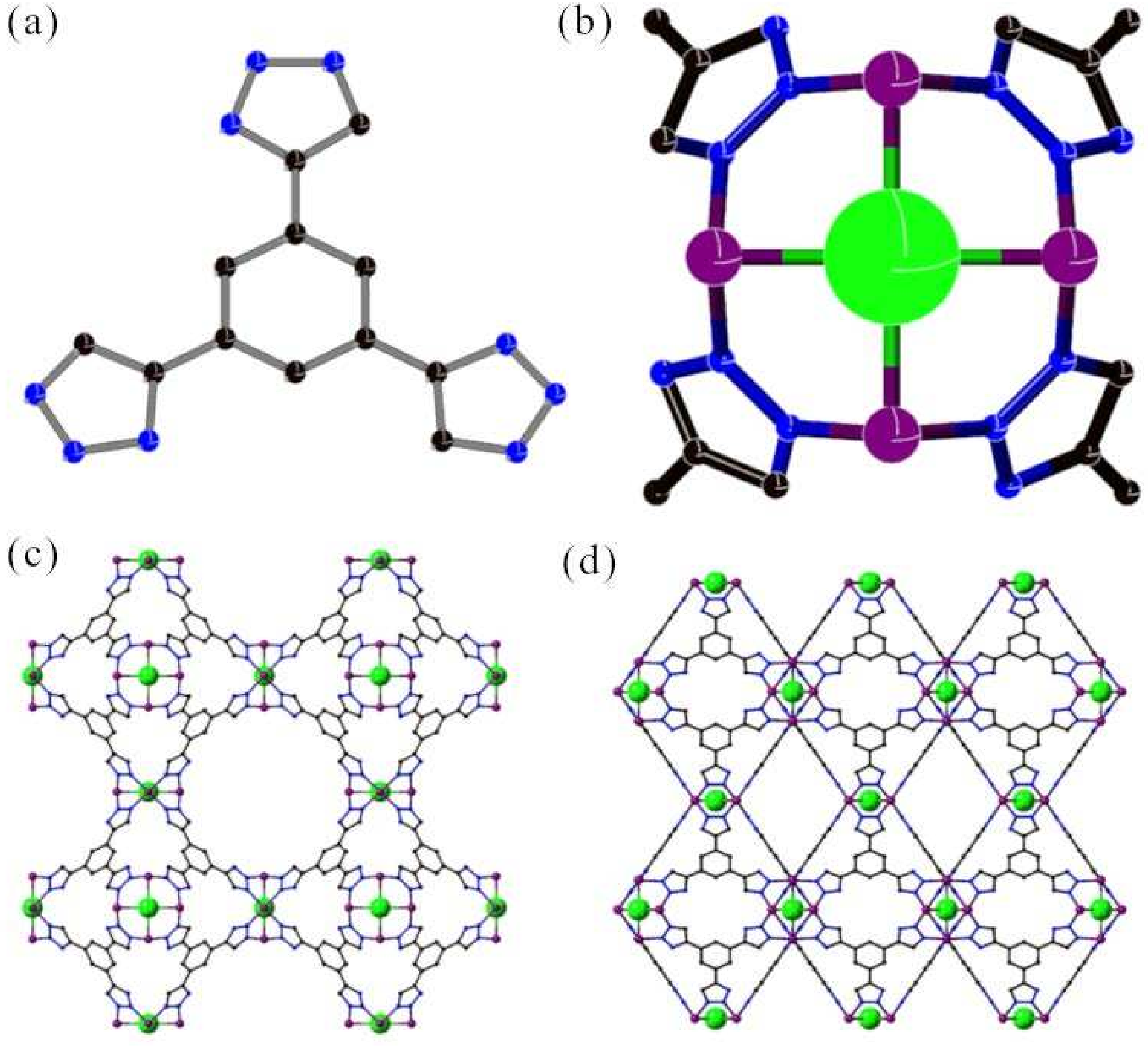

Figure 1.25. Components of the CuBTTri MOF (a) structure of the BTTri ligand that binds with six different copper species (b) SBU with square planar geometry (c) viewed along the a-axis (d) view along the (110) plane.

The concept of localizing the MOF to the surfaces of polymers and metals has been investigated [464,465]. The direct growth of CuBTC on carboxymethylated cotton fabric was demonstrated using LbL methodology [464]. Evaluation of the coated fabric indicated that the material was able to induce NO formation from *S*-nitrosocysteamine at rates comparable to unsupported CuBTC particles. Overall, this work demonstrated that CuBTC can be deposited onto a flexible polymeric material with excellent surface coverage, and that NO release can be catalyzed at therapeutically-relevant levels. Further work by Neufeld *et al.* incorporated CuBTTri into films made from PVC, a polymer used to fabricate the tubing used to transport blood in extra corporeal circuits [466]. The ability of CuBTTri to enhance the rate of NO generation from SNAP was retained following incorporation within PVC. Following exposure to SNAP at ambient temperature and physiological pH, it was observed that CuBTTri/PVC films were able to generate NO at a level frequently associated with antithrombogenic surfaces. However, until recently, the absence of definitive evidence that either CuBTC or CuBTTri could initiate the decomposition of the physiological RSNO reservoir (which is largely composed of *S*-nitrosoalbumin and GSNO) remained a significant obstacle to further development. Further efforts toward increasing catalytic NO-generation have transitioned to inclusion into polymer formulations with increased hydrophilic character, such as chitosan and poly(vinyl alcohol) (PVA) [467,468]. These reports first demonstrated MOF-induced NO generation from GSNO, the most abundant small-molecule RSNO, at physiologically relevant concentrations. In particular, upon incorporation into PVA, NO release occurred at a surface flux that falls within the range associated with the natural endothelium.

Biomaterials that include CuBTTri possess significant clinical potential due to the ability of the MOF to modulate biological processes such as clotting. These MOF materials have been shown to maintain platelet function. In a recent report by the Batchinsky and Reynolds groups, exposure of blood to a MOF decreased clot strength and accelerated fibrinolysis at 30 min and 60 min post- clot strength detection in the *ex vivo* preparation, demonstrating the antiplatelet function of the MOF material [469]. This observation of reduced clot strength and accelerated clot lysis was hypothesized to result from NO through inhibition of platelet aggregation and promotion of clot dissolution.

The development of MOFs for biomedical applications is at an early stage, with no current use in patient care. An understanding of the biodegradability, stability, and toxicity of MOFs is an undeveloped field with information regarding these critical factors limited to only a handful of publications. In regards to the use of MOFs for biomedical applications, the majority of reports have focused their attention specifically on MOF particles. However, potential applications will remain limited unless the materials are incorporated within a polymeric support. Towards this end, MOFs are fabricated into thin films or membranes through two generalized approaches: the direct blending of the MOF within the polymer matrix and chemical attachment of MOFs to a substrate via *in situ* growth. Direct incorporation of MOF particles into commercially available polymeric materials allows the potential to maintain properties of the parent material while adding the desired properties of the MOF. MOF incorporation to various metal or polymer substances and the amount of RSNOs available near the device site remain as challenges to the manufacturability of these materials. For example, medical devices made from materials that are not easily modified and need thin polymer layers are not as accessible as the materials that can be easily extruded or surface modified, like heparin-bonded surfaces through EDC modifications. PU, polymethacrylates and PVC are easily surface modified, whereas materials like poly(methyl pentene) are more difficult to pre-treat in a manner similar to heparin coatings. Excitingly, given the potential for sustained activity, the manufacturability of the MOF materials, the ability to combine them with other technologies and the safety profile of these materials, on-going research efforts in this area are likely to produce a translational pathway to the clinic.

When developing materials specifically for blood-contacting applications, NO release function is a well-established, promising approach to preventing thrombus formation. As polymeric encapsulation can significantly influence NO generation using MOFs, another challenge involves identification of polymers that optimize the productive, NO-forming interaction between aqueous-phase RSNOs and the encapsulated MOF. The future investigation and assessment of their *in vivo* activity will aid in the refinement and advancement of these promising systems for medical applications.

1.5. Summary and outlook for future research

The robustness with which blood is able to respond to foreign materials—particularly through clotting and inflammatory responses—represents many challenges in the quest for blood-compatible materials. While the risks presented by these physiological responses can be mitigated through drugs, the long-term systemic administration of drugs to alleviate risks associated with cardiovascular implants and extracorporeal blood circuits is not ideal, and is insufficient to prevent device failure. To address this need, materials scientists and engineers have taken up the grand challenge of developing blood-compatible materials that locally reduce or prevent negative blood-material interactions.

The design of blood-compatible materials requires an understanding of the physiological mechanisms that give rise to undesirable blood-material interactions, such as blood clotting and inflammation. For example, the early focus on preventing nonspecific protein adsorption is gradually being supplanted by more informed approaches, which seek to optimize protein stability, and the interactions of surfaces with specific proteins. Surfaces with features that drive or control cellular responses, such as platelet activation and macrophage polarization, either indirectly (by selective protein adsorption and stabilization) or directly (by presentation of specific signals) also show promise for improving blood-material interactions. By understanding the underlying mechanisms driving the physiological responses of the blood to materials, the impacts of the physical, chemical, and structural properties of the material on these processes can be elucidated. Only then can useful design principles for blood-compatible materials be developed.

Within the several approaches reviewed here, perhaps the predominant recurring challenge is the stability or durability of the material and its blood-compatible properties. Blood contains many proteins and living cells, and the cardiovascular system is a dynamic environment. There are many chemical and physical processes that can alter the surface features of even the most intricately tuned material, ultimately altering its blood-compatibility. One strategy to overcome this challenge is develop materials which synergistically combine multiple blood-compatibilizing properties, so that as the blood has multiple mechanisms of responding, the material likewise has multiple mechanisms of compatibilization.

The biochemical and cellular mechanisms giving rise to blood-clotting and inflammation are robust, containing redundant mechanisms and positive feedback. Therefore, multiple functions and features may be required to ultimately suppress these mechanisms in long-term applications. For some applications (e.g. stents), the promotion of re-endothelialization is recognized as the best clinical outcome, so that in the long term, the blood does not contact the implanted material at all, but instead interacts with a living, multifunctional endothelial surface. This outcome may not be realizable for all blood-contacting applications, however. One particularly promising related approach that can be used to develop multifunctional blood compatible materials is strategic biomimicry. In this approach, some features of the healthy vascular endothelium are strategically selected and combined to produce a surface with multiple features that impart blood-compatibility (e.g. surface nanostructure, protein stabilization, anti-coagulant chemistry, and NO release).

Despite advances in biomimetic materials and the remarkable advances made via this and other strategies reviewed here, few of the materials developed by these approaches have been translated to clinical use. The translation of materials to clinically used devices is a slow process. Several thousand new materials are reported each year, focused on improving the biocompatibility of devices, yet very few enter a product development pathway. One reason for this may be differences in research objectives for discovery-based research versus commercialization-based research. Discovery-based research often aims to elucidate how new approaches can be optimized with respect to a particular blood-material interaction. Commercialization requires far more in-depth demonstration of safety and efficacy, as well development of reproducible manufacturing methods that can be scaled to production. Materials used in FDA-approved devices have to be manufactured using industry standards, sterilized using hospital protocols, packaged and stored under appropriate conditions and demonstrated to be safe following ISO-10993. From a materials science perspective, however, materials are often designed to address one problem associated with interactions with the blood over time scales that are not clinically translatable. This review provided a sampling of hundreds of papers in the past few years addressing proteins, platelets and inflammation. The term “biocompatibility” is used in many of these reports, yet when taken as a whole, very few of these reports focus on the safety of the material from a clinical perspective; rather the focus is often on the aspects related to thrombus formation and the kinetics of the blood-material interactions.

New materials that focus on the dynamic and changing interface between the blood and material will likely provide the most rapid progress towards the truly biocompatible surface. At the same time, our *in vitro* testing methods should be expanded to move beyond short-term (e.g. a 2-hour time point) experiments to long-term (e.g. a time-scale that more closely matches both the long-term effects at the blood-material interface and the ultimate end use). Finally, discussion between clinicians and materials scientists and engineers needs to occur more frequently, to facilitate a better pairing between the end user (physicians) and the new materials. As long as materials researchers and clinicians do not engage in fruitful, tangible discussion, then we are unlikely to move more materials from the bench to clinic.

The recent advances in blood-compatible materials reviewed here collectively demonstrate several promising avenues for future research. Materials science and engineering is offering many new technologies based on the ability to tune chemistry and structure of materials to achieve durable and robust biological functions. Some of the most promising recent avenues of research reviewed here are those which establish performance limits and relevant design criteria for new blood-compatible materials. While these pursuits have not yet produced the ‘holy grail’ of an ideal blood-contacting material, they have yielded substantial improvements in our understanding of the mechanisms governing blood compatibility, and exciting new approaches which expand the horizon of possibilities for addressing the grand challenge of truly blood-compatible materials.

REFERENCES

[1] M. Hedayati, M.J. Neufeld, M.M. Reynolds, M.J. Kipper, The quest for blood-compatible materials: Recent advances and future technologies, Materials Science and Engineering: R: Reports. 138 (2019) 118–152. doi:10.1016/j.mser.2019.06.002.

[2] I. Reviakine, F. Jung, S. Braune, J.L. Brash, R. Latour, M. Gorbet, W. van Oeveren, Stirred, shaken, or stagnant: What goes on at the blood–biomaterial interface, Blood Reviews. 31 (2017) 11–21. doi:10.1016/j.blre.2016.07.003.

[3] N. Barsoum, C. Kleeman, Now and then, the history of parenteral fluid administration, Am. J. Nephrol. 22 (2002) 284–289. doi:10.1159/000063775.

[4] A.M. Rivera, K.W. Strauss, A. van Zundert, E. Mortier, The history of peripheral intravenous catheters: how little plastic tubes revolutionized medicine, Acta Anaesthesiol Belg. 56 (2005) 271–282.

[5] J.B. Haycraft, E.W. Carlier, 2. A New Method for Preserving the Blood in a Fluid State outside the Body., Proceedings of the Royal Society of Edinburgh. 15 (1889) 130–131. doi:10.1017/S0370164600005186.

[6] J.B. Haycraft, An Account of Some Experiments which show that Fibrin-Ferment is Absent from Circulating Blood, J Anat Physiol. 22 (1888) 172–190.

[7] J. Tait, J.D. Gunn, THE BLOOD OF ASTACUS FLUVIATILIS: A STUDY IN CRUSTACEAN BLOOD, WITH SPECIAL REFERENCE TO COAGULATION AND PHAGOCYTOSIS, Quarterly Journal of Experimental Physiology. 12 (1918) 35–80. doi:10.1113/expphysiol.1918.sp000251.

[8] X. Liu, L. Yuan, D. Li, Z. Tang, Y. Wang, G. Chen, H. Chen, J.L. Brash, Blood compatible materials: state of the art, J. Mater. Chem. B. 2 (2014) 5718–5738. doi:10.1039/C4TB00881B.

[9] J.M. Anderson, A. Rodriguez, D.T. Chang, Foreign body reaction to biomaterials, Semin. Immunol. 20 (2008) 86–100. doi:10.1016/j.smim.2007.11.004.

[10] C.M. Jackson, Y. Nemerson, Blood Coagulation, Annual Review of Biochemistry. 49 (1980) 765–811. doi:10.1146/annurev.bi.49.070180.004001.

[11] J.M. Anderson, Biological Responses to Materials, Annual Review of Materials Research. 31 (2001) 81–110. doi:10.1146/annurev.matsci.31.1.81.

[12] J.L. Harding, M.M. Reynolds, Combating medical device fouling, Trends in Biotechnology. 32 (2014) 140–146. doi:10.1016/j.tibtech.2013.12.004.

[13] I.H. Jaffer, J.C. Fredenburgh, J. Hirsh, J.I. Weitz, Medical device-induced thrombosis: what causes it and how can we prevent it?, Journal of Thrombosis and Haemostasis. 13 (2015) S72–S81. doi:10.1111/jth.12961.

[14] K.N. Ekdahl, S. Huang, B. Nilsson, Y. Teramura, Complement inhibition in biomaterial- and biosurface-induced thromboinflammation, Seminars in Immunology. 28 (2016) 268–277. doi:10.1016/j.smim.2016.04.006.

[15] R. Klopfleisch, F. Jung, The pathology of the foreign body reaction against biomaterials: Foreign Body Reaction to Biomaterials, Journal of Biomedical Materials Research Part A. 105 (2017) 927–940. doi:10.1002/jbm.a.35958.

[16] M.B. Gorbet, M.V. Sefton, Biomaterial-associated thrombosis: roles of coagulation factors, complement, platelets and leukocytes, Biomaterials. 25 (2004) 5681–5703. doi:10.1016/j.biomaterials.2004.01.023.

[17] A.E. Zerati, N. Wolosker, N. de Luccia, P. Puech-Leão, Cateteres venosos totalmente implantáveis: histórico, técnica de implante e complicações, Jornal Vascular Brasileiro. 16 (2017) 128–139. doi:10.1590/1677-5449.008216.

[18] B.D. Ratner, The blood compatibility catastrophe, J. Biomed. Mater. Res. 27 (1993) 283–287. doi:10.1002/jbm.820270302.

[19] R.A. Byrne, M. Joner, A. Kastrati, Stent thrombosis and restenosis: what have we learned and where are we going? The Andreas Grüntzig Lecture ESC 2014, European Heart Journal. 36 (2015) 3320–3331. doi:10.1093/eurheartj/ehv511.

[20] G.D. Dangas, J.I. Weitz, G. Giustino, R. Makkar, R. Mehran, Prosthetic Heart Valve Thrombosis, Journal of the American College of Cardiology. 68 (2016) 2670–2689. doi:10.1016/j.jacc.2016.09.958.

[21] F. Jung, S. Braune, Thrombogenicity and hemocompatibility of biomaterials, Biointerphases. 11 (2016) 029601. doi:10.1116/1.4938557.

[22] G.M. Annich, Extracorporeal life support: the precarious balance of hemostasis, Journal of Thrombosis and Haemostasis. 13 (2015) S336–S342. doi:10.1111/jth.12963.

[23] M. Mazzeffi, J. Greenwood, K. Tanaka, J. Menaker, R. Rector, D. Herr, Z. Kon, J. Lee, B. Griffith, K. Rajagopal, S. Pham, Bleeding, Transfusion, and Mortality on Extracorporeal Life Support: ECLS Working Group on Thrombosis and Hemostasis, Ann. Thorac. Surg. 101 (2016) 682–689. doi:10.1016/j.athoracsur.2015.07.046.

[24] H.J. Dalton, P. Garcia-Filion, R. Holubkov, F.W. Moler, T. Shanley, S. Heidemann, K. Meert, R.A. Berg, J. Berger, J. Carcillo, C. Newth, R. Harrison, A. Doctor, P. Rycus, J.M. Dean, T. Jenkins, C. Nicholson, Association of Bleeding and Thrombosis With Outcome in Extracorporeal Life Support*:, Pediatric Critical Care Medicine. 16 (2015) 167–174. doi:10.1097/PCC.0000000000000317.

[25] J. Laster, D. Silver, Heparin-coated catheters and heparin-induced thrombocytopenia, J. Vasc. Surg. 7 (1988) 667–672.

[26] S.V. Pamboukian, A.P. Ignaszewski, H.J. Ross, Management strategies for heparin-induced thrombocytopenia in heart-transplant candidates: case report and review of the literature, J. Heart Lung Transplant. 19 (2000) 810–814.

[27] Cohen, Heparin Induced Thrombocytopenia: Case Presentation and Review, Journal of Clinical Medicine Research. (2012). doi:10.4021/jocmr751w.

[28] L. Vroman, When Blood Is Touched, Materials. 2 (2009) 1547–1557. doi:10.3390/ma2041547.

[29] B. Furie, B.C. Furie, Mechanisms of Thrombus Formation, New England Journal of Medicine. 359 (2008) 938–949. doi:10.1056/NEJMra0801082.

[30] R.W. Colman, Chapter 3 Mechanisms of thrombus formation and dissolution, Cardiovascular Pathology. 2 (1993) 23–31. doi:10.1016/1054-8807(93)90044-3.

[31] G.H.R. Rao, T. Chandy, Role of platelets in blood-biomaterial interactions, Bulletin of Materials Science. 22 (1999) 633–639. doi:10.1007/BF02749979.

[32] C.E. Hansen, Y. Qiu, O.J.T. McCarty, W.A. Lam, Platelet Mechanotransduction, Annual Review of Biomedical Engineering. 20 (2018) 253–275. doi:10.1146/annurev-bioeng-062117-121215.

[33] L.F. Brass, Thrombin and Platelet Activation, Chest. 124 (2003) 18S-25S. doi:10.1378/chest.124.3_suppl.18S.

[34] J.G. Kelton, M.A. Blajchman, Prostaglandin I2 (prostacyclin), Can Med Assoc J. 122 (1980) 175–179.

[35] M.T. Kalathottukaren, J.N. Kizhakkedathu, Mechanisms of blood coagulation in response to biomaterials: Extrinsic factors, in: Hemocompatibility of Biomaterials for Clinical Applications, Elsevier, 2018: pp. 29–49. doi:10.1016/B978-0-08-100497-5.00003-3.

[36] B.S. Smith, S. Yoriya, L. Grissom, C.A. Grimes, K.C. Popat, Hemocompatibility of titania nanotube arrays, Journal of Biomedical Materials Research Part A. 95A (2010) 350–360. doi:10.1002/jbm.a.32853.

[37] R. Simon-Walker, R. Romero, J.M. Staver, Y. Zang, M.M. Reynolds, K.C. Popat, M.J. Kipper, Glycocalyx-Inspired Nitric Oxide-Releasing Surfaces Reduce Platelet Adhesion and Activation on Titanium, ACS Biomaterials Science & Engineering. 3 (2017) 68–77. doi:10.1021/acsbiomaterials.6b00572.

[38] H. Kato, Y. Tomiyama, Platelet Membrane Glycoproteins, in: Y. Ishida, Y. Tomiyama (Eds.), Autoimmune Thrombocytopenia, Springer Singapore, Singapore, 2017: pp. 21–37. doi:10.1007/978-981-10-4142-6_3.

[39] L. Ju, J. Dong, M.A. Cruz, C. Zhu, The N-terminal Flanking Region of the A1 Domain Regulates the Force-dependent Binding of von Willebrand Factor to Platelet Glycoprotein Ibα, Journal of Biological Chemistry. 288 (2013) 32289–32301. doi:10.1074/jbc.M113.504001.

[40] B.J. Fredrickson, J.F. Dong, L.V. McIntire, J.A. López, Shear-dependent rolling on von Willebrand factor of mammalian cells expressing the platelet glycoprotein Ib-IX-V complex, Blood. 92 (1998) 3684–3693.

[41] L.-C. Xu, J.W. Bauer, C.A. Siedlecki, Proteins, platelets, and blood coagulation at biomaterial interfaces, Colloids and Surfaces B: Biointerfaces. 124 (2014) 49–68. doi:10.1016/j.colsurfb.2014.09.040.

[42] A.L. Frelinger, Using flow cytometry to monitor glycoprotein IIb-IIIa activation, Platelets. 29 (2018) 670–676. doi:10.1080/09537104.2018.1478073.

[43] L.B. Koh, I. Rodriguez, S.S. Venkatraman, The effect of topography of polymer surfaces on platelet adhesion, Biomaterials. 31 (2010) 1533–1545. doi:10.1016/j.biomaterials.2009.11.022.

[44] Y. Ding, Y. Leng, N. Huang, P. Yang, X. Lu, X. Ge, F. Ren, K. Wang, L. Lei, X. Guo, Effects of microtopographic patterns on platelet adhesion and activation on titanium oxide surfaces, Journal of Biomedical Materials Research Part A. 101A (2013) 622–632. doi:10.1002/jbm.a.34361.

[45] G.M. Annich, O. Zaulan, M. Neufeld, D. Wagner, M.M. Reynolds, Thromboprophylaxis in Extracorporeal Circuits: Current Pharmacological Strategies and Future Directions, American Journal of Cardiovascular Drugs. 17 (2017) 425–439. doi:10.1007/s40256-017-0229-0.

[46] K.N. Ekdahl, Y. Teramura, O.A. Hamad, S. Asif, C. Duehrkop, K. Fromell, E. Gustafson, J. Hong, H. Kozarcanin, P.U. Magnusson, M. Huber-Lang, P. Garred, B. Nilsson, Dangerous liaisons: complement, coagulation, and kallikrein/kinin cross-talk act as a linchpin in the events leading to thromboinflammation, Immunological Reviews. 274 (2016) 245–269. doi:10.1111/imr.12471.

[47] M.M. Reynolds, G.M. Annich, The artificial endothelium, Organogenesis. 7 (2011) 42–49. doi:10.4161/org.7.1.14029.

[48] K. Bridge, H. Philippou, R. Ariëns, Clot properties and cardiovascular disease, Thrombosis and Haemostasis. 112 (2014) 901–908. doi:10.1160/th14-02-0184.

[49] J.W. Weisel, R.I. Litvinov, Mechanisms of fibrin polymerization and clinical implications, Blood. 121 (2013) 1712–1719. doi:10.1182/blood-2012-09-306639.

[50] A. Mazurkiewicz-Pisarek, G. Płucienniczak, T. Ciach, A. Płucienniczak, The factor VIII protein and its function, Acta Biochim. Pol. 63 (2016) 11–16. doi:10.18388/abp.2015_1056.

[51] S. Reitsma, D.W. Slaaf, H. Vink, M.A.M.J. van Zandvoort, M.G.A. oude Egbrink, The endothelial glycocalyx: composition, functions, and visualization, Pflügers Archiv - European Journal of Physiology. 454 (2007) 345–359. doi:10.1007/s00424-007-0212-8.

[52] C. Sperling, M.F. Maitz, C. Werner, Test methods for hemocompatibility of biomaterials, in: Hemocompatibility of Biomaterials for Clinical Applications, Elsevier, 2018: pp. 77–104. doi:10.1016/B978-0-08-100497-5.00005-7.

[53] S. Braune, A. Lendlein, F. Jung, Developing standards and test protocols for testing the hemocompatibility of biomaterials, in: Hemocompatibility of Biomaterials for Clinical Applications, Elsevier, 2018: pp. 51–76. doi:10.1016/B978-0-08-100497-5.00004-5.

[54] Z. Xia, J.T. Triffitt, A review on macrophage responses to biomaterials, Biomedical Materials. 1 (2006) R1–R9. doi:10.1088/1748-6041/1/1/R01.

[55] T.H. Rogers, J.E. Babensee, Altered adherent leukocyte profile on biomaterials in Toll-like receptor 4 deficient mice, Biomaterials. 31 (2010) 594–601. doi:10.1016/j.biomaterials.2009.09.077.

[56] A. Grandjean-Laquerriere, O. Tabary, J. Jacquot, D. Richard, P. Frayssinet, M. Guenounou, D. Laurent-Maquin, P. Laquerriere, S. Gangloff, Involvement of toll-like receptor 4 in the inflammatory reaction induced by hydroxyapatite particles, Biomaterials. 28 (2007) 400–404. doi:10.1016/j.biomaterials.2006.09.015.

[57] F. Ginhoux, S. Jung, Monocytes and macrophages: developmental pathways and tissue homeostasis, Nature Reviews Immunology. 14 (2014) 392–404. doi:10.1038/nri3671.

[58] J.M. Anderson, Biocompatibility and Bioresponse to Biomaterials, in: Principles of Regenerative Medicine, Elsevier, 2019: pp. 675–694. doi:10.1016/B978-0-12-809880-6.00039-4.

[59] L.B. Moore, T.R. Kyriakides, Molecular Characterization of Macrophage-Biomaterial Interactions, in: J.D. Lambris, K.N. Ekdahl, D. Ricklin, B. Nilsson (Eds.), Immune Responses to Biosurfaces, Springer International Publishing, Cham, 2015: pp. 109–122. doi:10.1007/978-3-319-18603-0_7.

[60] R. Sridharan, A.R. Cameron, D.J. Kelly, C.J. Kearney, F.J. O'Brien, Biomaterial based modulation of macrophage polarization: a review and suggested design principles, Materials Today. 18 (2015) 313–325. doi:10.1016/j.mattod.2015.01.019.

[61] K.L. Spiller, R.R. Anfang, K.J. Spiller, J. Ng, K.R. Nakazawa, J.W. Daulton, G. Vunjak-Novakovic, The role of macrophage phenotype in vascularization of tissue engineering scaffolds, Biomaterials. 35 (2014) 4477–4488. doi:10.1016/j.biomaterials.2014.02.012.

[62] M. Weber, H. Steinle, S. Golombek, L. Hann, C. Schlensak, H.P. Wendel, M. Avci-Adali, Blood-Contacting Biomaterials: In Vitro Evaluation of the Hemocompatibility, Frontiers in Bioengineering and Biotechnology. 6 (2018). doi:10.3389/fbioe.2018.00099.

[63] P.-A. Mouthuy, S.J.B. Snelling, S.G. Dakin, L. Milković, A.Č. Gašparović, A.J. Carr, N. Žarković, Biocompatibility of implantable materials: An oxidative stress viewpoint, Biomaterials. 109 (2016) 55–68. doi:10.1016/j.biomaterials.2016.09.010.

[64] F.Y. McWhorter, T. Wang, P. Nguyen, T. Chung, W.F. Liu, Modulation of macrophage phenotype by cell shape, Proceedings of the National Academy of Sciences. 110 (2013) 17253–17258. doi:10.1073/pnas.1308887110.

[65] K.M. Hotchkiss, N.M. Clark, R. Olivares-Navarrete, Macrophage response to hydrophilic biomaterials regulates MSC recruitment and T-helper cell populations, Biomaterials. 182 (2018) 202–215. doi:10.1016/j.biomaterials.2018.08.029.

[66] W.-C. Xu, X. Dong, J.-L. Ding, J.-C. Liu, J.-J. Xu, Y.-H. Tang, Y.-P. Yi, C. Lu, W. Yang, J.-S. Yang, Y. Gong, J.-L. Zhou, Nanotubular TiO_2 regulates macrophage M2 polarization and increases macrophage secretion of VEGF to accelerate endothelialization via the ERK1/2 and PI3K/AKT pathways, International Journal of Nanomedicine. Volume 14 (2019) 441–455. doi:10.2147/IJN.S188439.

[67] M.B. Ariganello, D. Guadarrama Bello, A. Rodriguez-Contreras, S. Sadeghi, G. Isola, F. Variola, A. Nanci, Surface nanocavitation of titanium modulates macrophage activity, International Journal of Nanomedicine. Volume 13 (2018) 8297–8308. doi:10.2147/IJN.S185436.

[68] L. Lv, Y. Xie, K. Li, T. Hu, X. Lu, Y. Cao, X. Zheng, Unveiling the Mechanism of Surface Hydrophilicity-Modulated Macrophage Polarization, Advanced Healthcare Materials. 7 (2018) 1800675. doi:10.1002/adhm.201800675.

[69] S. Sohrabi, Y. Liu, A Cellular Model of Shear-Induced Hemolysis: A Cellular Model of Shear-Induced Hemolysis, Artificial Organs. 41 (2017) E80–E91. doi:10.1111/aor.12832.

[70] C.Q. Lai, J. Chia Wei Shen, W. Chua Wei Cheng, C.H. Yap, A near-superhydrophobic surface reduces hemolysis of blood flow in tubes, RSC Advances. 6 (2016) 62451–62459. doi:10.1039/C6RA12376G.

[71] R. Maraj, L.E. Jacobs, A. Ioli, M.N. Kotler, Evaluation of hemolysis in patients with prosthetic heart valves, Clinical Cardiology. 21 (1998) 387–392. doi:10.1002/clc.4960210604.

[72] H.R. Omar, M. Mirsaeidi, S. Socias, C. Sprenker, C. Caldeira, E.M. Camporesi, D. Mangar, Plasma Free Hemoglobin Is an Independent Predictor of Mortality among Patients on Extracorporeal Membrane Oxygenation Support, PLoS ONE. 10 (2015) e0124034. doi:10.1371/journal.pone.0124034.

[73] B.-K. Lam, D.M. Cosgrove, S.K. Bhudia, A.M. Gillinov, Hemolysis after mitral valve repair: mechanisms and treatment, The Annals of Thoracic Surgery. 77 (2004) 191–195. doi:10.1016/S0003-4975(03)01455-3.

[74] X. Wang, F. Zhang, C. Li, Z. Zheng, X. Wang, X. Liu, A. Chen, Z. Jiang, Improvement of blood compatibility of artificial heart valves via titanium oxide film coated on low temperature isotropic carbon, Surface and Coatings Technology. 128–129 (2000) 36–42. doi:10.1016/S0257-8972(00)00659-9.

[75] M. Rabe, D. Verdes, S. Seeger, Understanding protein adsorption phenomena at solid surfaces, Advances in Colloid and Interface Science. 162 (2011) 87–106. doi:10.1016/j.cis.2010.12.007.

[76] K.S. Lavery, C. Rhodes, A. Mcgraw, M.J. Eppihimer, Anti-thrombotic technologies for medical devices, Advanced Drug Delivery Reviews. 112 (2017) 2–11. doi:10.1016/j.addr.2016.07.008.

[77] L. Vroman, A.L. Adams, Findings with the recording ellipsometer suggesting rapid exchange of specific plasma proteins at liquid/solid interfaces, Surface Science. 16 (1969) 438–446. doi:10.1016/0039-6028(69)90037-5.

[78] S.L. Hirsh, D.R. McKenzie, N.J. Nosworthy, J.A. Denman, O.U. Sezerman, M.M.M. Bilek, The Vroman effect: Competitive protein exchange with dynamic multilayer protein aggregates, Colloids and Surfaces B: Biointerfaces. 103 (2013) 395–404. doi:10.1016/j.colsurfb.2012.10.039.

[79] S. Morsbach, G. Gonella, V. Mailänder, S. Wegner, S. Wu, T. Weidner, R. Berger, K. Koynov, D. Vollmer, N. Encinas, S.L. Kuan, T. Bereau, K. Kremer, T. Weil, M. Bonn, H.-J. Butt, K. Landfester, Engineering Proteins at Interfaces: From Complementary Characterization to Material Surfaces with Designed Functions, Angewandte Chemie International Edition. 57 (2018) 12626–12648. doi:10.1002/anie.201712448.

[80] P. Roach, D. Farrar, C.C. Perry, Interpretation of Protein Adsorption: Surface-Induced Conformational Changes, Journal of the American Chemical Society. 127 (2005) 8168–8173. doi:10.1021/ja042898o.

[81] Z. Othman, B. Cillero Pastor, S. van Rijt, P. Habibovic, Understanding interactions between biomaterials and biological systems using proteomics, Biomaterials. 167 (2018) 191–204. doi:10.1016/j.biomaterials.2018.03.020.

[82] J.M. Anderson, A. Rodriguez, D.T. Chang, Foreign body reaction to biomaterials, Seminars in Immunology. 20 (2008) 86–100. doi:10.1016/j.smim.2007.11.004.

[83] W.-B. Tsai, J.M. Grunkemeier, T.A. Horbett, Variations in the ability of adsorbed fibrinogen to mediate platelet adhesion to polystyrene-based materials: A multivariate statistical analysis of antibody binding to the platelet binding sites of fibrinogen, Journal of Biomedical Materials Research Part A. 67A (2003) 1255–1268. doi:10.1002/jbm.a.20024.

[84] T. Riedel, J. Suttnar, E. Brynda, M. Houska, L. Medved, J.E. Dyr, Fibrinopeptides A and B release in the process of surface fibrin formation, Blood. 117 (2011) 1700–1706. doi:10.1182/blood-2010-08-300301.

[85] T.A. Horbett, Fibrinogen adsorption to biomaterials: FIBRINOGEN ADSORPTION TO BIOMATERIALS, Journal of Biomedical Materials Research Part A. 106 (2018) 2777–2788. doi:10.1002/jbm.a.36460.

[86] Z.M. Ruggeri, Platelet Adhesion under Flow, Microcirculation. 16 (2009) 58–83. doi:10.1080/10739680802651477.

[87] X. Shi, J. Yang, J. Huang, Z. Long, Z. Ruan, B. Xiao, X. Xi, Effects of different shear rates on the attachment and detachment of platelet thrombi, Molecular Medicine Reports. 13 (2016) 2447–2456. doi:10.3892/mmr.2016.4825.

[88] J.N. Lindon, G. McManama, L. Kushner, E.W. Merrill, E.W. Salzman, Does the conformation of adsorbed fibrinogen dictate platelet interactions with artificial surfaces?, Blood. 68 (1986) 355–362.

[89] L. Yang, L. Han, Q. Liu, Y. Xu, L. Jia, Galloyl groups-regulated fibrinogen conformation: Understanding antiplatelet adhesion on tannic acid coating, Acta Biomaterialia. 64 (2017) 187–199. doi:10.1016/j.actbio.2017.09.034.

[90] K. Broos, H.B. Feys, S.F. De Meyer, K. Vanhoorelbeke, H. Deckmyn, Platelets at work in primary hemostasis, Blood Reviews. 25 (2011) 155–167. doi:10.1016/j.blre.2011.03.002.

[91] Y. Tomiyama, T. Tsubakio, Y. Kurata, J.C. Loftus, T.J. Kunicki, The Arg-Gly-Asp (RGD) Recognition Site of Platelet Glycoprotein IIb-IIIa on Nonactivated Platelets Is Accessible to High-Affinity Macromolecules, (n.d.) 11.

[92] L. Zhang, B. Casey, D.K. Galanakis, C. Marmorat, S. Skoog, K. Vorvolakos, M. Simon, M.H. Rafailovich, The influence of surface chemistry on adsorbed fibrinogen conformation, orientation, fiber formation and platelet adhesion, Acta Biomaterialia. 54 (2017) 164–174. doi:10.1016/j.actbio.2017.03.002.

[93] A.C. Brown, T.H. Barker, Fibrin-based biomaterials: Modulation of macroscopic properties through rational design at the molecular level, Acta Biomaterialia. 10 (2014) 1502–1514. doi:10.1016/j.actbio.2013.09.008.

[94] S. Kattula, J.R. Byrnes, A.S. Wolberg, Fibrinogen and Fibrin in Hemostasis and Thrombosis, Arteriosclerosis, Thrombosis, and Vascular Biology. 37 (2017). doi:10.1161/ATVBAHA.117.308564.

[95] M.H. Wood, C.G. Payagalage, T. Geue, Bovine Serum Albumin and Fibrinogen Adsorption at the 316L Stainless Steel/Aqueous Interface, The Journal of Physical Chemistry B. 122 (2018) 5057–5065. doi:10.1021/acs.jpcb.8b01347.

[96] Q. Wei, B. Li, N. Yi, B. Su, Z. Yin, F. Zhang, J. Li, C. Zhao, Improving the blood compatibility of material surfaces via biomolecule-immobilized mussel-inspired coatings, Journal of Biomedical Materials Research Part A. 96A (2011) 38–45. doi:10.1002/jbm.a.32956.

[97] B. Fang, Q. Ling, W. Zhao, Y. Ma, P. Bai, Q. Wei, H. Li, C. Zhao, Modification of polyethersulfone membrane by grafting bovine serum albumin on the surface of polyethersulfone/poly(acrylonitrile-co-acrylic acid) blended membrane, Journal of Membrane Science. 329 (2009) 46–55. doi:10.1016/j.memsci.2008.12.008.

[98] J.H. Park, J.A. Jackman, A.R. Ferhan, G.J. Ma, B.K. Yoon, N.-J. Cho, Temperature-Induced Denaturation of BSA Protein Molecules for Improved Surface Passivation Coatings, ACS Appl. Mater. Interfaces. 10 (2018) 32047–32057. doi:10.1021/acsami.8b13749.

[99] B. Sivaraman, R.A. Latour, The Adherence of platelets to adsorbed albumin by receptor-mediated recognition of binding sites exposed by adsorption-induced unfolding, Biomaterials. 31 (2010) 1036–1044. doi:10.1016/j.biomaterials.2009.10.017.

[100] B. Sivaraman, R.A. Latour, Time-Dependent Conformational Changes in Adsorbed Albumin and Its Effect on Platelet Adhesion, Langmuir. 28 (2012) 2745–2752. doi:10.1021/la204777x.

[101] B. Sivaraman, R.A. Latour, Delineating the roles of the GPIIb/IIIa and GP-Ib-IX-V platelet receptors in mediating platelet adhesion to adsorbed fibrinogen and albumin, Biomaterials. 32 (2011) 5365–5370. doi:10.1016/j.biomaterials.2011.04.011.

[102] T.A. Springer, Biology and physics of von Willebrand factor concatamers: von Willebrand factor concatamers, Journal of Thrombosis and Haemostasis. 9 (2011) 130–143. doi:10.1111/j.1538-7836.2011.04320.x.

[103] T.A. Springer, von Willebrand factor, Jedi knight of the bloodstream, Blood. 124 (2014) 1412–1425. doi:10.1182/blood-2014-05-378638.

[104] Mannucci Pier Mannuccio, von Willebrand Factor, Arteriosclerosis, Thrombosis, and Vascular Biology. 18 (1998) 1359–1362. doi:10.1161/01.ATV.18.9.1359.

[105] S.F.D. Meyer, H. Deckmyn, K. Vanhoorelbeke, von Willebrand factor to the rescue, Blood. 113 (2009) 5049–5057. doi:10.1182/blood-2008-10-165621.

[106] M.A.H. Sonneveld, M.P.M. de Maat, F.W.G. Leebeek, Von Willebrand factor and ADAMTS13 in arterial thrombosis: a systematic review and meta-analysis, Blood Reviews. 28 (2014) 167–178. doi:10.1016/j.blre.2014.04.003.

[107] H. Ulrichts, M. Udvardy, P.J. Lenting, I. Pareyn, N. Vandeputte, K. Vanhoorelbeke, H. Deckmyn, Shielding of the A1 Domain by the D′D3 Domains of von Willebrand Factor Modulates Its Interaction with Platelet Glycoprotein Ib-IX-V, Journal of Biological Chemistry. 281 (2006) 4699–4707. doi:10.1074/jbc.M513314200.

[108] A. Löf, J.P. Müller, M. Benoit, M.A. Brehm, Biophysical approaches promote advances in the understanding of von Willebrand factor processing and function, Advances in Biological Regulation. 63 (2017) 81–91. doi:10.1016/j.jbior.2016.09.010.

[109] S.W. Schneider, S. Nuschele, A. Wixforth, C. Gorzelanny, A. Alexander-Katz, R.R. Netz, M.F. Schneider, Shear-induced unfolding triggers adhesion of von Willebrand factor fibers, PNAS. 104 (2007) 7899–7903. doi:10.1073/pnas.0608422104.

[110] A.J. Reininger, Mechanism of platelet adhesion to von Willebrand factor and microparticle formation under high shear stress, Blood. 107 (2006) 3537–3545. doi:10.1182/blood-2005-02-0618.

[111] K. De Ceunynck, S.F. De Meyer, K. Vanhoorelbeke, Unwinding the von Willebrand factor strings puzzle, Blood. 121 (2013) 270–277. doi:10.1182/blood-2012-07-442285.

[112] H. Fu, Y. Jiang, D. Yang, F. Scheiflinger, W.P. Wong, T.A. Springer, Flow-induced elongation of von Willebrand factor precedes tension-dependent activation, Nature Communications. 8 (2017). doi:10.1038/s41467-017-00230-2.

[113] L.D.C. Casa, D.H. Deaton, D.N. Ku, Role of high shear rate in thrombosis, Journal of Vascular Surgery. 61 (2015) 1068–1080. doi:10.1016/j.jvs.2014.12.050.

[114] C. Valladolid, A. Yee, M.A. Cruz, von Willebrand Factor, Free Hemoglobin and Thrombosis in ECMO, Frontiers in Medicine. 5 (2018). doi:10.3389/fmed.2018.00228.

[115] M.H. Kroll, J.D. Hellums, L.V. McIntire, A.I. Schafer, J.L. Moake, Platelets and shear stress, Blood. 88 (1996) 1525–1541.

[116] M. Bryckaert, J.-P. Rosa, C.V. Denis, P.J. Lenting, Of von Willebrand factor and platelets, Cellular and Molecular Life Sciences. 72 (2015) 307–326. doi:10.1007/s00018-014-1743-8.

[117] Y. Ikeda, M. Handa, K. Kawano, T. Kamata, M. Murata, Y. Araki, H. Anbo, Y. Kawai, K. Watanabe, I. Itagaki, The role of von Willebrand factor and fibrinogen in platelet aggregation under varying shear stress., Journal of Clinical Investigation. 87 (1991) 1234–1240. doi:10.1172/JCI115124.

[118] B. Savage, E. Saldívar, Z.M. Ruggeri, Initiation of Platelet Adhesion by Arrest onto Fibrinogen or Translocation on von Willebrand Factor, Cell. 84 (1996) 289–297. doi:10.1016/S0092-8674(00)80983-6.

[119] M. Zhang, T.A. Horbett, Tetraglyme coatings reduce fibrinogen and von Willebrand factor adsorption and platelet adhesion under both static and flow conditions, Journal of Biomedical Materials Research Part A. 89A (2009) 791–803. doi:10.1002/jbm.a.32085.

[120] Dennis E Hourcade, Christine TN Pham, Complement Activation: Challenges to Nanomedicine Development, in: R. Bawa, J. Szebeni, T.J. Webster, Audette (Eds.), Immune Aspects of Biopharmaceuticals and Nanomedicines, CRC Press, 2019: p. 311.

[121] A.E. Engberg, P.H. Nilsson, S. Huang, K. Fromell, O.A. Hamad, T.E. Mollnes, J.P. Rosengren-Holmberg, K. Sandholm, Y. Teramura, I.A. Nicholls, B. Nilsson, K.N. Ekdahl, Prediction of inflammatory responses induced by biomaterials in contact with human blood using protein fingerprint from plasma, Biomaterials. 36 (2015) 55–65. doi:10.1016/j.biomaterials.2014.09.011.

[122] S. Jiang, Z. Cao, Ultralow-Fouling, Functionalizable, and Hydrolyzable Zwitterionic Materials and Their Derivatives for Biological Applications, Advanced Materials. 22 (2010) 920–932. doi:10.1002/adma.200901407.

[123] S.R. Meyers, M.W. Grinstaff, Biocompatible and Bioactive Surface Modifications for Prolonged In Vivo Efficacy, Chemical Reviews. 112 (2012) 1615–1632. doi:10.1021/cr2000916.

[124] W.-B. Tsai, J.M. Grunkemeier, T.A. Horbett, Human plasma fibrinogen adsorption and platelet adhesion to polystyrene, Journal of Biomedical Materials Research. 44 (1999) 130–139. doi:10.1002/(SICI)1097-4636(199902)44:2<130::AID-JBM2>3.0.CO;2-9.

[125] K. Park, F.W. Mao, H. Park, The minimum surface fibrinogen concentration necessary for platelet activation on dimethyldichlorosilane-coated glass, Journal of Biomedical Materials Research. 25 (1991) 407–420. doi:10.1002/jbm.820250311.

[126] C.A. Haynes, W. Norde, Globular proteins at solid/liquid interfaces, Colloids and Surfaces B: Biointerfaces. 2 (1994) 517–566. doi:10.1016/0927-7765(94)80066-9.

[127] F. MacRitchie, Spread monolayers of proteins, Advances in Colloid and Interface Science. 25 (1986) 341–385. doi:10.1016/0001-8686(86)80013-6.

[128] W. Norde, Driving forces for protein adsorption at solid surfaces, Macromolecular Symposia. 103 (1996) 5–18. doi:10.1002/masy.19961030104.

[129] E.A. Vogler, Protein adsorption in three dimensions, Biomaterials. 33 (2012) 1201–1237. doi:10.1016/j.biomaterials.2011.10.059.

[130] Q. Wei, T. Becherer, S. Angioletti-Uberti, J. Dzubiella, C. Wischke, A.T. Neffe, A. Lendlein, M. Ballauff, R. Haag, Protein Interactions with Polymer Coatings and Biomaterials, Angewandte Chemie International Edition. 53 (2014) 8004–8031. doi:10.1002/anie.201400546.

[131] G. Jackler, R. Steitz, C. Czeslik, Effect of Temperature on the Adsorption of Lysozyme at the Silica/Water Interface Studied by Optical and Neutron Reflectometry, Langmuir. 18 (2002) 6565–6570. doi:10.1021/la025605i.

[132] I. Kiesel, M. Paulus, J. Nase, S. Tiemeyer, C. Sternemann, K. Rüster, F.J. Wirkert, K. Mende, T. Büning, M. Tolan, Temperature-Driven Adsorption and Desorption of Proteins at Solid–Liquid Interfaces, Langmuir. 30 (2014) 2077–2083. doi:10.1021/la404884a.

[133] M. Wahlgren, T. Arnebrant, Protein adsorption to solid surfaces, Trends in Biotechnology. 9 (1991) 201–208. doi:10.1016/0167-7799(91)90064-O.

[134] T. Wei, S. Kaewtathip, K. Shing, Buffer Effect on Protein Adsorption at Liquid/Solid Interface, J. Phys. Chem. C. 113 (2009) 2053–2062. doi:10.1021/jp806586n.

[135] J.H. Park, T.N. Sut, J.A. Jackman, A.R. Ferhan, B.K. Yoon, N.-J. Cho, Controlling adsorption and passivation properties of bovine serum albumin on silica surfaces by ionic strength modulation and cross-linking, Physical Chemistry Chemical Physics. 19 (2017) 8854–8865. doi:10.1039/C7CP01310H.

[136] R.L. Baldwin, How Hofmeister ion interactions affect protein stability, Biophysical Journal. 71 (1996) 2056–2063. doi:10.1016/S0006-3495(96)79404-3.

[137] M.G. Cacace, E.M. Landau, J.J. Ramsden, The Hofmeister series: salt and solvent effects on interfacial phenomena, Q. Rev. Biophys. 30 (1997) 241–277.

[138] C. Blaszykowski, S. Sheikh, M. Thompson, Surface chemistry to minimize fouling from blood-based fluids, Chemical Society Reviews. 41 (2012) 5599. doi:10.1039/c2cs35170f.

[139] I. Firkowska-Boden, X. Zhang, K.D. Jandt, Controlling Protein Adsorption through Nanostructured Polymeric Surfaces, Advanced Healthcare Materials. 7 (2018) 1700995. doi:10.1002/adhm.201700995.

[140] B.K.D. Ngo, M.A. Grunlan, Protein Resistant Polymeric Biomaterials, ACS Macro Letters. 6 (2017) 992–1000. doi:10.1021/acsmacrolett.7b00448.

[141] E. Ostuni, R.G. Chapman, R.E. Holmlin, S. Takayama, G.M. Whitesides, A Survey of Structure−Property Relationships of Surfaces that Resist the Adsorption of Protein, Langmuir. 17 (2001) 5605–5620. doi:10.1021/la010384m.

[142] M.S. Lord, M. Foss, F. Besenbacher, Influence of nanoscale surface topography on protein adsorption and cellular response, Nano Today. 5 (2010) 66–78. doi:10.1016/j.nantod.2010.01.001.

[143] D. Nandakumar, A. Bendavid, P.J. Martin, K.D. Harris, A.J. Ruys, M.S. Lord, Fabrication of Semiordered Nanopatterned Diamond-like Carbon and Titania Films for Blood Contacting Applications, ACS Applied Materials & Interfaces. 8 (2016) 6802–6810. doi:10.1021/acsami.5b11614.

[144] L.C.Y. Lee, N. Gadegaard, M.C. de Andrés, L.-A. Turner, K.V. Burgess, S.J. Yarwood, J. Wells, M. Salmeron-Sanchez, D. Meek, R.O.C. Oreffo, M.J. Dalby, Nanotopography controls cell cycle changes involved with skeletal stem cell self-renewal and multipotency, Biomaterials. 116 (2017) 10–20. doi:10.1016/j.biomaterials.2016.11.032.

[145] L. Pocivavsek, J. Pugar, R. O'Dea, S.-H. Ye, W. Wagner, E. Tzeng, S. Velankar, E. Cerda, Topography-driven surface renewal, Nature Physics. 14 (2018) 948–953. doi:10.1038/s41567-018-0193-x.

[146] L.E. Gonzalez Garcia, M. MacGregor-Ramiasa, R.M. Visalakshan, K. Vasilev, Protein Interactions with Nanoengineered Polyoxazoline Surfaces Generated via Plasma Deposition, Langmuir. 33 (2017) 7322–7331. doi:10.1021/acs.langmuir.7b01279.

[147] K. Rechendorff, M.B. Hovgaard, M. Foss, V.P. Zhdanov, F. Besenbacher, Enhancement of Protein Adsorption Induced by Surface Roughness, Langmuir. 22 (2006) 10885–10888. doi:10.1021/la0621923.

[148] A. Dolatshahi-Pirouz, K. Rechendorff, M.B. Hovgaard, M. Foss, J. Chevallier, F. Besenbacher, Bovine serum albumin adsorption on nano-rough platinum surfaces studied by QCM-D, Colloids and Surfaces B: Biointerfaces. 66 (2008) 53–59. doi:10.1016/j.colsurfb.2008.05.010.

[149] K. Cai, J. Bossert, K.D. Jandt, Does the nanometre scale topography of titanium influence protein adsorption and cell proliferation?, Colloids and Surfaces B: Biointerfaces. 49 (2006) 136–144. doi:10.1016/j.colsurfb.2006.02.016.

[150] D. Quéré, Wetting and Roughness, Annual Review of Materials Research. 38 (2008) 71–99. doi:10.1146/annurev.matsci.38.060407.132434.

[151] W.J. Brittain, S. Minko, A structural definition of polymer brushes, Journal of Polymer Science Part A: Polymer Chemistry. 45 (2007) 3505–3512. doi:10.1002/pola.22180.

[152] W.-L. Chen, R. Cordero, H. Tran, C.K. Ober, *50th Anniversary Perspective* : Polymer Brushes: Novel Surfaces for Future Materials, Macromolecules. 50 (2017) 4089–4113. doi:10.1021/acs.macromol.7b00450.

[153] L. Moroni, M. Klein Gunnewiek, E.M. Benetti, Polymer brush coatings regulating cell behavior: Passive interfaces turn into active, Acta Biomaterialia. 10 (2014) 2367–2378. doi:10.1016/j.actbio.2014.02.048.

[154] A. Hucknall, S. Rangarajan, A. Chilkoti, In Pursuit of Zero: Polymer Brushes that Resist the Adsorption of Proteins, Advanced Materials. 21 (2009) 2441–2446. doi:10.1002/adma.200900383.

[155] L. Michalek, L. Barner, C. Barner-Kowollik, Polymer on Top: Current Limits and Future Perspectives of Quantitatively Evaluating Surface Grafting, Advanced Materials. 30 (2018) 1706321. doi:10.1002/adma.201706321.

[156] C.J. Galvin, J. Genzer, Applications of surface-grafted macromolecules derived from post-polymerization modification reactions, Progress in Polymer Science. 37 (2012) 871–906. doi:10.1016/j.progpolymsci.2011.12.001.

[157] S. Lowe, N.M. O'Brien-Simpson, L.A. Connal, Antibiofouling polymer interfaces: poly(ethylene glycol) and other promising candidates, Polymer Chemistry. 6 (2015) 198–212. doi:10.1039/C4PY01356E.

[158] T. Riedel, Z. Riedelová-Reicheltová, P. Májek, C. Rodriguez-Emmenegger, M. Houska, J.E. Dyr, E. Brynda, Complete Identification of Proteins Responsible for Human Blood Plasma Fouling on Poly(ethylene glycol)-Based Surfaces, Langmuir. 29 (2013) 3388–3397. doi:10.1021/la304886r.

[159] C. Rodriguez-Emmenegger, E. Brynda, T. Riedel, M. Houska, V. Šubr, A.B. Alles, E. Hasan, J.E. Gautrot, W.T.S. Huck, Polymer Brushes Showing Non-Fouling in Blood Plasma Challenge the Currently Accepted Design of Protein Resistant Surfaces, Macromolecular Rapid Communications. 32 (2011) 952–957. doi:10.1002/marc.201100189.

[160] F. Surman, T. Riedel, M. Bruns, N.Yu. Kostina, Z. Sedláková, C. Rodriguez-Emmenegger, Polymer Brushes Interfacing Blood as a Route Toward High Performance Blood Contacting Devices: Polymer Brushes Interfacing Blood as a Route Toward, Macromolecular Bioscience. 15 (2015) 636–646. doi:10.1002/mabi.201400470.

[161] N. Adams, U.S. Schubert, Poly(2-oxazolines) in biological and biomedical application contexts, Advanced Drug Delivery Reviews. 59 (2007) 1504–1520. doi:10.1016/j.addr.2007.08.018.

[162] R. Hoogenboom, Poly(2-oxazoline)s: A Polymer Class with Numerous Potential Applications, Angewandte Chemie International Edition. 48 (2009) 7978–7994. doi:10.1002/anie.200901607.

[163] I. Szleifer, Polymers and proteins: interactions at interfaces, Current Opinion in Solid State and Materials Science. 2 (1997) 337–344. doi:10.1016/S1359-0286(97)80125-8.

[164] M. Heuberger, T. Drobek, N.D. Spencer, Interaction Forces and Morphology of a Protein-Resistant Poly(ethylene glycol) Layer, Biophysical Journal. 88 (2005) 495–504. doi:10.1529/biophysj.104.045443.

[165] S. Chen, L. Li, C. Zhao, J. Zheng, Surface hydration: Principles and applications toward low-fouling/nonfouling biomaterials, Polymer. 51 (2010) 5283–5293. doi:10.1016/j.polymer.2010.08.022.

[166] J. Satulovsky, M.A. Carignano, I. Szleifer, Kinetic and thermodynamic control of protein adsorption, PNAS. 97 (2000) 9037–9041. doi:10.1073/pnas.150236197.

[167] G. Emilsson, K. Xiong, Y. Sakiyama, B. Malekian, V. Ahlberg Gagnér, R.L. Schoch, R.Y.H. Lim, A.B. Dahlin, Polymer brushes in solid-state nanopores form an impenetrable entropic barrier for proteins, Nanoscale. 10 (2018) 4663–4669. doi:10.1039/C7NR09432A.

[168] W. Taylor, R.A.L. Jones, Protein Adsorption on Well-Characterized Polyethylene Oxide Brushes on Gold: Dependence on Molecular Weight and Grafting Density, Langmuir. 29 (2013) 6116–6122. doi:10.1021/la4005483.

[169] J. Jin, Y. Han, C. Zhang, J. Liu, W. Jiang, J. Yin, H. Liang, Effect of grafted PEG chain conformation on albumin and lysozyme adsorption: A combined study using QCM-D and DPI, Colloids and Surfaces B: Biointerfaces. 136 (2015) 838–844. doi:10.1016/j.colsurfb.2015.10.025.

[170] L.D. Unsworth, H. Sheardown, J.L. Brash, Protein-Resistant Poly(ethylene oxide)-Grafted Surfaces: Chain Density-Dependent Multiple Mechanisms of Action, Langmuir. 24 (2008) 1924–1929. doi:10.1021/la702310t.

[171] D. Faulón Marruecos, M. Kastantin, D.K. Schwartz, J.L. Kaar, Dense Poly(ethylene glycol) Brushes Reduce Adsorption and Stabilize the Unfolded Conformation of Fibronectin, Biomacromolecules. 17 (2016) 1017–1025. doi:10.1021/acs.biomac.5b01657.

[172] E. Schneck, I. Berts, A. Halperin, J. Daillant, G. Fragneto, Neutron reflectometry from poly (ethylene-glycol) brushes binding anti-PEG antibodies: Evidence of ternary adsorption, Biomaterials. 46 (2015) 95–104. doi:10.1016/j.biomaterials.2014.12.041.

[173] W. Dai, C. Zheng, B. Zhao, K. Chen, P. Jia, J. Yang, J. Zhao, A negative correlation between water content and protein adsorption on polymer brushes, Journal of Materials Chemistry B. (2019). doi:10.1039/C8TB03061H.

[174] U.R. Dahal, Z. Wang, E.E. Dormidontova, Hydration and Mobility of Poly(ethylene oxide) Brushes, Macromolecules. 50 (2017) 6722–6732. doi:10.1021/acs.macromol.7b01369.

[175] D. Faulón Marruecos, D.F. Kienle, J.L. Kaar, D.K. Schwartz, Grafting Density Impacts Local Nanoscale Hydrophobicity in Poly(ethylene glycol) Brushes, ACS Macro Letters. 7 (2018) 498–503. doi:10.1021/acsmacrolett.8b00004.

[176] K.M. Hansson, S. Tosatti, J. Isaksson, J. Wetterö, M. Textor, T.L. Lindahl, P. Tengvall, Whole blood coagulation on protein adsorption-resistant PEG and peptide functionalised PEG-coated titanium surfaces, Biomaterials. 26 (2005) 861–872. doi:10.1016/j.biomaterials.2004.03.036.

[177] M. Sun, J. Deng, Z. Tang, J. Wu, D. Li, H. Chen, C. Gao, A correlation study of protein adsorption and cell behaviors on substrates with different densities of PEG chains, Colloids and Surfaces B: Biointerfaces. 122 (2014) 134–142. doi:10.1016/j.colsurfb.2014.06.041.

[178] A. Al-Ani, A. Boden, M. Al Kobaisi, H. Pingle, P.-Y. Wang, P. Kingshott, The influence of PEG-thiol derivatives on controlling cellular and bacterial interactions with gold surfaces, Applied Surface Science. 462 (2018) 980–990. doi:10.1016/j.apsusc.2018.08.136.

[179] J. Pei, H. Hall, N.D. Spencer, The role of plasma proteins in cell adhesion to PEG surface-density-gradient-modified titanium oxide, Biomaterials. 32 (2011) 8968–8978. doi:10.1016/j.biomaterials.2011.08.034.

[180] S. Lee, J. Vörös, An Aqueous-Based Surface Modification of Poly(dimethylsiloxane) with Poly(ethylene glycol) to Prevent Biofouling, Langmuir. 21 (2005) 11957–11962. doi:10.1021/la051932p.

[181] P. Hamilton-Brown, T. Gengenbach, H.J. Griesser, L. Meagher, End Terminal, Poly(ethylene oxide) Graft Layers: Surface Forces and Protein Adsorption, Langmuir. 25 (2009) 9149–9156. doi:10.1021/la900703e.

[182] G. Emilsson, R.L. Schoch, L. Feuz, F. Höök, R.Y.H. Lim, A.B. Dahlin, Strongly Stretched Protein Resistant Poly(ethylene glycol) Brushes Prepared by Grafting-To, ACS Applied Materials & Interfaces. 7 (2015) 7505–7515. doi:10.1021/acsami.5b01590.

[183] R. Ortiz, S. Olsen, E. Thormann, Salt-Induced Control of the Grafting Density in Poly(ethylene glycol) Brush Layers by a Grafting-to Approach, Langmuir. 34 (2018) 4455–4464. doi:10.1021/acs.langmuir.8b00030.

[184] B. Pidhatika, M. Rodenstein, Y. Chen, E. Rakhmatullina, A. Mühlebach, C. Acikgöz, M. Textor, R. Konradi, Comparative Stability Studies of Poly(2-methyl-2-oxazoline) and Poly(ethylene glycol) Brush Coatings, Biointerphases. 7 (2012) 1. doi:10.1007/s13758-011-0001-y.

[185] Y. Chen, B. Pidhatika, T. von Erlach, R. Konradi, M. Textor, H. Hall, T. Lühmann, Comparative assessment of the stability of nonfouling poly(2-methyl-2-oxazoline) and poly(ethylene glycol) surface films: An *in vitro* cell culture study, Biointerphases. 9 (2014) 031003. doi:10.1116/1.4878461.

[186] A. Roosjen, J. de Vries, H.C. van der Mei, W. Norde, H.J. Busscher, Stability and effectiveness against bacterial adhesion of poly(ethylene oxide) coatings in biological fluids, Journal of Biomedical Materials Research Part B: Applied Biomaterials. 73B (2005) 347–354. doi:10.1002/jbm.b.30227.

[187] D. Branch, Long-term stability of grafted polyethylene glycol surfaces for use with microstamped substrates in neuronal cell culture, Biomaterials. 22 (2001) 1035–1047. doi:10.1016/S0142-9612(00)00343-4.

[188] M. Shen, L. Martinson, M.S. Wagner, D.G. Castner, B.D. Ratner, T.A. Horbett, PEO-like plasma polymerized tetraglyme surface interactions with leukocytes and proteins: in vitro and in vivo studies, Journal of Biomaterials Science, Polymer Edition. 13 (2002) 367–390. doi:10.1163/156856202320253910.

[189] J. Ulbricht, R. Jordan, R. Luxenhofer, On the biodegradability of polyethylene glycol, polypeptoids and poly(2-oxazoline)s, Biomaterials. 35 (2014) 4848–4861. doi:10.1016/j.biomaterials.2014.02.029.

[190] R. Konradi, C. Acikgoz, M. Textor, Polyoxazolines for Nonfouling Surface Coatings - A Direct Comparison to the Gold Standard PEG, Macromolecular Rapid Communications. 33 (2012) 1663–1676. doi:10.1002/marc.201200422.

[191] G. Morgese, E.M. Benetti, Polyoxazoline biointerfaces by surface grafting, European Polymer Journal. 88 (2017) 470–485. doi:10.1016/j.eurpolymj.2016.11.003.

[192] L. Tauhardt, K. Kempe, M. Gottschaldt, U.S. Schubert, Poly(2-oxazoline) functionalized surfaces: from modification to application, Chemical Society Reviews. 42 (2013) 7998. doi:10.1039/c3cs60161g.

[193] H. Wang, L. Li, Q. Tong, M. Yan, Evaluation of Photochemically Immobilized Poly(2-ethyl-2-oxazoline) Thin Films as Protein-Resistant Surfaces, ACS Applied Materials & Interfaces. 3 (2011) 3463–3471. doi:10.1021/am200690s.

[194] G. Morgese, Y. Gombert, S.N. Ramakrishna, E.M. Benetti, Mixing Poly(ethylene glycol) and Poly(2-alkyl-2-oxazoline)s Enhances Hydration and Viscoelasticity of Polymer Brushes and Determines Their Nanotribological and Antifouling Properties, ACS Applied Materials & Interfaces. 10 (2018) 41839–41848. doi:10.1021/acsami.8b17193.

[195] J. Yang, L. Li, C. Ma, X. Ye, Degradable polyurethane with poly(2-ethyl-2-oxazoline) brushes for protein resistance, RSC Advances. 6 (2016) 69930–69938. doi:10.1039/C6RA13663J.

[196] X. Zheng, C. Zhang, L. Bai, S. Liu, L. Tan, Y. Wang, Antifouling property of monothiol-terminated bottle-brush poly(methylacrylic acid)-graft-poly(2-methyl-2-oxazoline) copolymer on gold surfaces, Journal of Materials Chemistry B. 3 (2015) 1921–1930. doi:10.1039/C4TB01766H.

[197] C. Zhang, S. Liu, L. Tan, H. Zhu, Y. Wang, Star-shaped poly(2-methyl-2-oxazoline)-based films: rapid preparation and effects of polymer architecture on antifouling properties, Journal of Materials Chemistry B. 3 (2015) 5615–5628. doi:10.1039/C5TB00732A.

[198] R. Konradi, B. Pidhatika, A. Mühlebach, M. Textor, Poly-2-methyl-2-oxazoline: A Peptide-like Polymer for Protein-Repellent Surfaces, Langmuir. 24 (2008) 613–616. doi:10.1021/la702917z.

[199] H. Zhu, F. Mumtaz, C. Zhang, L. Tan, S. Liu, Y. Zhang, C. Pan, Y. Wang, A rapid approach to prepare poly(2-methyl-2-oxazoline)-based antifouling coating by UV irradiation, Applied Surface Science. 426 (2017) 817–826. doi:10.1016/j.apsusc.2017.07.260.

[200] P. Tang, S. di Cio, W. Wang, J. E. Gautrot, Surface-Initiated Poly(oligo(2-alkyl-2-oxazoline)methacrylate) Brushes, Langmuir. 34 (2018) 10019–10027. doi:10.1021/acs.langmuir.8b01682.

[201] G. Morgese, B. Verbraeken, S.N. Ramakrishna, Y. Gombert, E. Cavalli, J.-G. Rosenboom, M. Zenobi-Wong, N.D. Spencer, R. Hoogenboom, E.M. Benetti, Chemical Design of Non-Ionic Polymer Brushes as Biointerfaces: Poly(2-oxazine)s Outperform Both Poly(2-oxazoline)s and PEG, Angewandte Chemie International Edition. 57 (2018) 11667–11672. doi:10.1002/anie.201805620.

[202] F. Yang, Y. Liu, Y. Zhang, B. Ren, J. Xu, J. Zheng, Synthesis and Characterization of Ultralow Fouling Poly(*N* -acryloyl-glycinamide) Brushes, Langmuir. 33 (2017) 13964–13972. doi:10.1021/acs.langmuir.7b03435.

[203] Q. Liu, A. Singh, R. Lalani, L. Liu, Ultralow Fouling Polyacrylamide on Gold Surfaces via Surface-Initiated Atom Transfer Radical Polymerization, Biomacromolecules. 13 (2012) 1086–1092. doi:10.1021/bm201814p.

[204] H. Zhao, B. Zhu, S.-C. Luo, H.-A. Lin, A. Nakao, Y. Yamashita, H. Yu, Controlled Protein Absorption and Cell Adhesion on Polymer-Brush-Grafted Poly(3,4-ethylenedioxythiophene) Films, ACS Applied Materials & Interfaces. 5 (2013) 4536–4543. doi:10.1021/am400135c.

[205] C. Zhao, L. Li, Q. Wang, Q. Yu, J. Zheng, Effect of Film Thickness on the Antifouling Performance of Poly(hydroxy-functional methacrylates) Grafted Surfaces, Langmuir. 27 (2011) 4906–4913. doi:10.1021/la200061h.

[206] N. Zhang, T. Pompe, I. Amin, R. Luxenhofer, C. Werner, R. Jordan, Tailored Poly(2-oxazoline) Polymer Brushes to Control Protein Adsorption and Cell Adhesion, Macromolecular Bioscience. 12 (2012) 926–936. doi:10.1002/mabi.201200026.

[207] M.C.R. Tria, C.D.T. Grande, R.R. Ponnapati, R.C. Advincula, Electrochemical Deposition and Surface-Initiated RAFT Polymerization: Protein and Cell-Resistant PPEGMEMA Polymer Brushes, Biomacromolecules. 11 (2010) 3422–3431. doi:10.1021/bm1009365.

[208] D. Shen, B. Xu, X. Huang, Q. Zhuang, S. Lin, (P *t* BA- *co* -PPEGMEMA- *co* -PDOMA)- *g* -PPFA polymer brushes synthesized by sequential RAFT polymerization and ATRP, Polymer Chemistry. 9 (2018) 2821–2829. doi:10.1039/C8PY00470F.

[209] A. de los Santos Pereira, S. Sheikh, C. Blaszykowski, O. Pop-Georgievski, K. Fedorov, M. Thompson, C. Rodriguez-Emmenegger, Antifouling Polymer Brushes Displaying Antithrombogenic Surface Properties, Biomacromolecules. 17 (2016) 1179–1185. doi:10.1021/acs.biomac.6b00019.

[210] I. Buzzacchera, M. Vorobii, N.Yu. Kostina, A. de los Santos Pereira, T. Riedel, M. Bruns, W. Ogieglo, M. Möller, C.J. Wilson, C. Rodriguez-Emmenegger, Polymer Brush-Functionalized Chitosan Hydrogels as Antifouling Implant Coatings, Biomacromolecules. 18 (2017) 1983–1992. doi:10.1021/acs.biomac.7b00516.

[211] J.B. Schlenoff, Zwitteration: Coating Surfaces with Zwitterionic Functionality to Reduce Nonspecific Adsorption, Langmuir. 30 (2014) 9625–9636. doi:10.1021/la500057j.

[212] Q. Shao, S. Jiang, Molecular Understanding and Design of Zwitterionic Materials, Advanced Materials. 27 (2015) 15–26. doi:10.1002/adma.201404059.

[213] Z.G. Estephan, P.S. Schlenoff, J.B. Schlenoff, Zwitteration As an Alternative to PEGylation, Langmuir. 27 (2011) 6794–6800. doi:10.1021/la200227b.

[214] A.M. Alswieleh, N. Cheng, I. Canton, B. Ustbas, X. Xue, V. Ladmiral, S. Xia, R.E. Ducker, O. El Zubir, M.L. Cartron, C.N. Hunter, G.J. Leggett, S.P. Armes, Zwitterionic Poly(amino acid methacrylate) Brushes, Journal of the American Chemical Society. 136 (2014) 9404–9413. doi:10.1021/ja503400r.

[215] A. Venault, M.-W. Lai, J.-F. Jhong, C.-C. Yeh, L.-C. Yeh, Y. Chang, Superior Bioinert Capability of Zwitterionic Poly(4-vinylpyridine propylsulfobetaine) Withstanding Clinical Sterilization for Extended Medical Applications, ACS Applied Materials & Interfaces. 10 (2018) 17771–17783. doi:10.1021/acsami.8b05466.

[216] M.-C. Sin, Y.-M. Sun, Y. Chang, Zwitterionic-Based Stainless Steel with Well-Defined Polysulfobetaine Brushes for General Bioadhesive Control, ACS Applied Materials & Interfaces. 6 (2014) 861–873. doi:10.1021/am4041256.

[217] G.V. Dizon, Y.-N. Chou, L.-C. Yeh, A. Venault, J. Huang, Y. Chang, Bio-inert interfaces via biomimetic anchoring of a zwitterionic copolymer on versatile substrates, Journal of Colloid and Interface Science. 529 (2018) 77–89. doi:10.1016/j.jcis.2018.05.073.

[218] C. Zhang, J. Lu, Y. Hou, W. Xiong, K. Sheng, H. Lu, Investigation on the Linker Length of Synthetic Zwitterionic Polypeptides for Improved Nonfouling Surfaces, ACS Applied Materials & Interfaces. 10 (2018) 17463–17470. doi:10.1021/acsami.8b02854.

[219] Y.-N. Chou, A. Venault, Y.-H. Wang, A. Chinnathambi, A. Higuchi, Y. Chang, Surface zwitterionization on versatile hydrophobic interfaces *via* a combined copolymerization/self-assembling process, Journal of Materials Chemistry B. 6 (2018) 4909–4919. doi:10.1039/C8TB01054D.

[220] C.-M. Xing, F.-N. Meng, M. Quan, K. Ding, Y. Dang, Y.-K. Gong, Quantitative fabrication, performance optimization and comparison of PEG and zwitterionic polymer antifouling coatings, Acta Biomaterialia. 59 (2017) 129–138. doi:10.1016/j.actbio.2017.06.034.

[221] S.-H. Chen, Y. Chang, K. Ishihara, Reduced Blood Cell Adhesion on Polypropylene Substrates through a Simple Surface Zwitterionization, Langmuir. 33 (2017) 611–621. doi:10.1021/acs.langmuir.6b03295.

[222] B.L. Leigh, E. Cheng, L. Xu, A. Derk, M.R. Hansen, C.A. Guymon, Antifouling Photograftable Zwitterionic Coatings on PDMS Substrates, Langmuir. (2018). doi:10.1021/acs.langmuir.8b00838.

[223] X. Lin, P. Jain, K. Wu, D. Hong, H.-C. Hung, M.B. O'Kelly, B. Li, P. Zhang, Z. Yuan, S. Jiang, Ultralow Fouling and Functionalizable Surface Chemistry Based on Zwitterionic Carboxybetaine Random Copolymers, Langmuir. (2018). doi:10.1021/acs.langmuir.8b02540.

[224] H.-C. Hung, P. Jain, P. Zhang, F. Sun, A. Sinclair, T. Bai, B. Li, K. Wu, C. Tsao, E.J. Liu, H.S. Sundaram, X. Lin, P. Farahani, T. Fujihara, S. Jiang, A Coating-Free Nonfouling Polymeric Elastomer, Advanced Materials. 29 (2017) 1700617. doi:10.1002/adma.201700617.

[225] W. Yang, H. Xue, W. Li, J. Zhang, S. Jiang, Pursuing "Zero" Protein Adsorption of Poly(carboxybetaine) from Undiluted Blood Serum and Plasma, Langmuir. 25 (2009) 11911–11916. doi:10.1021/la9015788.

[226] Y. Chang, Y.-J. Shih, C.-J. Lai, H.-H. Kung, S. Jiang, Blood-Inert Surfaces via Ion-Pair Anchoring of Zwitterionic Copolymer Brushes in Human Whole Blood, Advanced Functional Materials. 23 (2013) 1100–1110. doi:10.1002/adfm.201201386.

[227] H. Wang, Y. Hu, D. Lynch, M. Young, S. Li, H. Cong, F.-J. Xu, G. Cheng, Zwitterionic Polyurethanes with Tunable Surface and Bulk Properties, ACS Applied Materials & Interfaces. 10 (2018) 37609–37617. doi:10.1021/acsami.8b10450.

[228] S.-H. Ye, Y. Hong, H. Sakaguchi, V. Shankarraman, S.K. Luketich, A. D'Amore, W.R. Wagner, Nonthrombogenic, Biodegradable Elastomeric Polyurethanes with Variable Sulfobetaine Content, ACS Applied Materials & Interfaces. 6 (2014) 22796–22806. doi:10.1021/am506998s.

[229] C. Wang, C. Ma, C. Mu, W. Lin, A Novel Approach for Synthesis of Zwitterionic Polyurethane Coating with Protein Resistance, Langmuir. 30 (2014) 12860–12867. doi:10.1021/la503426e.

[230] P. Liu, T. Huang, P. Liu, S. Shi, Q. Chen, L. Li, J. Shen, Zwitterionic modification of polyurethane membranes for enhancing the anti-fouling property, Journal of Colloid and Interface Science. 480 (2016) 91–101. doi:10.1016/j.jcis.2016.07.005.

[231] R.S. Smith, Z. Zhang, M. Bouchard, J. Li, H.S. Lapp, G.R. Brotske, D.L. Lucchino, D. Weaver, L.A. Roth, A. Coury, J. Biggerstaff, S. Sukavaneshvar, R. Langer, C. Loose, Vascular Catheters with a Nonleaching Poly-Sulfobetaine Surface Modification Reduce Thrombus Formation and Microbial Attachment, Science Translational Medicine. 4 (2012) 153ra132-153ra132. doi:10.1126/scitranslmed.3004120.

[232] D.A. Murphy, L.E. Hockings, R.K. Andrews, C. Aubron, E.E. Gardiner, V.A. Pellegrino, A.K. Davis, Extracorporeal Membrane Oxygenation—Hemostatic Complications, Transfusion Medicine Reviews. 29 (2015) 90–101. doi:10.1016/j.tmrv.2014.12.001.

[233] M. He, K. Gao, L. Zhou, Z. Jiao, M. Wu, J. Cao, X. You, Z. Cai, Y. Su, Z. Jiang, Zwitterionic materials for antifouling membrane surface construction, Acta Biomaterialia. 40 (2016) 142–152. doi:10.1016/j.actbio.2016.03.038.

[234] A. Venault, C.-C. Ye, Y.-C. Lin, C.-W. Tsai, J.-F. Jhong, R.-C. Ruaan, A. Higuchi, A. Chinnathambi, H.-T. Ho, Y. Chang, Zwitterionic fibrous polypropylene assembled with amphiphatic carboxybetaine copolymers for hemocompatible blood filtration, Acta Biomaterialia. 40 (2016) 130–141. doi:10.1016/j.actbio.2016.01.031.

[235] J. Zhao, Q. Shi, S. Luan, L. Song, H. Yang, H. Shi, J. Jin, X. Li, J. Yin, P. Stagnaro, Improved biocompatibility and antifouling property of polypropylene non-woven fabric membrane by surface grafting zwitterionic polymer, Journal of Membrane Science. 369 (2011) 5–12. doi:10.1016/j.memsci.2010.10.046.

[236] Y. Chang, W.-J. Chang, Y.-J. Shih, T.-C. Wei, G.-H. Hsiue, Zwitterionic Sulfobetaine-Grafted Poly(vinylidene fluoride) Membrane with Highly Effective Blood Compatibility via Atmospheric Plasma-Induced Surface Copolymerization, ACS Applied Materials & Interfaces. 3 (2011) 1228–1237. doi:10.1021/am200055k.

[237] L.-J. Zhu, F. Liu, X.-M. Yu, A.-L. Gao, L.-X. Xue, Surface zwitterionization of hemocompatible poly(lactic acid) membranes for hemodiafiltration, Journal of Membrane Science. 475 (2015) 469–479. doi:10.1016/j.memsci.2014.11.004.

[238] F. Obstals, M. Vorobii, T. Riedel, A. de los Santos Pereira, M. Bruns, S. Singh, C. Rodriguez-Emmenegger, Improving Hemocompatibility of Membranes for Extracorporeal Membrane Oxygenators by Grafting Nonthrombogenic Polymer Brushes, Macromolecular Bioscience. 18 (2018) 1700359. doi:10.1002/mabi.201700359.

[239] Y.-B. Wang, K.-H. Shi, H.-L. Jiang, Y.-K. Gong, Significantly reduced adsorption and activation of blood components in a membrane oxygenator system coated with crosslinkable zwitterionic copolymer, Acta Biomaterialia. 40 (2016) 153–161. doi:10.1016/j.actbio.2016.02.036.

[240] O. Larm, R. Larsson, P. Olsson, A New Non-Thrombogenic Surface Prepared by Selective Covalent Binding of Heparin Via a Modified Reducing Terminal Residue, Biomaterials, Medical Devices, and Artificial Organs. 11 (1983) 161–173. doi:10.3109/10731198309118804.

[241] R. Biran, D. Pond, Heparin coatings for improving blood compatibility of medical devices, Advanced Drug Delivery Reviews. 112 (2017) 12–23. doi:10.1016/j.addr.2016.12.002.

[242] L. Jin, J.P. Abrahams, R. Skinner, M. Petitou, R.N. Pike, R.W. Carrell, The anticoagulant activation of antithrombin by heparin, Proceedings of the National Academy of Sciences. 94 (1997) 14683–14688. doi:10.1073/pnas.94.26.14683.

[243] R.A. Hoshi, R. Van Lith, M.C. Jen, J.B. Allen, K.A. Lapidos, G. Ameer, The blood and vascular cell compatibility of heparin-modified ePTFE vascular grafts, Biomaterials. 34 (2013) 30–41. doi:10.1016/j.biomaterials.2012.09.046.

[244] A. Gao, F. Liu, L. Xue, Preparation and evaluation of heparin-immobilized poly (lactic acid) (PLA) membrane for hemodialysis, Journal of Membrane Science. 452 (2014) 390–399. doi:10.1016/j.memsci.2013.10.016.

[245] Z. Xiong, F. Liu, H. Lin, J. Li, Y. Wang, Covalent Bonding of Heparin on the Crystallized Poly(lactic acid) (PLA) Membrane to Improve Hemocompability via Surface Cross-Linking and Glycidyl Ether Reaction, ACS Biomaterials Science & Engineering. 2 (2016) 2207–2216. doi:10.1021/acsbiomaterials.6b00413.

[246] X. Qiu, B.L.-P. Lee, X. Ning, N. Murthy, N. Dong, S. Li, End-point immobilization of heparin on plasma-treated surface of electrospun polycarbonate-urethane vascular graft, Acta Biomaterialia. 51 (2017) 138–147. doi:10.1016/j.actbio.2017.01.012.

[247] G. Li, P. Yang, W. Qin, M.F. Maitz, S. Zhou, N. Huang, The effect of coimmobilizing heparin and fibronectin on titanium on hemocompatibility and endothelialization, Biomaterials. 32 (2011) 4691–4703. doi:10.1016/j.biomaterials.2011.03.025.

[248] G. Li, P. Yang, Y. Liao, N. Huang, Tailoring of the Titanium Surface by Immobilization of Heparin/Fibronectin Complexes for Improving Blood Compatibility and Endothelialization: An in Vitro Study, Biomacromolecules. 12 (2011) 1155–1168. doi:10.1021/bm101468v.

[249] H.-Y. Mi, X. Jing, J.A. Thomsom, L.-S. Turng, Promoting endothelial cell affinity and antithrombogenicity of polytetrafluoroethylene (PTFE) by mussel-inspired modification and RGD/heparin grafting, Journal of Materials Chemistry B. 6 (2018) 3475–3485. doi:10.1039/C8TB00654G.

[250] S. Gore, J. Andersson, R. Biran, C. Underwood, J. Riesenfeld, Heparin surfaces: Impact of immobilization chemistry on hemocompatibility and protein adsorption: Heparin Surfaces: Impact of Immobilization Chemistry, Journal of Biomedical Materials Research Part B: Applied Biomaterials. 102 (2014) 1817–1824. doi:10.1002/jbm.b.33154.

[251] E.M. Muñoz, R.J. Linhardt, Heparin-Binding Domains in Vascular Biology, Arteriosclerosis, Thrombosis, and Vascular Biology. 24 (2004) 1549–1557. doi:10.1161/01.ATV.0000137189.22999.3f.

[252] P. Klement, Y.J. Du, L.R. Berry, P. Tressel, A.K.C. Chan, Chronic performance of polyurethane catheters covalently coated with ATH complex: A rabbit jugular vein model, Biomaterials. 27 (2006) 5107–5117. doi:10.1016/j.biomaterials.2006.05.005.

[253] K.N. Sask, I. Zhitomirsky, L.R. Berry, A.K.C. Chan, J.L. Brash, Surface modification with an antithrombin–heparin complex for anticoagulation: Studies on a model surface with gold as substrate, Acta Biomaterialia. 6 (2010) 2911–2919. doi:10.1016/j.actbio.2010.02.043.

[254] J.M. Leung, L.R. Berry, H.M. Atkinson, R.M. Cornelius, D. Sandejas, N. Rochow, P.R. Selvaganapathy, C. Fusch, A.K.C. Chan, J.L. Brash, Surface modification of poly(dimethylsiloxane) with a covalent antithrombin–heparin complex for the prevention of thrombosis: use of polydopamine as bonding agent, Journal of Materials Chemistry B. 3 (2015) 6032–6036. doi:10.1039/C5TB00808E.

[255] C. Cheng, S. Sun, C. Zhao, Progress in heparin and heparin-like/mimicking polymer-functionalized biomedical membranes, J. Mater. Chem. B. 2 (2014) 7649–7672. doi:10.1039/C4TB01390E.

[256] L. Ma, B. Su, C. Cheng, Z. Yin, H. Qin, J. Zhao, S. Sun, C. Zhao, Toward highly blood compatible hemodialysis membranes via blending with heparin-mimicking polyurethane: Study in vitro and in vivo, Journal of Membrane Science. 470 (2014) 90–101. doi:10.1016/j.memsci.2014.07.030.

[257] C. Nie, L. Ma, Y. Xia, C. He, J. Deng, L. Wang, C. Cheng, S. Sun, C. Zhao, Novel heparin-mimicking polymer brush grafted carbon nanotube/PES composite membranes for safe and efficient blood purification, Journal of Membrane Science. 475 (2015) 455–468. doi:10.1016/j.memsci.2014.11.005.

[258] S.-S. Li, Y. Xie, T. Xiang, L. Ma, C. He, S. Sun, C.-S. Zhao, Heparin-mimicking polyethersulfone membranes – hemocompatibility, cytocompatibility, antifouling and antibacterial properties, Journal of Membrane Science. 498 (2016) 135–146. doi:10.1016/j.memsci.2015.09.054.

[259] H. Wang, W. Hou, F. Liu, Q. Han, T. Li, H. Lin, G. Deng, J. He, Preparation and evaluation of a self-anticlotting dialyzer via an interface crosslinking approach, Journal of Membrane Science. 563 (2018) 115–125. doi:10.1016/j.memsci.2018.05.056.

[260] X. Chen, H. Gu, Z. Lyu, X. Liu, L. Wang, H. Chen, J.L. Brash, Sulfonate Groups and Saccharides as Essential Structural Elements in Heparin-Mimicking Polymers Used as Surface Modifiers: Optimization of Relative Contents for Antithrombogenic Properties, ACS Applied Materials & Interfaces. 10 (2018) 1440–1449. doi:10.1021/acsami.7b16723.

[261] S.R. Stone, J. Hofsteenge, Kinetics of the inhibition of thrombin by hirudin, Biochemistry. 25 (1986) 4622–4628. doi:10.1021/bi00364a025.

[262] J. Lahann, D. Klee, W. Pluester, H. Hoecker, Bioactive immobilization of r-hirudin on CVD-coated metallic implant devices, Biomaterials. 22 (2001) 817–826. doi:10.1016/S0142-9612(00)00244-1.

[263] S. Alibeik, S. Zhu, J.L. Brash, Surface modification with PEG and hirudin for protein resistance and thrombin neutralization in blood contact, Colloids and Surfaces B: Biointerfaces. 81 (2010) 389–396. doi:10.1016/j.colsurfb.2010.07.024.

[264] J. Li, F. Liu, Y. Qin, J. He, Z. Xiong, G. Deng, Q. Li, A novel natural hirudin facilitated anti-clotting polylactide membrane via hydrogen bonding interaction, Journal of Membrane Science. 523 (2017) 505–514. doi:10.1016/j.memsci.2016.10.027.

[265] Z. Yang, Q. Tu, M.F. Maitz, S. Zhou, J. Wang, N. Huang, Direct thrombin inhibitor-bivalirudin functionalized plasma polymerized allylamine coating for improved biocompatibility of vascular devices, Biomaterials. 33 (2012) 7959–7971. doi:10.1016/j.biomaterials.2012.07.050.

[266] E. Grouzi, Update on argatroban for the prophylaxis and treatment of heparin-induced thrombocytopenia type II, J Blood Med. 5 (2014) 131–141. doi:10.2147/JBM.S38762.

[267] J. Yu, E. Brisbois, H. Handa, G. Annich, M. Meyerhoff, R. Bartlett, T. Major, The immobilization of a direct thrombin inhibitor to a polyurethane as a nonthrombogenic surface coating for extracorporeal circulation, Journal of Materials Chemistry B. 4 (2016) 2264–2272. doi:10.1039/C5TB02419F.

[268] Y.K. Kim, E.Y. Chen, W.F. Liu, Biomolecular strategies to modulate the macrophage response to implanted materials, Journal of Materials Chemistry B. 4 (2016) 1600–1609. doi:10.1039/C5TB01605C.

[269] S.J. Stachelek, M.J. Finley, I.S. Alferiev, F. Wang, R.K. Tsai, E.C. Eckells, N. Tomczyk, J.M. Connolly, D.E. Discher, D.M. Eckmann, R.J. Levy, The effect of CD47 modified polymer surfaces on inflammatory cell attachment and activation, Biomaterials. 32 (2011) 4317–4326. doi:10.1016/j.biomaterials.2011.02.053.

[270] M.J. Finley, L. Rauova, I.S. Alferiev, J.W. Weisel, R.J. Levy, S.J. Stachelek, Diminished adhesion and activation of platelets and neutrophils with CD47 functionalized blood contacting surfaces, Biomaterials. 33 (2012) 5803–5811. doi:10.1016/j.biomaterials.2012.04.051.

[271] J.B. Slee, I.S. Alferiev, C. Nagaswami, J.W. Weisel, R.J. Levy, I. Fishbein, S.J. Stachelek, Enhanced biocompatibility of CD47-functionalized vascular stents, Biomaterials. 87 (2016) 82–92. doi:10.1016/j.biomaterials.2016.02.008.

[272] A. Gao, R. Hang, W. Li, W. Zhang, P. Li, G. Wang, L. Bai, X.-F. Yu, H. Wang, L. Tong, P.K. Chu, Linker-free covalent immobilization of heparin, SDF-1α, and CD47 on PTFE surface for antithrombogenicity, endothelialization and anti-inflammation, Biomaterials. 140 (2017) 201–211. doi:10.1016/j.biomaterials.2017.06.023.

[273] I. Cicha, R. Singh, C.D. Garlichs, C. Alexiou, Nano-biomaterials for cardiovascular applications: Clinical perspective, Journal of Controlled Release. 229 (2016) 23–36. doi:10.1016/j.jconrel.2016.03.015.

[274] M. Rychter, A. Baranowska-Korczyc, J. Lulek, Progress and perspectives in bioactive agent delivery via electrospun vascular grafts, RSC Advances. 7 (2017) 32164–32184. doi:10.1039/C7RA04735E.

[275] E. Luong-Van, L. Grøndahl, K.N. Chua, K.W. Leong, V. Nurcombe, S.M. Cool, Controlled release of heparin from poly(ε-caprolactone) electrospun fibers, Biomaterials. 27 (2006) 2042–2050. doi:10.1016/j.biomaterials.2005.10.028.

[276] P. Punnakitikashem, D. Truong, J.U. Menon, K.T. Nguyen, Y. Hong, Electrospun biodegradable elastic polyurethane scaffolds with dipyridamole release for small diameter vascular grafts, Acta Biomaterialia. 10 (2014) 4618–4628. doi:10.1016/j.actbio.2014.07.031.

[277] C. Del Gaudio, E. Ercolani, P. Galloni, F. Santilli, S. Baiguera, L. Polizzi, A. Bianco, Aspirin-loaded electrospun poly(ε-caprolactone) tubular scaffolds: potential small-diameter vascular grafts for thrombosis prevention, Journal of Materials Science: Materials in Medicine. 24 (2013) 523–532. doi:10.1007/s10856-012-4803-3.

[278] Y. Yang, X. Li, H. Qiu, P. Li, P. Qi, M.F. Maitz, T. You, R. Shen, Z. Yang, W. Tian, N. Huang, Polydopamine Modified TiO $_2$ Nanotube Arrays for Long-Term Controlled Elution of Bivalirudin and Improved Hemocompatibility, ACS Applied Materials & Interfaces. 10 (2018) 7649–7660. doi:10.1021/acsami.7b06108.

[279] A.M. Stahl, Y.P. Yang, Tunable Elastomers with an Antithrombotic Component for Cardiovascular Applications, Advanced Healthcare Materials. 7 (2018) 1800222. doi:10.1002/adhm.201800222.

[280] C. Xu, A.E. Kuriakose, D. Truong, P. Punnakitikashem, K.T. Nguyen, Y. Hong, Enhancing anti-thrombogenicity of biodegradable polyurethanes through drug molecule incorporation, Journal of Materials Chemistry B. 6 (2018) 7288–7297. doi:10.1039/C8TB01582A.

[281] Y. Lu, A.A. Aimetti, R. Langer, Z. Gu, Bioresponsive materials, Nature Reviews Materials. 2 (2017). doi:10.1038/natrevmats.2016.75.

[282] J. Leijten, J. Seo, K. Yue, G. Trujillo-de Santiago, A. Tamayol, G.U. Ruiz-Esparza, S.R. Shin, R. Sharifi, I. Noshadi, M.M. Álvarez, Y.S. Zhang, A. Khademhosseini, Spatially and temporally controlled hydrogels for tissue engineering, Materials Science and Engineering: R: Reports. 119 (2017) 1–35. doi:10.1016/j.mser.2017.07.001.

[283] M.F. Maitz, U. Freudenberg, M.V. Tsurkan, M. Fischer, T. Beyrich, C. Werner, Bio-responsive polymer hydrogels homeostatically regulate blood coagulation, Nature Communications. 4 (2013). doi:10.1038/ncomms3168.

[284] Y. Zhang, J. Yu, J. Wang, N.J. Hanne, Z. Cui, C. Qian, C. Wang, H. Xin, J.H. Cole, C.M. Gallippi, Y. Zhu, Z. Gu, Thrombin-Responsive Transcutaneous Patch for Auto-Anticoagulant Regulation, Advanced Materials. 29 (2017) 1604043. doi:10.1002/adma.201604043.

[285] H. Du, C. Li, Y. Luan, Q. Liu, W. Yang, Q. Yu, D. Li, J.L. Brash, H. Chen, An antithrombotic hydrogel with thrombin-responsive fibrinolytic activity: breaking down the clot as it forms, Materials Horizons. 3 (2016) 556–562. doi:10.1039/C6MH00307A.

[286] M.C. Koetting, J.T. Peters, S.D. Steichen, N.A. Peppas, Stimulus-responsive hydrogels: Theory, modern advances, and applications, Materials Science and Engineering: R: Reports. 93 (2015) 1–49. doi:10.1016/j.mser.2015.04.001.

[287] G.-A. Junter, P. Thébault, L. Lebrun, Polysaccharide-based antibiofilm surfaces, Acta Biomaterialia. 30 (2016) 13–25. doi:10.1016/j.actbio.2015.11.010.

[288] F. Wu, J. Li, K. Zhang, Z. He, P. Yang, D. Zou, N. Huang, Multifunctional Coating Based on Hyaluronic Acid and Dopamine Conjugate for Potential Application on Surface Modification of Cardiovascular Implanted Devices, ACS Applied Materials & Interfaces. 8 (2016) 109–121. doi:10.1021/acsami.5b07427.

[289] J. Li, F. Wu, K. Zhang, Z. He, D. Zou, X. Luo, Y. Fan, P. Yang, A. Zhao, N. Huang, Controlling Molecular Weight of Hyaluronic Acid Conjugated on Amine-rich Surface: Toward Better Multifunctional Biomaterials for Cardiovascular Implants, ACS Applied Materials & Interfaces. 9 (2017) 30343–30358. doi:10.1021/acsami.7b07444.

[290] P. Xue, Q. Li, Y. Li, L. Sun, L. Zhang, Z. Xu, Y. Kang, Surface Modification of Poly(dimethylsiloxane) with Polydopamine and Hyaluronic Acid To Enhance Hemocompatibility for Potential Applications in Medical Implants or Devices, ACS Applied Materials & Interfaces. 9 (2017) 33632–33644. doi:10.1021/acsami.7b10260.

[291] J.J. Richardson, M. Bjornmalm, F. Caruso, Technology-driven layer-by-layer assembly of nanofilms, Science. 348 (2015) aaa2491–aaa2491. doi:10.1126/science.aaa2491.

[292] J.J. Richardson, J. Cui, M. Björnmalm, J.A. Braunger, H. Ejima, F. Caruso, Innovation in Layer-by-Layer Assembly, Chemical Reviews. 116 (2016) 14828–14867. doi:10.1021/acs.chemrev.6b00627.

[293] J.M. Silva, R.L. Reis, J.F. Mano, Biomimetic Extracellular Environment Based on Natural Origin Polyelectrolyte Multilayers, Small. 12 (2016) 4308–4342. doi:10.1002/smll.201601355.

[294] Q. An, T. Huang, F. Shi, Covalent layer-by-layer films: chemistry, design, and multidisciplinary applications, Chemical Society Reviews. 47 (2018) 5061–5098. doi:10.1039/C7CS00406K.

[295] L. Wang, H. Li, S. Chen, C. Nie, C. Cheng, C. Zhao, Interfacial Self-Assembly of Heparin-Mimetic Multilayer on Membrane Substrate as Effective Antithrombotic, Endothelialization, and Antibacterial Coating, ACS Biomaterials Science & Engineering. 1 (2015) 1183–1193. doi:10.1021/acsbiomaterials.5b00320.

[296] S. Jin, H. Gu, X. Chen, X. Liu, W. Zhan, T. Wei, X. Sun, C. Ren, H. Chen, A facile method to prepare a versatile surface coating with fibrinolytic activity, vascular cell selectivity and antibacterial properties, Colloids and Surfaces B: Biointerfaces. 167 (2018) 28–35. doi:10.1016/j.colsurfb.2018.03.047.

[297] R.J. Smith, M.G. Moule, P. Sule, T. Smith, J.D. Cirillo, J.C. Grunlan, Polyelectrolyte Multilayer Nanocoating Dramatically Reduces Bacterial Adhesion to Polyester Fabric, ACS Biomaterials Science & Engineering. 3 (2017) 1845–1852. doi:10.1021/acsbiomaterials.7b00250.

[298] L. Séon, P. Lavalle, P. Schaaf, F. Boulmedais, Polyelectrolyte Multilayers: A Versatile Tool for Preparing Antimicrobial Coatings, Langmuir. 31 (2015) 12856–12872. doi:10.1021/acs.langmuir.5b02768.

[299] T. Wei, Q. Yu, H. Chen, Responsive and Synergistic Antibacterial Coatings: Fighting against Bacteria in a Smart and Effective Way, Advanced Healthcare Materials. (2019) 1801381. doi:10.1002/adhm.201801381.

[300] S. Lu, P. Zhang, X. Sun, F. Gong, S. Yang, L. Shen, Z. Huang, C. Wang, Synthetic ePTFE Grafts Coated with an Anti-CD133 Antibody-Functionalized Heparin/Collagen Multilayer with Rapid in vivo Endothelialization Properties, ACS Applied Materials & Interfaces. 5 (2013) 7360–7369. doi:10.1021/am401706w.

[301] I. Banerjee, R.C. Pangule, R.S. Kane, Antifouling Coatings: Recent Developments in the Design of Surfaces That Prevent Fouling by Proteins, Bacteria, and Marine Organisms, Advanced Materials. 23 (2011) 690–718. doi:10.1002/adma.201001215.

[302] S.Y. Wong, L. Han, K. Timachova, J. Veselinovic, M.N. Hyder, C. Ortiz, A.M. Klibanov, P.T. Hammond, Drastically Lowered Protein Adsorption on Microbicidal Hydrophobic/Hydrophilic Polyelectrolyte Multilayers, Biomacromolecules. 13 (2012) 719–726. doi:10.1021/bm201637e.

[303] S. Boddohi, C.E. Killingsworth, M.J. Kipper, Polyelectrolyte Multilayer Assembly as a Function of pH and Ionic Strength Using the Polysaccharides Chitosan and Heparin, Biomacromolecules. 9 (2008) 2021–2028. doi:10.1021/bm8002573.

[304] S. Boddohi, J. Almodóvar, H. Zhang, P.A. Johnson, M.J. Kipper, Layer-by-layer assembly of polysaccharide-based nanostructured surfaces containing polyelectrolyte complex nanoparticles, Colloids and Surfaces B: Biointerfaces. 77 (2010) 60–68. doi:10.1016/j.colsurfb.2010.01.006.

[305] J. Almodóvar, S. Bacon, J. Gogolski, J.D. Kisiday, M.J. Kipper, Polysaccharide-Based Polyelectrolyte Multilayer Surface Coatings can Enhance Mesenchymal Stem Cell Response to Adsorbed Growth Factors, Biomacromolecules. 11 (2010) 2629–2639. doi:10.1021/bm1005799.

[306] J. Almodóvar, L.W. Place, J. Gogolski, K. Erickson, M.J. Kipper, Layer-by-Layer Assembly of Polysaccharide-Based Polyelectrolyte Multilayers: A Spectroscopic Study of Hydrophilicity, Composition, and Ion Pairing, Biomacromolecules. 12 (2011) 2755–2765. doi:10.1021/bm200519y.

[307] G. Xu, P. Liu, D. Pranantyo, K.-G. Neoh, E.-T. Kang, Dextran- and Chitosan-Based Antifouling, Antimicrobial Adhesion, and Self-Polishing Multilayer Coatings from pH-Responsive Linkages-Enabled Layer-by-Layer Assembly, ACS Sustainable Chemistry & Engineering. 6 (2018) 3916–3926. doi:10.1021/acssuschemeng.7b04286.

[308] A. Barrantes, J. Wengenroth, T. Arnebrant, H.J. Haugen, Poly- l -lysine/heparin multilayer coatings prevent blood protein adsorption, Journal of Colloid and Interface Science. 485 (2017) 288–295. doi:10.1016/j.jcis.2016.09.046.

[309] P.-F. Ren, H.-C. Yang, H.-Q. Liang, X.-L. Xu, L.-S. Wan, Z.-K. Xu, Highly Stable, Protein-Resistant Surfaces via the Layer-by-Layer Assembly of Poly(sulfobetaine methacrylate) and Tannic Acid, Langmuir. 31 (2015) 5851–5858. doi:10.1021/acs.langmuir.5b00920.

[310] J. Deng, X. Liu, L. Ma, C. Cheng, W. Shi, C. Nie, C. Zhao, Heparin-Mimicking Multilayer Coating on Polymeric Membrane via LbL Assembly of Cyclodextrin-Based Supramolecules, ACS Applied Materials & Interfaces. 6 (2014) 21603–21614. doi:10.1021/am506249r.

[311] C. Nie, L. Ma, C. Cheng, J. Deng, C. Zhao, Nanofibrous Heparin and Heparin-Mimicking Multilayers as Highly Effective Endothelialization and Antithrombogenic Coatings, Biomacromolecules. 16 (2015) 992–1001. doi:10.1021/bm501882b.

[312] T. He, D. Jańczewski, S. Guo, S.M. Man, S. Jiang, W.S. Tan, Stable pH responsive layer-by-layer assemblies of partially hydrolysed poly(2-ethyl-2-oxazoline) and poly(acrylic acid) for effective prevention of protein, cell and bacteria surface attachment, Colloids and Surfaces B: Biointerfaces. 161 (2018) 269–278. doi:10.1016/j.colsurfb.2017.10.031.

[313] X. Zhang, G. Zhang, H. Zhang, J. Li, X. Yao, B. Tang, Surface immobilization of heparin and chitosan on titanium to improve hemocompatibility and antibacterial activities, Colloids and Surfaces B: Biointerfaces. 172 (2018) 338–345. doi:10.1016/j.colsurfb.2018.08.060.

[314] S. Meng, Z. Liu, L. Shen, Z. Guo, L.L. Chou, W. Zhong, Q. Du, J. Ge, The effect of a layer-by-layer chitosan–heparin coating on the endothelialization and coagulation properties of a coronary stent system, Biomaterials. 30 (2009) 2276–2283. doi:10.1016/j.biomaterials.2008.12.075.

[315] S. Liu, W. Guo, Anti-Biofouling and Healable Materials: Preparation, Mechanisms, and Biomedical Applications, Advanced Functional Materials. 28 (2018) 1800596. doi:10.1002/adfm.201800596.

[316] D. Chen, M. Wu, B. Li, K. Ren, Z. Cheng, J. Ji, Y. Li, J. Sun, Layer-by-Layer-Assembled Healable Antifouling Films, Advanced Materials. 27 (2015) 5882–5888. doi:10.1002/adma.201501726.

[317] L. Feng, S. Li, Y. Li, H. Li, L. Zhang, J. Zhai, Y. Song, B. Liu, L. Jiang, D. Zhu, Super-Hydrophobic Surfaces: From Natural to Artificial, Advanced Materials. 14 (2002) 1857–1860. doi:10.1002/adma.200290020.

[318] G. Wen, Z. Guo, W. Liu, Biomimetic polymeric superhydrophobic surfaces and nanostructures: from fabrication to applications, Nanoscale. 9 (2017) 3338–3366. doi:10.1039/C7NR00096K.

[319] H.F. Bohn, W. Federle, Insect aquaplaning: Nepenthes pitcher plants capture prey with the peristome, a fully wettable water-lubricated anisotropic surface, PNAS. 101 (2004) 14138–14143. doi:10.1073/pnas.0405885101.

[320] P. Zhang, L. Lin, D. Zang, X. Guo, M. Liu, Designing Bioinspired Anti-Biofouling Surfaces based on a Superwettability Strategy, Small. 13 (2017) 1503334. doi:10.1002/smll.201503334.

[321] J. Yong, F. Chen, Q. Yang, J. Huo, X. Hou, Superoleophobic surfaces, Chemical Society Reviews. 46 (2017) 4168–4217. doi:10.1039/C6CS00751A.

[322] W. He, P. Liu, J. Zhang, X. Yao, Emerging Applications of Bioinspired Slippery Surfaces in Biomedical Fields, Chemistry - A European Journal. 24 (2018) 14864–14877. doi:10.1002/chem.201801368.

[323] Y. Su, C. Luo, Z. Zhang, H. Hermawan, D. Zhu, J. Huang, Y. Liang, G. Li, L. Ren, Bioinspired surface functionalization of metallic biomaterials, Journal of the Mechanical Behavior of Biomedical Materials. 77 (2018) 90–105. doi:10.1016/j.jmbbm.2017.08.035.

[324] T. Kong, G. Luo, Y. Zhao, Z. Liu, Bioinspired Superwettability Micro/Nanoarchitectures: Fabrications and Applications, Advanced Functional Materials. (2019) 1808012. doi:10.1002/adfm.201808012.

[325] M. Cao, D. Guo, C. Yu, K. Li, M. Liu, L. Jiang, Water-Repellent Properties of Superhydrophobic and Lubricant-Infused “Slippery” Surfaces: A Brief Study on the Functions and Applications, ACS Applied Materials & Interfaces. 8 (2016) 3615–3623. doi:10.1021/acsami.5b07881.

[326] M. Zhang, S. Feng, L. Wang, Y. Zheng, Lotus effect in wetting and self-cleaning, Biotribology. 5 (2016) 31–43. doi:10.1016/j.biotri.2015.08.002.

[327] I. Scholz, M. Buckins, L. Dolge, T. Erlinghagen, A. Weth, F. Hischen, J. Mayer, S. Hoffmann, M. Riederer, M. Riedel, W. Baumgartner, Slippery surfaces of pitcher plants: Nepenthes wax crystals minimize insect attachment via microscopic surface roughness, Journal of Experimental Biology. 213 (2010) 1115–1125. doi:10.1242/jeb.035618.

[328] V. Jokinen, E. Kankuri, S. Hoshian, S. Franssila, R.H.A. Ras, Superhydrophobic Blood-Repellent Surfaces, Advanced Materials. 30 (2018) 1705104. doi:10.1002/adma.201705104.

[329] L. Wen, Y. Tian, L. Jiang, Bioinspired Super-Wettability from Fundamental Research to Practical Applications, Angewandte Chemie International Edition. 54 (2015) 3387–3399. doi:10.1002/anie.201409911.

[330] T. Darmanin, F. Guittard, Recent advances in the potential applications of bioinspired superhydrophobic materials, J. Mater. Chem. A. 2 (2014) 16319–16359. doi:10.1039/C4TA02071E.

[331] Q. Huang, L. Lin, Y. Yang, R. Hu, E.A. Vogler, C. Lin, Role of trapped air in the formation of cell-and-protein micropatterns on superhydrophobic/superhydrophilic microtemplated surfaces, Biomaterials. 33 (2012) 8213–8220. doi:10.1016/j.biomaterials.2012.08.017.

[332] E.S. Leibner, N. Barnthip, W. Chen, C.R. Baumrucker, J.V. Badding, M. Pishko, E.A. Vogler, Superhydrophobic effect on the adsorption of human serum albumin, Acta Biomaterialia. 5 (2009) 1389–1398. doi:10.1016/j.actbio.2008.11.003.

[333] E.J. Falde, S.T. Yohe, Y.L. Colson, M.W. Grinstaff, Superhydrophobic materials for biomedical applications, Biomaterials. 104 (2016) 87–103. doi:10.1016/j.biomaterials.2016.06.050.

[334] G.B. Hwang, K. Page, A. Patir, S.P. Nair, E. Allan, I.P. Parkin, The Anti-Biofouling Properties of Superhydrophobic Surfaces are Short-Lived, ACS Nano. 12 (2018) 6050–6058. doi:10.1021/acsnano.8b02293.

[335] T. Sun, H. Tan, D. Han, Q. Fu, L. Jiang, No Platelet Can Adhere—Largely Improved Blood Compatibility on Nanostructured Superhydrophobic Surfaces, Small. 1 (2005) 959–963. doi:10.1002/smll.200500095.

[336] Y. Yang, Y. Lai, Q. Zhang, K. Wu, L. Zhang, C. Lin, P. Tang, A novel electrochemical strategy for improving blood compatibility of titanium-based biomaterials, Colloids and Surfaces B: Biointerfaces. 79 (2010) 309–313. doi:10.1016/j.colsurfb.2010.04.013.

[337] Q. Huang, Y. Yang, R. Hu, C. Lin, L. Sun, E.A. Vogler, Reduced platelet adhesion and improved corrosion resistance of superhydrophobic TiO2-nanotube-coated 316L stainless steel, Colloids and Surfaces B: Biointerfaces. 125 (2015) 134–141. doi:10.1016/j.colsurfb.2014.11.028.

[338] S. Movafaghi, V. Leszczak, W. Wang, J.A. Sorkin, L.P. Dasi, K.C. Popat, A.K. Kota, Hemocompatibility of Superhemophobic Titania Surfaces, Advanced Healthcare Materials. 6 (2017) 1600717. doi:10.1002/adhm.201600717.

[339] S. Moradi, N. Hadjesfandiari, S.F. Toosi, J.N. Kizhakkedathu, S.G. Hatzikiriakos, Effect of Extreme Wettability on Platelet Adhesion on Metallic Implants: From Superhydrophilicity to Superhydrophobicity, ACS Applied Materials & Interfaces. 8 (2016) 17631–17641. doi:10.1021/acsami.6b03644.

[340] J.M. Nokes, R. Liedert, M.Y. Kim, A. Siddiqui, M. Chu, E.K. Lee, M. Khine, Reduced Blood Coagulation on Roll-to-Roll, Shrink-Induced Superhydrophobic Plastics, Advanced Healthcare Materials. 5 (2016) 593–601. doi:10.1002/adhm.201500697.

[341] S. Hoshian, E. Kankuri, R.H.A. Ras, S. Franssila, V. Jokinen, Water and Blood Repellent Flexible Tubes, Scientific Reports. 7 (2017). doi:10.1038/s41598-017-16369-3.

[342] K. Han, T.Y. Park, K. Yong, H.J. Cha, Combinational Biomimicking of Lotus Leaf, Mussel, and Sandcastle Worm for Robust Superhydrophobic Surfaces with Biomedical Multifunctionality: Antithrombotic, Antibiofouling, and Tissue Closure Capabilities, ACS Applied Materials & Interfaces. (2019). doi:10.1021/acsami.8b21122.

[343] D.L. Bark, H. Vahabi, H. Bui, S. Movafaghi, B. Moore, A.K. Kota, K. Popat, L.P. Dasi, Hemodynamic Performance and Thrombogenic Properties of a Superhydrophobic Bileaflet Mechanical Heart Valve, Annals of Biomedical Engineering. 45 (2017) 452–463. doi:10.1007/s10439-016-1618-2.

[344] Z. Li, B.L. Nguyen, Y.C. Cheng, J. Xue, G. MacLaren, C.H. Yap, Durable, flexible, superhydrophobic and blood-repelling surfaces for use in medical blood pumps, Journal of Materials Chemistry B. 6 (2018) 6225–6233. doi:10.1039/C8TB01547C.

[345] T.-S. Wong, S.H. Kang, S.K.Y. Tang, E.J. Smythe, B.D. Hatton, A. Grinthal, J. Aizenberg, Bioinspired self-repairing slippery surfaces with pressure-stable omniphobicity, Nature. 477 (2011) 443–447. doi:10.1038/nature10447.

[346] C. Howell, A. Grinthal, S. Sunny, M. Aizenberg, J. Aizenberg, Designing Liquid-Infused Surfaces for Medical Applications: A Review, Advanced Materials. 30 (2018) 1802724. doi:10.1002/adma.201802724.

[347] J. Li, E. Ueda, D. Paulssen, P.A. Levkin, Slippery Lubricant-Infused Surfaces: Properties and Emerging Applications, Advanced Functional Materials. (2018) 1802317. doi:10.1002/adfm.201802317.

[348] J. Yong, F. Chen, Q. Yang, Y. Fang, J. Huo, J. Zhang, X. Hou, *Nepenthes* Inspired Design of Self-Repairing Omniphobic Slippery Liquid Infused Porous Surface (SLIPS) by Femtosecond Laser Direct Writing, Advanced Materials Interfaces. 4 (2017) 1700552. doi:10.1002/admi.201700552.

[349] J. Yong, J. Huo, Q. Yang, F. Chen, Y. Fang, X. Wu, L. Liu, X. Lu, J. Zhang, X. Hou, Femtosecond Laser Direct Writing of Porous Network Microstructures for Fabricating Super-Slippery Surfaces with Excellent Liquid Repellence and Anti-Cell Proliferation, Advanced Materials Interfaces. 5 (2018) 1701479. doi:10.1002/admi.201701479.

[350] K. Doll, E. Fadeeva, J. Schaeske, T. Ehmke, A. Winkel, A. Heisterkamp, B.N. Chichkov, M. Stiesch, N.S. Stumpp, Development of Laser-Structured Liquid-Infused Titanium with Strong Biofilm-Repellent Properties, (2017). doi:10.1021/acsami.6b16159.

[351] D.C. Leslie, A. Waterhouse, J.B. Berthet, T.M. Valentin, A.L. Watters, A. Jain, P. Kim, B.D. Hatton, A. Nedder, K. Donovan, E.H. Super, C. Howell, C.P. Johnson, T.L. Vu, D.E. Bolgen, S. Rifai, A.R. Hansen, M. Aizenberg, M. Super, J. Aizenberg, D.E. Ingber, A bioinspired omniphobic surface coating on medical devices prevents thrombosis and biofouling, Nature Biotechnology. 32 (2014) 1134–1140. doi:10.1038/nbt.3020.

[352] N. Vogel, R.A. Belisle, B. Hatton, T.-S. Wong, J. Aizenberg, Transparency and damage tolerance of patternable omniphobic lubricated surfaces based on inverse colloidal monolayers, Nature Communications. 4 (2013). doi:10.1038/ncomms3176.

[353] K. Manabe, K.-H. Kyung, S. Shiratori, Biocompatible Slippery Fluid-Infused Films Composed of Chitosan and Alginate via Layer-by-Layer Self-Assembly and Their Antithrombogenicity, ACS Applied Materials & Interfaces. 7 (2015) 4763–4771. doi:10.1021/am508393n.

[354] J. Aizenberg, B. Hatton, D.E. INGBER, M. Super, T.S. Wong, Slippery liquid-infused porous surfaces and biological applications thereof, WO2012100100A3, 2012. https://patents.google.com/patent/WO2012100100A3/zh (accessed December 17, 2018).

[355] S. Yuan, Z. Li, L. Song, H. Shi, S. Luan, J. Yin, Liquid-Infused Poly(styrene- *b* -isobutylene- *b* -styrene) Microfiber Coating Prevents Bacterial Attachment and Thrombosis, ACS Applied Materials & Interfaces. 8 (2016) 21214–21220. doi:10.1021/acsami.6b06407.

[356] N. MacCallum, C. Howell, P. Kim, D. Sun, R. Friedlander, J. Ranisau, O. Ahanotu, J.J. Lin, A. Vena, B. Hatton, T.-S. Wong, J. Aizenberg, Liquid-Infused Silicone As a Biofouling-Free Medical Material, ACS Biomaterials Science & Engineering. 1 (2015) 43–51. doi:10.1021/ab5000578.

[357] G. Mackie, L. Gao, S. Yau, D.C. Leslie, A. Waterhouse, Clinical Potential of Immobilized Liquid Interfaces: Perspectives on Biological Interactions, Trends in Biotechnology. (2018). doi:10.1016/j.tibtech.2018.08.003.

[358] J. Chen, C. Howell, C.A. Haller, M.S. Patel, P. Ayala, K.A. Moravec, E. Dai, L. Liu, I. Sotiri, M. Aizenberg, J. Aizenberg, E.L. Chaikof, An immobilized liquid interface prevents device associated bacterial infection in vivo, Biomaterials. 113 (2017) 80–92. doi:10.1016/j.biomaterials.2016.09.028.

[359] S. Nishioka, M. Tenjimbayashi, K. Manabe, T. Matsubayashi, K. Suwabe, K. Tsukada, S. Shiratori, Facile design of plant-oil-infused fine surface asperity for transparent blood-repelling endoscope lens, RSC Advances. 6 (2016) 47579–47587. doi:10.1039/C6RA08390K.

[360] M. Badv, S.M. Imani, J.I. Weitz, T.F. Didar, Lubricant-Infused Surfaces with Built-In Functional Biomolecules Exhibit Simultaneous Repellency and Tunable Cell Adhesion, ACS Nano. 12 (2018) 10890–10902. doi:10.1021/acsnano.8b03938.

[361] H. Ait-Oufella, E. Maury, S. Lehoux, B. Guidet, G. Offenstadt, The endothelium: physiological functions and role in microcirculatory failure during severe sepsis, Intensive Care Medicine. 36 (2010) 1286–1298. doi:10.1007/s00134-010-1893-6.

[362] S. Weinbaum, J.M. Tarbell, E.R. Damiano, The Structure and Function of the Endothelial Glycocalyx Layer, Annual Review of Biomedical Engineering. 9 (2007) 121–167. doi:10.1146/annurev.bioeng.9.060906.151959.

[363] N.K. Karamanos, Z. Piperigkou, A.D. Theocharis, H. Watanabe, M. Franchi, S. Baud, S. Brézillon, M. Götte, A. Passi, D. Vigetti, S. Ricard-Blum, R.D. Sanderson, T. Neill, R.V. Iozzo, Proteoglycan Chemical Diversity Drives Multifunctional Cell Regulation and Therapeutics, Chemical Reviews. 118 (2018) 9152–9232. doi:10.1021/acs.chemrev.8b00354.

[364] R.P. Richter, N.S. Baranova, A.J. Day, J.C. Kwok, Glycosaminoglycans in extracellular matrix organisation: are concepts from soft matter physics key to understanding the formation of perineuronal nets?, Current Opinion in Structural Biology. 50 (2018) 65–74. doi:10.1016/j.sbi.2017.12.002.

[365] I. Sieve, A.K. Münster-Kühnel, D. Hilfiker-Kleiner, Regulation and function of endothelial glycocalyx layer in vascular diseases, Vascular Pharmacology. 100 (2018) 26–33. doi:10.1016/j.vph.2017.09.002.

[366] B.F. Becker, D. Chappell, D. Bruegger, T. Annecke, M. Jacob, Therapeutic strategies targeting the endothelial glycocalyx: acute deficits, but great potential, Cardiovascular Research. 87 (2010) 300–310. doi:10.1093/cvr/cvq137.

[367] N.B. Holland, Y. Qiu, M. Ruegsegger, R.E. Marchant, Biomimetic engineering of non-adhesive glycocalyx-like surfaces using oligosaccharide surfactant polymers, Nature. 392 (1998) 799–801. doi:10.1038/33894.

[368] C.S. Alphonsus, R.N. Rodseth, The endothelial glycocalyx: a review of the vascular barrier, Anaesthesia. 69 (2014) 777–784. doi:10.1111/anae.12661.

[369] A.I.S. Sobczak, S.J. Pitt, A.J. Stewart, Glycosaminoglycan Neutralization in Coagulation Control, Arteriosclerosis, Thrombosis, and Vascular Biology. 38 (2018) 1258–1270. doi:10.1161/ATVBAHA.118.311102.

[370] J. Rnjak-Kovacina, F. Tang, J.M. Whitelock, M.S. Lord, Glycosaminoglycan and Proteoglycan-Based Biomaterials: Current Trends and Future Perspectives, Advanced Healthcare Materials. 7 (2018) 1701042. doi:10.1002/adhm.201701042.

[371] A. Köwitsch, G. Zhou, T. Groth, Medical application of glycosaminoglycans: a review: Medical Application of Glycosaminoglycans, Journal of Tissue Engineering and Regenerative Medicine. 12 (2018) e23–e41. doi:10.1002/term.2398.

[372] A. Sen Gupta, S. Wang, E. Link, E.H. Anderson, C. Hofmann, J. Lewandowski, K. Kottke-Marchant, R.E. Marchant, Glycocalyx-mimetic dextran-modified poly(vinyl amine) surfactant coating reduces platelet adhesion on medical-grade polycarbonate surface, Biomaterials. 27 (2006) 3084–3095. doi:10.1016/j.biomaterials.2006.01.002.

[373] G. Zhou, M.S. Niepel, S. Saretia, T. Groth, Reducing the inflammatory responses of biomaterials by surface modification with glycosaminoglycan multilayers: REDUCING THE INFLAMMATORY RESPONSES OF BIOMATERIALS, Journal of Biomedical Materials Research Part A. 104 (2016) 493–502. doi:10.1002/jbm.a.35587.

[374] A. Köwitsch, M.S. Niepel, G.P.A. Michanetzis, Y.F. Missirlis, T. Groth, Effect of Immobilized Thiolated Glycosaminoglycans on Fibronectin Adsorption and Behavior of Fibroblasts, Macromolecular Bioscience. 16 (2016) 381–394. doi:10.1002/mabi.201500276.

[375] F. Xu, C.E. Flanagan, A. Ruiz, W.C. Crone, K.S. Masters, Polyurethane/Dermatan Sulfate Copolymers as Hemocompatible, Non-Biofouling Materials, Macromolecular Bioscience. 11 (2011) 257–266. doi:10.1002/mabi.201000313.

[376] K. Yu, B.F.L. Lai, J.N. Kizhakkedathu, Carbohydrate Structure Dependent Hemocompatibility of Biomimetic Functional Polymer Brushes on Surfaces, Advanced Healthcare Materials. 1 (2012) 199–213. doi:10.1002/adhm.201100042.

[377] H.O. Ham, S.H. Park, J.W. Kurutz, I.G. Szleifer, P.B. Messersmith, Antifouling Glycocalyx-Mimetic Peptoids, Journal of the American Chemical Society. 135 (2013) 13015–13022. doi:10.1021/ja404681x.

[378] P.K. Thalla, H. Fadlallah, B. Liberelle, P. Lequoy, G. De Crescenzo, Y. Merhi, S. Lerouge, Chondroitin Sulfate Coatings Display Low Platelet but High Endothelial Cell Adhesive Properties Favorable for Vascular Implants, Biomacromolecules. 15 (2014) 2512–2520. doi:10.1021/bm5003762.

[379] M.S. Lord, W. Yu, B. Cheng, A. Simmons, L. Poole-Warren, J.M. Whitelock, The modulation of platelet and endothelial cell adhesion to vascular graft materials by perlecan, Biomaterials. 30 (2009) 4898–4906. doi:10.1016/j.biomaterials.2009.05.063.

[380] M. Hedayati, M.J. Kipper, Atomic force microscopy of adsorbed proteoglycan mimetic nanoparticles: Toward new glycocalyx-mimetic model surfaces, Carbohydrate Polymers. 190 (2018) 346–355. doi:10.1016/j.carbpol.2018.02.023.

[381] J. Rostgaard, K. Qvortrup, Electron Microscopic Demonstrations of Filamentous Molecular Sieve Plugs in Capillary Fenestrae, Microvascular Research. 53 (1997) 1–13. doi:10.1006/mvre.1996.1987.

[382] M. Hedayati, M.M. Reynolds, D. Krapf, M.J. Kipper, Nanostructured Surfaces That Mimic the Vascular Endothelial Glycocalyx Reduce Blood Protein Adsorption and Prevent Fibrin Network Formation, ACS Applied Materials & Interfaces. 10 (2018) 31892–31902. doi:10.1021/acsami.8b09435.

[383] S. Weinbaum, X. Zhang, Y. Han, H. Vink, S.C. Cowin, Mechanotransduction and flow across the endothelial glycocalyx, Proceedings of the National Academy of Sciences. 100 (2003) 7988–7995. doi:10.1073/pnas.1332808100.

[384] S. Katsuki, W. Arnold, C. Mittal, F. Murad, Stimulation of guanylate cyclase by sodium nitroprusside, nitroglycerin and nitric oxide in various tissue preparations and comparison to the effects of sodium azide and hydroxylamine, J Cyclic Nucleotide Res. 3 (1977) 23–35.

[385] W.P. Arnold, C.K. Mittal, S. Katsuki, F. Murad, Nitric oxide activates guanylate cyclase and increases guanosine 3':5'-cyclic monophosphate levels in various tissue preparations, Proc. Natl. Acad. Sci. U.S.A. 74 (1977) 3203–3207.

[386] L.J. Ignarro, B. Ballot, K.S. Wood, Regulation of soluble guanylate cyclase activity by porphyrins and metalloporphyrins, J. Biol. Chem. 259 (1984) 6201–6207.

[387] L.J. Ignarro, Haem-dependent activation of guanylate cyclase and cyclic GMP formation by endogenous nitric oxide: a unique transduction mechanism for transcellular signaling, Pharmacol. Toxicol. 67 (1990) 1–7.

[388] R.F. Furchgott, J.V. Zawadzki, The obligatory role of endothelial cells in the relaxation of arterial smooth muscle by acetylcholine, Nature. 288 (1980) 373–376.

[389] P.D. Cherry, R.F. Furchgott, J.V. Zawadzki, D. Jothianandan, Role of endothelial cells in relaxation of isolated arteries by bradykinin, Proc. Natl. Acad. Sci. U.S.A. 79 (1982) 2106–2110.

[390] L.J. Ignarro, R.E. Byrns, G.M. Buga, K.S. Wood, Endothelium-derived relaxing factor from pulmonary artery and vein possesses pharmacologic and chemical properties identical to those of nitric oxide radical, Circ. Res. 61 (1987) 866–879.

[391] L.J. Ignarro, G.M. Buga, K.S. Wood, R.E. Byrns, G. Chaudhuri, Endothelium-derived relaxing factor produced and released from artery and vein is nitric oxide, Proc. Natl. Acad. Sci. U.S.A. 84 (1987) 9265–9269.

[392] A.L. Kleschyov, The NO-heme signaling hypothesis, Free Radical Biology and Medicine. 112 (2017) 544–552. doi:10.1016/j.freeradbiomed.2017.08.025.

[393] G.M. Rubanyi, J.C. Romero, P.M. Vanhoutte, Flow-induced release of endothelium-derived relaxing factor, Am. J. Physiol. 250 (1986) H1145-1149. doi:10.1152/ajpheart.1986.250.6.H1145.

[394] C. de Wit, C. Schäfer, P. von Bismarck, S.S. Bolz, U. Pohl, Elevation of plasma viscosity induces sustained NO-mediated dilation in the hamster cremaster microcirculation in vivo, Pflugers Arch. 434 (1997) 354–361. doi:10.1007/s004240050408.

[395] U. Pohl, K. Herlan, A. Huang, E. Bassenge, EDRF-mediated shear-induced dilation opposes myogenic vasoconstriction in small rabbit arteries, Am. J. Physiol. 261 (1991) H2016-2023. doi:10.1152/ajpheart.1991.261.6.H2016.

[396] S.R. Jaffrey, S.H. Snyder, Nitric oxide: a neural messenger, Annu. Rev. Cell Dev. Biol. 11 (1995) 417–440. doi:10.1146/annurev.cb.11.110195.002221.

[397] M.B. Witte, A. Barbul, Role of nitric oxide in wound repair, Am. J. Surg. 183 (2002) 406–412.

[398] F.C. Fang, Perspectives series: host/pathogen interactions. Mechanisms of nitric oxide-related antimicrobial activity, J. Clin. Invest. 99 (1997) 2818–2825. doi:10.1172/JCI119473.

[399] J.C. Toledo, O. Augusto, Connecting the chemical and biological properties of nitric oxide, Chem. Res. Toxicol. 25 (2012) 975–989. doi:10.1021/tx300042g.

[400] S. Goldstein, G. Czapski, Kinetics of Nitric Oxide Autoxidation in Aqueous Solution in the Absence and Presence of Various Reductants. The Nature of the Oxidizing Intermediates, Journal of the American Chemical Society. 117 (1995) 12078–12084. doi:10.1021/ja00154a007.

[401] P.J. Andrew, B. Mayer, Enzymatic function of nitric oxide synthases, Cardiovasc. Res. 43 (1999) 521–531.

[402] E. Weitzberg, M. Hezel, J.O. Lundberg, Nitrate-nitrite-nitric oxide pathway: implications for anesthesiology and intensive care, Anesthesiology. 113 (2010) 1460–1475. doi:10.1097/ALN.0b013e3181fcf3cc.

[403] J.O. Lundberg, E. Weitzberg, NO generation from inorganic nitrate and nitrite: Role in physiology, nutrition and therapeutics, Arch. Pharm. Res. 32 (2009) 1119–1126. doi:10.1007/s12272-009-1803-z.

[404] J.O. Lundberg, E. Weitzberg, M.T. Gladwin, The nitrate-nitrite-nitric oxide pathway in physiology and therapeutics, Nat Rev Drug Discov. 7 (2008) 156–167. doi:10.1038/nrd2466.

[405] J.S. Stamler, O. Jaraki, J. Osborne, D.I. Simon, J. Keaney, J. Vita, D. Singel, C.R. Valeri, J. Loscalzo, Nitric oxide circulates in mammalian plasma primarily as an S-nitroso adduct of serum albumin., Proceedings of the National Academy of Sciences. 89 (1992) 7674–7677. doi:10.1073/pnas.89.16.7674.

[406] J.S. Scharfstein, J.F. Keaney, A. Slivka, G.N. Welch, J.A. Vita, J.S. Stamler, J. Loscalzo, In vivo transfer of nitric oxide between a plasma protein-bound reservoir and low molecular weight thiols, J. Clin. Invest. 94 (1994) 1432–1439. doi:10.1172/JCI117480.

[407] A. Nedospasov, R. Rafikov, N. Beda, E. Nudler, An autocatalytic mechanism of protein nitrosylation, Proc. Natl. Acad. Sci. U.S.A. 97 (2000) 13543–13548. doi:10.1073/pnas.250398197.

[408] O. Rafikova, R. Rafikov, E. Nudler, Catalysis of S-nitrosothiols formation by serum albumin: the mechanism and implication in vascular control, Proc. Natl. Acad. Sci. U.S.A. 99 (2002) 5913–5918. doi:10.1073/pnas.092048999.

[409] D. Jourd'heuil, F.L. Jourd'heuil, M. Feelisch, Oxidation and nitrosation of thiols at low micromolar exposure to nitric oxide. Evidence for a free radical mechanism, J. Biol. Chem. 278 (2003) 15720–15726. doi:10.1074/jbc.M300203200.

[410] A. Martínez-Ruiz, I.M. Araújo, A. Izquierdo-Álvarez, P. Hernansanz-Agustín, S. Lamas, J.M. Serrador, Specificity in S-Nitrosylation: A Short-Range Mechanism for NO Signaling?, Antioxidants & Redox Signaling. 19 (2013) 1220–1235. doi:10.1089/ars.2012.5066.

[411] G.R. Wang, Y. Zhu, P.V. Halushka, T.M. Lincoln, M.E. Mendelsohn, Mechanism of platelet inhibition by nitric oxide: in vivo phosphorylation of thromboxane receptor by cyclic GMP-dependent protein kinase, Proc. Natl. Acad. Sci. U.S.A. 95 (1998) 4888–4893.

[412] L.J. Ignarro, Biological actions and properties of endothelium-derived nitric oxide formed and released from artery and vein, Circ. Res. 65 (1989) 1–21.

[413] P.N. Coneski, M.H. Schoenfisch, Nitric oxide release: part III. Measurement and reporting, Chem Soc Rev. 41 (2012) 3753–3758. doi:10.1039/c2cs15271a.

[414] A. Barbul, S.A. Lazarou, D.T. Efron, H.L. Wasserkrug, G. Efron, Arginine enhances wound healing and lymphocyte immune responses in humans, Surgery. 108 (1990) 331–336; discussion 336-337.

[415] M.W. Vaughn, L. Kuo, J.C. Liao, Estimation of nitric oxide production and reaction rates in tissue by use of a mathematical model, Am. J. Physiol. 274 (1998) H2163-2176.

[416] T.S. Hakim, K. Sugimori, E.M. Camporesi, G. Anderson, Half-life of nitric oxide in aqueous solutions with and without haemoglobin, Physiol Meas. 17 (1996) 267–277.

[417] D.D. Thomas, X. Liu, S.P. Kantrow, J.R. Lancaster, The biological lifetime of nitric oxide: implications for the perivascular dynamics of NO and O2, Proc. Natl. Acad. Sci. U.S.A. 98 (2001) 355–360. doi:10.1073/pnas.011379598.

[418] X. Liu, A. Samouilov, J.R. Lancaster, J.L. Zweier, Nitric oxide uptake by erythrocytes is primarily limited by extracellular diffusion not membrane resistance, J. Biol. Chem. 277 (2002) 26194–26199. doi:10.1074/jbc.M201939200.

[419] M.S. Navati, W. Chung, J.M. Friedman, Trehalose-Based Glassy Matrices as an Effective Tool to Trap Short-Lived Intermediates in the Nitric Oxide Dioxygenation (NOD) Reaction of Hemoglobin, J Phys Chem B. 120 (2016) 4529–4539. doi:10.1021/acs.jpcb.5b12778.

[420] M.C. Jen, M.C. Serrano, R. van Lith, G.A. Ameer, Polymer-Based Nitric Oxide Therapies: Recent Insights for Biomedical Applications, Adv Funct Mater. 22 (2012) 239–260. doi:10.1002/adfm.201101707.

[421] M.C. Frost, M.M. Reynolds, M.E. Meyerhoff, Polymers incorporating nitric oxide releasing/generating substances for improved biocompatibility of blood-contacting medical devices, Biomaterials. 26 (2005) 1685–1693. doi:10.1016/j.biomaterials.2004.06.006.

[422] D.A. Riccio, M.H. Schoenfisch, Nitric oxide release: part I. Macromolecular scaffolds, Chem Soc Rev. 41 (2012) 3731–3741. doi:10.1039/c2cs15272j.

[423] A. Lutzke, A.C. Melvin, M.J. Neufeld, C.L. Allison, M.M. Reynolds, Nitric oxide generation from S-nitrosoglutathione: New activity of indium and a survey of metal ion effects, Nitric Oxide. 84 (2019) 16–21. doi:10.1016/j.niox.2019.01.005.

[424] D. Giustarini, A. Milzani, R. Colombo, I. Dalle-Donne, R. Rossi, Nitric oxide and S-nitrosothiols in human blood, Clin. Chim. Acta. 330 (2003) 85–98.

[425] M.E. Mendelsohn, S. O'Neill, D. George, J. Loscalzo, Inhibition of fibrinogen binding to human platelets by S-nitroso-N-acetylcysteine, J. Biol. Chem. 265 (1990) 19028–19034.

[426] S.M. Lantvit, B.J. Barrett, M.M. Reynolds, Nitric oxide releasing material adsorbs more fibrinogen, Journal of Biomedical Materials Research Part A. 101 (2013) 3201–3210. doi:10.1002/jbm.a.34627.

[427] Y. Zang, K.C. Popat, M.M. Reynolds, Nitric oxide-mediated fibrinogen deposition prevents platelet adhesion and activation, Biointerphases. 13 (2018) 06E403. doi:10.1116/1.5042752.

[428] D.J. Smith, D. Chakravarthy, S. Pulfer, M.L. Simmons, J.A. Hrabie, M.L. Citro, J.E. Saavedra, K.M. Davies, T.C. Hutsell, D.L. Mooradian, S.R. Hanson, L.K. Keefer, Nitric oxide-releasing polymers containing the [N(O)NO]- group, J. Med. Chem. 39 (1996) 1148–1156. doi:10.1021/jm950652b.

[429] S.M. Marxer, A.R. Rothrock, B.J. Nablo, M.E. Robbins, M.H. Schoenfisch, Preparation of Nitric Oxide (NO)-Releasing Sol−Gels for Biomaterial Applications, Chemistry of Materials. 15 (2003) 4193–4199. doi:10.1021/cm034347n.

[430] M.E. Robbins, B.K. Oh, E.D. Hopper, M.H. Schoenfisch, Nitric Oxide-Releasing Xerogel Microarrays Prepared with Surface-Tailored Poly(dimethylsiloxane) Templates, Chemistry of Materials. 17 (2005) 3288–3296. doi:10.1021/cm050374x.

[431] P.N. Coneski, J.A. Nash, M.H. Schoenfisch, Nitric Oxide-Releasing Electrospun Polymer Microfibers, ACS Applied Materials & Interfaces. 3 (2011) 426–432. doi:10.1021/am101010e.

[432] R.J. Soto, L. Yang, M.H. Schoenfisch, Functionalized Mesoporous Silica via an Aminosilane Surfactant Ion Exchange Reaction: Controlled Scaffold Design and Nitric Oxide Release, ACS Applied Materials & Interfaces. 8 (2016) 2220–2231. doi:10.1021/acsami.5b10942.

[433] A. Koh, A.W. Carpenter, D.L. Slomberg, M.H. Schoenfisch, Nitric Oxide-Releasing Silica Nanoparticle-Doped Polyurethane Electrospun Fibers, ACS Applied Materials & Interfaces. 5 (2013) 7956–7964. doi:10.1021/am402044s.

[434] A. Lutzke, B.H. Neufeld, M.J. Neufeld, M.M. Reynolds, Nitric oxide release from a biodegradable cysteine-based polyphosphazene, Journal of Materials Chemistry B. 4 (2016) 1987–1998. doi:10.1039/C6TB00037A.

[435] A. Lutzke, A. Pegalajar-Jurado, B.H. Neufeld, M.M. Reynolds, Nitric oxide-releasing S-nitrosated derivatives of chitin and chitosan for biomedical applications, J. Mater. Chem. B. 2 (2014) 7449–7458. doi:10.1039/C4TB01340A.

[436] A. Lutzke, J.B. Tapia, M.J. Neufeld, M.M. Reynolds, Sustained Nitric Oxide Release from a Tertiary S-Nitrosothiol-based Polyphosphazene Coating, ACS Appl. Mater. Interfaces. 9 (2017) 2104–2113. doi:10.1021/acsami.6b12888.

[437] A.B. Seabra, R. da Silva, G.F.P. de Souza, M.G. de Oliveira, Antithrombogenic Polynitrosated Polyester/Poly(methyl methacrylate) Blend for the Coating of Blood-Contacting Surfaces, Artificial Organs. 32 (2008) 262–267. doi:10.1111/j.1525-1594.2008.00540.x.

[438] S.P. Hopkins, J. Pant, M.J. Goudie, C. Schmiedt, H. Handa, Achieving Long-Term Biocompatible Silicone via Covalently Immobilized *S* -Nitroso- *N* -acetylpenicillamine (SNAP) That Exhibits 4 Months of Sustained Nitric Oxide Release, ACS Applied Materials & Interfaces. 10 (2018) 27316–27325. doi:10.1021/acsami.8b08647.

[439] S. Hopkins, M. Frost, Synthesis and Characterization of Controlled Nitric Oxide Release from S-Nitroso-N-Acetyl-d-Penicillamine Covalently Linked to Polyvinyl Chloride (SNAP-PVC), Bioengineering. 5 (2018) 72. doi:10.3390/bioengineering5030072.

[440] L.-C. Xu, M.E. Meyerhoff, C.A. Siedlecki, Blood coagulation response and bacterial adhesion to biomimetic polyurethane biomaterials prepared with surface texturing and nitric oxide release, Acta Biomaterialia. 84 (2019) 77–87. doi:10.1016/j.actbio.2018.11.035.

[441] Y. Wo, Z. Li, E.J. Brisbois, A. Colletta, J. Wu, T.C. Major, C. Xi, R.H. Bartlett, A.J. Matzger, M.E. Meyerhoff, Origin of Long-Term Storage Stability and Nitric Oxide Release Behavior of CarboSil Polymer Doped with S-Nitroso-N-acetyl-d-penicillamine, ACS Appl. Mater. Interfaces. 7 (2015) 22218–22227. doi:10.1021/acsami.5b07501.

[442] Y. Wo, E.J. Brisbois, R.H. Bartlett, M.E. Meyerhoff, Recent advances in thromboresistant and antimicrobial polymers for biomedical applications: just say yes to nitric oxide (NO), Biomater Sci. 4 (2016) 1161–1183. doi:10.1039/c6bm00271d.

[443] W. Cha, M.E. Meyerhoff, Catalytic generation of nitric oxide from S-nitrosothiols using immobilized organoselenium species, Biomaterials. 28 (2007) 19–27. doi:10.1016/j.biomaterials.2006.08.019.

[444] S. Hwang, M.E. Meyerhoff, Organoditelluride-mediated catalytic S-nitrosothiol decomposition, Journal of Materials Chemistry. 17 (2007) 1462. doi:10.1039/b700375g.

[445] W. Cai, J. Wu, C. Xi, A.J. Ashe, M.E. Meyerhoff, Carboxyl-ebselen-based layer-by-layer films as potential antithrombotic and antimicrobial coatings, Biomaterials. 32 (2011) 7774–7784. doi:10.1016/j.biomaterials.2011.06.075.

[446] J. Yang, J.L. Welby, M.E. Meyerhoff, Generic Nitric Oxide (NO) Generating Surface by Immobilizing Organoselenium Species via Layer-by-Layer Assembly, Langmuir. 24 (2008) 10265–10272. doi:10.1021/la801466e.

[447] V. Wonoputri, C. Gunawan, S. Liu, N. Barraud, L.H. Yee, M. Lim, R. Amal, Copper Complex in Poly(vinyl chloride) as a Nitric Oxide-Generating Catalyst for the Control of Nitrifying Bacterial Biofilms, ACS Appl Mater Interfaces. 7 (2015) 22148–22156. doi:10.1021/acsami.5b07971.

[448] T.C. Major, D.O. Brant, C.P. Burney, K.A. Amoako, G.M. Annich, M.E. Meyerhoff, H. Handa, R.H. Bartlett, The hemocompatibility of a nitric oxide generating polymer that catalyzes S-nitrosothiol decomposition in an extracorporeal circulation model, Biomaterials. 32 (2011) 5957–5969. doi:10.1016/j.biomaterials.2011.03.036.

[449] B.K. Oh, M.E. Meyerhoff, Spontaneous Catalytic Generation of Nitric Oxide from *S* -Nitrosothiols at the Surface of Polymer Films Doped with Lipophilic Copper(II) Complex, Journal of the American Chemical Society. 125 (2003) 9552–9553. doi:10.1021/ja035775x.

[450] S.C. Puiu, Z. Zhou, C.C. White, L.J. Neubauer, Z. Zhang, L.E. Lange, J.A. Mansfield, M.E. Meyerhoff, M.M. Reynolds, Metal ion-mediated nitric oxide generation from polyurethanes via covalently linked copper(II)-cyclen moieties, J. Biomed. Mater. Res. Part B Appl. Biomater. 91 (2009) 203–212. doi:10.1002/jbm.b.31391.

[451] B.K. Oh, M.E. Meyerhoff, Catalytic generation of nitric oxide from nitrite at the interface of polymeric films doped with lipophilic CuII-complex: a potential route to the preparation of thromboresistant coatings, Biomaterials. 25 (2004) 283–293.

[452] S. Hwang, W. Cha, Mark.E. Meyerhoff, Polymethacrylates with a Covalently Linked CuII–Cyclen Complex for the In Situ Generation of Nitric Oxide from Nitrosothiols in Blood, Angewandte Chemie International Edition. 45 (2006) 2745–2748. doi:10.1002/anie.200503588.

[453] S. Hwang, M.E. Meyerhoff, Polyurethane with tethered copper(II)-cyclen complex: preparation, characterization and catalytic generation of nitric oxide from S-nitrosothiols, Biomaterials. 29 (2008) 2443–2452. doi:10.1016/j.biomaterials.2008.02.004.

[454] Y. Hou, Z. Guo, J. Li, P.G. Wang, Seleno compounds and glutathione peroxidase catalyzed decomposition of S-nitrosothiols, Biochem. Biophys. Res. Commun. 228 (1996) 88–93. doi:10.1006/bbrc.1996.1620.

[455] V. Wonoputri, C. Gunawan, S. Liu, N. Barraud, L.H. Yee, M. Lim, R. Amal, Iron Complex Facilitated Copper Redox Cycling for Nitric Oxide Generation as Nontoxic Nitrifying Biofilm Inhibitor, ACS Applied Materials & Interfaces. 8 (2016) 30502–30510. doi:10.1021/acsami.6b10357.

[456] S. Moncada, E.A. Higgs, The discovery of nitric oxide and its role in vascular biology: The discovery of nitric oxide and its role in vascular biology, British Journal of Pharmacology. 147 (2009) S193–S201. doi:10.1038/sj.bjp.0706458.

[457] H. Ren, J. Wu, C. Xi, N. Lehnert, T. Major, R.H. Bartlett, M.E. Meyerhoff, Electrochemically Modulated Nitric Oxide (NO) Releasing Biomedical Devices via Copper(II)-Tri(2-pyridylmethyl)amine Mediated Reduction of Nitrite, ACS Applied Materials & Interfaces. 6 (2014) 3779–3783. doi:10.1021/am406066a.

[458] H. Ren, A. Colletta, D. Koley, J. Wu, C. Xi, T.C. Major, R.H. Bartlett, M.E. Meyerhoff, Thromboresistant/anti-biofilm catheters via electrochemically modulated nitric oxide release, Bioelectrochemistry. 104 (2015) 10–16. doi:10.1016/j.bioelechem.2014.12.003.

[459] L. Höfler, D. Koley, J. Wu, C. Xi, M.E. Meyerhoff, Electromodulated release of nitric oxide through polymer material from reservoir of inorganic nitrite salt, RSC Advances. 2 (2012) 6765. doi:10.1039/c2ra20853a.

[460] J.L. Harding, M.M. Reynolds, Metal organic frameworks as nitric oxide catalysts, Journal of the American Chemical Society. 134 (2012) 3330–3333.

[461] J.L. Harding, J.M. Metz, M.M. Reynolds, A Tunable, Stable, and Bioactive MOF Catalyst for Generating a Localized Therapeutic from Endogenous Sources, Advanced Functional Materials. 24 (2014) 7503–7509. doi:10.1002/adfm.201402529.

[462] S.S. Chui, S.M. Lo, J.P. Charmant, A.G. Orpen, I.D. Williams, A chemically functionalizable nanoporous material [Cu3(TMA)2(H2O)3]n, Science. 283 (1999) 1148–1150.

[463] A. Demessence, D.M. D'Alessandro, M.L. Foo, J.R. Long, Strong CO $_2$ Binding in a Water-Stable, Triazolate-Bridged Metal−Organic Framework Functionalized with Ethylenediamine, Journal of the American Chemical Society. 131 (2009) 8784–8786. doi:10.1021/ja903411w.

[464] M.J. Neufeld, J.L. Harding, M.M. Reynolds, Immobilization of Metal-Organic Framework Copper(II) Benzene-1,3,5-tricarboxylate (CuBTC) onto Cotton Fabric as a Nitric Oxide Release Catalyst, ACS Appl Mater Interfaces. 7 (2015) 26742–26750. doi:10.1021/acsami.5b08773.

[465] Q. Zhao, Y. Fan, Y. Zhang, J. Liu, W. Li, Y. Weng, Copper-Based SURMOFs for Nitric Oxide Generation: Hemocompatibility, Vascular Cell Growth, and Tissue Response, ACS Applied Materials & Interfaces. 11 (2019) 7872–7883. doi:10.1021/acsami.8b22731.

[466] M.J. Neufeld, B.R. Ware, A. Lutzke, S.R. Khetani, M.M. Reynolds, Water-Stable Metal-Organic Framework/Polymer Composites Compatible with Human Hepatocytes, ACS Appl Mater Interfaces. 8 (2016) 19343–19352. doi:10.1021/acsami.6b05948.

[467] M.J. Neufeld, A. Lutzke, J.B. Tapia, M.M. Reynolds, Metal-Organic Framework/Chitosan Hybrid Materials Promote Nitric Oxide Release from S-Nitrosoglutathione in Aqueous Solution, ACS Appl Mater Interfaces. 9 (2017) 5139–5148. doi:10.1021/acsami.6b14937.

[468] M.J. Neufeld, A. Lutzke, W.M. Jones, M.M. Reynolds, Nitric Oxide Generation from Endogenous Substrates Using Metal–Organic Frameworks: Inclusion within Poly(vinyl alcohol) Membranes To Investigate Reactivity and Therapeutic Potential, ACS Applied Materials & Interfaces. 9 (2017) 35628–35641. doi:10.1021/acsami.7b11846.

[469] T.R. Roberts, M.J. Neufeld, M.A. Meledeo, A.P. Cap, L.C. Cancio, M.M. Reynolds, A.I. Batchinsky, A metal organic framework reduces thrombus formation and platelet aggregation ex vivo, J Trauma Acute Care Surg. 85 (2018) 572–579. doi:10.1097/TA.0000000000001982.

Chapter 2: ATOMIC FORCE MICROSCOPY OF ADSORBED PROTEOGLYCAN MIMETIC NANOPARTICLES: TOWARD NEW GLYCOCALYX-MIMETIC MODEL SURFACES[1]

OVERVIEW

Blood vessels present a dense, non-uniform, polysaccharide-rich layer, called the endothelial glycocalyx. The polysaccharides in the glycocalyx include polyanionic glycosaminoglycans (GAGs). This polysaccharide-rich surface has excellent and unique blood compatibility. We report new methods for preparing and characterizing dense GAG surfaces that can serve as models of the vascular endothelial glycocalyx. The GAG-rich surfaces are prepared by adsorbing heparin and chondroitin sulfate-containing polyelectrolyte complex nanoparticles (PCNs) to chitosan-hyaluronan polyelectrolyte multilayers (PEMs). The surfaces are characterized by PeakForce tapping atomic force microscopy, both in air and in aqueous pH 7.4 buffer, and by PeakForce quantitative nanomechanics (PF-QNM) mode with high spatial resolution. These new surfaces provide access to heparin-rich or chondroitin sulfate-rich coatings that mimic both composition and nanoscale structural features of the vascular endothelial glycocalyx.

2.1. Introduction

Despite the widespread need of blood-compatible materials for medical devices and decades of research in this area, obstacles to designing blood-compatible surfaces remain. The inside surface of healthy blood vessels is the only known material that is blood-compatible when

---

[1] This work was published in *Carbohydrate Polymers* and is reproduced in modified form here with permission [1]. M. Hedayati was responsible for designing and conducting experiments, managing data, and preparing the manuscript. M.J. Kipper conceived of the research, advised and oversaw the experimental work, and edited the manuscript.

in long-term contact with flowing whole blood [2]. Blood vessel walls are lined with a layer of endothelial cells, which present a network of membrane-bound proteoglycans and glycoproteins known as the endothelial glycocalyx [3,4]. The thickness of the endothelial glycocalyx varies throughout the vasculature, with reported glycocalyx thickness ranging from 200 to 2000 nm [3,5]. The composition of the glycocalyx also varies, as a dynamic equilibrium exists between this layer and the soluble components in the flowing plasma [3].

Proteoglycans and glycoproteins connect the endothelial glycocalyx to the endothelium [6]. Proteoglycans are composed of a core protein chain with glycosaminoglycan (GAG) side chains connected to them. The most common GAG in the endothelial glycocalyx is heparan sulfate, followed by chondroitin sulfate and dermatan sulfate [3]. The glycocalyx plays an important role in the anticoagulant activity of the endothelium. The negative charge of the GAGs repels circulating platelets [3,5], and some anticoagulant mediators can bind to the glycocalyx to enhance their anticoagulant activity [7–9].

The structure of the endothelial glycocalyx arising from the organization of proteoglycans has been investigated to better understand structure-function relationships. This structure is illustrated in Figure 2.1 [10,11]. Rostgaard and Qvortrup show electron microscopy of renal capillaries with features they describe as (gooseberry) bush-like spherical features about 300-400 nm in diameter, composed of smaller filaments [10]. Foundational work by Squire *et al.* provided a detailed structural analysis of Fourier transformed electron micrographs of frog capillaries [12]. Their analysis resulted in a structural model in which clusters or “tufts” of glycoproteins about 100 nm in diameter are organized into a quasi-hexagonal lattice, with thicknesses between about 100 and 200 nm [12]. Within these clusters organized into 100-nm domains, glycoproteins are further clustered into features with approximately 20-nm spacing [12]. Squire et al. proposed that the regular spacing of these “tufts” or “bushes” is consistent with a proposed model in which the proteoglycans are organized by anchoring foci in the underlying actin cortical cytoskeleton [12,13]. Subsequent improvements to experimental techniques have improved estimates of the glycocalyx thickness [14]. However, for 20 years, this general description has persisted as the dominant basis for structural and mechanical models of the endothelial glycocalyx [6,15,16]. In the present work, we aim to develop and characterize model surfaces that have similar bush-like organization of GAGs, as those found in the endothelial glycocalyx, shown in Figure 2.1.

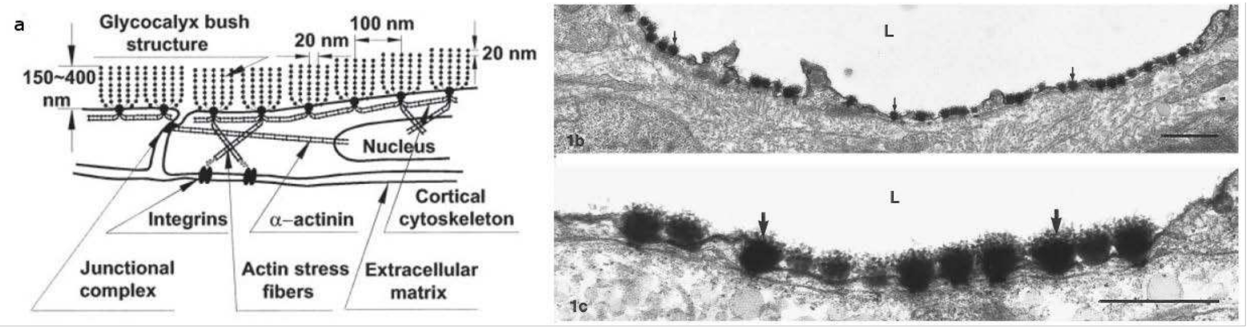

Figure 2.1. (a) Sketch of endothelial surface layer (not to scale) showing core protein arrangement and spacing of scattering centers along core proteins and their relationship to the actin cortical cytoskeleton as proposed in [12], from [11], copyright 2003, National Academy of Sciences. (b and c) Electron micrographs of capillary from small intestine. Bush-like structures are indicated by the arrows. The capillary lumen in b and c is labeled “L”. Bars: (b) 1.0 µm; (c) 0.5 µm. (b and c) are Reprinted from Microvascular Research, 53, Jørgen Rostgaard and Klaus Qvortrup, Electron Microscopic Demonstrations of Filamentous. Molecular Sieve Plugs in Capillary Fenestrae, 1-13, Copyright (1997), with permission from Elsevier.

The structures illustrated in Figure 2.1 are determined using electron microscopy on prepared tissue samples. The endothelial glycocalyx has also been characterized by atomic force microscopy (AFM) techniques to measure and map its mechanical properties, both on endothelial cell cultures and on tissue samples [17–19]. In all three of these reports the AFM imaging and mechanical property mapping is conducted at a resolution that is too low to observe the sub-micron features described by electron microscopy (Figure 2.1). Nonetheless, these previous publications establish that the mechanical properties of the endothelial glycocalyx can be characterized by AFM, and provide possible benchmark for the mechanical properties of glycocalyx mimics.

Glycocalyx-mimetic surfaces should present a high density of saccharide residues. In particular, heparin-containing polyelectrolyte multilayers can modulate cell-surface interactions and improve the blood compatibility of surfaces [20–23]. Saccharide-modified surfaces can be prepared by a variety of techniques, including self-assembled monolayers containing saccharides (“glyco-SAMs”) [24,25], glycopolymers containing monosaccharide or oligosaccharide pendant groups [26–30], and brushes formed from polysaccharides, graft copolymers, or dendrimers [31–34]. These approaches are often described as “glycocalyx mimics” or “glycocalyx substitutes”. These surfaces offer control over surface chemistry for protein binding studies. In some cases they have been used to modify cell-surface and protein-surface interactions. However, these examples primarily use neutral saccharide residues (e.g. glucose and mannose), and the resultant surfaces have thicknesses limited to about 20 nm or less, and therefore do not present structures similar to those in Figure 2.1. The recent work by Goren *et al.*, grafting dextran to an azide-modified surface is a notable exception to this surface thickness limitation [34]. These approaches provide platforms for studying biomolecule interactions with ultrathin glyco-coatings on surfaces that may mimic some features of cell surfaces that have a very thin glycocalyx. Nonetheless, the formation of dense GAG-rich surfaces with composition, negatively charged functional groups, and structural features similar to that of the much thicker vascular endothelial glycocalyx shown in Figure 2.1 has not been demonstrated by these techniques.

In this work we demonstrate a new method for preparing surfaces that mimic the structure and composition of the endothelial glycocalyx. This method is based on the layer-by-layer (LbL) assembly of polyelectrolyte multilayers (PEMs) and their subsequent modification with polyelectrolyte complex nanoparticles (PCNs). The polyelectrolytes used are polyanionic polysaccharides, like those found in the glycocalyx. The PEMs provide a uniform surface for deposition of the PCNs, and the PCNs provide the bush-like structures with dimensions (approximately 100 to 200 nm diameter) similar to those shown in Figure 2.1.

Here we report initial characterization of these GAG-rich surfaces prepared via LbL assembly of PEMs containing PCNs by atomic force microscopy. We used the hyaluronan (HA) as a polyanion and chitosan (CHI) as a polycationic polysaccharide (Scheme 2.1) for PEM construction. PEM formation is monitored using in-situ Fourier-transform surface plasmon resonance (FT-SPR), and surface chemistry is confirmed using X-ray photoelectron spectroscopy (XPS). Both techniques confirm LbL adsorption of the polysaccharides. The surface structure and mechanical properties are characterized at high resolution using atomic force microscopy (AFM) and PeakForce quantitative nanomechanics (PF-QNM). In this work, we hypothesize that adsorption of PCNs to PEMs, illustrated in Scheme 2.1, will provide access to dense GAG-rich surfaces with dimensions and features approaching those of the vascular endothelial glycocalyx, shown in Figure 2.1. These surfaces could serve as model systems to study the structure-composition-property relationships of glycocalyx-mimetic surfaces, providing new insights into the design of blood-compatible surfaces. The structure and organization of GAGs in the vascular endothelial glycocalyx has been reported in the literature for over 30 years. However, to the best of our knowledge no report in the literature has demonstrated preparation of a surface that mimics this structure and composition.

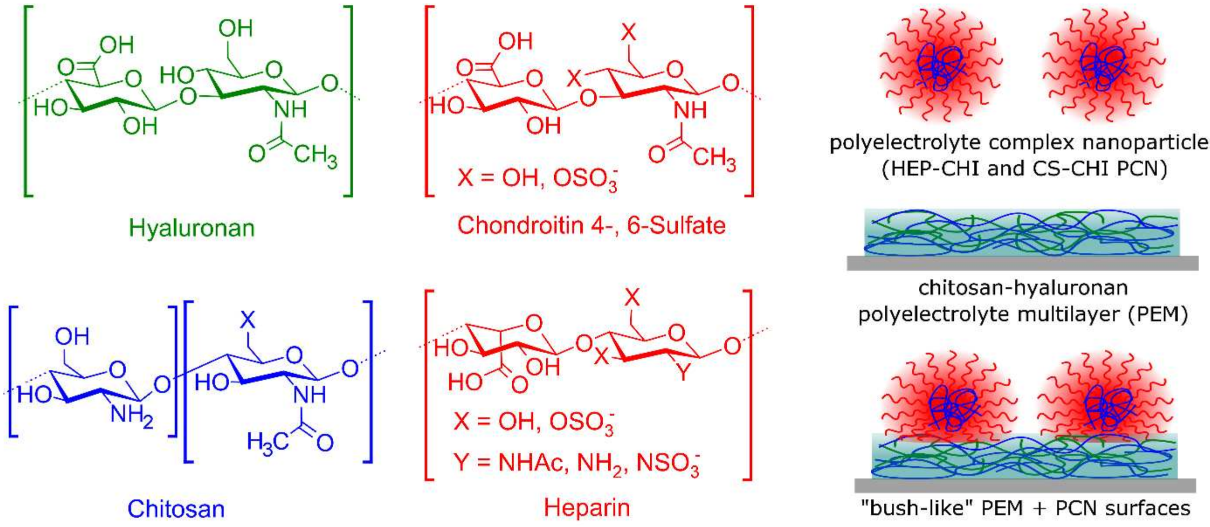

Scheme 2.1. Chemical structure of each polysaccharide used in this study (left). Schematic of GAG-rich polyelectrolyte complex nanoparticles, formed from CS and CHI or HEP and CHI, polyelectrolyte multilayers formed from HA and CHI, and the PEM+PCN surfaces we propose as mimics of the “bush-like” structures of the endothelial glycocalyx shown in Figure 2.1.

2.2 Materials and methods

2.2.1 Materials

Chitosan (CHI) (Protosan UP B 90/20, 5%) was purchased from Novamatrix. Chondroitin sulfate sodium (CS) salt (from shark cartilage, 6% sulfur, 6-sulfate/4-sulfate = 1.24, Mw =84.3 kDa; PDI = 1.94) and hyaluronic acid (HA) sodium salt (Mw = 743 kDa; PDI = 1.16) were purchased from Sigma Aldrich (St. Louis, MO). Heparin sodium (HEP) (from porcine intestinal mucosa, 12.5% sulfur) was purchased from Celsus Laboratories (Cincinnati, OH). 11-Mercaptoundecanioc acid 95% (MUA), rhodamine B isothiocyanate, and fluorescein isothiocyanate were purchased from Sigma-Aldrich (St. Louis, MO). Glacial acetic acid and ethanol (200 proof 99.5+ %) were purchased from Acros Organics (Geel, Belgium). Sodium acetate was purchased from Fisher Scientific (Pittsburgh, PA). Phosphate buffered saline without calcium and magnesium (PBS) was purchased from Gibco (Grand Island, NY). A Millipore

Synthesis water purification unit was used to obtain 18.2 MΩ cm water, used for making all aqueous solutions.

2.2.2. PCN preparation and characterization by dynamic light scattering (DLS) and zeta potential measurements

We form PCNs, as we have reported previously, by combining a solution containing a polyanionic GAG (heparin or chondroitin sulfate) with a solution containing a polycation (the polysaccharide chitosan) (Figure 2.1), so that the negatively charged groups (sulfate and carboxylate) on the GAG are in stoichiometric excess relative to the positively charged groups (ammonium) groups on the chitosan [35–37]. Briefly, chitosan, heparin sodium, and chondroitin sulfate solutions were prepared at concentrations of 0.9, 0.95, and 1.9 mg mL^{-1}, respectively, in each of three acetate buffer solutions (0.1 M sodium acetate and acetic acid at pH 4.6, 5.0, and 5.4). Solutions were filtered using 0.22 µm syringe filters (PVDF, Fisher Scientific). To prepare chondroitin sulfate PCNs (CS-CHI) the chondroitin sulfate solution was added to the stirring chitosan solution in a 6:1 volume ratio (36 mL of chondroitin sulfate solution to 6 mL of chitosan solution). To prepare heparin PCNs (HEP-CHI) the heparin solution was added to the stirring chitosan solution in a 4:1 volume ratio of heparin solution to a chitosan solution (24 mL heparin solution to 6 mL chitosan solution). CS-CHI and HEP-CHI PCNs were prepared at each of the three pH values. The mixtures were stirred for 3 h at 1100 rpm. After 3 h of stirring, all solutions were allowed to settle overnight to remove aggregated particles. After settling, the supernatant was decanted, containing the colloidally stable nanoparticles, while the aggregated particles were disposed of. DLS analysis demonstrated that CS-CHI nanoparticles have a reliable polydispersity index and do not require further separation. The HEP-CHI solution was centrifuged at 7000 × *g* for 5 min to separate the particles from uncomplexed polymer, using an Eppendorf 5804 centrifuge, (Eppendorf, Westbury, NY).

A Zetasizer Nano ZS (Malvern) was used to analyze size and zeta-potential using a 633 nm laser. All measurements were performed at a fixed angle of 175° at 25 °C. All measurements were performed in 0.1 M acetate buffer solution. Three measurements for each sample were taken.

2.2.3 Layer-by-layer assembly of PEMs and PEM+PCN

PEM structure and properties can be modulated through parameters including solution pH, salt concentration, polymer charge density, and number of layers deposited [38–42]. PEM were prepared from polysaccharides as we have described previously [41,43–46]. Gold-coated glass chips with 47 nm gold thickness (NanoSPR LLC, Chicago, IL) were used as a substrates for PEM deposition. The chips were rinsed exhaustively in ethanol. The chips were then modified with a monolayer of MUA by soaking the gold chip in a 1 mM MUA solution in ethanol for at least 20 h. The MUA-modified gold chips were dried with a gentle stream of dry nitrogen.

Polysaccharide solutions were prepared in similar acetate buffer solutions as those used for the PCN preparation (0.1 M sodium acetate and acetic acid at pH 4.6, 5.0, and 5.4). Chitosan (1.8 mg mL^{-1}) and hyaluronan (1 mg mL^{-1}) solutions were prepared at each pH, by stirring for 2 h at room temperature. Solutions were clarified by filtration through 0.22 μm syringe filters for chitosan and 0.45 μm syringe filters for hyaluronan solution (PVDF, Fisher Scientific).

Fourier transform surface plasmon resonance (FT-SPR) was used for measuring the intensity of *p*-polarized light reflected from the back side of the gold film on which the PEMs were assembled, as a function of wavenumber. MUA-modified chips were mounted in the flow cell of an SPR-100 module on a Thermo Electron 8700 FT-IR spectrometer. A Masterflex peristaltic pump (Cole-Parmer, Vernon Hills, IL) was used to pump polysaccharide and rinse solutions through the FT-SPR flow cell, with a flow rate of 0.8 mL min^{-1}. A low flow rate was used to ensure laminar flow over the gold chip surface. The interferometer in the FT-IR instrument was used to scan wavelengths at a fixed angle of incidence. In these experiments, FT-SPR was performed using a white light/near-infrared source with a CaF_2 beam splitter at the interferometer and an InGaS detector. Data were collected using Omnic 7.3 software (Thermo Electron), at 8 cm^{-1} resolution from 6000 to 12000 cm^{-1}. PEMs were constructed with CHI as the polycation and HA as the polyanion at each of three pH values. SPR peak position at each time point was determined from the center of gravity method provided in the OMNIC software. First, the surface was exposed to an acidified water rinse (pH 4.0, acidified with acetic acid), for six minutes. The LbL process was conducted by alternatively flowing solutions through the flow cell in the following sequence: polycation (CHI), rinse, polyanion (HA), rinse. The sequence was repeated until a 13-layer PEM (terminating with CHI) had been adsorbed. PEM+PCN samples were prepared similarly. After the LbL assembly of 13-layer CHI-HA PEMs at each pH, either CS-CHI PCNs or HEP-CHI PCNs were adsorbed, at the same pH as the rest of the PEM assembly was conducted (either pH 4.6, 5.0 or 5.4). The resulting samples are referred to as PEM+PCN(CS-CHI) and PEM+PCN(HEP-CHI). The length of the adsorption steps was doubled to 12 minutes for the PCN adsorption, followed by a final acidified water rinse.

2.2.4. X-ray photoelectron spectroscopy (XPS)

The surface chemistry of PEM and PEM+PCN samples were evaluated by Physical Electronics 5800 spectrometer (Chanhassen, MN). This system has a monochromatic Al kα X-ray source (hν = 1486.6 eV), hemispherical analyzer, and multichannel detector. The binding energy scales for the samples were referenced to the C1s peak at 284.8 eV. High resolution spectra of the

N1s and S2p envelopes were acquired with 0.1 eV steps, and an X-ray spot size of 800 μm. All XPS analyses were performed at a photoelectron take-off angle of 45°. Peak fitting of the N1s envelope was performed in MultiPak (version 9.3.0.3, Ulvac-Phi, Inc.), assuming three Gaussian/Lorentzian peaks and a Shirley background correction.

2.2.5 Microscopic evaluation of PEM+PCN

To enable imaging of PEM+PCN samples by TIRF microscopy, surfaces were prepared on glass-bottom petri dishes (35 mm diameter WillCo Wells, Amsterdam, Netherlands). Petri dishes were first treated with oxygen plasma for 10 minutes, to ensure a clean, oxidized surface. Rhodamine-modified chitosan and fluorescein-modified chitosan were used for preparation of PCNs and PEMs respectively. Rhodamine- and fluorescein-modified chitosan were prepared by dissolving 100 mg of chitosan in 10 ml of 0.1 M acetic acid, adding 10 ml of methanol to the solution, adding 3.25 ml of 2 mg ml^{-1} rhodamine B isothiocyanate or fluorescein isothiocyanate in methanol, and allowing the solution to react overnight. Rhodamine- and fluorescein-modified chitosan were purified via dialysis, freeze dried and stored at 4 °C protected from light until use. LbL adsorption was conducted by exposing the glass surfaces to alternating polycation, rinse, and polyanion solutions, as described above, for PEM preparation on gold-coated surfaces. The PEM was prepared using fluorescein-labeled CHI as the polycation and HA as the polyanion. CS-CHI PCN were prepared as described above, using rhodamine-labeled CHI. TIRF microscopy images of a PEM+PCN(CS-CHI) surface were acquired using an objective-type total internal reflection fluorescence microscope. The microscope was home-built around an Olympus IX71 body. A 473 nm and a 561 nm laser line with 2.5 mW of power after the objective (Olympus PlanApo 100 × ⁄1.45) were used as excitation sources. A back-illuminated electron-multiplied charge coupled device (EMCCD) camera (Andor iXon DU-888) operated at −85 °C with an electronic gain of 100 was used to collect images.

2.2.6 Atomic force microscopy (AFM)

AFM was performed on the surfaces prepared on the gold-coated chips used for FT-SPR. AFM imaging was performed in air, and in pH 7.4 PBS using a BioScope Resolve^{TM} BIOAFM (Bruker). The ScanAsyst mode was used, with a V-shaped silicon nitride cantilever with a nominal tip radius of 20 nm, spring constant of 0.35 N m^{-1}, and a reflective gold-coating on the back side (DNP-10, Bruker). For all topographical imaging the peak force setpoint was selected near 2 nN, and this setting was optimized by the Bruker Nanoscope software. All images were taken at room temperature, and the images and surface roughness are representative of at least three non-overlapping 5 μm × 5 μm areas. Image analysis was performed using NanoScope Analysis version 1.8 software. The mechanical surface properties of PEM and PEM+PCN samples were quantitatively assessed using the PeakForce quantitative nano-mechanics (PF-QNM) mode with a V-shaped silicon nitride cantilever with an actual tip radius of 65 nm and a spring constant of 0.098 N m^{-1} (PF-QNM, Bruker). This tip is calibrated by the manufacturer. The scan rate was set to 0.5 Hz; the peak force tapping frequency was set to 1 kHz, and the peak force set point was set to 500 pN. The PF-QNM mode is based on force-versus-distance measurements in which the probe oscillates at a frequency well below the resonance frequency of cantilever f_0. Once a force curve is obtained, it is then converted to a force versus separation plot for fitting and further analysis. Young’s modulus of the sample surface is extracted from the retract curve of the force-versus-distance data using a Hertzian model for indentation of an elastic solid by a spherical indenter, accounting for the adhesion force using the Derjaguin−Muller−Toporov (DMT) model. In these experiments the indentation depth is around 10 nm, which is much less than the 65 nm tip radius.

This ensures that the radius of the contact area is less than the tip radius, enabling use of the Hertzian model. The force on the cantilever is related to the modulus, tip radius, and indentation depth by

$$F - F_{adh} = \frac{4}{3} E^* \sqrt{R(d - d_0)^3} \qquad (1)$$

where $F - F_{adh}$ is the force on the cantilever relative to the adhesion force, R is the tip end radius, and $d - d_0$ is the deformation of the sample. The result of the fit is the reduced modulus E^*. The reduced elastic modulus E^* depends on the elastic moduli of both the tip E_{tip} and the sample E_s as well as on their Poisson ratios v_{tip} and v_s.

$$E^* = \left(\frac{1 - v_s^2}{E_s} + \frac{1 - v_{tip}^2}{E_{tip}} \right)^{-1} \approx \frac{E_s}{1 - v_s^2} \qquad (2)$$

The tip modulus E_{tip} is assumed to be infinite, so equation 2 depends only upon the sample modulus and Poisson's ratio. in this work, we assumed $v_s = 0.3$ for all samples.

2.3. Results

2.3.1. PCN preparation and characterization

The average size and zeta potential of PCNs was examined with DLS (Table 2.1). The PCN size is more sensitive to changes in composition (CS-CHI or HEP-CHI) than to changes in pH over the pH range from 4.6 to 5.4. The HEP-CHI PCNs have much smaller hydrodynamic diameters than the CS-CHI PCNs at all pH values. The low polydispersity indices (PDI) indicate a reliable distribution of diameter. Moreover, the negative zeta potential of PCNs confirms that negatively charged PCNs can be formed from both the CS-CHI and HEP-CHI polysaccharide pairs, with the polyanion in excess. Figure S1 in the Appendix A shows example size distribution by intensity for CS-CHI and HEP-CHI PCNs prepared at pH 5.0.

Table 2.1. Intensity-average size, PDI, and zeta potential of PCNs

PCN composition (pH)	hydrodynamic diameter (nm)	PDI	zeta potential (mV)
CS-CHI (4.6)	219 ± 2	0.12 ± 0.03	-41 ± 3
CS-CHI (5.0)	235 ± 2	0.11 ± 0.04	-36 ± 3
CS-CHI (5.4)	228 ± 1	0.10 ± 0.04	-33 ± 2
HEP-CHI (4.6)	93 ± 3	0.20 ± 0.04	-28 ± 2
HEP-CHI (5.0)	94 ± 2	0.21 ± 0.04	-23 ± 1
HEP-CHI (5.4)	110 ± 5	0.29 ± 0.05	-24 ± 2

2.3.2. Layer-by-layer assembly of PEMs and PEM+PCN

An example of in situ FT-SPR peak position as a function of time during PEM assembly at pH 5.0 is shown in the Appendix A Figure S2, and an example of in situ FT-SPR data for a PEM+PCN sample is shown in Appendix A Figure S3. The thickness of the adsorbed PEM can be estimated from theoretical predictions we have published previously [39,41]. We previously showed that there is pH dependence of PEM thickness for HEP-CHI PEMs, when the buffer ionic strength is higher than the ionic strength used here, but that there is little pH dependence of PEM thickness when 0.1 M buffer is used [41]. The range of thickness obtained for replicate samples was between 16 nm and 24 nm for all three pH values used. These data confirm that all three conditions yield 13-layer PEMs with similar thickness.

2.3.3. Confirmation of PCN adsorption by XPS and TIRF microscopy

PEM and PEM+PCN surfaces are characterized using XPS. Figure 2.2 left and right show high-resolution N1s and S2p envelopes, respectively, for PEM+PCN prepared at each of the three pH values. In the N1s envelope, three peaks can be resolved. The peak at 402.1, 400.7, and 399.6 eV represent ammonium, amide, and amine groups, respectively. The S2p envelope shows a contribution from the sulfate in HEP or CS, and *N*-sulfonate in HEP (169 eV). There is no S2p signal for the surface coated with only PEMs because the surface contains only CHI and HA. Table S1 in the Appendix A shows the sulfur to nitrogen atom ratio (S/N ratio, calculated from the S2p and N1s envelopes) for the PEM+PCN surfaces formed at each pH value. At each pH, the S/N ratio is higher for samples with HEP-CHI PCNs, than for samples with CS-CHI PCNs. This is consistent with the relative S content of the GAGs (Figure 2.1).

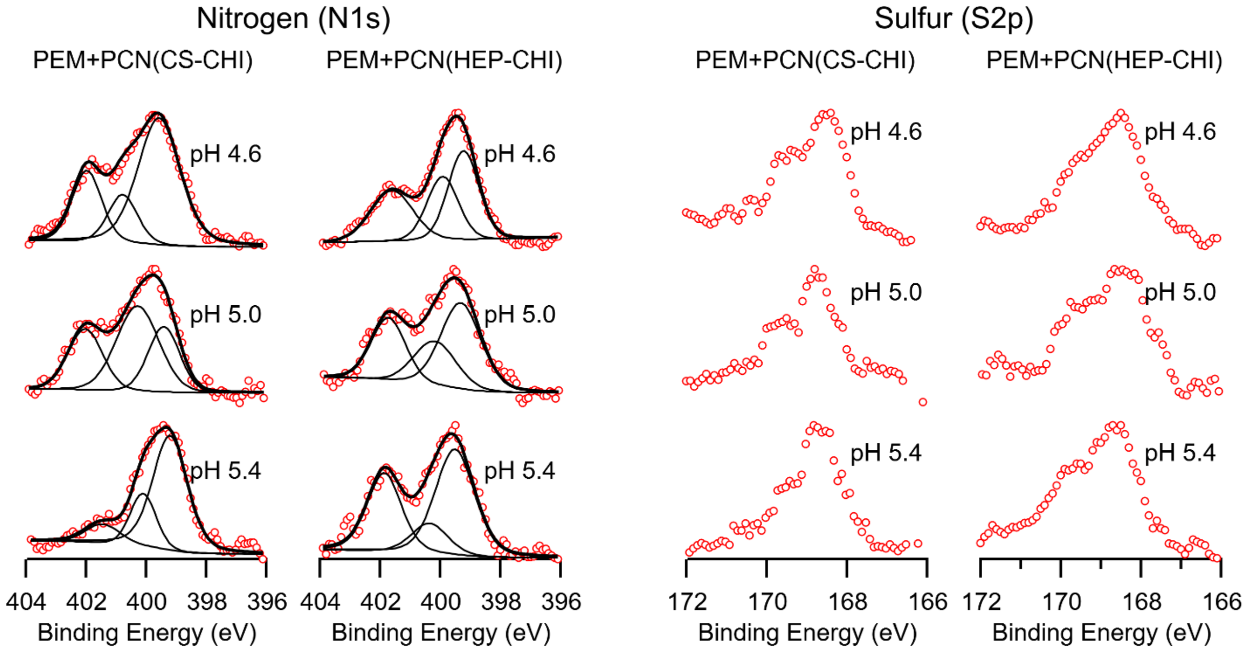

Figure 2.2. N1s envelopes (left) and S2p envelopes (right) for each of the PEM+PCN. Circles correspond to raw data. In the N1s envelope, thick solid line is the sum of the peaks; thin lines corresponds to fitted peaks for amine, amide, and ammonium contributions.

Although the PEM thickness and PCN size are not strongly affected by pH, the chemistry of the PEM+PCN surfaces is influenced by pH. For the PEM+PCN (CS-CHI) samples, there is an increase in the relative amount of ammonium as the pH is reduced. The zeta potential of the PCNs is also reduced when they are formed at lower pH. (Compare to Table 2.1.) Therefore, we can conclude that there is increased ionization of the chitosan, and increased ion pairing at lower pH, for the CS-CHI PCNs. Furthermore, as the pH increases, the relative intensity of the sulfur signal is increased. This is apparent from S/N ratio in Table S1. Therefore, preparation of PEM+PCN at higher pH results in an increase in the surface concentration of the sulfated polysaccharide (CS or HEP).

PEM+PCN surfaces were imaged using TIRF microscopy to confirm adsorption of the rhodamine-labelled nanoparticles. An example of a PEM+PCN (CS-CHI) samples labelled with fluorescein-chitosan in the PEM and rhodamine-chitosan in the PCNs is shown in the Figure S4 in the Appendix A. The PEM has only green fluorescence from the fluorescein-labelled chitosan; whereas the PEM+PCN sample also has punctate red fluorescence, corresponding to rhodamine-labelled PCNs, confirming adsorbed PCNs are present.

2.3.4. Atomic force microscopy (AFM)

AFM is used to evaluate the surface morphology and roughness of the PEM and PEM+PCN surfaces, in both air and liquid. AFM is also used to characterize the mechanical properties of both PEM and PEM+PCN samples. AFM in ScanAsyst mode provides information about both the surface topography, and surface homogeneity. Figure 2.3 shows representative three-dimensional topography images of the surfaces modified with the PEM and with PEM+PCN, assembled at pH 5.0, imaged in both air and PBS, with corresponding in-phase and quadrature channels. Additional AFM topography images of the gold-coated glass, PEM and PEM+PCN samples formed at pH 4.6 and at pH 5.4, acquired in air and PBS are shown in Figure S5, S6, and S7 in the Appendix A.

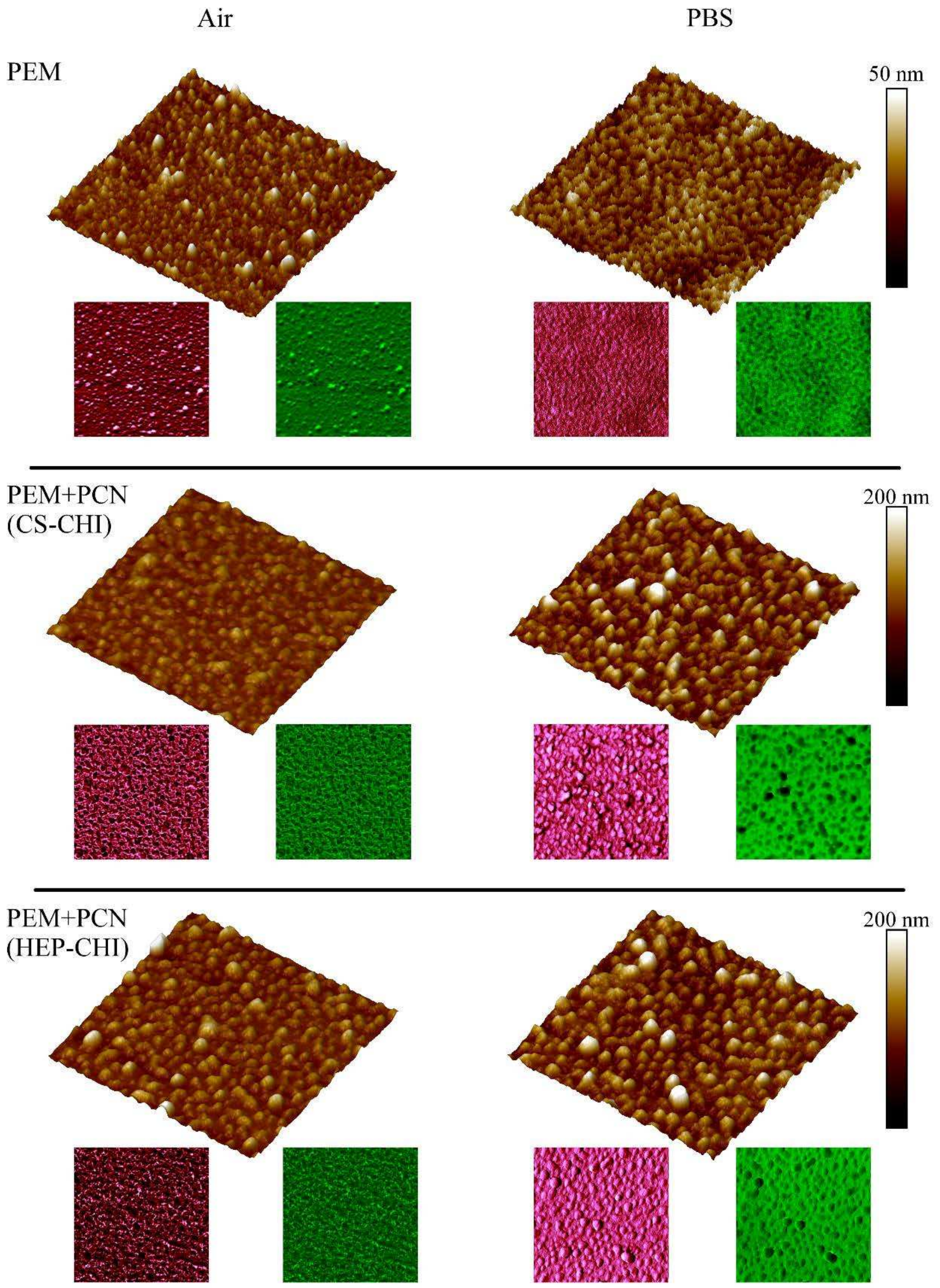

Figure 2.3. Representative 5 µm × 5 µm AFM topographic images acquired using the DNP tip (20 nm radius) taken in air (left) and in PBS (right) for PEM and PEM+PCN assembled at pH 5.0. The corresponding in-phase (magenta) and quadrature (green) channels are shown below each height image. When the PEM is swollen in PBS, the features on the surface are eliminated. The PEM+PCN samples clearly contain 80-200 nm diameter nanoparticles on the surfaces,

corresponding to the PCNs. When these are swollen in PBS, the PCN features swell, and have different properties from the underlying PEM, as is evident by the features in the in-phase and quadrature channels.

When the PEM surface is imaged in air (Figure 2.3 top left) it is dominated by small features, generally less than 100 nm in diameter and less than 30 nm in height. These features are polyelectrolyte complexes that form on the surface during LbL assembly of the PEMs. When the PEM surface is hydrated and imaged in PBS (Figure 2.3 top right), the surface roughness increases, and the features observed in air are no longer distinct. When PEM+PCN surfaces are imaged in air (Figure 2.3 middle and bottom left), the PCNs can be observed, as features that are larger than the features on the PEM surface. The HEP-CHI PCNs are generally over 100 nm in diameter and over 50 nm high. The CS-CHI PCNs are smaller in air than the HEP-CHI PCNs. When imaged in PBS, the PCNs on the PEM+PCN surfaces swell to 200 to 300 nm in diameter and many are 100 to 150 nm high (Figure 2.3 middle and bottom right). These characteristic sizes are similar to the sizes of the PCNs measured by DLS (Table 2.1 and Figure S1). Importantly, these features are similar in size and GAG composition to the "bush-like" features of the glycocalyx shown in Figure 2.1.

The root-mean-square surface roughness, R_q, is used to compare the surface roughness of samples prepared from different pH solutions, and imaged in air and water (Table 2.2). R_q is defined as:

$$R_q = \sqrt{\frac{\sum_i (Z_i - \bar{Z})^2}{N}} \qquad (3)$$

Where Z_i is the distance of the i^{th} the pixel from the mean height, $\bar{Z}$, and N is the number of pixels. The PEM+PCN samples prepared at pH 5.0 have larger feature sizes than those prepared at either pH 4.6 or 5.4, for both types of PCNs.

Table 2.2. Root-mean-square roughness, R_q (nm), for PEM and PEM+PCN samples.

	pH = 4.6		pH = 5.0		pH = 5.4	
Surface	air	PBS	air	PBS	air	PBS
PEM	3 ± 1	6 ± 3	5 ± 2	6 ± 3	4 ± 2	9 ± 3
CS-CHI	9 ± 2	14 ± 3	11 ± 3	25 ± 1	6 ± 2	14 ± 3
HEP-CHI	9 ± 2	18 ± 3	17 ± 3	25 ± 1	10 ± 1	18 ± 5

The in-phase and quadrature channels of the AFM images are compared to the height images for the samples prepared at pH 5.0, in Figure 2.3. Contrast in the in-phase and quadrature channels is characteristic of differences in the sample composition that result in different mechanical properties of the surface features. The height features observed in the PEM imaged in air are not observed when the PEM is imaged in PBS (Figure 2.3 top row). Hydrating the sample causes these features to blend with the rest of the surface, indicating that these features have similar composition to the rest of the surface. However, the PEM+PCN samples have distinct height features both in air and in PBS. Unlike the PEM sample, when the PEM+PCN samples are hydrated in PBS, the height features are enlarged, rather than disappearing (Figure 2.3 middle and bottom row). Furthermore, when hydrated, these features have different surface mechanical properties than the surface on which they are deposited, evidenced by the contrast, particularly in the quadrature channel. We interpret these features as highly hydrated PCNs that present GAG-rich surface features when hydrated similar to the bush-like “tufts” that are described as features of the endothelial glycocalyx (Figure 2.1 and Scheme 2.1) [10–12].

To further investigate the nature of the adsorbed PCNs, AFM in PF-QNM mode is used to measure the mechanical properties of the PCNs and the PEMs in PBS, using a larger radius (65-

nm) tip and with a reduced peak force set point (500 pN) on PEM+PCN(CS-CHI) surfaces. The PF-QNM mode provides high-resolution mapping of the mechanical properties of the surface. These surfaces were prepared at pH 5.0. Figure 2.4 shows the height channel and the log-modulus channel of a PF-QNM micrograph imaged in liquid for both the PEM and the PEM+PCN(CS-CHI).

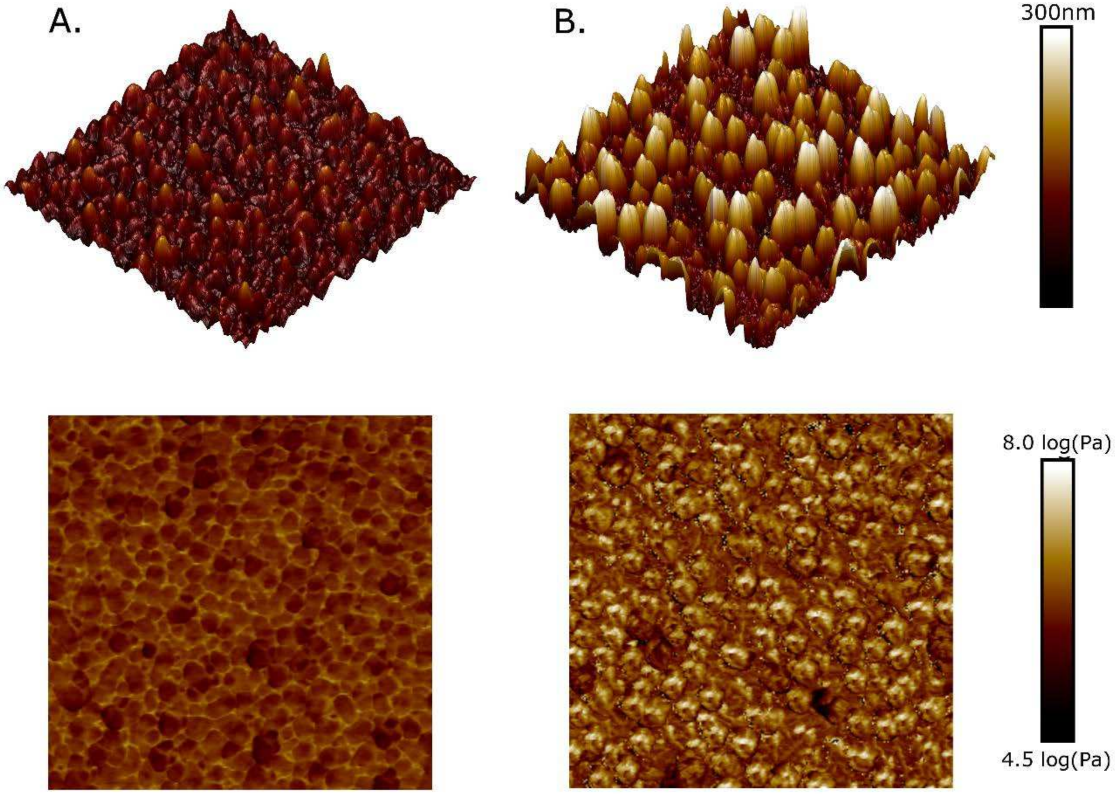

Figure 2.4. Representative 5 μm × 5 μm AFM images acquired in DI water using the PF-QNM tip (65 nm radius, 500 pN peak force), showing the height channel (top) and log-modulus channel (bottom) for (A.) PEM and (B.) PEM + PCN(CS-CHI). The color scales for the height and log modulus channels apply to both images for comparison.

Interestingly, the height features on the PEM correspond to regions of lower Young's modulus, whereas the height features on the PEM+PCN correspond to regions of higher Young's modulus. This further confirms that the proteoglycan-mimetic PCN adsorbed to the PEM have modified the surface structure. Figure 2.5 shows corresponding histograms of the log-modulus channel for the PEM and PEM+PCN(CS-CHI). Figure 2.5 also shows examples of force versus distance data for representative pixels in the PEM (C.) and the PEM+PCN(CS-CHI) (D.) and (E.) samples. In Figure 2.5 (C.) both the extend (blue) and retract (red) curves are shown. Figure 2.5 (D.) and (E.) show representative force curves near the means of the two distributions represented in the histogram (B.). In Figure 2.5 (C.), (D.) and (E.), the modulus is obtained by fitting equation (1) to the retract curve over the region from 30 % to 90 % of the maximum force (solid black line).

The Young's modulus values are compared in Table 2.4. The PEM image has an approximately log-normal distribution of Young's modulus with an average modulus of about 1.51 MPa, and a range from about [0.89 – 2.33] MPa (average ± one standard deviation). In contrast, the PEM+PCN sample does not have a log-normal distribution, but the distribution is fit well by the sum of two log-normal distributions, as shown in Figure 2.5 (B.). We interpret these two distributions as measurements of the PCN modulus, and measurements of the underlying PEM modulus in the spaces between the PCN. The distribution corresponding to the blue curve in Figure 2.5 (B.) has a very similar average and range of modulus as the PEM distribution (Figure 2.5 (A.). The distribution represented by the red curve has a larger mean, 4.24 MPa, and a broader range of [1.16 – 9.54] MPa. This represents the Young's modulus of the adsorbed PCNs (Table 2.3). We also imaged the PEM+PCN(HEP-CHI) surfaces using PF-QNM (not shown), however, the force curves have very high adhesion (greater than 500 pN). While the measured modulus is in a similar range, less than 10 MPa, the very high adhesion force gives us less confidence in the reliability of the model fit to the experimental force versus distance data.

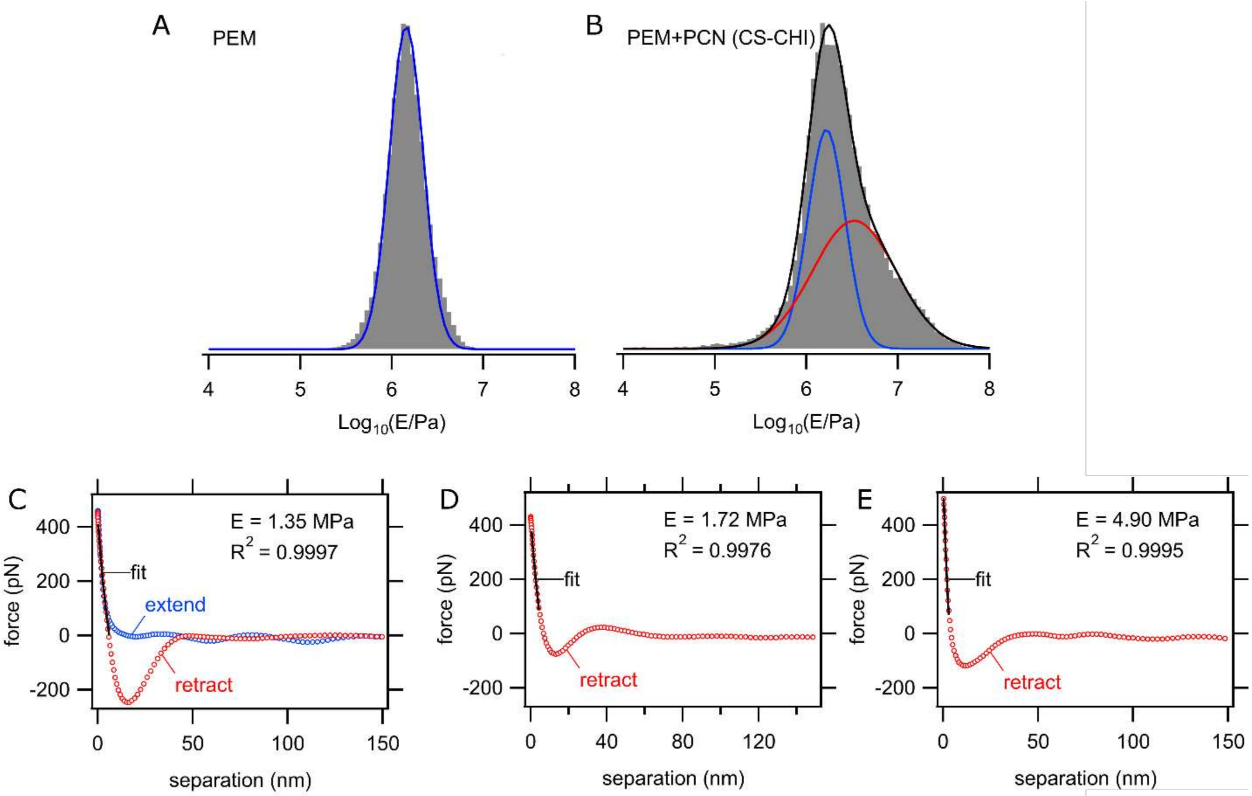

Figure 2.5. Histograms of the log modulus channels shown in Figure 2.4 for the PEM (A.) and PEM+PCN (CS-CHI) (B.). The histogram of the log modulus channel for the PEM (A.) shows that modulus is log-normally distributed (blue curve). The histogram of the log modulus channel for the PEM+PCN (CS-CHI) (B.), is best described by the sum (black curve) of two log-normal distributions (blue and red curves). Examples of force versus distance data for representative pixels in the PEM (C.) and the PEM+PCN (CS-CHI) (D.) and (E.) samples. In (C.) both the extend (blue) and retract (red) curves are shown. (D.) and (E.) show representative force curves near the means of the two distributions represented in the histogram (B.). In (C.), (D.) and (E.), the modulus is obtained by fitting equation (1) to the retract curve over the region from 30 % to 90 % of the maximum force (solid black line).

Table 2.3. Modulus of samples computed using equation (1) and (2).

sample	PEM (blue curves in Figure 2.5) $E_{s,avg}$ (MPa)	 $E_{s,avg} \pm \sigma$ (MPa)	PCN (red curve in Figure 2.5) $E_{s,avg}$ (MPa)	 $E_{s,avg} \pm \sigma$ (MPa)
PEM	1.51	[0.89, 2.33]	-	-
PEM+PCN	1.74	[1.04, 2.64]	4.24	[1.16, 9.54]

2.4. Discussion

In previous work [39], we showed that CHI-HA multilayers, like the ones used here, swell substantially in water, and have relatively weak degree of ion pairing between the carboxylate and amine groups. This may make these PEMs relatively soft. In contrast, CS-CHI and HEP-CHI PEMs demonstrated a higher degree of ion pairing, and reduced swelling. In the present work, we assume that the core of the CS-CHI and HEP-CHI PCNs are characterized by a greater degree of ion pairing, whereas the corona of the non-stoichiometric particles has a large number of residual negatively charged sulfate groups. These bind counterions, increasing the osmotic pressure of the PCNs, as evidenced by their swelling in buffer (Figure 2.3), and causing them to adopt "bush-like" conformation on the surfaces when hydrated (Scheme 2.1). This high osmotic pressure and electrostatic repulsion also makes them more resistant to compression by the AFM tip than the underlying PEM, contributing to the higher observed Young's modulus for the PCN compared to the PEM (Figures 2.4 and 2.5, and Table 2.3).

Recently, Andreeva *et al.* characterized similar CHI-HA PEMs, by AFM and ellipsometry, and also measured albumin adsorption [47]. They showed that using different small molecule ions in the surface preparation modulated the thickness, roughness, hydrophilicity, and Young's modulus [47]. While the Young's modulus measurements made by Andreeva *et al.* on their CHI-

HA PEMs are lower than ours, their samples were characterized using a much smaller radius tip (< 10 nm), by force volume mapping of 10 points on the surface. Here, we demonstrate a method for preparing surfaces with additional heterogeneous surface features, by adsorbing the proteoglycan mimetic PCNs to the PEM surfaces. We also provide a much more detailed measurement of the surface mechanical properties by mapping the modulus and correlating modulus features to the adsorbed PEM and PCNs. These features may more closely mimic the surface organization of proteoglycans in the endothelial glycocalyx found from experimental characterization of real endothelia (Figure 2.1).

The mechanical properties of the endothelial glycocalyx on live cells and tissues has been characterized by AFM [17–19]. In the work by O'Callaghan et al. on endothelial cell cultures and the work by Wiesinger et al. on aorta tissue samples, very large diameter AFM tips (17 or 10 μm) were used to reduce the pressure applied by the AFM probe on the cell membranes. The work by Bai and Wang uses a smaller AFM tip (40 nm diameter), however the AFM images reported are at the length scale of the cell (75 μm × 75 μm). Therefore these previous AFM experiments on cell and tissue samples are not capable of resolving the sub-micron the bush-like structures observed in electron microscopy images (Figure 2.1). In the experiments by Bai and Wang on live endothelial cells, the glycocalyx modulus is obtained from 200-nm indentation depth using a linear mechanical model that includes two moduli, a modulus of the cell and a modulus of the glycocalyx. Experiments were conducted before and after treatment with an enzyme to remove the glycocalyx. They report a modulus for the glycocalyx that is less than 1 kPa, which is far lower than the modulus of our surfaces [17]. Others have used a similar indentation depth with AFM of endothelial cells showing that the measured mechanical properties correspond to intracellular features [48]. O'Callaghan also report much lower modulus of endothelial cell cultures (between

1 and 2 kPa), than what we measure for our surfaces, also using a large indentation depth (> 200 nm) [18]. Indentation experiments with greater than 200 nm depth are also reported by Wiesinger et al. on bovine aorta tissue samples and cultured endothelial cells [19]. These authors do not use a mechanical model to extract modulus from their indentation data. While none of these reports maps the mechanical properties of the cell or tissue at high resolution, these important experiments demonstrate that it is possible in principle to characterize the glycocalyx on live cells using AFM. To compare our results to measurements on live cells, however, further experiments should be done on live cells at higher resolution and under similar imaging conditions (lower indentation depth, higher indentation frequency). Nonetheless the consensus from reports in the literature is that the endothelial surface, including the cells and the glycocalyx, should have an elastic modulus in the range of kPa. While our surfaces may mimic the composition and supermolecular assembly (sub-micron "bush-like" structures) of the glycocalyx, they clearly do not have the same mechanical properties as the endothelial cell surface. As further experiments are reported in the literature to better characterize the mechanical properties of the endothelial glycocalyx at higher resolution, this information can be used to guide the development of glycocalyx mimics, like the surfaces we report here.

The surface reported here have high-GAG composition and sub-micron features that mimic some features of the endothelial glycocalyx. This may make these model surfaces an ideal platform for studying how composition, supermolecular assembly, and nanoscale surface topography can be tuned to make surfaces more blood compatible. However, before these surfaces can be translated to useful applications in blood-contacting materials, their stability at physiological conditions, their behavior under physiological shear rates, and their interactions with blood cells and blood proteins should also be investigated. These future investigations should guide the design of glycocalyx mimetic surfaces with improved blood compatibility.

2.5. Conclusions

In this study, we demonstrate that by combining LbL assembly of PEMs with GAG-rich PCNs, dense polysaccharide-rich surface coatings can be prepared, that have nanoscale features of similar dimensions to those found in the endothelial glycocalyx. AFM imaging in both air and liquid, combined with high-resolution mechanical property mapping by PF-QNM mode imaging in liquid provide details about the structure and topography of these new glycocalyx mimics. When proteoglycan mimetic PCNs are adsorbed to PEMs, the resulting features present dense GAG-rich regions that swell when hydrated, and have higher Young's modulus than the underlying PEM. This surface heterogeneity is likely due to electrostatic repulsion among neighboring PCNs that precludes more complete surface coverage. In the regions where the proteoglycan mimetic PCNs are adsorbed, a dense GAG surface with high osmotic pressure is presented, with height features from 100 to 150 nm high, indicating stretched polymer chains. The resulting surface heterogeneity may mimic the structure and organization of proteoglycans presented in the vascular endothelial glycocalyx. These new surfaces will provide a tunable platform for studying how blood proteins and blood cells interact with polyanionic glycocalyx-like surfaces composed of different GAGs. We propose that these surfaces could provide further insights into how composition and micro/nanostructure of GAG-modified surfaces should be designed to improve the blood compatibility of biomaterials surfaces.

REFERENCES

[1] M. Hedayati, M.J. Kipper, Atomic force microscopy of adsorbed proteoglycan mimetic nanoparticles: Toward new glycocalyx-mimetic model surfaces, Carbohydrate Polymers. 190 (2018) 346–355. doi:10.1016/j.carbpol.2018.02.023.

[2] X. Liu, L. Yuan, D. Li, Z. Tang, Y. Wang, G. Chen, H. Chen, J.L. Brash, Blood compatible materials: state of the art, Journal of Materials Chemistry B. 2 (2014) 5718–5738.

[3] S. Reitsma, D.W. Slaaf, H. Vink, M.A.M.J. van Zandvoort, M.G.A. oude Egbrink, The endothelial glycocalyx: composition, functions, and visualization, Pflügers Archiv - European Journal of Physiology. 454 (2007) 345–359. doi:10.1007/s00424-007-0212-8.

[4] H. Vink, B.R. Duling, Identification of Distinct Luminal Domains for Macromolecules, Erythrocytes, and Leukocytes Within Mammalian Capillaries, Circulation Research. 79 (1996) 581–589. doi:10.1161/01.RES.79.3.581.

[5] B.F. Becker, D. Chappell, D. Bruegger, T. Annecke, M. Jacob, Therapeutic strategies targeting the endothelial glycocalyx: acute deficits, but great potential, Cardiovascular Research. 87 (2010) 300–310. doi:10.1093/cvr/cvq137.

[6] S. Weinbaum, J.M. Tarbell, E.R. Damiano, The Structure and Function of the Endothelial Glycocalyx Layer, Annual Review of Biomedical Engineering. 9 (2007) 121–167. doi:10.1146/annurev.bioeng.9.060906.151959.

[7] H. Ait-Oufella, E. Maury, S. Lehoux, B. Guidet, G. Offenstadt, The endothelium: physiological functions and role in microcirculatory failure during severe sepsis, Intensive Care Med. 36 (2010) 1286–1298. doi:10.1007/s00134-010-1893-6.

[8] R. Larsson, P. Olsson, U. Lindahl, Inhibition of thrombin on surfaces coated with immobilized heparin and heparin-like polysaccharides: A crucial non-thrombogenic principle, Thromb. Res. 19 (1980) 43–54. doi:10.1016/0049-3848(80)90402-8.

[9] C.S. Alphonsus, R.N. Rodseth, The endothelial glycocalyx: a review of the vascular barrier, Anaesthesia. 69 (2014) 777–784. doi:10.1111/anae.12661.

[10] J. Rostgaard, K. Qvortrup, Electron Microscopic Demonstrations of Filamentous Molecular Sieve Plugs in Capillary Fenestrae, Microvascular Research. 53 (1997) 1–13. doi:10.1006/mvre.1996.1987.

[11] S. Weinbaum, X. Zhang, Y. Han, H. Vink, S.C. Cowin, Mechanotransduction and flow across the endothelial glycocalyx, Proceedings of the National Academy of Sciences. 100 (2003) 7988–7995. doi:10.1073/pnas.1332808100.

[12] J.M. Squire, M. Chew, G. Nneji, C. Neal, J. Barry, C. Michel, Quasi-Periodic Substructure in the Microvessel Endothelial Glycocalyx: A Possible Explanation for Molecular Filtering?, Journal of Structural Biology. 136 (2001) 239–255.

[13] R. Satcher, C.F. Dewey, J.H. Hartwig, Mechanical Remodeling of the Endothelial Surface and Actin Cytoskeleton Induced by Fluid Flow, Microcirculation. 4 (1997) 439–453. doi:10.3109/10739689709146808.

[14] E.E. Ebong, F.P. Macaluso, D.C. Spray, J.M. Tarbell, Imaging the Endothelial Glycocalyx In Vitro by Rapid Freezing/Freeze Substitution Transmission Electron Microscopy, Arterioscler. Thromb. Vasc. Biol. 31 (2011) 1908–1915. doi:10.1161/atvbaha.111.225268.

[15] K. Haase, A.E. Pelling, Investigating cell mechanics with atomic force microscopy, Journal of The Royal Society Interface. 12 (2015) 20140970–20140970. doi:10.1098/rsif.2014.0970.

[16] N.L. Pillinger, P. Kam, Endothelial glycocalyx: basic science and clinical implications, Anaesth Intensive Care. 45 (2017) 295–307.

[17] K. Bai, W. Wang, Spatio-temporal development of the endothelial glycocalyx layer and its mechanical property in vitro, J. R. Soc. Interface. 9 (2012) 2290–2298. doi:10.1098/rsif.2011.0901.

[18] R. O'Callaghan, K.M. Job, R.O. Dull, V. Hlady, Stiffness and heterogeneity of the pulmonary endothelial glycocalyx measured by atomic force microscopy, American Journal of Physiology-Lung Cellular and Molecular Physiology. 301 (2011) L353–L360. doi:10.1152/ajplung.00342.2010.

[19] A. Wiesinger, W. Peters, D. Chappell, D. Kentrup, S. Reuter, H. Pavenstädt, H. Oberleithner, P. Kümpers, Nanomechanics of the Endothelial Glycocalyx in Experimental Sepsis, PLoS ONE. 8 (2013) e80905. doi:10.1371/journal.pone.0080905.

[20] S. Boddohi, M.J. Kipper, Engineering Nanoassemblies of Polysaccharides, Advanced Materials. 22 (2010) 2998–3016.

[21] R. Simon-Walker, R. Romero, J.M. Staver, Y. Zang, M.M. Reynolds, K.C. Popat, M.J. Kipper, Glycocalyx-Inspired Nitric Oxide-Releasing Surfaces Reduce Platelet Adhesion and Activation on Titanium, ACS Biomaterials Science & Engineering. (2016). doi:10.1021/acsbiomaterials.6b00572.

[22] X. Ye, H. Wang, J. Zhou, H. Li, J. Liu, Z. Wang, A. Chen, Q. Zhao, The Effect of Heparin-VEGF Multilayer on the Biocompatibility of Decellularized Aortic Valve with Platelet and Endothelial Progenitor Cells, PLoS ONE. 8 (2013) e54622. doi:10.1371/journal.pone.0054622.

[23] X. Ye, X. Hu, H. Wang, J. Liu, Q. Zhao, Polyelectrolyte multilayer film on decellularized porcine aortic valve can reduce the adhesion of blood cells without affecting the growth of human circulating progenitor cells, Acta Biomaterialia. 8 (2012) 1057–1067. doi:10.1016/j.actbio.2011.11.011.

[24] M. Kleinert, N. Rockendorf, T.K. Lindhorst, Glyco-SAMs as glycocalyx mimetics: Synthesis of L-fucose- and D-mannose-terminated building blocks, Eur. J. Org. Chem. (2004) 3931–3940. doi:10.1002/ejoc.200400239.

[25] A.G. Barrientos, J.M. de la Fuente, T.C. Rojas, A. Fernandez, S. Penades, Gold glyconanoparticles: Synthetic polyvalent ligands mimicking glycocalyx-like surfaces as tools for glycobiological studies, Chem.-Eur. J. 9 (2003) 1909–1921. doi:10.1002/chem.200204544.

[26] K. Yu, A.L. Creagh, C.A. Haynes, J.N. Kizhakkedathu, Lectin Interactions on Surface-Grafted Glycostructures: Influence of the Spatial Distribution of Carbohydrates on the Binding Kinetics and Rupture Forces, Anal. Chem. 85 (2013) 7786–7793. doi:10.1021/ac401306b.

[27] K. Godula, M.L. Umbel, D. Rabuka, Z. Botyanszki, C.R. Bertozzi, R. Parthasarathy, Control of the Molecular Orientation of Membrane-Anchored Biomimetic Glycopolymers, J. Am. Chem. Soc. 131 (2009) 10263–10268. doi:10.1021/ja903114g.

[28] K.M. Faucher, X.L. Sun, E.L. Chaikof, Fabrication and characterization of glycocalyx-mimetic surfaces, Langmuir. 19 (2003) 1664–1670. doi:10.1021/la0263864.

[29] K. Yu, B.F.L. Lai, J.N. Kizhakkedathu, Carbohydrate Structure Dependent Hemocompatibility of Biomimetic Functional Polymer Brushes on Surfaces, Adv. Healthc. Mater. 1 (2012) 199–213. doi:10.1002/adhm.201100042.

[30] N.B. Holland, Y.X. Qiu, M. Ruegsegger, R.E. Marchant, Biomimetic engineering of non-adhesive glycocalyx-like surfaces using oligosaccharide surfactant polymers, Nature. 392 (1998) 799–801.

[31] W.T.E. Bosker, K. Patzsch, M.A.C. Stuart, W. Norde, Sweet brushes and dirty proteins, Soft Matter. 3 (2007) 754–762. doi:10.1039/b618259c.

[32] A. Sen Gupta, S. Wang, E. Link, E.H. Anderson, C. Hofmann, J. Lewandowski, K. Kottke-Marchant, R.E. Marchant, Glycocalyx-mimetic dextran-modified poly(vinyl amine) surfactant coating reduces platelet adhesion on medical-grade polycarbonate surface, Biomaterials. 27 (2006) 3084–3095. doi:10.1016/j.biomaterials.2006.01.002.

[33] J. van der Vlist, I. Schonen, K. Loos, Utilization of Glycosyltransferases for the Synthesis of a Densely Packed Hyperbranched Polysaccharide Brush Coating as Artificial Glycocalyx, Biomacromolecules. 12 (2011) 3728–3732. doi:10.1021/bm2009763.

[34] T. Goren, N. Spencer, R. Crockett, Impact of chain morphology on the lubricity of surface-grafted polysaccharides, RSC Advances. 4 (2014) 21497–21503.

[35] S. Boddohi, N. Moore, P.A. Johnson, M.J. Kipper, Polysaccharide-Based Polyelectrolyte Complex Nanoparticles from Chitosan, Heparin, and Hyaluronan, Biomacromolecules. 10 (2009) 1402–1409. doi:10.1021/bm801513e.

[36] L.W. Place, M. Sekyi, M.J. Kipper, Aggrecan-mimetic, glycosaminoglycan-containing nanoparticles for growth factor stabilization and delivery, Biomacromolecules. 15 (2014) 680–689.

[37] F.Z. Volpato, J. Almodovar, K. Erickson, K.C. Popat, C. Migliaresi, M.J. Kipper, Preservation of FGF-2 bioactivity using heparin-based nanoparticles, and their delivery from electrospun chitosan fibers, Acta Biomaterialia. 8 (2012) 1551–1559. doi:10.1016/j.actbio.2011.12.023.

[38] J. Almodóvar, S. Bacon, J. Gogolski, J.D. Kisiday, M.J. Kipper, Polysaccharide-based polyelectrolyte multilayer surface coatings can enhance mesenchymal stem cell response to adsorbed growth factors, Biomacromolecules. 11 (2010) 2629–2639.

[39] J. Almodóvar, L.W. Place, J. Gogolski, K. Erickson, M.J. Kipper, Layer-by-Layer Assembly of Polysaccharide-Based Polyelectrolyte Multilayers: A Spectroscopic Study of Hydrophilicity, Composition, and Ion Pairing, Biomacromolecules. 12 (2011) 2755–2765. doi:10.1021/bm200519y.

[40] S. Boddohi, J. Almodóvar, H. Zhang, P.A. Johnson, M.J. Kipper, Layer-by-layer assembly of polysaccharide-based nanostructured surfaces containing polyelectrolyte complex nanoparticles, Colloids and Surfaces B-Biointerfaces. 77 (2010) 60–68.

[41] S. Boddohi, C.E. Killingsworth, M.J. Kipper, Polyelectrolyte Multilayer Assembly as a Function of pH and Ionic Strength Using the Polysaccharides Chitosan and Heparin, Biomacromolecules. 9 (2008) 2021–2028. doi:10.1021/bm8002573.

[42] J. Borges, J.F. Mano, Molecular Interactions Driving the Layer-by-Layer Assembly of Multilayers, Chemical Reviews. 114 (2014) 8883–8942. doi:10.1021/cr400531v.

[43] J. Almodovar, J. Mower, A. Banerjee, A.K. Sarkar, N.P. Ehrhart, M.J. Kipper, Chitosan-heparin polyelectrolyte multilayers on cortical bone: Periosteum-mimetic, cytophilic, antibacterial coatings, Biotechnology and Bioengineering. 110 (2013) 609–618. doi:10.1002/bit.24710.

[44] C. Lin, R. Romero, L.V. Sorokina, K.R. Ballinger, L.W. Place, M.J. Kipper, S.R. Khetani, A polyelectrolyte multilayer platform for investigating growth factor delivery modes in human liver cultures: HEPATOCYTE-GROWTH FACTOR INTERACTIONS ON CHITOSAN-HEPARIN PEMS, Journal of Biomedical Materials Research Part A. (2017). doi:10.1002/jbm.a.36293.

[45] R. Romero, L. Chubb, J.K. Travers, T.R. Gonzales, N.P. Ehrhart, M.J. Kipper, Coating Cortical Bone Allografts with Periosteum-Mimetic Scaffolds made of Chitosan, Trimethyl Chitosan, and Heparin, Carbohydrate Polymers. 122 (2015) 144–151. doi:10.1016/j.carbpol.2015.01.015.

[46] R. Romero, J.K. Travers, E. Asbury, A. Pennybaker, L. Chubb, R. Rose, N.P. Ehrhart, M.J. Kipper, Combined delivery of FGF-2, TGF-β1, and adipose-derived stem cells from an engineered periosteum to a critical-sized mouse femur defect: COMBINED DELIVERY OF FGF-2, TGF-B1, AND ASCS FROM ENGINEERED PERIOSTEUM, Journal of Biomedical Materials Research Part A. 105 (2017) 900–911. doi:10.1002/jbm.a.35965.

[47] T.D. Andreeva, H. Hartmann, S.G. Taneva, R. Krastev, Regulation of the growth, morphology, mechanical properties and biocompatibility of natural polysaccharide-based multilayers by Hofmeister anions, J. Mater. Chem. B. 4 (2016) 7092–7100. doi:10.1039/C6TB01638C.

[48] K.D. Costa, A.J. Sim, F.C.-P. Yin, Non-Hertzian Approach to Analyzing Mechanical Properties of Endothelial Cells Probed by Atomic Force Microscopy, Journal of Biomechanical Engineering. 128 (2006) 176. doi:10.1115/1.2165690.

CHAPTER 3: PROTEIN ADSORPTION MEASUREMENTS ON LOW FOULING AND ULTRALOW FOULING SURFACES: A CRITICAL COMPARISON OF SURFACE CHARACTERIZATION TECHNIQUES[1]

Overview

Ultralow protein fouling behavior is a common target for new high-performance materials. Ultralow fouling is often defined based on the amount of irreversibly adsorbed protein (< 5 ng cm^{-2}) measured by a surface ensemble averaging method. Protein adsorption at solid interfaces is a dynamic process involving multiple steps, which may include adsorption, desorption, and protein denaturation. In order to better optimize the performance of antifouling surfaces, it is imperative to fully understand how proteins interact with surfaces, including kinetics of adsorption and desorption, conformation, stability, and amount of adsorbed proteins. Defining ultralow fouling surfaces based on a measurement at or near the limit of detection of a surface-averaged measurement may not capture all of this behavior. Single-molecule microscopy techniques can resolve individual protein-surface interactions in high time and space resolution. This information could be used to tune the properties of surfaces to better resist protein adsorption. In this work we demonstrate how combining surface plasmon resonance, X-ray spectroscopy, atomic force microscopy, and single-molecule total internal reflection fluorescence microscopy provides a more complete picture of protein adsorption on ultralow fouling polyelectrolyte multilayer and polymer

---

[1] This work is under review in *Acta Biomaterialia*. M. Hedayati was responsible for designing and conducting experiments, managing data, and preparing the manuscript. D. Marruecos prepared PEG brush surfaces. M.J. Kipper, D. Krapf, and J. Kaar conceived of the research, advised and oversaw the experimental work, and edited the manuscript.

brush surfaces, over different regimes of protein concentration. In this example comparing the surfaces using surface plasmon resonance alone is insufficient to rank their resistance to protein adsorption. However, the combination of surface ensemble averaging and single-molecule microscopy provides a more complete characterization of the protein adsorption phenomena. We propose that the definition of ultralow fouling surfaces based on a single technique should not be considered a gold-standard for qualifying new advanced antifouling materials.

3.1. Introduction

Nonspecific biomolecular adsorption on surfaces is a universal phenomenon that is detrimental to the functionality of materials used in medical implants, medical devices, drug delivery carriers, and biosensors [1]. Therefore, measuring non-specific protein adsorption on surfaces is important for predicting and optimizing material performance in biological applications. Surface ensemble-averaging techniques measure physical or chemical properties averaged over a surface. In controlled experiments, changes in these average properties are attributed to protein adsorption. For example, infrared spectroscopy or X-ray spectroscopy can be used to measure ensemble changes in chemical signatures due to the presence of surfaced adhered proteins [2,3]. Widespread techniques used to measure protein adsorption based on changes in physical properties include surface plasmon resonance (SPR) and quartz crystal microbalance (QCM) [4–8]. SPR and QCM are optical and acoustic sensors, respectively, that are used to quantify the amount of protein adsorption on material surfaces, and to compare and qualify non-fouling surfaces. These techniques rely on measuring a resonant frequency of an electronic (SPR) or acoustic (QCM) oscillation in which physical changes on the surface lead to resonance shift of an evanescent wave propagating from the surface [9,10]. Since these techniques measure a mean property change in both the surface and the nearby solution, they cannot directly distinguish between signal changes due to reversible or irreversible protein adsorption and signal changes due to introduction of the protein to the medium in contact with the sensor surface. For example, SPR can have sensitivity in the range of 10^{-5} - 10^{-6} refractive index units [11]. The refractive index increment of many proteins in solution is between 0.185 and 0.195 mL g^{-1} [12]. Hence the addition of protein to a solution even at concentrations below 0.1 mg mL^{-1} creates a significant background signal, regardless of whether the protein adsorbs to the surface. Therefore, although they are amenable to *in situ* measurements, these techniques also require that the surface (optical or acoustic) properties be compared before and after protein adsorption to quantify the amount adsorbed, resulting in a static measurement of irreversibly adsorbed protein. Vibrational and X-ray spectroscopy are also surface-averaging techniques can be used to directly measure adsorbed proteins, but are not usually conducted *in situ*, and generally have lower limits of detection than QCM or SPR [3].

To rationally design advanced ultralow fouling materials, it may be even more critical to understand the dynamics underlying protein-surface interactions and possible changes in protein conformational at the solution-solid interface. Protein adsorption can result in reversible or irreversible adsorption [13]. Reversibly adsorbed proteins do not permanently modify the surface physical chemistry. Irreversible adsorption, however, is often accompanied by protein unfolding, which can affect the protein's biological function and ultimately modify the surface physical chemistry. The physical ensemble-averaging techniques (SPR and QCM), and complementary chemical spectroscopic techniques cannot provide direct information about the molecular mechanisms of protein adsorption, because they do not permit the direct observation of the interfacial dynamics [14]. In contrast to the surface ensemble-averaged methods, single-molecule microscopy with high signal-to-noise ratio provides unique spatiotemporal information on the dynamic behavior of individual protein molecules [15–19]. Single-molecule total internal reflection fluorescence (TIRF) microscopy can specifically detect and track in real time the interactions of proteins directly with the surface [20–23]. In this technique, fluorescent molecules located near the surface (< 150 nm) or directly in contact with the surface are excited by the evanescent wave of the incident laser. Hence, the background signal of fluorescence from the protein solution is eliminated from outside the focal plane. Furthermore, freely diffusing molecules in solution move too rapidly to be captured by the microscopy. Therefore only surface-immobilized protein molecules are detected. However, the TIRF experiments are so sensitive that they must be conducted at very low protein concentration to enable the single particle detection. On the other hand SPR enables measurement of protein adsorption in real time at physiologically relevant concentrations, without requiring protein labeling. For techniques such as QCM and SPR, the limit of detection is on the order of 0.1 - 2 of ng cm^{-2} [10,23]. Therefore ultralow fouling is often defined based upon a signal at or near the limit of detection of SPR or QCM, or based on lack of detection altogether. In contrast, TIRF microscopy can in theory be used to detect a single protein in a field of view of the microscope, achieving detection limits two to three orders of magnitude lower than what is achievable by QCM and SPR [25]. Furthermore, the detection can be made with both high space and time resolution to provide more detailed information about the dynamics of protein-surface interactions [25].

It has already been widely acknowledged in the literature that experiments using ensemble-averaging techniques may demonstrate ultralow fouling behavior, but that these results often do not predict the effects of long-term protein exposure, or exposure to complex biological media containing multiple proteins. Therefore, they should not be relied upon as the only techniques used for qualifying ultralow fouling surfaces. Here, we propose that a suite of complementary analytical techniques providing a more comprehensive description of protein adsorption should include single-molecule techniques.

In the present study, we combine single-molecule microscopy and ensemble-averaging techniques to study protein adsorption phenomenon on ultralow fouling surfaces. Both *in situ* SPR, and single-molecule TIRF microscopy were performed to measure protein adsorption. Surfaces are also characterized before and after protein adsorption using X-ray photoelectron spectroscopy (XPS) and atomic force microscopy (AFM). These techniques were uniquely combined to analyze the adsorption of two different proteins, bovine serum albumin and fibrinogen, on four well-characterized low fouling or ultralow fouling surfaces: high- and low-grafting density polyethylene glycol (PEG) brush surfaces (PEG_{hg} and PEG_{lg}) and polysaccharide-based polyelectrolyte multilayer (PEM) surfaces with different terminal layers (PEM_{10} and PEM_{11}). We show that SPR alone is not sufficient to characterize the antifouling properties of surfaces, and that combining SPR and single-molecule TIRF microscopy can paint a more complete picture of the protein adsorption at the solution-solid interface.

3.2. Materials and Methods

3.2.1. Materials

α-Methoxy-ω-triethoxy PEG (Mw = 5,000 Da) and α-methoxy-ω-thiol PEG (Mw = 5,000 Da) were purchased from Laysan Bio Inc. and Nanocs respectively. Chitosan (CHI) was purchased from Heppe Medical Chitosan, GmbH (Halle, Germany). Hyaluronic acid (HA) sodium salt (Mw = 743 kDa; PDI = 1.16), bovine serum albumin (BSA), fibrinogen (FIB) from human plasma, thrombin from bovine plasma, 11-mercaptoundecanoic acid (MUA, 95%), sodium acetate, β-mercaptoethanol, catalase from bovine liver, and glucose oxidase were purchased from Sigma

Aldrich. Glacial acetic acid and ethanol (200 proof 99.5+%) were purchased from Acros Organics. BSA conjugated to Alexa Fluor 647 and FIB from human plasma Alexa Fluor 647 conjugate were purchased from Thermo Fisher Scientific (Waltham, MA). Phosphate-buffered saline (PBS) without Ca^{2+} and Mg^{2+} was purchased from Gibco (Grand Island, NY). 18.2 MΩ cm water from a Millipore water purification unit was used for making all aqueous solutions.

3.2.2. Preparation of PEG brush surfaces

Surfaces functionalized with PEG brushes were constructed via a grafting-to approach [27]. The grafting density was changed by changing the solvent quality of the PEG deposition solution. For TIRF microscopy experiments, the underlying substrates were fused silica wafers. Prior to functionalization, the wafers were thoroughly washed with Micro-90 (International Product Corp.), ultrapure water, and piranha solution, followed by a UV/ozone treatment for 30 min. Next, the wafers were immersed in a 1 mM solution of α-methoxy-ω-triethoxy PEG (Mw 5,000 Da) in either 100% acetone (low grafting density PEG brushes) or 50% acetone/50% diethyl ether (high grafting density PEG brushes) for 15 h at 30 °C. The surface grafting reaction was catalyzed by *N*-butylamine at a 1:20 volumetric ratio of the catalyst-to-reaction mixture. Finally, surfaces were rinsed multiple times with acetone and water and dried with ultrapure N_2. For SPR measurements, gold chips were used as the underlying substrate. Prior to functionalization, the chips were rinsed with ethanol and exposed to UV/ozone treatment for 30 min. Next, the surfaces were immersed in a 0.4 mM solution of α-methoxy-ω-thiol PEG (Mw = 5,000 Da) in either 100% acetone (low grafting density) or 100% ethanol (high grafting density) for 1 h at room temperature. Finally, surfaces were thoroughly washed with ethanol and water and dried with ultrapure N_2. All surfaces were prepared in triplicate per condition in separate batches. The high grafting density

PEG sample (PEG_{hg}) on the cover glass had a similar grafting density to the low grafting density PEG sample (PEG_{lg}) on the gold-coated glass.

3.2.3. PEG brush thickness determination

The thickness of the dry brush was measured by ellipsometry using a J.A. Woollam variable angle spectroscopic ellipsometer (model VASE-VB-250). Each surface was spectrally scanned with an incident angle between 60-80°, in increments of 5°, over a range of 500-900 nm. The collected spectra were fit to a three-layer planar model of the solid surface, which accounts for the refractive index of air (n = 1.003), PEG (n = 1.45), silicon oxide layer (n = 1.457), and silicon (n = 3.881). For the gold chips, the silicon oxide layer was replaced by a gold layer (n = 0.1810). The dry PEG brush thickness (h_{dry}) was obtained and subsequently related to grafting density (σ) as $\sigma = \rho_{dry} h_{dry} N_A / M_w$, where ρ_{dry} is the dry density of the PEG monomer repeat unit (1 g/cm^3), N_A is Avogadro's number, and M_w is the average molecular weight of the PEG polymer (5 kDa). Dry thicknesses were measured on triplicate samples for each condition to account for sample variability. Additionally, for each sample, dry thickness was measured on three different spots to account for sample heterogeneity. All nine measurements were included in the determination of the standard deviation of the measured thickness values.

3.2.4. Layer-by-layer surface preparation of PEM

Polysaccharide solutions were prepared in acetate buffer solutions (0.2 M sodium acetate and acetic acid at pH =5.0). Chitosan (1 mg mL^{-1}) and hyaluronan (0.5 mg mL^{-1}) solutions were prepared by stirring for 1 h at room temperature. Solutions were clarified by filtration through 0.22 μm syringe filters for CHI and 0.45 μm syringe filters for HA solution.

Gold-coated glass chips (47 nm gold thickness) were rinsed exhaustively in ethanol, then modified with a self-assembled monolayer of MUA by soaking the gold-coated glass chip in a 1 mM MUA solution in ethanol for 24 h. First, the surface was exposed to an acidified water rinse (pH 4.0, acidified with acetic acid) for 4 minutes. The layer-by-layer process was conducted by immersing MUA-modified surfaces into an aqueous polycation (chitosan) solution (1 mg mL^{-1}) for 6 min rinsing with acidified water for 4 min. Subsequently, polycation modified surfaces were immersed into aqueous polyanion (hyaluronan) solutions (0.5 mg mL^{-1}) for 6 min, followed by acidified water rinse for another 4 min. The cycle was repeated until the desired layer number was reached. For TIRF microscopy experiments, the underlying substrates were fused silica wafers. Cover glasses were first treated with oxygen plasma for 10 min, to ensure a clean, oxidized surface. Then, layer-by-layer adsorption was conducted by exposing the glass surfaces to alternating polycation, rinse, and polyanion solutions, on an orbital shaker similar to the procedure used for the SPR. To confirm that the PEM surfaces prepared on MUA-modified, gold-coated glass are similar to those on cover glasses, examples of elemental composition from XPS and AFM images of the PEM_{11} on both substrates are shown in Table S1 and Figure S1 in the Appendix B.

3.2.5. Protein adsorption by SPR

Fourier Transform Surface Plasmon Resonance (FT-SPR) was used for measuring protein adsorption on the surface of PEMs and PEG brushes as a function of wavenumber using an SPR 100 module on a Thermo 8700 model FT-IR spectrometer (Thermo Electron). The average limit of detection for wavelength changes for the instrument was estimated to be 0.1 nm. A 1 nm SPR wavelength shift is equivalent to a surface coverage of ~ 20 ng cm^{-2} adsorbed proteins. Gold chips coated with PEG or PEM surfaces were mounted to the base of a prism on one side of a flow cell, and optical contact was established between the chip and the prism using a refractive index matching fluid. A Masterflex peristaltic pump was used to pump protein and PBS solutions through the flow cell, in contact with the PEG or PEM surfaces, with a flow rate of 0.1 mL min^{-1}. The interferometer in the FT-IR instrument was used to scan wavelengths at a fixed angle of incidence. In these experiments, FT-SPR was performed using a white light/near-infrared source with a CaF_2 beam splitter at the interferometer and an InGaS detector. Data were collected using Omnic 7.3 software (Thermo Electron), at 8 cm^{-1} resolution from 6000 to 12000 cm^{-1}.

3.2.6. Protein adsorption by XPS

After exposing samples to either PBS or to protein solutions in PBS by SPR, XPS (Physical Electronics 5800 spectrometer) was performed on PEG and PEM surfaces to characterize adsorbed proteins. High resolution spectra were collected for the C1s, N1s, and O1s envelopes using a pass energy of 23.5 eV. Peak fit analysis for high resolution carbon (C1s) peak was performed using the Multipak software. The binding energy scales for the samples were referenced to the C1s peak at 284.8 eV.

3.2.7. Protein adsorption by AFM

After exposing samples to either PBS or protein solutions by SPR, AFM was obtained to observe protein adsorption on PEG and PEM surfaces. The topography scan was performed using a BioScope Resolve BIOAFM (Bruker) with Nanoscope V controller. The measurements were performed under ambient conditions at room temperature in PBS to compare the nanoscale morphology of the surfaces before and after exposure to protein solution. The ScanAsyst mode was used, with a V-shaped silicon nitride cantilever (SNL-10, Bruker, nominal tip radius of 2 nm, spring constant of 0.35 N m^{-1}). For all topographical imaging, the peak force setpoint was selected near 500 pN, and this setting was optimized by the Bruker NanoScope software.

3.2.8. Protein adsorption study by single-molecule microscopy

Individual fluorescently-labeled protein molecules at the solution-solid interface were imaged by total internal reflection fluorescence (TIRF) microscopy to track individual fluorescently labeled protein molecules as they adsorb to and desorb from the solid-liquid interface. Proteins in solution within the total internal reflection range diffuse too quickly to be detected by the camera. The microscope was home-built around an Olympus IX71 body with 638 nm laser line as excitation source (DL638- 328 050, CrystaLaser) [14,28]. A back-illuminated electron-multiplied charge coupled device (EMCCD) camera (Andor iXon DU-888) liquid-cooled to −70 °C, with an electronic gain of 60 was used. An autofocus system (CRISP, Applied Scientific Instrumentation) in combination with a piezoelectric stage was used to maintain constant focus during imaging. To reduce photobleaching, an enzymatic oxygen scavenger system was used in the imaging buffer. Imaging buffer for screening protein adsorption was PBS (pH 7.4), 0.15 mg mL^{-1} glucose oxidase, 34 μg mL^{-1} catalase, 0.8% (w/v) glucose and 1% (v/v) β-mercaptoethanol. Albumin from bovine serum conjugated with Alexa Fluor 647 and fibrinogen from human plasma conjugated with Alexa Fluor 647 were used to observe protein adsorption on different surfaces.

For TIRF experiments, solutions were introduced into a microfluidic flow chamber, which was constructed with #1.5 cover glass (~170 μm thick) modified with the PEG or PEM surfaces. A schematic picture of the flow cell is depicted in Figure S2. The chamber was made by adhering a plastic cover slip to the modified cover glass via a double-sided SecureSeal adhesive sheet 360 μm thick (Grace Bio Labs, Bend, OR, USA). Two parallel rectangular channels of 1.6 mm width each were cut into the adhesive sheet, so that a channel is created. In order to introduce inlets and outlets in the plastic cover, four holes 0.5 mm in diameter were drilled. A plexiglass cover, also with four holes was clamped onto the cover glass sandwich. The holes on each end of the flow channel were connected through 1/32″ outer diameter PEEK tubing (1569, IDEX Health & Science, Middleborough, MA, USA). A Masterflex peristaltic pump was used to pump protein and PBS solutions through the flow channel with a flow rate of 0.1 mL min^{-1}. The surface shear rate profile across the width of the microchannel (x-direction) was calculated based on equation S1 in the Appendix B [29]. A wall shear rate of 50 s^{-1} was used for all the surfaces at $x = 0$.

3.3. Results

3.3.1. Surface characterization

3.3.1.1. PEG surfaces

The resulting grafting density (σ), tether distance of PEG brush surfaces (distance between chains on the surface), and the measured dry brush thickness were determined by ellipsometry (Table 3.1). The average surface roughness was measured by AFM in PBS (Table 3.1). In this study, we used two different PEG brush surfaces on both gold and glass substrates. On each surface, the lower grafting density is referred to as $\mathrm{PEG}_{\mathrm{lg}}$, and the higher grafting density is referred to as $\mathrm{PEG}_{\mathrm{hg}}$. The grafting densities on gold are higher than the grafting densities on glass, with the $\mathrm{PEG}_{\mathrm{lg}}$ on gold having similar grafting density to the $\mathrm{PEG}_{\mathrm{hg}}$ on glass.

Table 3.1. Structural parameters of PEG brush surfaces on both glass and gold. Results are expressed as mean values ± standard deviation (n = 3 different surfaces).

surface	average thickness (nm)	average grafting density (chains nm^{-2})	average tether distance (nm)	average roughness (nm)
$\mathrm{PEG}_{\mathrm{lg}}$ on glass	1.4 ± 0.1	0.16 ± 0.01	2.48 ± 0.08	--

PEG_{hg} on glass	2.9 ± 0.1	0.34 ± 0.01	1.73 ± 0.03	--
PEG_{lg} on gold	2.5 ± 0.2	0.29 ± 0.02	1.86 ± 0.06	1.2 ± 0.2
PEG_{hg} on gold	7.2 ± 0.2	0.83 ± 0.02	1.10 ± 0.01	1.3 ± 0.2

3.3.1.2. PEM surfaces

We previously reported the layer-by-layer assembly of the PEMs (from CHI and HA at pH 5.0) by *in situ* Fourier transform surface plasmon resonance (FT-SPR) on gold-coated glass substrates, modified with a self-assembled monolayer of MUA (Figure S3) [30]. The resulting dry and wet thickness of PEM surfaces, determined by ellipsometry and SPR is shown in Table 3.2. In this study, all the experiments were carried out on gold-coated glass substrates except for the TIRF microscopy experiments, which were performed on cover glass substrates.

Table 3.2. Structural parameters of PEM surfaces. Results are expressed as mean values ± standard deviation (n = 3 different surfaces).

surface	average dry thickness (nm)	average hydrated thickness (nm)	average hydrated roughness (nm)
PEM_{10}	6.4 ± 0.2	15 ± 2	6.3 ± 0.8
PEM_{11}	9 ± 0.8	16.5 ± 2	13 ± 2.2

3.3.2. Protein adsorption study by SPR

SPR was used to quantify the adsorption of protein on PEG and PEM surfaces. Surfaces were exposed to solutions (1 mg mL^{-1}) of albumin or fibrinogen in phosphate-buffered saline (PBS) for 30 min. During the protein adsorption step, the plasmon resonance absorption wavelength, λ_{res}, was monitored, as shown in Figure 3.1. The wavelength is expected to shift due to the difference in refractive index of the PBS with and without protein within the penetration depth of the SPR evanescent field. This change in refractive index arises due to protein adsorption on the surface as well as the refractive index increment of the protein in solution. In all experiments, the SPR signal equilibrated in approximately 10 min. The amount of irreversibly adsorbed protein was quantified as the difference in λ_{res} (i.e., $\Delta\lambda_{res}$) in PBS before and after incubation with protein solution (Table 3.3). On all the surfaces, a positive change was detected in λ_{res} when the surfaces were exposed to protein which means both albumin and fibrinogen were adsorbed on all surfaces. However, for some cases the adsorbed protein desorbed entirely during the subsequent rinse.

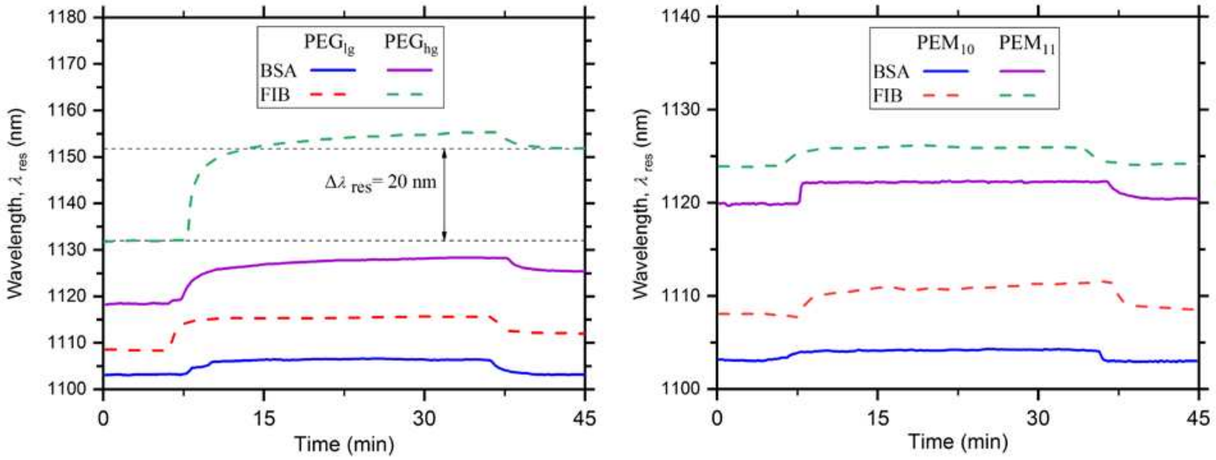

Figure 3.1. Protein adsorption on PEG (left) and PEM (right) surfaces from *in situ* SPR.

Table 3.3. SPR response to nonspecific protein adsorption $\Delta\lambda_{res}$ (nm). Results are expressed as mean values ± standard deviation (n = 3 independent experiments). n.d. indicates not detected.

surface	albumin	fibrinogen
PEG_{lg}	n.d.	4.0 ± 0.5
PEG_{hg}	7.1 ± 0.8	20 ± 1
PEM_{10}	n.d.	1.0 ± 0.2
PEM_{11}	0.5 ± 0.2	n.d.

As shown in Figure 3.1, albumin adsorption on PEG_{lg} is reversible, indicating excellent albumin resistance. However, on PEG_{hg} the signal does not return to the original value upon washing, indicating that some of the albumin adsorption on PEG_{hg} is irreversible, and that the surface is not resistant to albumin adsorption. Fibrinogen has much higher affinity with the PEG_{hg} compared to the PEG_{lg} surface. Both surfaces irreversibly adsorb fibrinogen, although the amount of adsorption for PEG_{hg} is higher than that for PEG_{lg}.

For PEM surfaces, as shown in Figure 3.1 and Table 3.3, the amount of protein that irreversibly adsorbs is much lower than for PEG surfaces. The terminal PEM layer can be chosen to select for resistance to different proteins. PEM_{10} exhibits albumin resistance, as the adsorbed albumin on the surface is completely desorbed during subsequent rinse step. However, PEM_{10} does not completely resist irreversible adsorption of fibrinogen. PEM_{11} has the opposite trend with respect to adsorbing these two proteins. PEM_{11} exhibits reversible fibrinogen adsorption, with no detectable fibrinogen adsorbed following the rinse. However, PEM_{11} does adsorb some albumin irreversibly. Using SPR, we are able to compare the amount of irreversible protein adsorption on different surfaces. SPR results from albumin and fibrinogen interactions with PEG and PEM surfaces indicate that PEM surfaces exhibit better antifouling activity toward protein adsorption.

3.3.3. Protein adsorption by XPS

Protein adsorption on different surfaces was also investigated by XPS. Surfaces exposed to solutions (1 mg mL^{-1}) of albumin or fibrinogen in PBS for 30 min in the SPR study were used to determine how much protein was adsorbed on the surface, following the rinse. To evaluate the accumulation of proteins on surfaces, C1s and N1s high resolution spectra were examined.

XPS high-resolution scans of the C1s envelopes are shown in Figure 3.2, top for PEG surfaces. The strong peak at 286.5 eV corresponds to the C–O bond on both PEG surfaces. Increasing the grafting density results in higher intensity of the C–O peak for PEG_{hg} in comparison to PEG_{lg} surfaces. Analysis of the N1s spectra on PEG surfaces indicates the presence of amino acids in the proteins. The N1s envelope of the PEG_{lg} surface after albumin adsorption shows no detectable nitrogen, indicating no detectable protein adsorption. However, fibrinogen adsorption is observed by XPS on PEG_{lg}. For PEG_{hg} surface, albumin adsorption causes some alteration to the C1s envelope, but no detectable nitrogen is observed in the N1s envelope. Fibrinogen adsorption on PEG_{hg} surface, however, is very obvious in Figure 3.2, top which shows a peak near 288 eV in the C1s spectrum (N–C=O) and a sharp peak near 400 eV in N1s spectrum, due to amide nitrogen from the adsorbed protein. The PEG_{hg} surface adsorbs more fibrinogen than the PEG_{lg} surface.

The high-resolution spectra in the region of the C1s and N1s envelopes for the PEM surfaces before and after exposure to the proteins are shown in Figure 3.2, bottom. Both surfaces show characteristic N1s spectra with the amine and amide group from the polysaccharides, near 400 eV. For the PEM_{11}, a strong ammonium contribution near 402 eV confirms the presence of chitosan as the terminal layer. The C1s spectra for the PEM samples have peaks near 288.2 eV (carboxylic acid), 286.5 (amide and alcohol), and 284.8 (aliphatic). After albumin or fibrinogen adsorption to either PEM_{10} or PEM_{11}, there is a significant change in the relative amount of amide in both the C1s and N1s envelopes. In the case of PEM_{10}, there is no observable ammonium in the unmodified surface, but after exposure to the protein an ammonium peak at 401-402 eV is observed. On the PEM_{11} surface, ammonium is observed on the PEM both before and after protein adsorption, which is consistent with the terminal layer being chitosan. These changes are evidence that both proteins adsorb to each of the PEM surfaces.

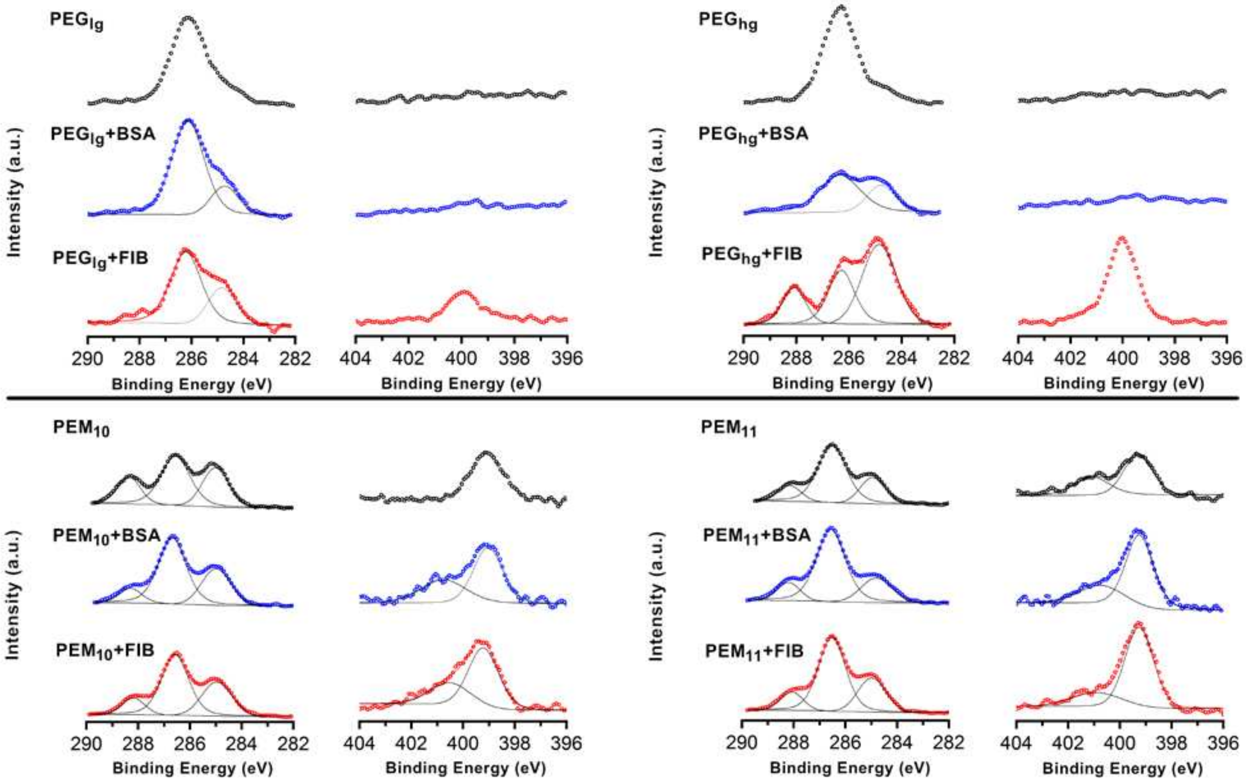

Figure 3.2. High-resolution XPS spectra of C1s and N1s envelopes of PEG (top) and PEM (bottom) surfaces before and after protein adsorption.

3.3.4. Protein adsorption by AFM

Protein adsorption on both PEG and PEM surfaces that were exposed to solutions (1 mg mL^{-1}) of albumin or fibrinogen in PBS for 30 min in the SPR was investigated by AFM (Figure

3.3). AFM images of both PEG surfaces in PBS before and after protein adsorption (Figure 3.3, top) provide information about both the surface topography and surface homogeneity. The average surface roughness for both surfaces before the protein adsorption is provided in Table 3.1. PEG samples represent smooth and homogeneous surfaces when imaged with AFM. Therefore, topographical variation upon exposure to the protein solution could be interpreted as protein adsorption. Albumin adsorption on PEG_{hg} changes the topography of the surface (evidenced by an increase of surface roughness by 1 nm), and this change is more pronounced than on the PEG_{lg} surface (0.6 nm), indicating greater albumin adsorption on the PEG_{hg} surface. Fibrinogen adsorption on the PEG_{lg} can be observed as individual features that lead to a rougher surface (evidenced by an increase of surface roughness by 1.3 nm). For the PEG_{hg}, fibrinogen adsorption leads to substantial topographical changes, with the surface roughness increasing by 1.6 nm, indicating more apparent fibrinogen adsorption on PEG_{hg} than on PEG_{lg}. Assuming that an increase in roughness and height is associated with the amount of protein adsorption, AFM suggests that for both proteins, PEG_{lg} has lower nonspecific protein adsorption than PEG_{hg}.

AFM images of both PEM surfaces in PBS before and after protein adsorption are shown in Figure 3.3, bottom. Surface features from LbL deposition of CHI and HA are apparent, and average surface roughness before protein adsorption is provided in Table 3.2. These surfaces have increased roughness compared to the PEG samples. Moreover, when the PEM surfaces are hydrated, the thickness increases. The PEM_{10} surface shows topographical changes following both albumin and fibrinogen adsorption with surface roughness increasing by 4 and 6 nm, respectively. The PEM_{11} surface is rough prior to the protein adsorption, and the surfaces following protein adsorption have slightly reduced roughness (evidenced by 3 and 2 nm reductions in surface roughness for albumin and fibrinogen, respectively).

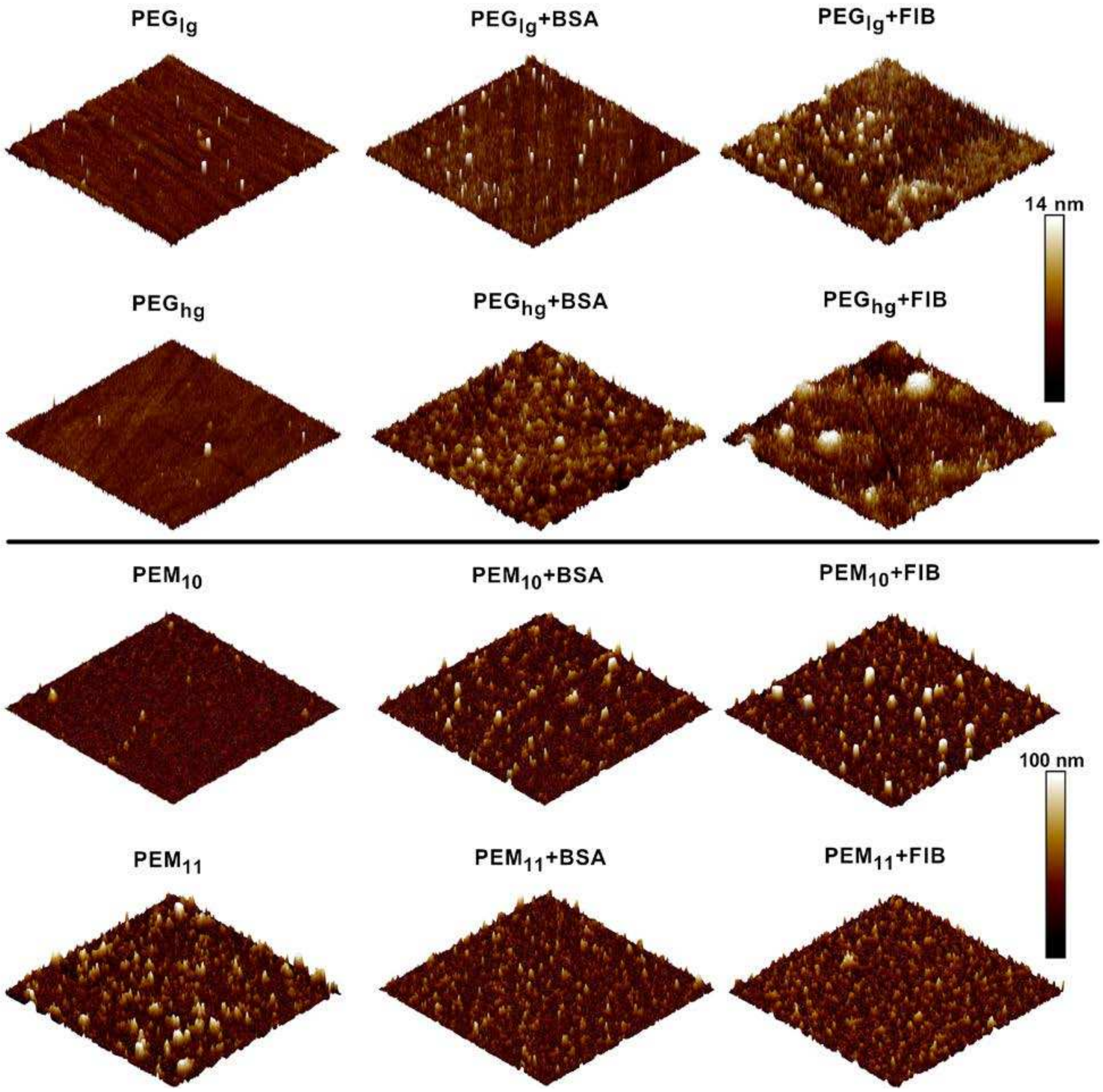

Figure 3.3. Representative 5 μm × 5 μm AFM topographic images of PEG (top) and PEM (bottom) surfaces before and after protein adsorption taken in PBS.

3.3.5. Protein adsorption by TIRF microscopy

Single-molecule adsorption experiments with fluorescently labeled albumin and fibrinogen were also used to evaluate the resistance of each surface to protein adsorption. Labeled proteins were diluted to 10 nM in PBS to enable single-molecule detection. Since the labeled protein was diluted substantially to enable single-molecule detection, two sets of experiments were conducted for each protein-surface pair. In the first experiment only diluted labeled protein was used (10 nM). In the second set of experiments, 10 nM labeled protein was combined with concentrated (1 mg $\mathrm{mL^{-1}}$) non-labeled protein, to match the concentration of protein used in the SPR experiments. The protein-surface interactions were assessed by exposing the surfaces to protein solution under very low shear rate (50 $\mathrm{s^{-1}}$ that corresponds to a flow rate $Q = 0.1\ \mathrm{mL\ min^{-1}}$) in a microfluidic flow channel as described in the Experimental Section and the Appendix B. First, PEG or PEM surfaces were exposed to flowing PBS for 5 min. Then PBS was switched to labeled protein solution and time-lapse imaging was started (0.5 frames $\mathrm{s^{-1}}$). Protein solution was flowed for at least 30 minutes for the PEM surfaces, and at least 40 minutes for the PEG surfaces. The surfaces were then rinsed with PBS at the same shear rate, for at least 20 minutes. Figure 3.4 and Figure 3.5 show microscopy images of PEG and PEM surfaces in contact with the dilute (10 nM) labeled protein solutions at different times.

At the very beginning of these experiments on PEG surfaces, both proteins adsorbed and desorbed, with a low total protein number on the surface. This observation demonstrates that the adsorption of albumin and fibrinogen on PEG are initially reversible. The number of adsorbed protein molecules increases over time eventually reaching a steady-state. The amount of both proteins adsorbed at the beginning of the experiment on the $\mathrm{PEG_{hg}}$ is higher than the amount adsorbed on the $\mathrm{PEG_{lg}}$ surface (evidenced by higher average intensity, Figure 3.4). Following surface rinsing with PBS, most of the protein molecules are removed, indicating that proteins are primarily adsorbed through weak, reversible physical interactions. A minor subpopulation of protein molecules are adsorbed irreversibly through stronger affinity interactions with the surface.

These irreversibly adsorbed molecules do not leave the surface, even after the rinsing step. This phenomenon could be the result of the aggregation of denatured protein molecules, which presumably may be retained on the surface irreversibly.

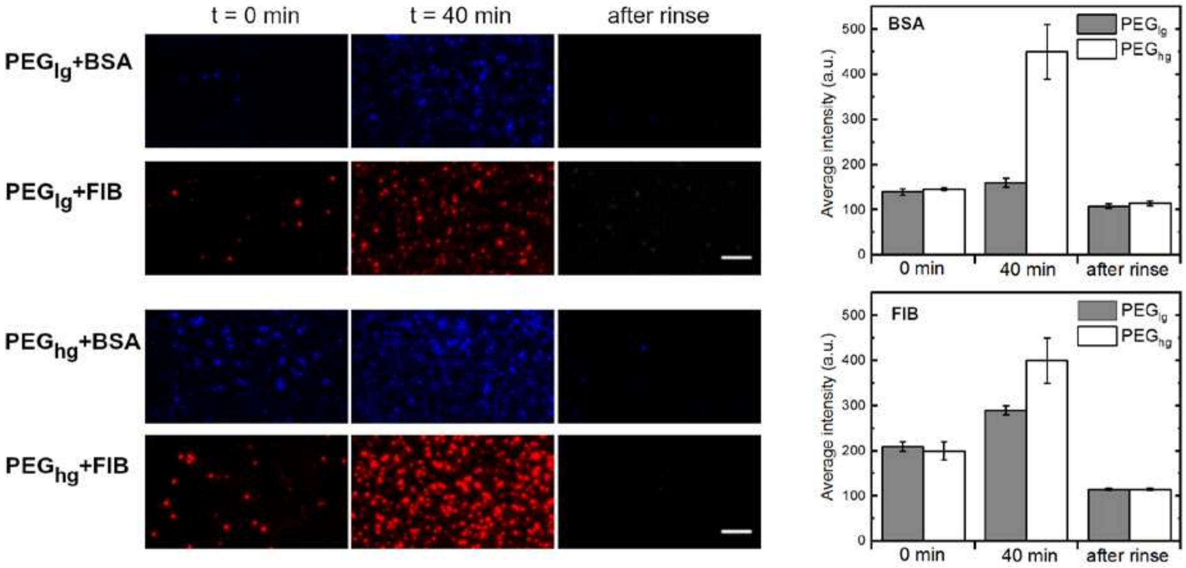

Figure 3.4. Representative TIRF micrographs during protein adsorption experiments on PEG surfaces (left). Scale bar = 5 μm. Average intensity of fluorescently labeled protein in the TIRF microscopy images (right). The error bars represent standard deviations (*n* = 3 independent experiments for each condition).

To better compare the results from single-molecule microscopy and SPR experiments, TIRF microscopy was also conducted with the same concentration of protein used in the SPR study. Both albumin and fibrinogen were mixed at a final concentrations of 1 mg mL^{-1} with labeled protein at a final concentration of 10 nM in PBS. The results, which are shown in Figure S4, are strikingly different from what we observe with low protein concentration. The experiments were conducted for two hours. During this time, individual labeled proteins were observed to interact dynamically with the surface, but these events are rare, and the molecules persist for only a few frames (corresponding to less than 1 minute dwell time). Even after two hours of continuous exposure to the concentrated protein solution, no irreversibly adsorbed molecules were observed on PEG surfaces, in any of the three replicates for both proteins on both PEG_{lg} and PEG_{hg}. This could be the result of higher diffusive flux of proteins to the surface at higher protein concentration in the solution. It has previously been proposed that when the local concentration of proteins at or near the surface is high, there is competition for surface sites, leading to crowding, which effectively reduces the ability of proteins to denature [31,32]. As the protein conformation is stabilized and denaturation is blocked by crowding, the protein has higher rates of reversible adsorption and desorption [32]. This crowding effect is apparent for both proteins on both PEG surfaces.

For PEM surfaces, very different results are observed in the TRIF microscopy. When low protein concentration (10 nM) is used, both PEM surfaces adsorb albumin and fibrinogen very fast at the very beginning of the experiment as shown in Figure 3.5. Albumin adsorption, however, is primarily irreversible for both PEM surfaces; after rinsing albumin molecules are still observed to adhere to the surface with high affinity (evidenced by approximately 6 times higher average intensity compared to the beginning of the experiment, Figure 3.5). This may arise due to albumin denaturing on the surface, leading to irreversible protein-surface interactions. Fibrinogen adsorption is more reversible on PEM surfaces than albumin adsorption. Nonetheless a fraction of the fibrinogen is irreversibly adsorbed.

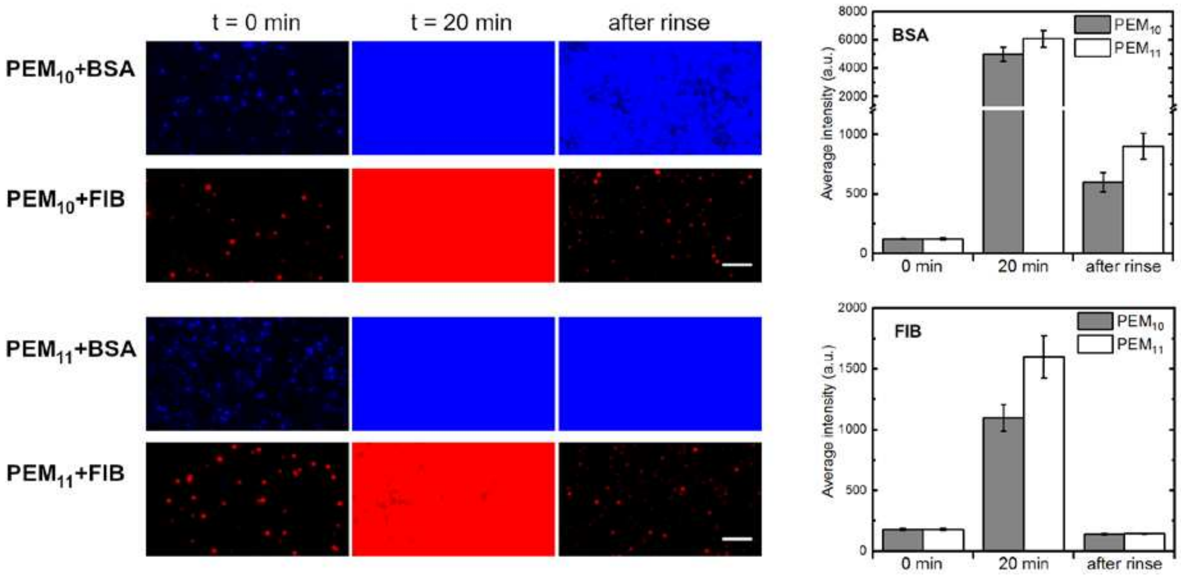

Figure 3.5. Representative TIRF micrographs during protein adsorption experiments on PEM surfaces (left). Scale bar = 5 μm. Average intensity of fluorescently labeled protein in the TIRF microscopy images (right). The error bars represent standard deviations (*n* = 3 independent experiments for each condition).

At high protein concentration (1 mg mL^{-1} unlabeled protein mixed with 10 nM labeled protein), the observed albumin interactions with the surface are similar to the observations made at low protein concentration, as shown in Figure S4. The crowding effect observed at high protein concentration on the PEG surfaces was not observed on the PEM surfaces. Therefore, albumin has very high affinity for the PEM surfaces, and even at high concentration, albumin molecules are able to adsorb and denature on the surface. Fibrinogen interaction at high concentration with PEM surfaces is different from the albumin interaction. At high concentration, the crowding effect is more obvious, as fewer labeled fibrinogen molecules adsorb to the surfaces (in comparison to the low concentration experiment) and a fraction of them desorb during the subsequent rinse step.

The kinetics of protein adsorption was quantified on both PEG and PEM surfaces with 10 nM concentration for both proteins. The measured adsorption rate coefficient, k_{ads}, is defined as the number of newly adsorbed molecules per second per μm^2, normalized to the concentration of the protein in the bulk solution. This adsorption rate coefficient is based on tracking at least 10^4 protein molecules on the surface, starting from t = 0 (when the protein solution is first introduced to the surface). When protein solution was flowed over the surface, the rate of adsorption was found to increase over time. As a result, the reported adsorption rate coefficient in Figure 3.6 is in a non-equilibrium state. For the PEG surfaces, the albumin adsorption rate is more than two times higher on PEG_{hg} than on PEG_{lg}. For fibrinogen, however, the adsorption rate is similar on PEG_{hg} and PEG_{lg}. Remarkably, for the PEM surfaces, the albumin adsorption rate increased approximately 6 times compared to the PEG_{lg} and 3 times compared to the PEG_{hg}. The fibrinogen adsorption rate was also higher for the PEM surfaces compared to the PEG surfaces.

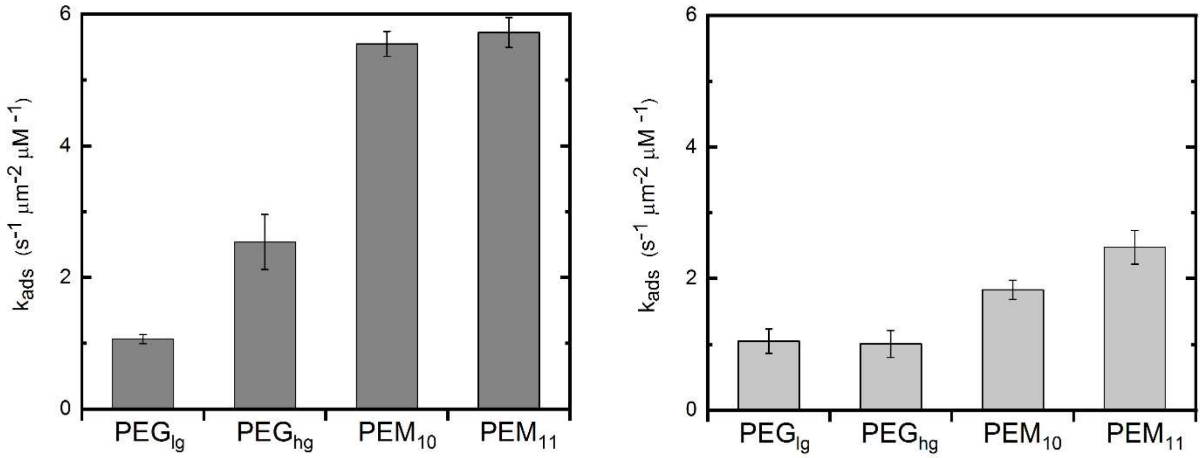

Figure 3.6. Average adsorption rate coefficients of albumin (left) and fibrinogen (right) under continuous flow (50 s^{-1} shear rate) on PEG and PEM surfaces. Error bars represent the standard deviation (*n* = 3, independent experiments for each condition).

Single-molecule results from albumin and fibrinogen interactions with PEG and PEM surfaces indicate that, at both low and high protein concentrations, PEG surfaces demonstrate better resistance to protein adsorption than the PEM. At high concentration (1 mg mL^{-1}), we did not observe any adsorption of labeled protein, even after 2 h of exposure of PEG surfaces to protein solutions. However, at low protein concentration, protein adsorption is observed on PEG surfaces, and this adsorbed protein is removed from the surface upon rinsing. PEM surfaces show much higher affinity for both proteins at both low and high concentrations, which indicates that these surfaces were not resistant to protein adsorption. The PEM surfaces adsorb much less fibrinogen than albumin at high protein concentration.

3.4. Discussion

When artificial materials are introduced into complex biological media such as blood, nonspecific protein adsorption is the first surface-mediated event impacting later biological processes [33]. This nonspecific protein adsorption determines the subsequent series of interactions that can lead to surface biofouling and device failure [34,35]. Thus, a significant amount of research effort has been invested in developing low fouling and ultralow fouling surfaces.

Understanding the nature of protein-surface interactions beyond measuring the amount of adsorbed protein may be critical to developing advanced ultralow fouling and non-fouling surfaces. Many reports have developed surfaces that strongly reduce protein adsorption. Zwitterionic and PEG interfaces are among gold standard biofouling resistant surfaces [36–40]. Layer-by-Layer assembly of PEM surfaces by alternating deposition of a polycation and a polyanion, is another popular surface functionalization method that has been used to reduce biofouling [41–45]. Even small amounts of irreversibly adsorbed protein on low fouling surfaces may permanently modify the nature of the material and cause subsequent significant adverse biological responses. Therefore, it is necessary to use very high-sensitivity techniques, such as single-molecule TIRF microscopy, to understand the mechanisms of protein interactions with materials to better characterize very small amounts of protein adsorption [24].

In this study, we used four different well-characterized surfaces and protein adsorption phenomena were investigated using ensemble-averaging and single-molecule methods. SPR and single-molecule TIRF microscopy can both be used *in situ* to sensitively detect protein adsorption on model synthetic surfaces. SPR can be conducted at physiologically relevant protein concentrations, but it is not sensitive enough to detect very rare protein adsorption events. The sensitivity of SPR requires > 0.1 ng cm^{-2} of protein adsorbed. In contrast, single-molecule TIRF microscopy can provide much more detail about individual protein surface interactions, but must be conducted at much lower protein concentration. The two techniques provide complementary information about protein-surface interactions at two very different concentration regimes.

At the concentrations used for SPR, the PEM surfaces studied here have resistance to nonspecific irreversible protein adsorption that is superior to both PEG surfaces, for both proteins. However, our single-molecule TIRF microscopy results at very low protein concentration tell a different story. The rate of protein adsorption to the PEG surfaces is lower than the rate of protein adsorption on either of the PEM surfaces. More interestingly, we observe a lower rate of albumin adsorption for the $\mathrm{PEG_{lg}}$ surface compared to the $\mathrm{PEG_{hg}}$ surface. In contrast, the rate of fibrinogen adsorption was similar on both PEG surfaces. This is evidence that individual proteins interact differently from one another, and that a single-protein assay may not be generalized to other protein behaviors on synthetic surfaces.

XPS and AFM experiments can sensitively discern changes in the surface chemistry and topography, respectively, only when there is not background interference from the surface of interest. These techniques provide limited information about the proteins adsorbed to the PEG and PEM surfaces. Fibrinogen adsorption on both PEG and PEM surfaces can be observed with XPS. For albumin, the XPS confirms surface chemistry changes on the PEMs, but does not show any conclusive evidence of adsorption on PEG. AFM images also provide qualitative information regarding both protein adsorption from changes of the surface topography and roughness on PEG surfaces. On PEM surfaces, roughness increases after protein adsorption on PEM_{10}, but decreases after protein adsorption on PEM_{11}. The high roughness of the original surfaces would make the use of AFM alone difficult for quantifying protein adsorption on PEM surfaces.

3.5. Conclusions

The use of ensemble averaging methods that measure a physical or optical change, averaged over a surface, have been widely proliferated for measuring protein adsorption on low fouling and ultralow fouling surfaces. These methods are common enough that ultralow fouling has come to be understood as a quality of a surface that adsorbs protein below a particular threshold in such experiments. When designing low fouling and ultralow fouling surfaces, we propose that results challenging the limits of detection of the commonly used techniques (e.g. SPR) should not be used as a benchmark to qualify such surfaces. Our experiments show that PEM surfaces, which would qualify as ultralow fouling by this criterion, do not completely prevent protein adsorption, as observed using single-molecule TIRF microscopy. Furthermore, extremely sensitive surface spectroscopy and atomic force microscopy may also be inconclusive. In contrast, PEG surfaces, which do irreversibly adsorb measureable amounts of protein by SPR, exhibit adsorption/desorption steady-state in dilute single-molecule measurements. At high protein concentration, the single-molecule TIRF microscopy results suggest that proteins may be stabilized by a crowding effect on PEG surfaces. As a complement to surface ensemble averaging techniques, single-molecule microscopy is capable of sensitively detecting individual protein adsorption events, in both concentrated and very dilute protein solutions. In the case of dilute protein experiments, single-molecule microscopy enables measurement of the protein adsorption rate, which cannot be directly obtained from SPR. Furthermore, both adsorption and desorption events can be precisely quantified using single-molecule methods, provided that the labeled protein is at sufficiently low concentrations. A more detailed description of protein-surface interactions enabled by single-molecule microscopy should lead to improved design of fouling-resistant surfaces.

REFERENCES

[1] M. Hedayati, M.J. Neufeld, M.M. Reynolds, M.J. Kipper, The quest for blood-compatible materials: Recent advances and future technologies, Materials Science and Engineering: R: Reports. 138 (2019) 118–152. doi:10.1016/j.mser.2019.06.002.

[2] E.A. Vogler, Protein adsorption in three dimensions, Biomaterials. 33 (2012) 1201–1237. doi:10.1016/j.biomaterials.2011.10.059.

[3] E. Migliorini, M. Weidenhaupt, C. Picart, Practical guide to characterize biomolecule adsorption on solid surfaces (Review), Biointerphases. 13 (2018) 06D303. doi:10.1116/1.5045122.

[4] S. Morsbach, G. Gonella, V. Mailänder, S. Wegner, S. Wu, T. Weidner, R. Berger, K. Koynov, D. Vollmer, N. Encinas, S.L. Kuan, T. Bereau, K. Kremer, T. Weil, M. Bonn, H.-J. Butt, K. Landfester, Engineering Proteins at Interfaces: From Complementary Characterization to Material Surfaces with Designed Functions, Angewandte Chemie International Edition. 57 (2018) 12626–12648. doi:10.1002/anie.201712448.

[5] C. Rodriguez Emmenegger, E. Brynda, T. Riedel, Z. Sedlakova, M. Houska, A.B. Alles, Interaction of Blood Plasma with Antifouling Surfaces, Langmuir. 25 (2009) 6328–6333. doi:10.1021/la900083s.

[6] P. Roach, D. Farrar, C.C. Perry, Interpretation of Protein Adsorption: Surface-Induced Conformational Changes, Journal of the American Chemical Society. 127 (2005) 8168–8173. doi:10.1021/ja042898o.

[7] F. Höök, B. Kasemo, T. Nylander, C. Fant, K. Sott, H. Elwing, Variations in Coupled Water, Viscoelastic Properties, and Film Thickness of a Mefp-1 Protein Film during Adsorption and Cross-Linking: A Quartz Crystal Microbalance with Dissipation Monitoring, Ellipsometry, and Surface Plasmon Resonance Study, Analytical Chemistry. 73 (2001) 5796–5804. doi:10.1021/ac0106501.

[8] S. Boujday, C. Méthivier, B. Beccard, C.-M. Pradier, Innovative surface characterization techniques applied to immunosensor elaboration and test: Comparing the efficiency of Fourier transform–surface plasmon resonance, quartz crystal microbalance with dissipation measurements, and polarization modulation–reflection absorption infrared spectroscopy, Analytical Biochemistry. 387 (2009) 194–201. doi:10.1016/j.ab.2009.01.031.

[9] S.S. Hinman, K.S. McKeating, Q. Cheng, Surface Plasmon Resonance: Material and Interface Design for Universal Accessibility, Analytical Chemistry. 90 (2018) 19–39. doi:10.1021/acs.analchem.7b04251.

[10] B. Liu, X. Liu, S. Shi, R. Huang, R. Su, W. Qi, Z. He, Design and mechanisms of antifouling materials for surface plasmon resonance sensors, Acta Biomaterialia. 40 (2016) 100–118. doi:10.1016/j.actbio.2016.02.035.

[11] J. Homola, Surface Plasmon Resonance Sensors for Detection of Chemical and Biological Species, Chemical Reviews. 108 (2008) 462–493. doi:10.1021/cr068107d.

[12] H. Zhao, P.H. Brown, P. Schuck, On the Distribution of Protein Refractive Index Increments, Biophysical Journal. 100 (2011) 2309–2317. doi:10.1016/j.bpj.2011.03.004.

[13] M. Rabe, D. Verdes, S. Seeger, Understanding protein adsorption phenomena at solid surfaces, Advances in Colloid and Interface Science. 162 (2011) 87–106. doi:10.1016/j.cis.2010.12.007.

[14] M. Hedayati, M.M. Reynolds, D. Krapf, M.J. Kipper, Nanostructured Surfaces That Mimic the Vascular Endothelial Glycocalyx Reduce Blood Protein Adsorption and Prevent Fibrin Network Formation, ACS Applied Materials & Interfaces. 10 (2018) 31892–31902. doi:10.1021/acsami.8b09435.

[15] W.E. Moerner, Y. Shechtman, Q. Wang, Single-molecule spectroscopy and imaging over the decades, Faraday Discussions. 184 (2015) 9–36. doi:10.1039/C5FD00149H.

[16] H. Coceancigh, D.A. Higgins, T. Ito, Optical Microscopic Techniques for Synthetic Polymer Characterization, Analytical Chemistry. 91 (2019) 405–424. doi:10.1021/acs.analchem.8b04694.

[17] D. Wang, H. Wu, D.K. Schwartz, Three-Dimensional Tracking of Interfacial Hopping Diffusion, Physical Review Letters. 119 (2017). doi:10.1103/PhysRevLett.119.268001.

[18] C. Manzo, M.F. Garcia-Parajo, A review of progress in single particle tracking: from methods to biophysical insights, Reports on Progress in Physics. 78 (2015) 124601. doi:10.1088/0034-4885/78/12/124601.

[19] L. Ma, Y. Cai, Y. Li, J. Jiao, Z. Wu, B. O'Shaughnessy, P. De Camilli, E. Karatekin, Y. Zhang, Single-molecule force spectroscopy of protein-membrane interactions, ELife. 6 (2017) e30493. doi:10.7554/eLife.30493.

[20] M.J. Skaug, J. Mabry, D.K. Schwartz, Intermittent Molecular Hopping at the Solid-Liquid Interface, Physical Review Letters. 110 (2013). doi:10.1103/PhysRevLett.110.256101.

[21] D. Krapf, G. Campagnola, K. Nepal, O.B. Peersen, Strange kinetics of bulk-mediated diffusion on lipid bilayers, Physical Chemistry Chemical Physics. 18 (2016) 12633–12641. doi:10.1039/C6CP00937A.

[22] G. Campagnola, K. Nepal, B.W. Schroder, O.B. Peersen, D. Krapf, Superdiffusive motion of membrane-targeting C2 domains, Scientific Reports. 5 (2015). doi:10.1038/srep17721.

[23] J.D. Knight, J.J. Falke, Single-Molecule Fluorescence Studies of a PH Domain: New Insights into the Membrane Docking Reaction, Biophysical Journal. 96 (2009) 566–582. doi:10.1016/j.bpj.2008.10.020.

[24] Y. Luan, D. Li, T. Wei, M. Wang, Z. Tang, J.L. Brash, H. Chen, "Hearing Loss" in QCM Measurement of Protein Adsorption to Protein Resistant Polymer Brush Layers, Analytical Chemistry. 89 (2017) 4184–4191. doi:10.1021/acs.analchem.7b00198.

[25] J.Y. Ryu, I.T. Song, K.H.A. Lau, P.B. Messersmith, T.-Y. Yoon, H. Lee, New Antifouling Platform Characterized by Single-Molecule Imaging, ACS Applied Materials & Interfaces. 6 (2014) 3553–3558. doi:10.1021/am4057387.

[26] H. Shen, L.J. Tauzin, R. Baiyasi, W. Wang, N. Moringo, B. Shuang, C.F. Landes, Single Particle Tracking: From Theory to Biophysical Applications, Chemical Reviews. 117 (2017) 7331–7376. doi:10.1021/acs.chemrev.6b00815.

[27] D. Faulón Marruecos, M. Kastantin, D.K. Schwartz, J.L. Kaar, Dense Poly(ethylene glycol) Brushes Reduce Adsorption and Stabilize the Unfolded Conformation of Fibronectin, Biomacromolecules. 17 (2016) 1017–1025. doi:10.1021/acs.biomac.5b01657.

[28] A.V. Weigel, B. Simon, M.M. Tamkun, D. Krapf, Ergodic and nonergodic processes coexist in the plasma membrane as observed by single-molecule tracking, Proceedings of the National Academy of Sciences. 108 (2011) 6438–6443. doi:10.1073/pnas.1016325108.

[29] R.R. Hansen, A.R. Wufsus, S.T. Barton, A.A. Onasoga, R.M. Johnson-Paben, K.B. Neeves, High Content Evaluation of Shear Dependent Platelet Function in a Microfluidic Flow Assay, Annals of Biomedical Engineering. 41 (2013) 250–262. doi:10.1007/s10439-012-0658-5.

[30] M. Hedayati, M.J. Kipper, Atomic force microscopy of adsorbed proteoglycan mimetic nanoparticles: Toward new glycocalyx-mimetic model surfaces, Carbohydrate Polymers. 190 (2018) 346–355. doi:10.1016/j.carbpol.2018.02.023.

[31] K.A. Wilson, C.A. Finch, P. Anderson, F. Vollmer, J.J. Hickman, Combining an optical resonance biosensor with enzyme activity kinetics to understand protein adsorption and denaturation, Biomaterials. 38 (2015) 86–96. doi:10.1016/j.biomaterials.2014.10.002.

[32] J. Kim, Mathematical modeling approaches to describe the dynamics of protein adsorption at solid interfaces, Colloids and Surfaces B: Biointerfaces. 162 (2018) 370–379. doi:10.1016/j.colsurfb.2017.12.006.

[33] Q. Wei, T. Becherer, S. Angioletti-Uberti, J. Dzubiella, C. Wischke, A.T. Neffe, A. Lendlein, M. Ballauff, R. Haag, Protein Interactions with Polymer Coatings and Biomaterials, Angewandte Chemie International Edition. 53 (2014) 8004–8031. doi:10.1002/anie.201400546.

[34] Z. Othman, B. Cillero Pastor, S. van Rijt, P. Habibovic, Understanding interactions between biomaterials and biological systems using proteomics, Biomaterials. 167 (2018) 191–204. doi:10.1016/j.biomaterials.2018.03.020.

[35] L. Yang, L. Han, Q. Liu, Y. Xu, L. Jia, Galloyl groups-regulated fibrinogen conformation: Understanding antiplatelet adhesion on tannic acid coating, Acta Biomaterialia. 64 (2017) 187–199. doi:10.1016/j.actbio.2017.09.034.

[36] W.-L. Chen, R. Cordero, H. Tran, C.K. Ober, *50th Anniversary Perspective* : Polymer Brushes: Novel Surfaces for Future Materials, Macromolecules. 50 (2017) 4089–4113. doi:10.1021/acs.macromol.7b00450.

[37] C. Zhang, J. Yuan, J. Lu, Y. Hou, W. Xiong, H. Lu, From neutral to zwitterionic poly(α-amino acid) nonfouling surfaces: Effects of helical conformation and anchoring orientation, Biomaterials. 178 (2018) 728–737. doi:10.1016/j.biomaterials.2018.01.052.

[38] C.-M. Xing, F.-N. Meng, M. Quan, K. Ding, Y. Dang, Y.-K. Gong, Quantitative fabrication, performance optimization and comparison of PEG and zwitterionic polymer antifouling coatings, Acta Biomaterialia. 59 (2017) 129–138. doi:10.1016/j.actbio.2017.06.034.

[39] B.L. Leigh, E. Cheng, L. Xu, A. Derk, M.R. Hansen, C.A. Guymon, Antifouling Photograftable Zwitterionic Coatings on PDMS Substrates, Langmuir. (2018). doi:10.1021/acs.langmuir.8b00838.

[40] X. Lin, P. Jain, K. Wu, D. Hong, H.-C. Hung, M.B. O'Kelly, B. Li, P. Zhang, Z. Yuan, S. Jiang, Ultralow Fouling and Functionalizable Surface Chemistry Based on Zwitterionic Carboxybetaine Random Copolymers, Langmuir. (2018). doi:10.1021/acs.langmuir.8b02540.

[41] Y. Wei, H.-C. Hung, F. Sun, T. Bai, P. Zhang, A.K. Nowinski, S. Jiang, Achieving low-fouling surfaces with oppositely charged polysaccharides via LBL assembly, Acta Biomaterialia. 40 (2016) 16–22. doi:10.1016/j.actbio.2016.04.013.

[42] P.-F. Ren, H.-C. Yang, H.-Q. Liang, X.-L. Xu, L.-S. Wan, Z.-K. Xu, Highly Stable, Protein-Resistant Surfaces via the Layer-by-Layer Assembly of Poly(sulfobetaine methacrylate) and Tannic Acid, Langmuir. 31 (2015) 5851–5858. doi:10.1021/acs.langmuir.5b00920.

[43] S. Guo, X. Zhu, M. Li, L. Shi, J.L.T. Ong, D. Jańczewski, K.G. Neoh, Parallel Control over Surface Charge and Wettability Using Polyelectrolyte Architecture: Effect on Protein Adsorption and Cell Adhesion, ACS Applied Materials & Interfaces. 8 (2016) 30552–30563. doi:10.1021/acsami.6b09481.

[44] X. Zhu, D. Jańczewski, S. Guo, S.S.C. Lee, F.J. Parra Velandia, S.L.-M. Teo, T. He, S.R. Puniredd, G.J. Vancso, Polyion Multilayers with Precise Surface Charge Control for Antifouling, ACS Applied Materials & Interfaces. 7 (2015) 852–861. doi:10.1021/am507371a.

[45] A. Barrantes, J. Wengenroth, T. Arnebrant, H.J. Haugen, Poly- l -lysine/heparin multilayer coatings prevent blood protein adsorption, Journal of Colloid and Interface Science. 485 (2017) 288–295. doi:10.1016/j.jcis.2016.09.046.

Chapter 4: NANOSTRUCTURED SURFACES THAT MIMIC THE VASCULAR ENDOTHELIAL GLYCOCALYX REDUCE BLOOD PROTEIN ADSORPTION AND PREVENT FIBRIN NETWORK FORMATION[1]

Overview

Blood-contacting materials are critical in many applications where long-term performance is desired. However, there are currently no engineered materials used in cardiovascular implants and devices that completely prevent clotting when in long-term contact with whole blood. The most common approach to developing next-generation blood-compatible materials is to design surface chemistries and structures that reduce or eliminate protein adsorption to prevent blood clotting. This work proposes a new paradigm for controlling protein-surface interactions by strategically mimicking key features of the glycocalyx lining the interior surfaces of blood vessels: negatively charged glycosaminoglycans organized into a polymer brush with nanoscale domains. The interactions of two important proteins from blood (albumin and fibrinogen) with these new glycocalyx mimics are revealed in detail using surface plasmon resonance and single-molecule microscopy. Surface plasmon resonance shows that these blood proteins interact reversibly with the glycocalyx mimics, but have no irreversible adsorption above the limit of detection. Single-molecule microscopy is used to compare albumin and fibrinogen interactions on surfaces with and without glycocalyx-mimetic nanostructures. Microscopy videos reveal a new mechanism whereby

---

[1] This work was published in *ACS Applied Materials & Interfaces* and is reproduced in modified form here with permission [1]. M. Hedayati was responsible for designing and conducting experiments, managing data, and preparing the manuscript. M.J. Kipper, D. Krapf, and M.M. Reynolds conceived of the research, advised and oversaw the experimental work, and edited the manuscript.

the glycocalyx-mimetic nanostructures eliminate the formation of fibrin networks on the surfaces. This approach shows for the first time that the nanoscale structure and organization of glycosaminoglycans in the glycocalyx are essential to (i) reduce protein adsorption, (ii) reversibly bind fibrin(ogen), and (iii) inhibit fibrin network formation on surfaces. The insights gained from this work suggest new design principles for blood-compatible surfaces. New surfaces developed using these design principles could reduce risk of catastrophic failures of blood-contacting medical devices.

4.1. Introduction

Clotting on blood-contacting medical devices is a persistent problem, leading to catastrophic failure of cardiovascular implants and extracorporeal blood circulation devices [2]. This necessitates antiplatelet and antithrombogenic therapies for patients with devices like stents, heart valves, and shunts, and those undergoing hemodialysis and membrane oxygenation [3]. The interior surface of healthy blood vessels is the only known surface that continuously prevents blood clotting while in constant contact with flowing whole blood [4,5].

When a biomaterial comes into contact with blood it rapidly becomes covered with a layer of nonspecifically adsorbed proteins. This protein layer mediates the subsequent platelet adhesion, activation, and aggregation; blood coagulation is initiated and fibrinogen is converted to fibrin monomers. These monomers subsequently polymerize into protofibrils, and eventually form a crosslinked network of fibrin fibers. The resulting fibrin network supports platelet aggregates and traps red cells in a thrombus, or blood clot. Protein adsorption from blood is recognized as the first key event leading to surface-induced blood clotting. Consequently, new blood-contacting materials are developed with a focus on the protein adsorption behavior at the surface [4,6].

The surface of blood vessels prevents blood clotting by several mechanisms. Importantly, this surface stabilizes plasma proteins and acts as a barrier that blocks proteins from reaching the endothelium [7,8]. The endothelial cells lining this surface present a layer, the endothelial glycocalyx, which is rich in proteoglycans bearing glycosaminoglycan side chains (GAGs) [7,8]. These cells expend energy to organize the membrane-bound proteoglycans in the glycocalyx, containing strong polyanionic GAGs, into nanoscale "bush-like" structures, 100-200 nm in diameter [9,10]. These macromolecular assemblies are organized by the underlying actin cortical cytoskeleton into domains with 100-200 nm spacing [9,10]. We recently proposed a new method for preparing surfaces that mimic these structural features of the endothelial glycocalyx, and elucidated how the preparation conditions affect the resulting structure [11]. In this work we show that the nanoscale structure of these new surfaces suppresses non-specific protein adsorption. Most importantly, these surfaces inhibit the formation of a fibrin network, by preventing both surface-mediated polymerization and adsorption of fibrin fibers from solution.

Heparan sulfate, chondroitin sulfate, and hyaluronan are the dominant GAGs found in the vascular endothelial glycocalyx. The current gold standard for preventing blood from clotting on surfaces of medical devices such as blood tubing, catheters, and other blood-contacting biomaterials, is to coat the surface with the GAG heparin (closely related to heparan sulfate) [12]. Over 40 years ago, Olsson and co-workers began investigating the interactions of blood components with heparinized surfaces. They showed that heparinized surfaces could reduce platelet adhesion [13,14]. Surface-bound heparin can also inhibit thrombosis by potentiating the activity of antithrombin III and platelet factor 4 [13–18]. Others have shown that heparinized surfaces may reduce fibrinogen adsorption, and alter the adsorption of other blood proteins [19]. This has led to the extensive use of heparinized surfaces to improve blood compatibility of blood-contacting devices, such as dialysis membranes, venous implants, arterial shunts, microfluidic channels, vascular grafts, and arterial stents [20–30]. More recent approaches have included synthetic chemistries and superhydrophobic surfaces with nanoscale structures to prevent blood protein adsorption [2,12,31–37].

Despite these advances, the challenges of blood clotting on biomedical material surfaces remains, in part because the mechanisms regulating blood clotting in blood-surface interactions are not completely understood [12]. We propose that by mimicking the supermolecular assembly of GAGs in the endothelial glycocalyx, we can design surfaces that reveal how blood proteins interact with the glycocalyx, and how these interactions prevent clotting. Materials that prevent blood clotting would improve outcomes and reduce risks for patients using extracorporeal blood circuits and for patients receiving cardiovascular implants.

The supermolecular assembly of highly sulfated, strong polyanions, such as heparin and chondroitin sulfate, into polymer brushes or the dense bush-like structures of the endothelial glycocalyx is energetically unfavorable due to electrostatic repulsion. We developed a technique to mimic these features on a surface and to overcome the electrostatic repulsion by polyelectrolyte complexation of polyanions with polycations, keeping the polyanions in excess [11]. We prepared polyelectrolyte multilayers (PEMs) from hyaluronan (a polyanionic GAG) and chitosan (a structurally similar, but polycationic polysaccharide) (Scheme 1). Adjusting the pH, molarity, number of layers, and chemistry of the terminal layer can enable fine control over the PEM composition, thickness, and physical chemistry [38,39]. We also formed polyelectrolyte complex nanoparticles (PCNs) containing heparin (HEP) or chondroitin sulfate (CS) as the polyanion, and chitosan (CHI) as the polycation (Scheme 1). When the polyanion was in excess, these particles formed with a collapsed core of neutralized charges, surrounded by a corona of pendent excess polyanion chains (Scheme 1). The size, zeta potential and composition of these PCNs can be tuned by altering the charge mixing ratio of the constituent polysaccharides [40,41]. We then adsorbed CS-CHI and HEP-CHI PCNs to the PEMs to form PEM+PCN surfaces [11,42]. As we have recently reported, these PEM+PCN surfaces have 100-200 nm hemispherical bush-like domains presenting a high density of HEP or CS glycosaminoglycan chains, which mimic nanostructures in the endothelial glycocalyx [11]. In this previous work we determined how the pH of the adsorption process affects the PCN coverage on 13-layer PEMs.

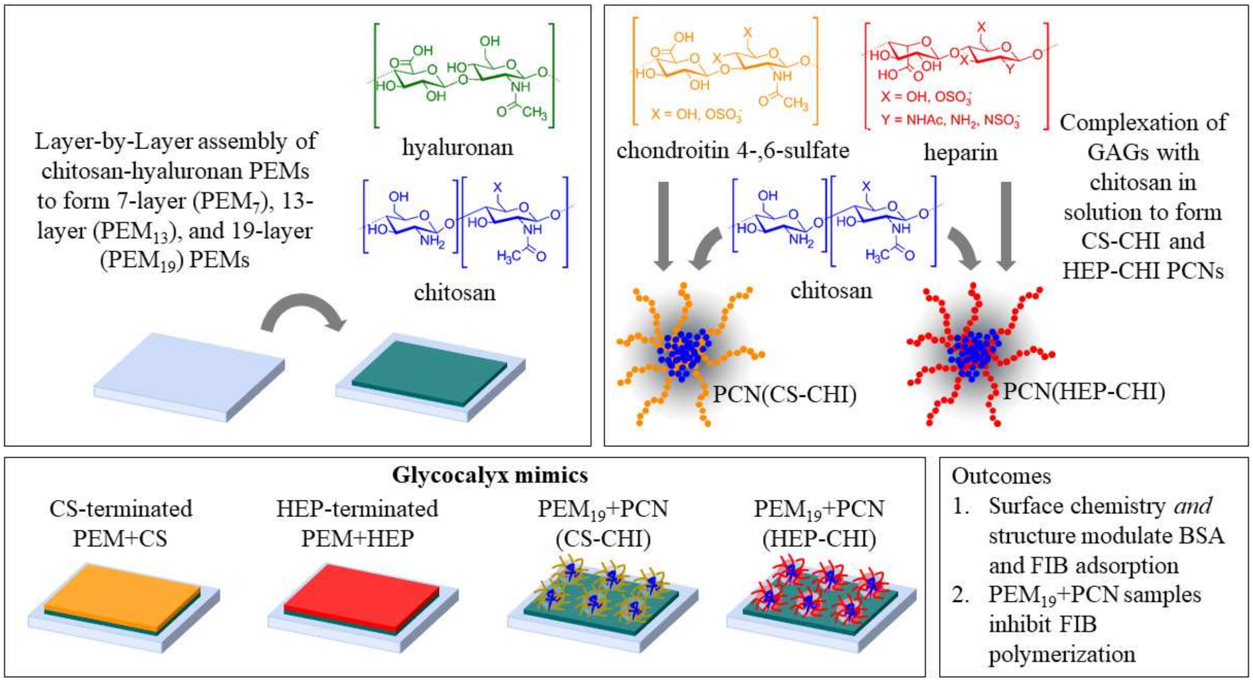

Scheme 4.1. Preparation of glycocalyx mimics from GAG-terminated PEMs and from PEMs combined with GAG-containing PCNs.

The outlined PEM+PCN strategy provides a new glycocalyx mimetic surface from which the effects of nanostructure on protein adsorption can be elucidated. In this work we study in detail the interactions of specific blood proteins with these glycocalyx mimics. We hypothesize that these new PEM+PCN surfaces can reduce the adsorption of two important blood proteins, serum albumin (BSA) and fibrinogen (FIB), and that fibrin fiber network formation is modulated by the

GAG-rich bush-like structures. Albumin is the most abundant protein in blood. It is amphiphilic, and its adsorption to surfaces has been promoted as a strategy for preventing platelet adhesion, since it does not contain adhesive peptide sequences. However, Latour *et al.* demonstrated that when albumin denatures beyond a critical degree on a surface it can promote platelet adhesion, which could lead to thrombosis [43]. Fibrinogen, a glycoprotein from blood plasma, is activated by the enzyme thrombin to form fibrin, which polymerizes to form fibers that stabilize blood clots [44–46]. Fibrin adsorption and polymerization can also be affected by surface chemistry and the orientation of the adsorbed proteins [45,47]. Therefore, controlling the specific interactions of albumin and fibrinogen with a surface may be more effective than attempting to prevent the protein adsorption altogether. To the best of our knowledge, we show for the first time that the structure of the PCNs on a surface inhibits the adsorption and formation of fibrin fibers on a surface, a key step in blood clot formation, even in the absence of the important inhibitor of fibrin polymerization, antithrombin III. This is a new mechanism of preventing blood clotting. Furthermore, these new surfaces serve as useful models for studying the structure-function relationships of the nanoscale features of the endothelial glycocalyx, and provide a new strategy for designing blood-contacting materials.

4.2. Experimental section

4.2.1. Materials

Chitosan (CHI) was purchased from MP Biomedicals. Chondroitin sulfate sodium (CS) salt (from shark cartilage, 6% sulfur, 6-sulfate/4-sulfate = 1.24, Mw =84.3 kDa; PDI = 1.94), hyaluronic acid (HA) sodium salt (Mw = 743 kDa; PDI = 1.16), bovine serum albumin (BSA), fibrinogen from human plasma (FIB), thrombin from bovine plasma, 11-mercaptoundecanoic acid

95% (MUA), sodium acetate, β-mercaptoethanol, catalase from bovine liver, and glucose oxidase, were purchased from Sigma Aldrich. Heparin sodium (HEP) (from porcine intestinal mucosa, 12.5% sulfur) was purchased from Celsus Laboratories (Cincinnati, OH). Glacial acetic acid and ethanol (200 proof 99.5+ %) were purchased from Acros Organics (Geel, Belgium). BSA conjugated to Alexa Fluor 647 and FIB from human plasma Alexa Fluor 647 conjugate were purchased from Thermo Fisher Scientific (Waltham, MA). Phosphate-buffered saline without Ca^{2+} and Mg^{2+} (PBS) was purchased from Gibco (Grand Island, NY). A Millipore water purification unit was used to obtain 18.2 MΩ cm water, used for making all aqueous solutions (Millipore, Billerica, MA).

4.2.2. PCN Preparation and Characterization

PCNs formed from chitosan and GAGs were made as previously described [40–42,48]. Briefly, chitosan, heparin sodium, and chondroitin sulfate solutions were prepared at concentrations of 1, 1.5, and 2.8 mg mL^{-1}, respectively, in acetate buffer solutions (0.2 M sodium acetate and acetic acid at pH 5.0). Solutions were filtered using 0.22-μm syringe filters. To prepare chondroitin sulfate-based PCNs (CS-CHI) the chondroitin sulfate solution was added to the stirring chitosan solution in a 6:1 volume ratio (36 mL of chondroitin sulfate solution to 6 mL of chitosan solution). To prepare heparin-based PCNs (HEP-CHI), the heparin solution was added to the stirring chitosan solution in a 4:1 volume ratio of heparin solution to a chitosan solution (24 mL heparin solution to 6 mL chitosan solution). The mixtures were stirred for 3 h at 1100 rpm. After 3 hours of stirring, all solutions were allowed to settle overnight to remove aggregated particles. After settling, the supernatant was decanted, containing the colloidally stable nanoparticles. The aggregated particles were discarded. DLS confirmed that CS-CHI nanoparticles have a reliable polydispersity index and do not require further separation. The HEP-CHI solution was centrifuged at 3000 × *g* for 5 min to separate the particles from uncomplexed polymer, using an Eppendorf 5804 centrifuge. A Zetasizer Nano ZS (Malvern) was used to analyze hydrodynamic diameter using a 633 nm laser. All measurements were performed at a fixed angle of 175° at 25 °C. All measurements were performed in 0.2 M acetate buffer solution. Three measurements were made on each of three separate samples for each composition. The mean ± standard deviation are reported for the hydrodynamic diameter.

4.2.3. Layer-by-Layer Surface Modification and Protein Adsorption by SPR

Polysaccharide solutions were prepared in similar acetate buffer solutions as those used for the PCN preparation (0.2 M sodium acetate and acetic acid at 5.0). This pH was selected based on our previous work [11]. Chitosan (1.33 mg mL^{-1}) and hyaluronan (0.66 mg mL^{-1}) solutions were prepared by stirring for 2 h at room temperature. Solutions were clarified by filtration through 0.22 μm syringe filters for CHI and 0.45 μm syringe filters for HA solution.

Fourier transform surface plasmon resonance (FT-SPR) was used for measuring the intensity of *p*-polarized light reflected from the back side of the gold film on which the samples were assembled, as a function of wavenumber, as we have described previously, using an SPR 100 module on a Thermo 8700 model FT-IR spectrometer (Thermo Electron) [39,49,50]. Briefly, gold-coated SF-10 glass chips (47 nm gold thickness, NanoSPR LLC, Chicago, IL) were rinsed exhaustively in ethanol, then modified with a self-assembled monolayer of MUA by soaking the gold-coated glass chip in a 1 mM MUA solution in ethanol for at least 20 h. The MUA-modified surfaces were dried with a gentle stream of dry nitrogen. MUA-modified chips were mounted to the base of a prism on one side of a flow cell, and optical contact was established between the chip and the prism using a refractive index matching fluid. A Masterflex peristaltic pump was used to pump polysaccharide and rinse solutions through the flow cell, in contact with the MUA-coated surface, with a flow rate of 0.5 mL min^{-1}. A low flow rate was used to ensure laminar flow over the gold chip surface. The interferometer in the FT-IR instrument was used to scan wavelengths at a fixed angle of incidence. In these experiments, FT-SPR was performed using a white light/near-infrared source with a CaF_2 beam splitter at the interferometer and an InGaS detector. Data were collected using Omnic 7.3 software (Thermo Electron), at 8 cm^{-1} resolution from 6000 to 12000 cm^{-1}. PEMs were constructed with CHI as the polycation and HA as the polyanion at pH 5.0 in the solutions described above. First, the surface was exposed to an acidified water rinse (pH 4.0, acidified with acetic acid), for six minutes. The layer-by-layer process was conducted by alternatively flowing solutions through the flow cell in the following sequence: polycation (CHI), rinse, polyanion (HA), rinse. The sequence was repeated until a seven-layer, 13-layer, or 19-layer PEM (terminating with CHI) had been adsorbed. PEM+PCN samples were prepared similarly. After the layer-by-layer assembly of 19-layer CHI-HA PEMs, either CS-CHI PCNs or HEP-CHI PCNs were adsorbed. The resulting samples are referred to as PEM_{19}+PCN(CS-CHI) and PEM_{19}+PCN(HEP-CHI). The length of the adsorption steps was doubled to 12 minutes for the PCN adsorption, followed by a final acidified water rinse. The layer-by-layer process was monitored by detecting the change in the plasmon resonance absorption wavenumber, caused by adsorption of each layer. Here the resonance peak position in wavenumber in converted to wavelength, λ_{res}. The thickness of these PEM and PEM_{19}+PCN samples is well within the range of sensitivity of the SPR, evidenced by changes in λ_{res} when the rinse solution is changed.

Once the PEM and PEM_{19}+PCN samples were prepared, protein adsorption was also monitored by FT-SPR. Each sample was exposed to PBS for 40 minutes to equilibrate the surface with the ions in the buffer solution. The experiment was continued by replacing the PBS buffer with 0.75 mg mL^{-1} BSA or FIB solution (approximately 12 μM for BSA and 3.5 μM for FIB) in

PBS for 30 minutes. During protein adsorption the plasmon resonance absorption wavelength shifts due to the difference in refractive index of the medium at the sensor surface, within the penetration depth of the SPR evanescent wave. This change in refractive index arises due to both protein deposition on the gold surface and due to the refractive index increment of the protein in solution. After reaching a steady-state value of λ_{res}, BSA or FIB solution was replaced with PBS. The amount of irreversibly adsorbed BSA and FIB was quantified as the difference in λ_{res} measured in PBS before and after incubation with BSA or FIB solution. This difference is the $\Delta\lambda_{res}$. The average limit of quantitation (LOQ) for our instrument was estimated to be 0.1 nm, which corresponds to approximately 20 pg of deposit per mm^2.

4.2.4. AFM Measurements in PeakForce QNM Mode

The PeakForce QNM AFM study was done using a BioScope Resolve BIOAFM (Bruker) with Nanoscope V controller. The measurements were performed under ambient conditions at room temperature in deionized water to characterize the morphology and the mechanical properties of the sample at the nanoscale. The calibrated probe PF-QNM-LC-CAL with a tip radius of 65 nm was used, and deflection sensitivity was measured against a hard surface. The scan size was typically 5 × 5 μm^2, with a digital resolution of 512 px × 512 px and a scanning rate of 0.5 Hz (lines per second). The oscillation frequency of the probe was set to 1 kHz, and the peak force set point was 500 pN. For every experiment, three measurements on three different samples were acquired. Image analysis was performed using NanoScope Analysis (version 1.8).

To enable imaging of PEM and PEM$_{19}$+PCN samples by AFM in liquid, samples were prepared on glass-bottom petri dishes (30 mm Pelco petri dishes, Willco Wells, Amsterdam) and mounted on the AFM stage. Petri dishes were first treated with oxygen plasma for 10 minutes, to ensure a clean, oxidized surface. Then layer-by-layer adsorption was conducted by exposing the glass surfaces to alternating polycation, rinse, and polyanion solutions, on an orbital shaker. The surfaces prepared on glass bottom petri dishes were prepared using a similar procedure as that used for the FT-SPR, listed above (polysaccharide solutions and adsorption times).

4.2.5. X-ray Photoelectron Spectroscopy

The surface chemistry of PEM_{19} and PEM_{19}+PCNs surfaces prepared on glass-bottom petri dishes was evaluated by X-ray photoelectron spectroscopy (XPS). Spectra were obtained with a monochromatic Al Kα X-ray source ($h\nu$ = 1486.6 eV), a hemispherical analyzer, and multichannel detector. High-resolution spectra were obtained using a 23.5 eV analyzer pass energy with 0.1 eV steps and an X-ray spot of 800 μm^2. All spectra were obtained with a photoelectron takeoff angle of 45°.The binding energy scales for the samples were referenced to the C1s peak at 284.8 eV. Spectra curve fitting was done using Phi Electronics Multipak version 9.3. Elemental compositions were computed according to the atom sensitivities.

4.2.6. Single-Molecule Microscopy Evaluation of Protein Adsorption and Fibrin Network Formation

For high-sensitivity detection of protein adsorption and fibrin network formation at solid-liquid interfaces, an objective-type TIRF microscope was used as previously described [51,52]. Specifically, the excitation was performed in oblique illumination mode for measuring protein adsorption, and in TIRF mode for characterizing fibrin network formation. The samples were prepared on glass-bottom petri dishes as described above for the AFM characterization. The microscope was home-built around an Olympus IX71 body with 638 nm laser line as excitation source (DL638- 328 050, CrystaLaser, Reno, NV). A back-illuminated electron-multiplied charge coupled device (EMCCD) camera (Andor iXon DU-888) liquid-cooled to −70 °C, with an electronic gain of 60 was used. In order to maintain constant focus during the whole imaging time we employed an autofocus system (CRISP, Applied Scientific Instrumentation, Eugene, OR) in combination with a piezoelectric stage (Z-100, Mad City Labs, Madison, WI). To reduce photobleaching, an enzymatic oxygen scavenger system was used in the imaging buffer. Imaging buffer for screening protein adsorption was 50 mM Tris-HCl (pH 8.0), 10 mM NaCl, 10% glucose, 0.15 mg ml^{-1} glucose oxidase, 34 µg ml^{-1} catalase, 10% glucose and 1% β-mercaptoethanol [53]. Fibrinogen from human plasma conjugated with Alexa Fluor 647 and albumin from bovine serum conjugated with Alexa Fluor 647 were used to observe protein adsorption on different surfaces. The perfusion chamber was filled with the solution containing the labeled protein, and after an incubation period of 10 minutes, with no subsequent rinse step, 105 seconds of microscopy videos were acquired at a frame rate of 9.5 frames/s, using a 100×/1.4 oil immersion objective. For each experimental condition, three independent replicates on three different samples were conducted. The protein adsorption data are reported as the mean fluorescence intensity ± standard deviation.

Fibrin polymerization was studied by mixing fibrinogen (at a final concentrations of 0.75 mg mL^{-1}), Alexa Fluor 647-conjugated fibrinogen (at a final concentration of 5 nM), and thrombin (at 1 NIH U mL^{-1}) in Tris-buffered saline (10 mM Tris, 150 mM NaCl, pH 7.4) with 5 mM $CaCl_2$, to activate thrombin at room temperature. TIRF videos were taken on at least five different regions of three different samples and one representative image is shown here for PEM_{19}, PEM+CS, PEM+HEP, PEM_{19}+PCN(CS-CHI), and PEM_{19}+PCN(HEP-CHI). A video of these fibrin/thrombin experiments is shown in the Appendix C.

4.3. Results

4.3.1. AFM of PEM and PEM_{19}+PCN Surfaces

Atomic force micrographs (AFM) obtained in fluid with peak-force quantitative nanomechanical property mapping (PF-QNM) of the PEM and PEM_{19}+PCN surfaces, prepared on glass-bottom petri dishes (Figure 4.1) show that the surface roughness increases as the number of PEM layers increases. The RMS surface roughness, R_q, calculated from 5 μm × 5 μm AFM images performed on triplicate ($n = 3$) samples for each condition, is reported in Table S.1 in the Appendix C. The apparent Young's modulus of the surface is also reduced as the layer number is increased. Furthermore, when the nanoparticles are adsorbed, they appear as approximately 200 nm-diameter domains densely covering the surface. These features are similar to the sizes of the PCNs obtained by dynamic light scattering (DLS) when the PCNs are in solution (Table 4.1). Notably, these features have similar dimensions and spacing to the dominant GAG structures found in the endothelial glycocalyx [9–11]. Furthermore, the negative zeta potential of the PCNs (Table 4.1) confirms that these are enriched in the polyanionic GAGs, HEP and CS. The AFM images also confirm the aqueous stability of the PEM and PEM+PCN coatings, as multiple AFM images were collected in DI water over the span of several hours, for each sample type.

Table 4.1. Intensity average size and polydispersity index (PDI) of PCNs.

PCN composition	hydrodynamic diameter (nm)	PDI	zeta potential (mV)
CS-CHI	238 ± 2	0.10 ± 0.02	-30 ± 3
HEP-CHI	235 ± 5	0.24 ± 0.05	-21 ± 5

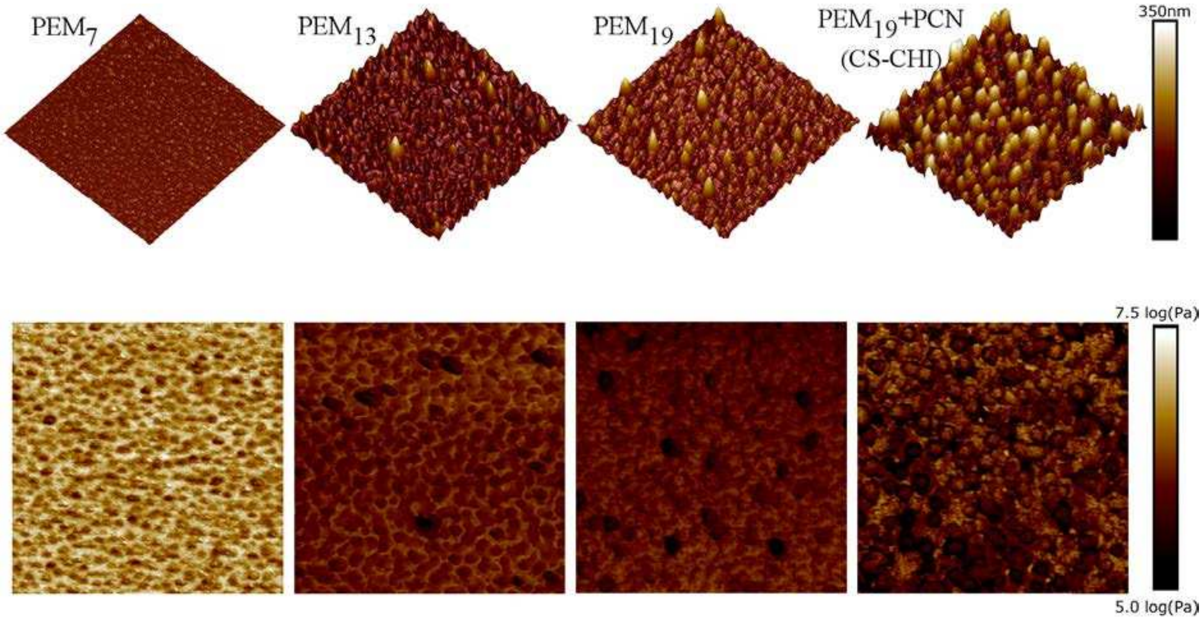

Figure 4.1. (top) Representative 5 μm × 5 μm AFM topographic images of PEMs and PEM$_{19}$+PCN(CS-CHI) taken in liquid. (bottom) Young's modulus (calculated using the DMT model) of representative samples shown in logarithmic scale.

4.3.2. XPS of PEM and PEM$_{19}$+PCN Surfaces

To further confirm the adsorption of PCNs, X-ray photoelectron spectroscopy was performed on PEM and PEM$_{19}$+PCN surfaces. The high-resolution scans of the N1s and S2p envelopes are shown in Figure 4.2. All samples show characteristic N1s spectra with the amine and amide group from the polysaccharides, near 400 eV, and a strong ammonium contribution between 402 eV and 402.5 eV. The ammonium contribution confirms the presence of chitosan within the PEM and PCNs as we have reported previously [38,48,54,55]. The addition of the PCN is confirmed by the strong sulfate signal in the S2p envelope. While the PEMs composed of CHI and HA contain no sulfate, adsorption of the CS- and HEP-containing PCNs results in a sulfur signal from the surface. The elemental compositions (C, O, N, and S) of these surfaces are reported in the Appendix C (Table S.2). To confirm that the PEM surfaces prepared on MUA-modified, gold-coated glass are similar to those on glass-bottom petri dishes, examples of XPS and AFM of the PEM_{13} and the PEM_{19}+PCN(CS-CHI) on both substrates are shown in Figures S.1 and S.2 in the Appendix C.

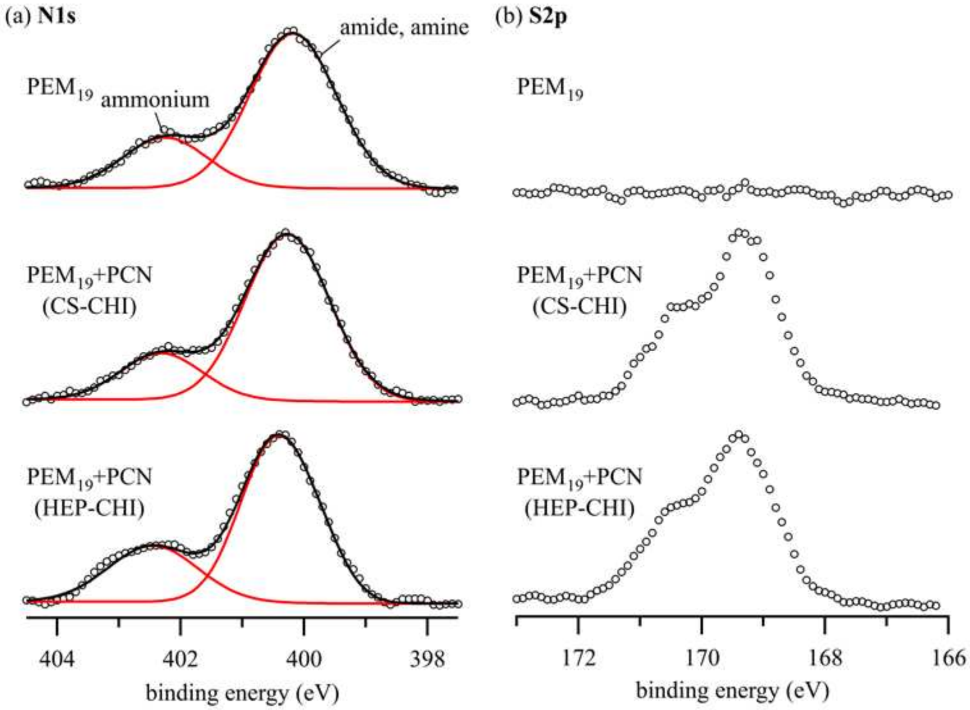

Figure 4.2. High resolution XPS spectra of the PEM_{19} and PEM_{19}+PCN samples in the region of the N1s and S2p envelopes confirms that all of the samples contain chitosan electrostatically complexed with the polyanions (evidenced by the ammonium peak) and that the PEM_{19}+PCN samples contain the sulfated CS and HEP (evidenced by the characteristic sulfate signal in the S2p envelope).

4.3.3. LbL Assembly of PEMs and Protein Adsorption by FT-SPR

The layer-by-layer assembly of the PEMs, the adsorption of PCNs, and subsequent adsorption of plasma proteins was monitored by *in situ* Fourier-transform surface plasmon resonance (FT-SPR). Layer-by-layer assembly was conducted on gold-coated glass substrates, modified with a self-assembled monolayer of MUA, as previously reported [38,39,49]. The FT-SPR data during the last steps of construction of a 19-layer chitosan-hyaluronan PEM (PEM_{19}), followed by CS-CHI PCN adsorption are shown in Figure 4.3 (a). During each polyelectrolyte adsorption step, the plasmon resonance absorbance wavelength, λ_{res}, increases by about 35 to 50 nm, due to surface adsorption and to changes in the refractive index between the rinse and polyelectrolyte solutions. Then, during the subsequent rinse step, λ_{res}, is reduced. The net change in λ_{res} measured during the rinses before and after each adsorption step is proportional to the changes in the surface thickness and refractive index, corresponding to the amount of irreversibly adsorbed polyelectrolyte at each step.

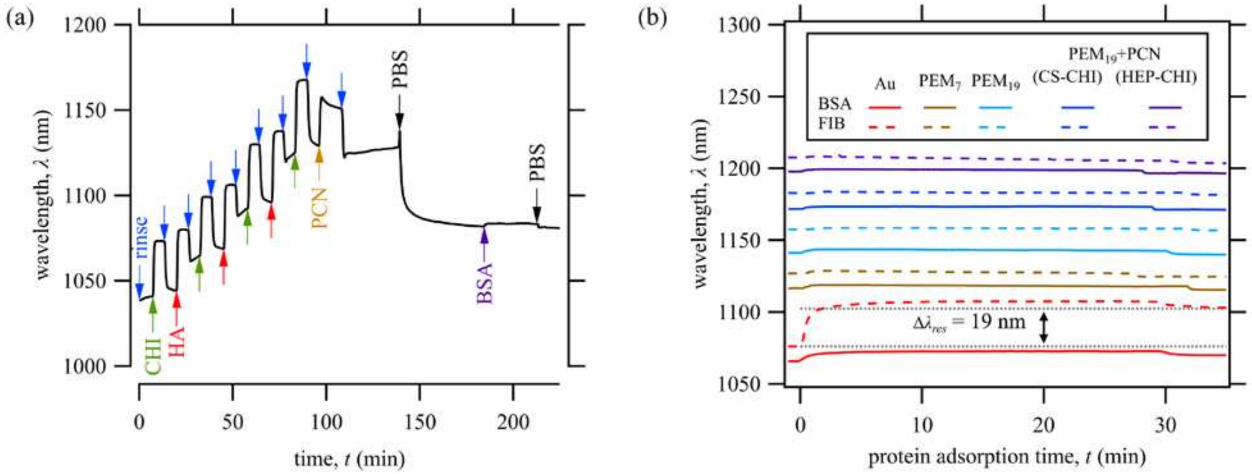

Figure 4.3. LbL assembly of PEM and protein adsorption from in situ FT-SPR. (a) Example of *in situ* FT-SPR data confirming the last 7 layers of CHI-HA PEM assembly. These data show PCN adsorption, a subsequent rinse with PBS, and a 30-minute BSA adsorption step. There is no measurable difference in wavelength before and after BSA adsorption. (b) BSA and FIB adsorption steps from in situ FT-SPR experiments. Irreversible protein adsorption is detected for both BSA and FIB on the control (gold-coated glass, modified with MUA self-assembled monolayer), but no irreversible adsorption of BSA or FIB adsorption is detected on any of the PEM or PEM_{19}+PCN surfaces.

To evaluate protein adsorption on the PEM and PEM_{19}+PCN surfaces, we exposed the surfaces to solutions (0.75 mg mL^{-1}) of BSA or FIB in phosphate-buffered saline (PBS) for 30 minutes. During the protein adsorption step, the plasmon resonance absorption wavelength, λ_{res}, was monitored, as shown in Figure 4.3 (b). The wavelength is expected to shift due to the difference in refractive index of the medium at the sensor surface, within the penetration depth of the SPR evanescent field. This change in refractive index arises due to changes in the surface (e.g. protein deposition) and due to the refractive index increment of the protein in solution. After reaching a steady-state value of λ_{res}, BSA or FIB solution was replaced with PBS. The amount of irreversibly adsorbed BSA and FIB was quantified as the difference in λ_{res} measured in PBS before and after incubation with BSA or FIB solution. This difference is $\Delta\lambda_{res}$. The average limit of quantitation for our instrument was estimated to be 0.1 nm, which corresponds to approximately 20 pg mm^{-2} of deposit. On control surfaces (gold-coated glass modified with a self-assembled monolayer of MUA), we detected 2.2 ng mm^{-2} of BSA adsorption, and 3.8 ng mm^{-2} of FIB adsorption. On all of the experimental PEM and PEM$_{19}$+PCN surfaces we detected a positive change in λ_{res} when the surfaces were exposed to protein (between 0.5 nm and 2.5 nm, corresponding to 0.1 to 0.5 ng mm^{-2}), which was completely reversed during the subsequent rinse. The values of $\Delta\lambda_{res}$ were either below the limit of detection or were slightly negative, indicating that the wavelength change is due to some other change on the surface. The positive change in λ_{res} during exposure to the protein solution likely indicates reversible protein adsorption, however no irreversible adsorption of either BSA or FIB is detected on PEM and PEM$_{19}$+PCN surfaces. This confirms that all of the experimental surfaces are comparable to ultra-low fouling surfaces [56,57]. Moreover, the inability to detect protein adsorption on PEM and PEM$_{19}$+PCN samples cannot be attributed to the thickness of the coatings. These coatings are within the evanescent field sensitivity of the SPR, evidenced by the change in the signal when the rinse solution is changed to PBS.

Although SPR shows that there is no irreversible adsorption on our PEM and PEM$_{19}$+PCN surfaces, the SPR signal does change during the protein adsorption and subsequent rinse steps. SPR is extremely sensitive for detecting changes in both the thickness and the refractive index of the surface. Therefore any change in the surface structure during protein adsorption, such as release of water and counterions, or desorption of polysaccharides may mask the detection of protein adsorption. Furthermore, the SPR technique requires that the surface be rinsed following adsorption, so that surface changes can be compared using the same refractive index background. To precisely quantify protein adsorption, a technique that distinguishes protein adsorption from these other phenomena, while the surface is exposed to protein solution, is required.

4.3.4. Protein Adsorption by Single-Molecule Fluorescence Microscopy

To better quantify protein adsorption on bare glass (control), PEM_7, PEM_{13}, PEM_{19}, PEM_{19}+PCN(CS-CHI), and PEM_{19}+PCN(HEP-CHI), we conducted single-molecule fluorescence microscopy using fluorescently-labeled BSA and FIB. (In these experiments, bare glass must be used as a control because the gold-coated glass control used for SPR cannot be used in TIRF microscopy.) To enable single-molecule detection, proteins were diluted to very low concentrations (100 pM, 500 pM, 1 nM, and 3 nM) in pH 8.0 imaging buffer, as described in the Experimental Section. Imaging conditions (laser power, excitation angle, exposure time, etc.) were the same across all concentrations and surfaces. The lowest concentration of protein (100 pM) was allowed to equilibrate with each surface for 10 minutes. Then microscopy videos were collected for 105 seconds (1000 frames) using oblique illumination to reduce background fluorescence. Subsequently, the protein solution concentration was incremented to the next concentration in the series (namely, 500 pM, 1 nM, and 3 nM), and the surface was again allowed to equilibrate for 10 minutes, before collecting 105 seconds of video. Separate surfaces were prepared for BSA and FIB. Figure 4.4 (a) shows representative images obtained by averaging 1000 frames under oblique illumination during protein adsorption from the BSA and FIB solutions at 1 nM, after 10 minutes of incubation with the fluorescently-labeled protein solution. Figures 4.4 (b) and (c) also show the mean fluorescence intensity of the adsorbed BSA and FIB on the surface of each experimental sample and the glass control, after 10 minutes of incubation with protein solution at different concentrations. When protein concentration is increased, the amount of adsorbed protein increases for all surface types. The clean glass control surface exhibits a measurable adsorption of BSA and FIB at all tested concentrations, as expected. When the glass is modified with chitosan-terminated PEM, the surface adsorbs more BSA than the glass, but the FIB adsorption is substantially reduced. For both proteins the amount adsorbed decreases as the number of PEM layers increases for PEM_7, PEM_{13}, and PEM_{19}, as others have reported for polysaccharide-based PEMs [36]. Adding either the CS-CHI or HEP-CHI PCNs to make PEM_{19}+PCN(CS-CHI) and PEM_{19}+PCN(HEP-CHI) surfaces results in a substantial reduction in BSA adsorption (Figure 4.4), even though these surfaces have higher surface area (Figure 4.1). Interestingly, there is a significant difference between the CS-CHI and the HEP-CHI PCNs, with respect to FIB adsorption. At higher FIB concentrations (1 nM and 3 nM), the HEP-CHI PCN surface adsorbs more FIB than the CS-CHI PCN. This effect could be due to specific binding between heparin and FIB, as FIB is a heparin-binding protein [58]. The reduction in surface protein adsorption as the layer number increases, suggests that neither protein diffuses into the PEM. Rather, both proteins adsorb only on the surfaces. If the proteins were diffusing into the PEMs, then the amount of protein would increase as the PEM layer number increases.

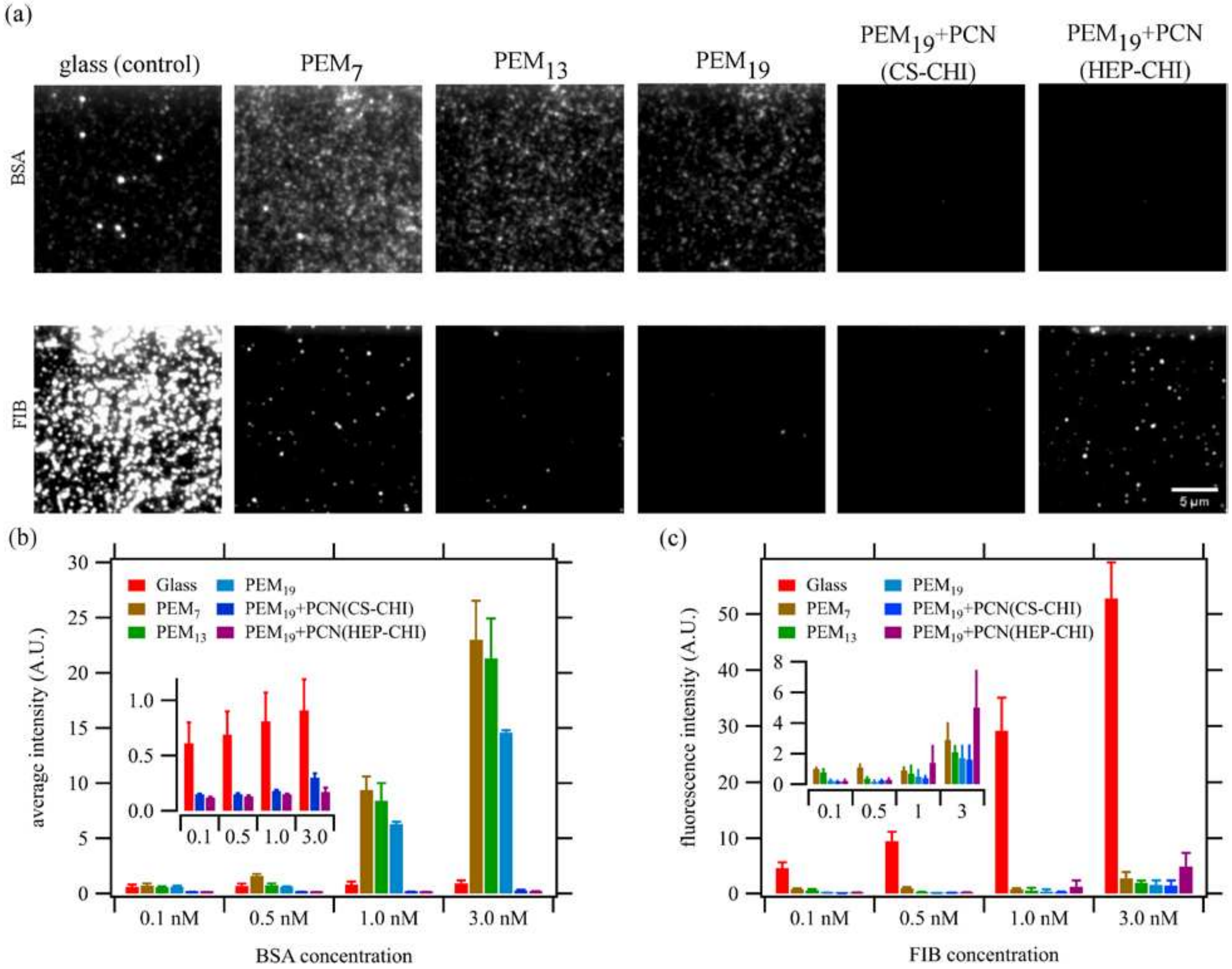

Figure 4.4. (a) Single-molecule fluorescence detection of BSA and FIB adsorption from 1 nM protein solutions on glass (control), 7-layer, 13-layer, 19-layer PEMs, and PEM_{19}+PCN(CS-CHI) and PEM_{19}+PCN(HEP-CHI) surfaces. (Scale bar is 5 μm). (b-c) Average fluorescence intensity from single-molecule fluorescence microscopy experiments at different protein concentrations. In (b) and (c) error bars represent standard deviation from experiments on 3 replicate surfaces (n = 3). Insets in (b) and (c) show the data without the PEM samples (b) and without the glass control samples (c), so that the very low-intensity signals can be compared.

4.3.5. Fibrin Network Formation on Surfaces by Single Molecule Fluorescence Microscopy

While the PCN-modified surfaces attract FIB, fibrin network formation is completely inhibited by the PCN structure. CHI-, CS-, and HEP-terminated PEMs and PEM_{19}+PCN surfaces were exposed to a solution containing physiologic concentration of fibrinogen solutions (0.75 mg/mL), thrombin (at 1 NIH U mL^{-1}), and fluorescently labeled fibrinogen (5 nM). Thrombin converts FIB to the polymerizable fibrin, which then forms polymerized fibrin fibers. On the experimental surfaces, the first evidence of polymerized fibrin fibers appears after 30 min. (See Figure S.3 in Appendix C). After 40 minutes of incubation, total internal reflection fluorescence (TIRF) microscopy videos were collected on chitosan-terminated PEMs (PEM_{19}) (control), HEP-terminated PEMs (PEM+HEP), CS-terminated PEMs (PEM+CS), and PCN-terminated surfaces [PEM_{19}+PCN(CS-CHI) and PEM_{19}+PCN(HEP-CHI)]. TIRF videos were taken on a minimum of five different regions of three different surfaces and one representative image is shown here for each surface type. In Figure 4.5 each image shows the average of 1500 frames after 40 minutes of incubation with the mixture of FIB and thrombin. These are the same fields of view shown in Figure S.3 in Appendix C). A video of fibrin(ogen) interaction with PEM surfaces is also available in the Appendix C.

On the PEM_{19} surface (Figure 4.5), intersecting fibers suggest that a network of fibrin is formed on the control surface before 40 minutes, evidenced by visible intersecting fibers incorporating the fluorescently labeled fibrin(ogen). Similar fibrin networks are also observed on the PEM surfaces terminated with CS and HEP (PEM+CS and PEM+HEP). Therefore, coating the surface with heparin or chondroitin sulfate does not suppress fibrin polymerization on the surface or fibrin fiber adsorption from solution onto the surface. The formation of fibrin fibers and a crosslinked fibrin network is expected in these experiments, because the only coagulation proteins present are fibrinogen and thrombin (e.g. there is no antithrombin III). Strikingly, in the case of PEM_{19}+PCN(CS-CHI) and PEM_{19}+PCN(HEP-CHI) no fibrin fibers are observed on the surfaces, even after 40 minutes (Figure 4.5). For both types of PEM_{19}+PCN surfaces, only sparse single molecules of fibrin(ogen) are adsorbed on the surface. Therefore, the PEM_{19}+PCN surfaces must be inhibiting both fibrin fiber adsorption from solution, and polymerization of fibrin on the surfaces. To further demonstrate the capacity of PEM$_{19}$+PCN surfaces to inhibit fibrin network formation, a PEM$_{19}$+PCN(CS-CHI) surface was incubated for 2 hours with the same FIB/thrombin mixture. No fibers were observed on the surface even after 2 hours. (See Figure S.3 in the Appendix C). This is remarkable since the PEM$_{19}$, PEM+CS and PEM$_{19}$+HEP surfaces all have obvious fiber formation after 30 minutes, and show intersecting fibers characteristic of fibrin networks, after only 40 minutes.

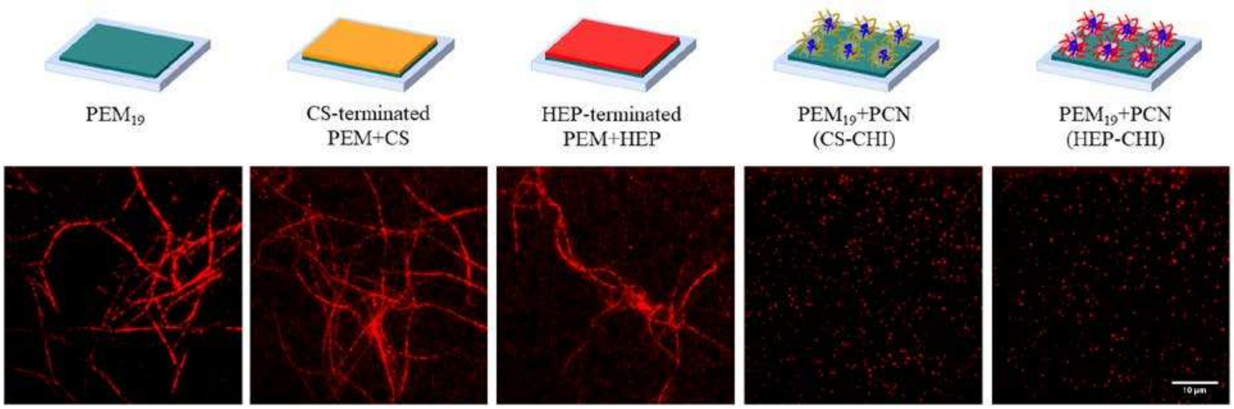

Figure 4.5. TIRF microscopy images of fluorescently-labeled fibrin fibers, polymerized from physiologic concentration of fibrinogen (0.75 mg/mL), in the presence of thrombin (1 NIH U/mL) on PEMs. The structure of the PEM$_{19}$+PCN samples does not prevent the adsorption of fibrin(ogen) monomers, but it completely prevents adsorption of fibrin fibers and fibrin polymerization on the surface.

4.4. Discussion

While some superhydrophobic surfaces, polymer brushes, and other surface chemistries can reduce protein adsorption to very low levels, no surface can completely eliminate all protein adsorption from a complex solution, containing many proteins, fats, sugars, cells, and polyvalent ions, such as blood [35,37,56,57,59]. When any biomaterial comes in contact with blood, a layer of nonspecifically adsorbed proteins will eventually form. Fibrin(ogen) and denatured albumin can bind platelets, promoting their attachment onto a biomaterial surface, ultimately leading to thrombus (blood clot) formation [4,43,60,61]. Fibrinogen on the surface of biomaterials can be converted to insoluble fibrin through thrombin-mediated cleavage of small fibrinopeptides A and B from the *N*-termini of the Aα and Bβ chains [44–46]. Activated fibrin molecules then polymerize into branched fibers, forming an elastic network, which traps red blood cells and ultimately forms a thrombus. On the inside surface of blood vessels, thrombin activity is inhibited by antithrombin III, which binds to sulfated glycosaminoglycans in the glycocalyx [15]. In this work we show that in the absence of antithrombin III, sulfated GAGs (PEM_{19}+PCNs) can inhibit fibrin network formation through a nanostructure-dependent mechanism, when they are presented in glycocalyx mimetic bush-like domains formed by the PCNs.

SPR is widely used to characterize protein adsorption when developing high-performance, ultra-low fouling surfaces [56,57]. The PEM and glycocalyx-mimetic PEM+PCN surfaces proposed here are complex, multicomponent surfaces that can undergo multiple changes when exposed to different solution conditions, complicating interpretation of very small SPR signal changes. To overcome this limitation, we use single-molecule fluorescence microscopy to directly observe the interactions of blood proteins with PEM and glycocalyx-mimetic PEM+PCN surfaces. Like SPR, single-molecule fluorescence microscopy can be performed in real time. However, unlike SPR, the microscopy technique provides microscopic resolution of the protein interactions with the surface and distinguishes differences between PEM and PEM_{19}+PCN surfaces. Furthermore, the SPR experiments also require a rinse step, so that the refractive index of the solution background is the same before and after protein adsorption. But in a long-term blood-contacting application, there is no periodic rinsing of the surface. Since the single-molecule fluorescence microscopy technique does not require that the surfaces be rinsed, these experiments provide detail about how proteins interact with the surface in a context that is more similar to a proposed blood-contacting application than the SPR experiments.

Single-molecule fluorescence microscopy also affords the ability to directly observe the formation of fibrin(ogen) fibers and fiber networks on the surfaces. The PEM_{19} surface has very low fibrinogen adsorption (Figure 4.4). However single-molecule microscopy reveals that a fibrin fiber network still forms before 40 minutes on this surface when fibrinogen and thrombin are combined. The introduction of heparin or chondroitin sulfate on the surface (PEM+HEP and PEM+CS, Figure 4.4) is also not sufficient to prevent this fibrin network formation. However, PEM_{19}+PCN have similarly low fibrinogen adsorption and also completely inhibit the fibrin network formation. The fibers and networks observed on the PEM_{19}, PEM_{19}+HEP, and PEM_{19}+CS are most likely a combination of fibers that polymerize from surface-adsorbed fibrin(ogen) and fibers formed in solution that subsequently adsorb. Neither of these phenomena occur on the PEM_{19}+PCN surfaces. Polymerization of surface-bound fibrin(ogen) could be inhibited by PCNs on PEM_{19}+PCN surfaces if the PCNs bind and isolate single fibrin(ogen) molecules, thereby suppressing their assembly to form fibers. In the TIRF videos (see Appendix C) some sparse fibrin(ogen) molecules appear to be irreversibly bound while others appear and disappear from the TIRF plane of view, indicating adsorption and desorption. The adsorption of fibrin fibers from solution onto the PEM_{19}+PCN surfaces may be inhibited by the surface topography introduced by the PCNs. The surface roughness of the PEM_{19}+PCN, characterized by high R_q and the 100-200 nm diameter hemispherical domains observed in the AFM images may restrict the relatively stiff fibrin fibers from conforming to the surface to form multiple adhesive contacts, thereby inhibiting adsorption.

The modification of surfaces with polysaccharide-based PEMs is a rapid, low-cost, and scalable process. Our group and others have demonstrated PEM modification of metals, polymers, composites (including bone tissue), and conformal coating of nanostructured materials [5,48–

50,54,55]. Therefore, this simple strategy could be generalized to many blood-contacting medical devices to control the interactions of blood proteins with surfaces. We envision adapting these surfaces for materials for long-term blood contacting applications, such as cardiovascular implants and extracorporeal blood circuits.

4.5. Conclusions

Protein adsorption from blood is the initiating event in surface-induced blood clotting. Therefore, many researchers have proposed that ideal blood-contacting materials should be developed with a focus on reducing protein adsorption at the surface to prevent blood clotting [4,6]. The inside surface of blood vessels has overcome protein adsorption by developing a barrier on the endothelial cells, the endothelial glycocalyx, to maintain blood compatibility of the intravascular luminal wall. Rather than attempting to completely eliminate protein adsorption, we propose that mimicking the endothelial glycocalyx layer on the surface of biomaterials has the potential to suppress nonspecific blood protein adsorption. This approach represents a new paradigm in preventing blood clotting on biomedical device surfaces.

The glycocalyx-mimetic surfaces proposed here have no irreversible adsorption of BSA and FIB above the limit of detection of SPR. Single-molecule TIRF microscopy experiments show that the PCN in the PEM_{19}+PCN surfaces inhibit both the surface-mediated polymerization of fibrin and the adsorption of fibrin fibers from solution, in the presence of thrombin. Further detailed investigation of how the structure and composition of these surfaces control protein-surface interactions in more complex protein solutions will enable elucidation of design principles for a new class of improved blood-contacting biomaterials based on mimics of the endothelial glycocalyx.

REFERENCES

[1] M. Hedayati, M.M. Reynolds, D. Krapf, M.J. Kipper, Nanostructured Surfaces That Mimic the Vascular Endothelial Glycocalyx Reduce Blood Protein Adsorption and Prevent Fibrin Network Formation, ACS Appl. Mater. Interfaces. 10 (2018) 31892–31902. doi:10.1021/acsami.8b09435.

[2] V. Jokinen, E. Kankuri, S. Hoshian, S. Franssila, R.H.A. Ras, Superhydrophobic Blood-Repellent Surfaces, Adv. Mater. (2018) 1705104. doi:10.1002/adma.201705104.

[3] K.S. Lavery, C. Rhodes, A. Mcgraw, M.J. Eppihimer, Anti-thrombotic technologies for medical devices, Adv. Drug Deliv. Rev. 112 (2017) 2–11. doi:10.1016/j.addr.2016.07.008.

[4] X. Liu, L. Yuan, D. Li, Z. Tang, Y. Wang, G. Chen, H. Chen, J.L. Brash, Blood compatible materials: state of the art, J. Mater. Chem. B. 2 (2014) 5718–5738.

[5] R. Simon-Walker, R. Romero, J.M. Staver, Y. Zang, M.M. Reynolds, K.C. Popat, M.J. Kipper, Glycocalyx-Inspired Nitric Oxide-Releasing Surfaces Reduce Platelet Adhesion and Activation on Titanium, ACS Biomater. Sci. Eng. (2016). doi:10.1021/acsbiomaterials.6b00572.

[6] I. Reviakine, F. Jung, S. Braune, J.L. Brash, R. Latour, M. Gorbet, W. van Oeveren, Stirred, shaken, or stagnant: What goes on at the blood–biomaterial interface, Blood Rev. 31 (2017) 11–21. doi:10.1016/j.blre.2016.07.003.

[7] S. Reitsma, D.W. Slaaf, H. Vink, M. van Zandvoort, M. Egbrink, The endothelial glycocalyx: composition, functions, and visualization, Pflugers Arch.-Eur. J. Physiol. 454 (2007) 345–359. doi:10.1007/s00424-007-0212-8.

[8] S. Weinbaum, J.M. Tarbell, E.R. Damiano, The structure and function of the endothelial glycocalyx layer, Annu Rev Biomed Eng. 9 (2007) 121–167.

[9] J. Rostgaard, K. Qvortrup, Electron Microscopic Demonstrations of Filamentous Molecular Sieve Plugs in Capillary Fenestrae, Microvasc. Res. 53 (1997) 1–13. doi:10.1006/mvre.1996.1987.

[10] J.M. Squire, M. Chew, G. Nneji, C. Neal, J. Barry, C. Michel, Quasi-Periodic Substructure in the Microvessel Endothelial Glycocalyx: A Possible Explanation for Molecular Filtering?, J. Struct. Biol. 136 (2001) 239–255.

[11] M. Hedayati, M.J. Kipper, Atomic force microscopy of adsorbed proteoglycan mimetic nanoparticles: toward new glycocalyx-mimetic model surfaces, Carbohydr. Polym. 190 (2018) 346–355. doi:10.1016/j.carbpol.2018.02.023.

[12] D.C. Leslie, A. Waterhouse, J.B. Berthet, T.M. Valentin, A.L. Watters, A. Jain, P. Kim, B.D. Hatton, A. Nedder, K. Donovan, E.H. Super, C. Howell, C.P. Johnson, T.L. Vu, D.E. Bolgen, S. Rifai, A.R. Hansen, M. Aizenberg, M. Super, J. Aizenberg, D.E. Ingber, A bioinspired omniphobic surface coating on medical devices prevents thrombosis and biofouling, Nat. Biotechnol. 32 (2014) 1134–1140. doi:10.1038/nbt.3020.

[13] P. Olsson, H. Lagergren, R. Larsson, K. Radegran, Prevention of Platelet-Adhesion and Aggregation by a Glutardialdehyde-Stabilized Heparin Surface, Thromb. Haemost. 37 (1977) 274–282.

[14] Lagergre.H, P. Olsson, Swedenbo.J, Inhibited Platelet Adhesion - Non-Thrombogenic Characteristic of a Heparin-Coated Surface, Surgery. 75 (1974) 643–650.

[15] R. Larsson, P. Olsson, U. Lindahl, Inhibition of Thrombin on Surfaces Coated with Immobilized Heparin and Heparin-Like Polysaccharides - a Crucial Non-Thrombogenic Principle, Thromb. Res. 19 (1980) 43–54.

[16] B. Pasche, K. Kodama, O. Larm, P. Olsson, J. Swedenborg, Thrombin Inactivation on Surfaces with Covalently Bonded Heparin, Thromb. Res. 44 (1986) 739–748.

[17] S. Boddohi, M.J. Kipper, Engineering Nanoassemblies of Polysaccharides, Adv. Mater. 22 (2010) 2998–3016.

[18] K.K. Wu, P. Thiagarajan, Role of endothelium in thrombosis and hemostasis, Annu. Rev. Med. 47 (1996) 315–331.

[19] N. Weber, H.P. Wendel, G. Ziemer, Hemocompatibility of heparin-coated surfaces and the role of selective plasma protein adsorption, Biomaterials. 23 (2002) 429–439.

[20] Y. Ito, Y. Imanishi, M. Sisido, Invitro Platelet-Adhesion and Invivo Antithrombogenicity of Heparinized Polyetherurethaneureas, Biomaterials. 9 (1988) 235–240.

[21] K.D. Park, W.G. Kim, H. Jacobs, T. Okano, S.W. Kim, Blood Compatibility of Spuu-Peo-Heparin Graft-Copolymers, J. Biomed. Mater. Res. 26 (1992) 739–756.

[22] Y.J. Kim, I.K. Kang, M.W. Huh, S.C. Yoon, Surface characterization and in vitro blood compatibility of poly(ethylene terephthalate) immobilized with insulin and/or heparin using plasma glow discharge, Biomaterials. 21 (2000) 121–130.

[23] A. Magnani, R. Barbucci, L. Montanaro, C.R. Arciola, S. Lamponi, In vitro study of blood-contacting properties and effect on bacterial adhesion of a polymeric surface with immobilized heparin and sulphated hyaluronic acid, J. Biomater. Sci.-Polym. Ed. 11 (2000) 801–815.

[24] S. Thorslund, J. Sanchez, R. Larsson, F. Nikolajeff, J. Bergquist, Bioactive heparin immobilized onto microfluidic channels in poly(dimethylsiloxane) results in hydrophilic surface properties, Colloids Surf. B-Biointerfaces. 46 (2005) 240–247. doi:10.1016/j.colsurfb.2005.10.009.

[25] J.L. Chen, Q.L. Li, J.Y. Chen, C. Chen, N. Huang, Improving blood-compatibility of titanium by coating collagen-heparin multilayers, Appl. Surf. Sci. 255 (2009) 6894–6900. doi:10.1016/j.apsusc.2009.03.011.

[26] Q.G. Tan, J. Ji, M.A. Barbosa, C. Fonseca, J.C. Shen, Constructing thromboresistant surface on biomedical stainless steel via layer-by-layer deposition anticoagulant, Biomaterials. 24 (2003) 4699–4705. doi:10.1016/s0142-9612(03)00363-6.

[27] W.C. Lin, T.Y. Liu, M.C. Yang, Hemocompatibility of polyacrylonitrile dialysis membrane immobilized with chitosan and heparin conjugate, Biomaterials. 25 (2004) 1947–1957. doi:10.1016/j.biomaterials.2003.08.027.

[28] C.G. Björck, D. Bergövist, C.O. Esquivel, R. Larsson, Y. Rudsvik, In vitro evaluation of a biologic graft surface. Effect of treatment with conventional and low molecular weight (LMW) heparin, Thromb. Res. 35 (1984) 653–663.

[29] M.C. Yang, W.C. Lin, Protein adsorption and platelet adhesion of polysulfone membrane immobilized with chitosan and heparin conjugate, Polym. Adv. Technol. 14 (2003) 103–113.

[30] H. Kito, T. Matsuda, Biocompatible coatings for luminal and outer surfaces of small-caliber artificial grafts, J. Biomed. Mater. Res. 30 (1996) 321–330.

[31] S. Movafaghi, V. Leszczak, W. Wang, J.A. Sorkin, L.P. Dasi, K.C. Popat, A.K. Kota, Hemocompatibility of Superhemophobic Titania Surfaces, Adv. Healthc. Mater. 6 (2017) 1600717. doi:10.1002/adhm.201600717.

[32] B.D. Ippel, P.Y.W. Dankers, Introduction of Nature's Complexity in Engineered Blood-compatible Biomaterials, Adv. Healthc. Mater. 7 (2018) 1700505. doi:10.1002/adhm.201700505.

[33] A. de los Santos Pereira, S. Sheikh, C. Blaszykowski, O. Pop-Georgievski, K. Fedorov, M. Thompson, C. Rodriguez-Emmenegger, Antifouling Polymer Brushes Displaying Antithrombogenic Surface Properties, Biomacromolecules. 17 (2016) 1179–1185. doi:10.1021/acs.biomac.6b00019.

[34] I. Buzzacchera, M. Vorobii, N.Yu. Kostina, A. de los Santos Pereira, T. Riedel, M. Bruns, W. Ogieglo, M. Möller, C.J. Wilson, C. Rodriguez-Emmenegger, Polymer Brush-Functionalized Chitosan Hydrogels as Antifouling Implant Coatings, Biomacromolecules. 18 (2017) 1983–1992. doi:10.1021/acs.biomac.7b00516.

[35] Q. Liu, A. Singh, R. Lalani, L. Liu, Ultralow Fouling Polyacrylamide on Gold Surfaces via Surface-Initiated Atom Transfer Radical Polymerization, Biomacromolecules. 13 (2012) 1086–1092. doi:10.1021/bm201814p.

[36] Y. Wei, H.-C. Hung, F. Sun, T. Bai, P. Zhang, A.K. Nowinski, S. Jiang, Achieving low-fouling surfaces with oppositely charged polysaccharides via LBL assembly, Acta Biomater. 40 (2016) 16–22. doi:10.1016/j.actbio.2016.04.013.

[37] A. Wörz, B. Berchtold, K. Moosmann, O. Prucker, J. Rühe, Protein-resistant polymer surfaces, J. Mater. Chem. 22 (2012) 19547. doi:10.1039/c2jm30820g.

[38] J. Almodóvar, L.W. Place, J. Gogolski, K. Erickson, M.J. Kipper, Layer-by-Layer Assembly of Polysaccharide-Based Polyelectrolyte Multilayers: A Spectroscopic Study of Hydrophilicity, Composition, and Ion Pairing, Biomacromolecules. 12 (2011) 2755–2765. doi:10.1021/bm200519y.

[39] S. Boddohi, C.E. Killingsworth, M.J. Kipper, Polyelectrolyte multilayer assembly as a function of pH and ionic strength using the polysaccharides chitosan and heparin., Biomacromolecules. 9 (2008) 2021–2028.

[40] S. Boddohi, N. Moore, P.A. Johnson, M.J. Kipper, Polysaccharide-based polyelectrolyte complex nanoparticles from chitosan, heparin, and hyaluronan, Biomacromolecules. 10 (2009) 1402–1409.

[41] L.W. Place, M. Sekyi, M.J. Kipper, Aggrecan-mimetic, glycosaminoglycan-containing nanoparticles for growth factor stabilization and delivery, Biomacromolecules. 15 (2014) 680–689.

[42] S. Boddohi, J. Almodóvar, H. Zhang, P.A. Johnson, M.J. Kipper, Layer-by-layer assembly of polysaccharide-based nanostructured surfaces containing polyelectrolyte complex nanoparticles, Colloids Surf. B-Biointerfaces. 77 (2010) 60–68.

[43] B. Sivaraman, R.A. Latour, The Adherence of platelets to adsorbed albumin by receptor-mediated recognition of binding sites exposed by adsorption-induced unfolding, Biomaterials. 31 (2010) 1036–1044. doi:10.1016/j.biomaterials.2009.10.017.

[44] S. Kattula, J.R. Byrnes, A.S. Wolberg, Fibrinogen and Fibrin in Hemostasis and Thrombosis, Arterioscler. Thromb. Vasc. Biol. 37 (2017) e13–e21. doi:10.1161/ATVBAHA.117.308564.

[45] T. Riedel, J. Suttnar, E. Brynda, M. Houska, L. Medved, J.E. Dyr, Fibrinopeptides A and B release in the process of surface fibrin formation, Blood. 117 (2011) 1700–1706. doi:10.1182/blood-2010-08-300301.

[46] J.W. Weisel, R.I. Litvinov, Mechanisms of fibrin polymerization and clinical implications, Blood. 121 (2013) 1712–1719. doi:10.1182/blood-2012-09-306639.

[47] K.M. Evans-Nguyen, M.H. Schoenfisch, Fibrin Proliferation at Model Surfaces: Influence of Surface Properties, Langmuir. 21 (2005) 1691–1694. doi:10.1021/la047303h.

[48] F.Z. Volpato, J. Almodovar, K. Erickson, K.C. Popat, C. Migliaresi, M.J. Kipper, Preservation of FGF-2 bioactivity using heparin-based nanoparticles, and their delivery from electrospun chitosan fibers, Acta Biomater. 8 (2012) 1551–1559. doi:10.1016/j.actbio.2011.12.023.

[49] J. Almodóvar, S. Bacon, J. Gogolski, J.D. Kisiday, M.J. Kipper, Polysaccharide-based polyelectrolyte multilayer surface coatings can enhance mesenchymal stem cell response to adsorbed growth factors, Biomacromolecules. 11 (2010) 2629–2639.

[50] C. Lin, R. Romero, L.V. Sorokina, K.R. Ballinger, L.W. Place, M.J. Kipper, S.R. Khetani, A polyelectrolyte multilayer platform for investigating growth factor delivery modes in human liver cultures: HEPATOCYTE-GROWTH FACTOR INTERACTIONS ON CHITOSAN-HEPARIN PEMS, J. Biomed. Mater. Res. A. (2017). doi:10.1002/jbm.a.36293.

[51] G. Campagnola, K. Nepal, B.W. Schroder, O.B. Peersen, D. Krapf, Superdiffusive motion of membrane-targeting C2 domains, Sci. Rep. 5 (2016). doi:10.1038/srep17721.

[52] M.G. Gervasi, X. Xu, B. Carbajal-Gonzalez, M.G. Buffone, P. Visconti, D. Krapf, The actin cytoskeleton of the mouse sperm flagellum is organized in a helical structure, (2018). doi:10.1101/252064.

[53] R.E. Benesch, R. Benesch, Enzymatic Removal of Oxygen for Polarography and Related Methods, Science. 118 (1953) 447–448. doi:10.1126/science.118.3068.447.

[54] R. Romero, L. Chubb, J.K. Travers, T.R. Gonzales, N.P. Ehrhart, M.J. Kipper, Coating Cortical Bone Allografts with Periosteum-Mimetic Scaffolds made of Chitosan, Trimethyl Chitosan, and Heparin, Carbohydr. Polym. 122 (2015) 144–151. doi:10.1016/j.carbpol.2015.01.015.

[55] R. Romero, J.K. Travers, E. Asbury, A. Pennybaker, L. Chubb, R. Rose, N.P. Ehrhart, M.J. Kipper, Combined delivery of FGF-2, TGF-β1, and adipose-derived stem cells from an engineered periosteum to a critical-sized mouse femur defect: COMBINED DELIVERY OF FGF-2, TGF-B1, AND ASCS FROM ENGINEERED PERIOSTEUM, J. Biomed. Mater. Res. A. 105 (2017) 900–911. doi:10.1002/jbm.a.35965.

[56] N.D. Brault, H.S. Sundaram, Y. Li, C.-J. Huang, Q. Yu, S. Jiang, Dry Film Refractive Index as an Important Parameter for Ultra-Low Fouling Surface Coatings, Biomacromolecules. 13 (2012) 589–593. doi:10.1021/bm3001217.

[57] D. Hong, H.-C. Hung, K. Wu, X. Lin, F. Sun, P. Zhang, S. Liu, K.E. Cook, S. Jiang, Achieving Ultralow Fouling under Ambient Conditions via Surface-Initiated ARGET ATRP of Carboxybetaine, ACS Appl. Mater. Interfaces. 9 (2017) 9255–9259. doi:10.1021/acsami.7b01530.

[58] H. Mohri, T. Ohkubo, Fibrinogen Binds to Heparin: The Relationship of the Binding of Other Adhesive Proteins to Heparin, Arch. Biochem. Biophys. 303 (1993) 27–31. doi:10.1006/abbi.1993.1251.

[59] G. Emilsson, R.L. Schoch, L. Feuz, F. Höök, R.Y.H. Lim, A.B. Dahlin, Strongly Stretched Protein Resistant Poly(ethylene glycol) Brushes Prepared by Grafting-To, ACS Appl. Mater. Interfaces. 7 (2015) 7505–7515. doi:10.1021/acsami.5b01590.

[60] B. Sivaraman, R.A. Latour, The relationship between platelet adhesion on surfaces and the structure versus the amount of adsorbed fibrinogen, Biomaterials. 31 (2010) 832–839. doi:10.1016/j.biomaterials.2009.10.008.

[61] L.-C. Xu, J.W. Bauer, C.A. Siedlecki, Proteins, platelets, and blood coagulation at biomaterial interfaces, Colloids Surf. B Biointerfaces. (2014) http://dx.doi.org/10.1016/j.colsurfb.2014.09.040. doi:10.1016/j.colsurfb.2014.09.040.

CHAPTER 5: SINGLE-MOLECULE MICROSCOPY REVEALS THE DYNAMICS OF PROTEIN ACCUMULATION IN LONG-TERM EXPERIMENTS ON LOW FOULING SURFACES[1]

Overview

Understanding the mechanism of protein interaction on surfaces is critical to a range of biomaterials applications. Here, we investigate the long-term albumin and fibrinogen adsorption on ultralow fouling and low fouling surfaces using single-molecule tracking methods to directly measure protein adsorption and desorption. These long-term experiments reveal two regimes of behavior for protein interactions at surfaces. In regime I, dynamic pseudo-equilibrium of proteins is observed for a limited time. In regime II, irreversible protein adsorption occurs that leads to protein accumulation on all surfaces. This work reveals that in long-term contact with protein solutions, all experimental surfaces investigated here eventually foul, indicating that the short-term measurements of protein adsorption using ensemble averaging methods may not be sufficient for designing antifouling materials.

---

[1] Manuscript in preparation for submission to *Biomacromolecules.*

CONCLUSIONS

In this project, we developed surfaces that mimic the endothelial glycocalyx layer. We showed that these surfaces substantially reduce nonspecific blood protein adsorption as a first step in the coagulation cascade on biomaterials surfaces. Moreover, it was shown that the topography and chemistry of these mimetic materials inhibit both the surface-mediated polymerization of fibrin and the adsorption of fibrin fibers from solution, in the presence of thrombin.

Furthermore, we demonstrated how combining surface plasmon resonance, X-ray spectroscopy, atomic force microscopy, and single-molecule total internal reflection fluorescence microscopy provides a more complete picture of protein adsorption on low fouling surfaces instead of just using one technique. With single-molecule TIRF microscopy both adsorption and desorption events were precisely quantified to provide a detailed description of protein surface interactions.

Finally, by using high-throughput single-molecule tracking methods we showed the long-term protein interactions with several biomaterials surfaces. Two regimes of protein adsorption were observed on all surfaces for two different blood proteins. In addition, a new mathematical model for protein adsorption was proposed to predict the long-term behavior of protein interactions on surfaces.

Further detailed investigation of how the structure and composition of these surfaces control protein-surface interactions in more complex protein solutions will enable elucidation of design principles for a new class of improved blood-contacting biomaterials based on mimics of the endothelial glycocalyx.

To combat thrombus formation on artificial blood-contacting surfaces various strategies such as incorporation of hydrophilic polymers, bioactive components, bioinspired surfaces, surface endothelialization, and NO release have been proposed. These strategies can be incorporated to glycocalyx-mimetic materials to reduce protein adsorption, control coagulation, and mitigate platelet adhesion and activation, and inflammation. Strategies to reduce protein adsorption have received the greatest amount of attention in this field; studies aimed at understanding how surface properties affect blood cells is also necessary for developing blood-compatible materials.

APPENDIX A: ATOMIC FORCE MICROSCOPY OF ADSORBED PROTEOGLYCAN MIMETIC NANOPARTICLES: TOWARD NEW GLYCOCALYX-MIMETIC MODEL SURFACES

In situ FT-SPR for PEM+PCN(HEP-CHI) sample pH 5.4.

PEM were constructed with CHI as the polycation and HA as the polyanion. During the last 12 min of the experiment, the PEM surface was exposed to the PCN(HEP-CHI). PCN do not interact the same with the surface as a polymer layer, as a result the rinse following PCN adsorption takes more time to equilibrate.

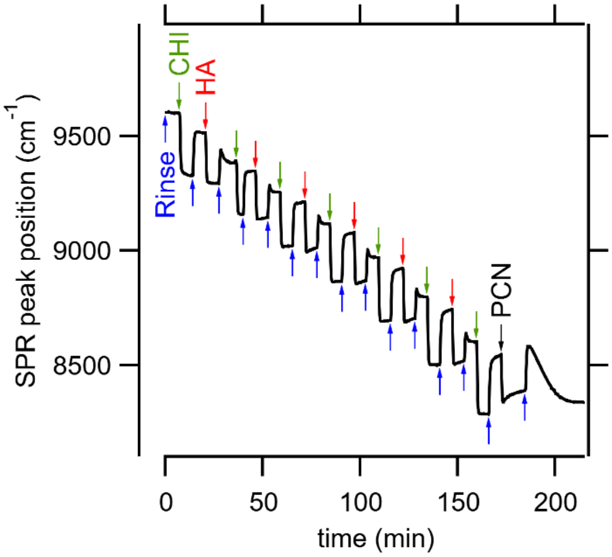

Figure S1. Representative kinetics of PEM+PCN(HEP-CHI) assembly from in situ FT-SPR for the PEM+PCN assembled at pH 5.4. Arrows represent the beginning of acidified water rinse (blue), chitosan adsorption (green), hyaluronan adsorption (red), and PCN adsorption (black). The rinse following PCN adsorption

Microscopic evaluation of PEM+PCN

PEM+PCN (CS-CHI) surface was imaged using TIRF microscopy with different laser line over an area of 5 µm × 5 µm.

Figure S2. TIRF microscopy image for CS-CHI. A. Taken by 473 nm laser line. B. Taken by 561 nm laser line and C. Both of the laser lines at the same time.

AFM topographic images for gold-coated glass, PEM, and PEM+PCN assembled at pH 4.6 and 5.4 in air and PBS

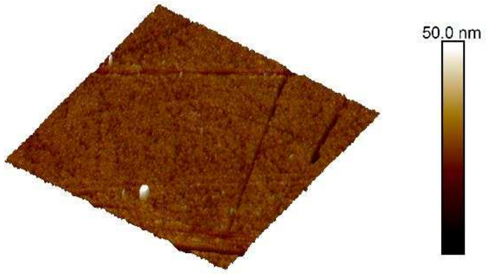

Figure S3. 5 µm × 5 µm AFM topography image of gold-coated glass.

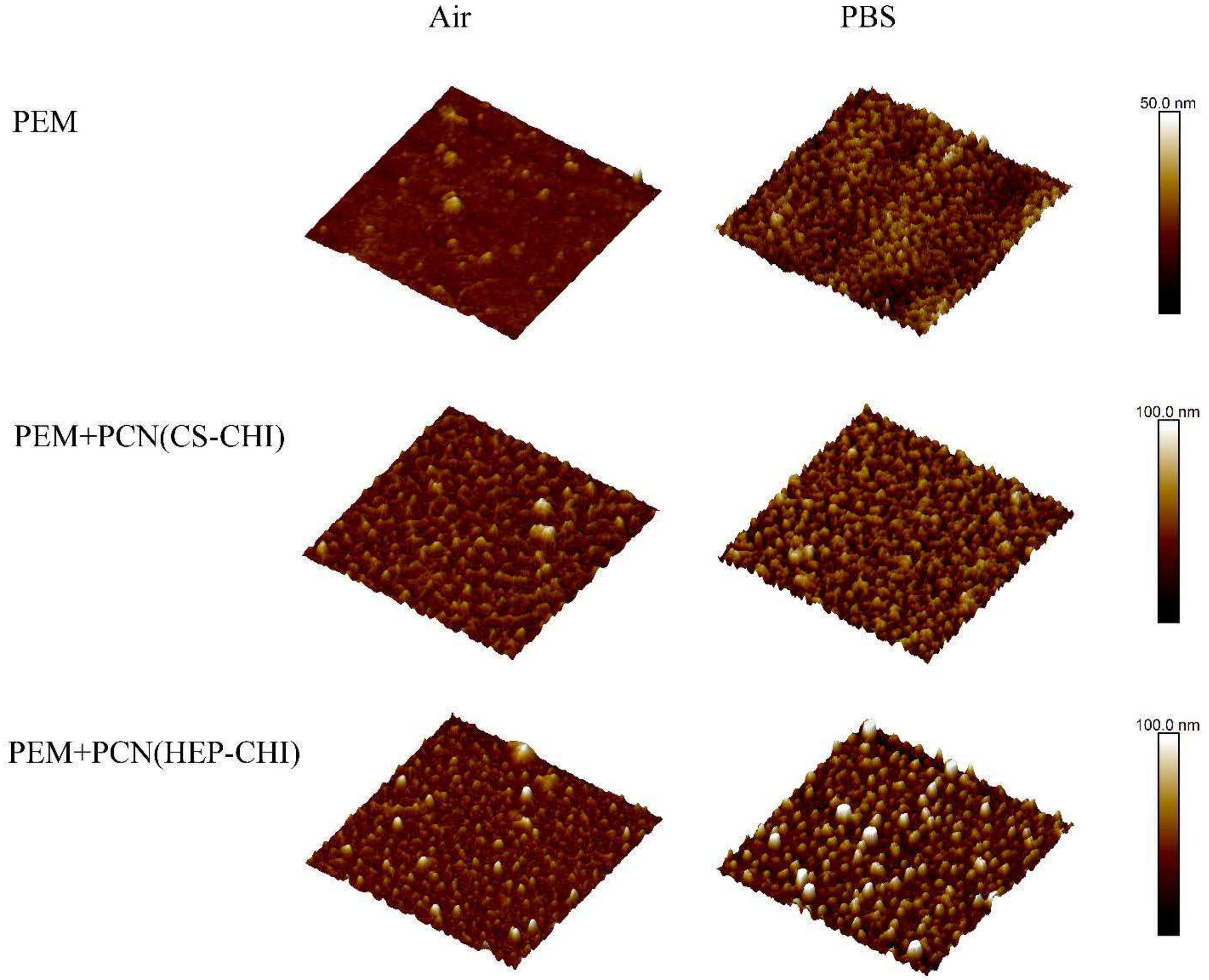

Figure S4. 5 µm × 5 µm AFM topography images in air and in PBS of PEM and PEM+PCN assembled at pH 4.6.

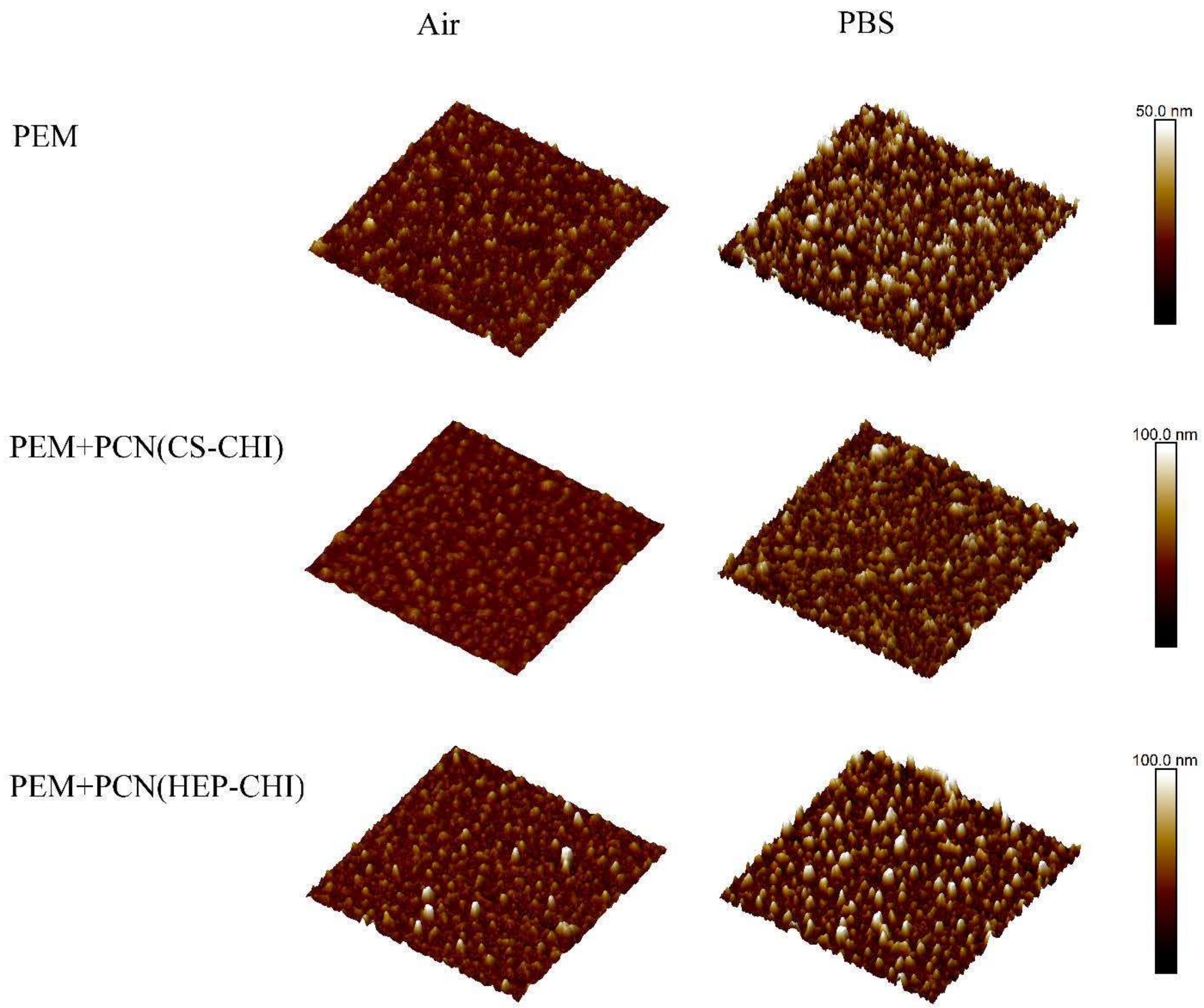

Figure S5. 5 µm × 5 µm AFM topography images in air and in PBS of PEM and PEM+PCN assembled at pH 5.4.

APPENDIX B: PROTEIN ADSORPTION MEASUREMENTS ON LOW FOULING AND ULTRALOW FOULING SURFACES: A CRITICAL COMPARISON OF SURFACE CHARACTERIZATION TECHNIQUES

For comparison of PEM surfaces on gold and gold-coated glass, XPS and AFM was used to compare the chemistry and topography of the surfaces. The elemental compositions of the PEM surfaces on gold and glass substrate were determined by XPS and are shown in **Table S1**. Both PEM_{10} and PEM_{11} surfaces represent similar elemental compositions (atom % values are all within 5 %).

Table S1. Elemental composition from X-ray photoelectron spectroscopy.

	Atom %		
Surface	C	O	N
PEM_{10} (on Au)	55%	40.8%	4.2%
PEM_{10} (on glass)	51.2%	43.5%	5.3%
PEM_{11} (on Au)	58.2%	34.9%	6.9%
PEM_{11} (on glass)	53.4%	41.3%	5.3%

5 µm × 5 µm AFM scans of the surfaces on glass and gold substrates in PBS show similar surface features. Although they are not identical, but polyelectrolyte feature complexes which form on the surface during LbL assembly of the PEMs are very similar. This confirms similarity of PEM surface topographies on gold and glass substrates.

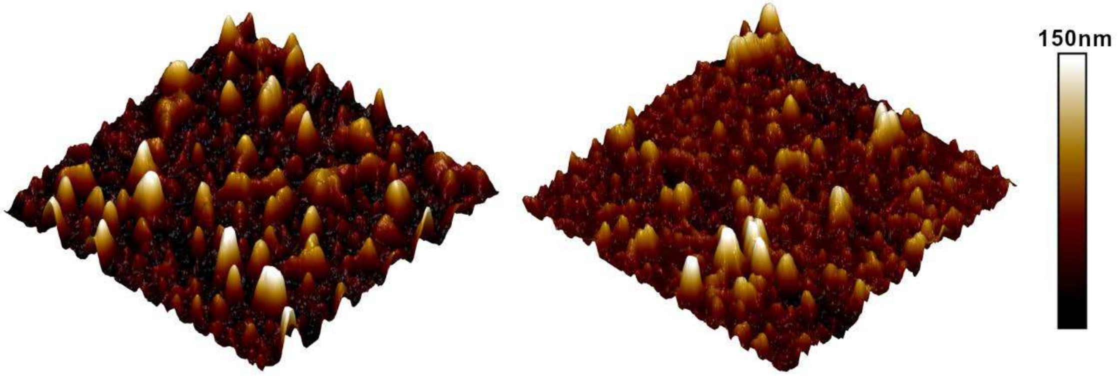

Figure. S1.5 µm × 5 µm AFM topography images in PBS of PEM_{11} on MUA-modified gold-coated glass (left) and glass (right).

Schematic of flow channel used in TIRF microscopy experiment.

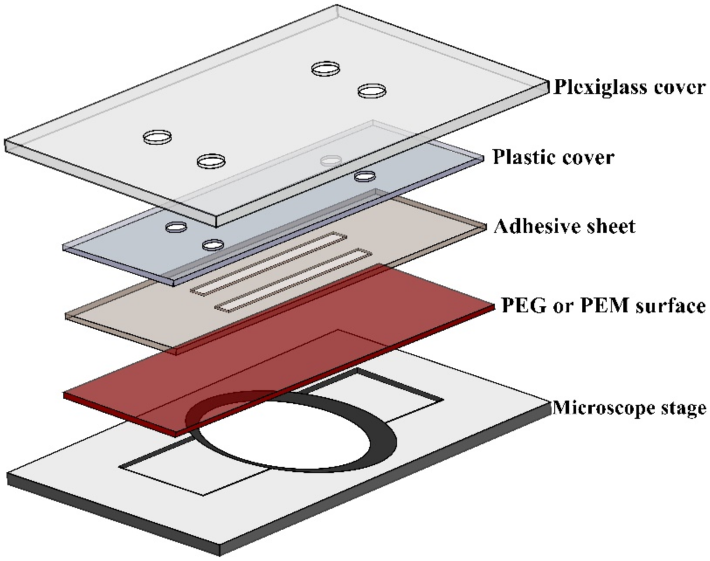

Figure. S2. Schematic diagram showing the multilayer structure of the flow channel used in TIRF microscopy.

The surface shear rate profile across the width of the microchannel (x-direction) was calculated by equation S1:

$$\gamma_{wall}(x) = \frac{48Q}{\pi^2 h^2 w} \frac{\sum_{n=1,3,5,\dots}^{\infty} \frac{1}{n^2}\left[1 - \frac{\cosh(n\pi \frac{x}{h})}{\cosh(n\pi \frac{w}{2h})}\right]}{\left[1 - \sum_{n=1,3,5,\dots}^{\infty} \frac{192h}{n^5 \pi^5 w} \tanh(n\pi \frac{w}{2h})\right]}$$

$$(-\frac{w}{2} \leq x \leq \frac{w}{2})$$

Where γ is the shear rate, Q is the volumetric flow rate, h is height, and w is width of the channel.

In situ FT-SPR for PEM construction on the gold chip.

PEM surfaces were constructed with CHI as the polycation and HA as the polyanion. **Figure. S3** represents PEM build-up with FT-SPR. The first 6 min (blue arrow) represents an acidified water rinse on the gold-coated glass chip modified with MUA. The green and red arrows respectively indicate the CHI and HA adsorption during LbL assembly. The difference between the FT-SPR peak position during the first and second rinse steps is due to the adsorption of CHI. Similarly, the difference between the peak position during the second and third rinse steps is due to the adsorption of HA on top of the CHI layer. The LbL process was repeated until a 10-layer PEM (terminating with HA for PEM_{10} surface) and 11-layer PEM (terminating with CHI for PEM_{11} surface) had been constructed. The approximate wet thickness of the PEM surfaces from theoretical predictions is reported based on **Figure. S3** which was published previously.

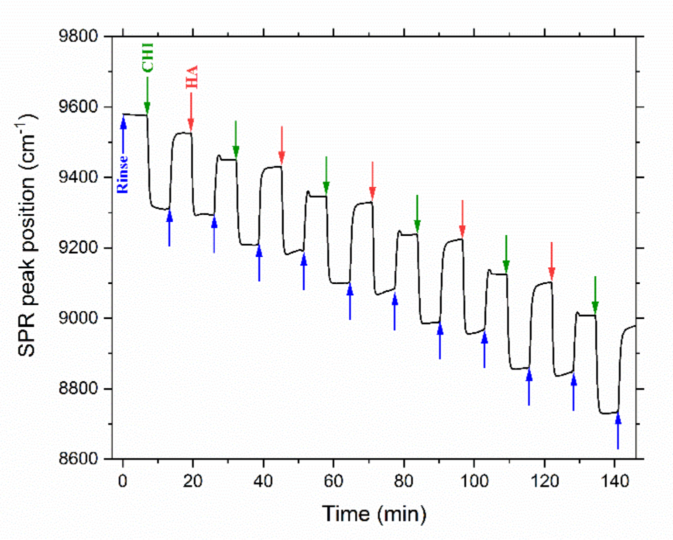

Figure. S3. Representative kinetics of PEM11 assembly from in situ FT-SPR for the PEMs assembled at pH 5.0. Arrows represent the beginning of acidified water rinse (blue), chitosan adsorption (green), and hyaluronan adsorption (red) steps.

Protein adsorption study at high concentration by TIRF microscopy.

TIRF microscopy was conducted with the same concentration of protein used in the SPR study. Albumin or fibrinogen were mixed at a final concentrations of 1 mg mL^{-1} with labeled protein at a final concentration of 10 nM in PBS.

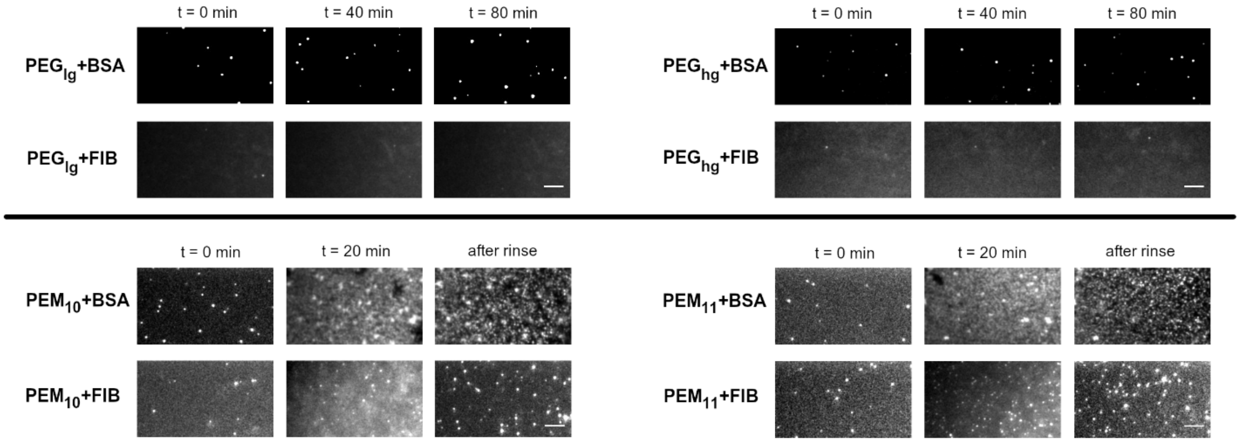

Figure. S4. Representative TIRF micrographs during protein adsorption at a concentrations of 1 mg mL^{-1} with labeled protein at a final concentration of 10 nM in PBS on PEG brush surfaces (top) and PEM surfaces (bottom). Scale bar = 5 µm.

APPENDIX C: NANOSTRUCTURED SURFACES THAT MIMIC THE VASCULAR ENDOTHELIAL GLYCOCALYX REDUCE BLOOD PROTEIN ADSORPTION AND PREVENT FIBRIN NETWORK FORMATION

Theoretical background for PeakForce QNM mode. The mechanical surface properties of PEMs and PEM+PCNs were quantitatively assessed using the PeakForce QNM mode. In PeakForce QNM mode, the tip oscillates at a frequency (f) well below the resonance frequency of cantilever (f_0), so that the cantilever follows the sinusoidal movement of the cantilever base. This mode is based on force-versus-distance measurements that are collected with a high acquisition rate, typically 1 to 2 kHz. During scanning, the maximum normal force applied to the surface (peak force) is controlled by the feedback mechanism of the AFM at each pixel. This enables the acquisition of force-distance data at each pixel. These force-distance data can be analyzed to provide information about modulus, deformation, adhesion, and dissipation, at the AFM image resolution

To obtain the elastic properties, the force-distance data must be interpreted with respect to a model describing the material properties and the tip-surface interaction mechanisms. The Derjaguin-Muller-Toporov (DMT) model is used to calculate the modulus. This model assumes spherical contact shape of the tip and is valid when the indentation depth is less than the tip radius. The DMT model also assumes that the force on the cantilever is ths sum of the stress on the material integrated over the inteaction area and some adhesion force between the tip and the surface. To calcualte the modulus of the material, the adhesion force is subtracted from the net force on the cantilever. By definition, the DMT model fits the equation (1)

$$F - F_{adh} = \frac{4}{3}E^* \sqrt{Rd^3} \tag{1}$$

Where F is the force on the tip, F_{adh} is the adhesion force, R is the tip radius, d is the sample deformation and E^* is the reduced modulus. This model is fit to the retract curve of the force-distance data over the region from 30% to 90% of the peak force. The result of the fit is the reduced modulus E^*. The reduced modulus E^* depends on the elastic moduli of both the tip E_{tip} and the sample E_s as well as on their Poisson ratios v_{tip} and v_s.

$$E^* = \left(\frac{1-v_s^2}{E_s} + \frac{1-v_{tip}^2}{E_{tip}}\right)^{-1} \approx \frac{E_s}{1-v_s^2} \tag{2}$$

In these experiments, the tip is made of silicon with modulus > 10 GPa so E_{tip} is assumed to be infinite, and calculation of the sample modulus is achieved by assuming a Poisson's ratio for the sample. Since the value of v_s is not known for the most samples studied in this work, we assumed $v_s = 0.3$ for all samples.

Surface Roughness Calculated from the AFM Images in Figure 1. The root-mean-square surface roughness, R_q, is used to compare the surface roughness of PEM_7, PEM_{13}, PEM_{19}, and PEM_{19}+PCN(CS-CHI) , imaged in deionized water (Table S.1). R_q is defined as:

$$R_q = \sqrt{\frac{\sum_i (Z_i - \bar{Z})^2}{N}} \tag{3}$$

where $Z_i - \bar{Z}$ is the difference between the height of the i^th^ the pixel from the mean height, and N is the number of pixels.

Table S.1. RMS roughness of surfaces from Figure 1.

Surface	PEM_7	PEM_{13}	PEM_{19}	PEM_{19}+PCN(CS-CHI)
R_q (nm)	4.6	18.3	22.7	53.6

Composition and Structure of Surfaces. The elemental compositions of the PEM_{13}, PEM_{19}, PEM_{19}+PCN(CS-CHI), and PEM_{19}+PCN(HEP-CHI) surfaces on glass determined from X-ray photoelectron spectroscopy are reported in Table S.2. For comparison, the elemental composition of the PEM_{13} surface obtained on the MUA-modified gold-coated glass chip is also shown in Table S.2.

Table S.2. Elemental composition from X-ray photoelectron spectroscopy.

	Atom %			
Surface	C	O	N	S
PEM_{13} (on Au)	59.9%	34.6%	5.5%	0%
PEM_{13} (on glass)	58.4%	36.1%	5.5%	0%
PEM_{19} (on glass)	54.7%	39.6%	5.7%	0%
PEM_{19}+PCN(CS-CHI) (on glass)	52.7%	40.2%	5.2%	1.9%
PEM_{19}+PCN(HEP-CHI) (on glass)	51.6%	42.1%	4.2%	2.1%

The elemental compositions of the PEM_{13} samples on glass and on MUA-modified gold-coated glass are similar (atom % values are all within 2 %). Figure S.1 shows the high-resolution XPS spectra of the O1s, N1s, C1s, and S2p envelopes of the PEM_{13} samples on glass and gold-coated glass, as well as 5 μm × 5 μm AFM scans of the surfaces. Both surfaces have strong signals from –OH, between 532.5 eV and 532.9 eV, with smaller contributions from amide and carboxylic acids at lower binding energy (between 351eV and 532 eV). The N1s envelope is dominated by amide and amine nitrogen at (between 399 eV and 400 eV), with a smaller contribution from ammonium nitrogen (above 400 eV). The dominant peak in the C1s envelope is from the C-OH at 286.5 eV to 286.7 eV. The signal at 288 eV is from C=O. The primary difference between the two spectra is the amount of aliphatic carbon (284.8 eV), which is primarily adventitious and not from these samples. No S is detected on either of these samples, as expected. The AFM scans of the surfaces on glass and MUA-modified gold-coated glass show similar surface roughness with features generally less than 100 nm in height.

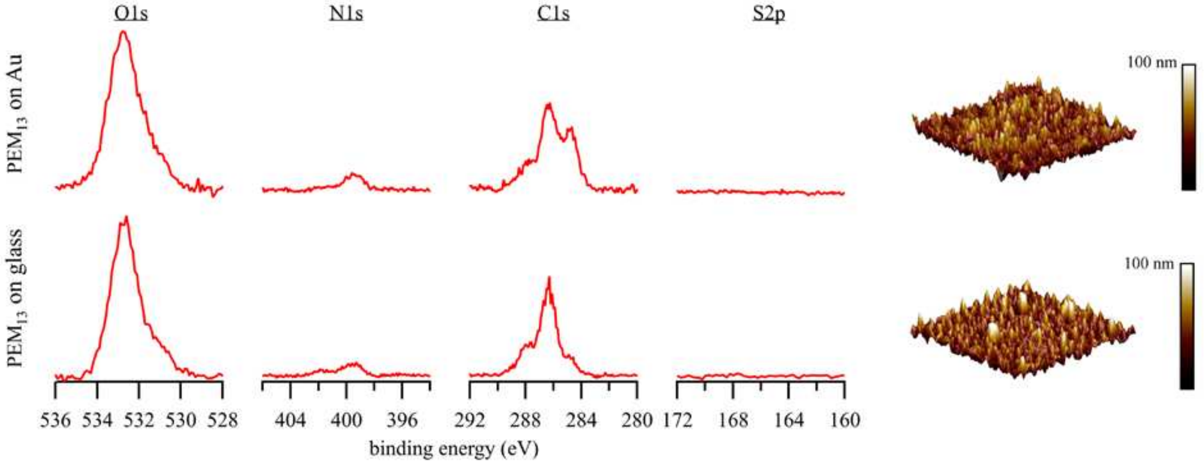

Figure S.1 High-resolution XPS spectra of the PEM$_{13}$ samples on MUA-modified gold-coated glass (top) and glass (bottom), with corresponding 5 µm × 5 µm AFM height images.

Addition of the PCNs to PEMs is achieved whether the PCNs are prepared on MUA-modified gold-coated glass or glass. Figure S.2 shows the high-resolution XPS spectra of the O1s, N1s, C1s, and S2p envelopes of PEM$_{19}$+PCN(CS-CHI) surfaces prepared on both substrates, as well as corresponding 5 µm × 5 µm AFM scans. Addition of PCNs results in appearance of the sulfate in the S2p envelope at 168.5 eV (corresponding to 1.8 to 1.9 atom %), broadening of the O1s peak due to sulfate near 532 eV, and ~250 nm to 300 nm high features in the AFM scans.

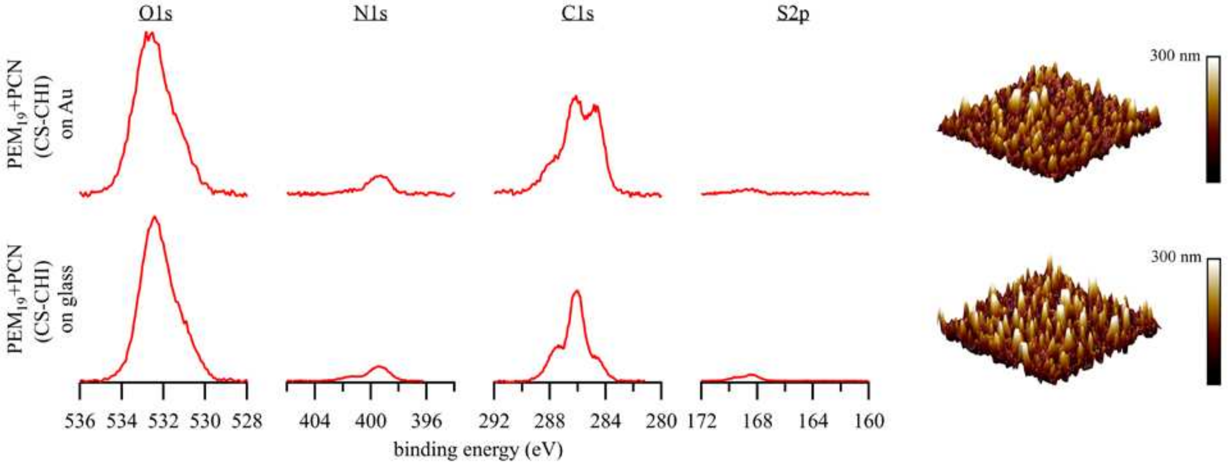

Figure S.2 High-resolution XPS spectra of the PEM$_{19}$+PCN(CS-CHI) samples on MUA-modified gold-coated glass (top) and glass (bottom), with corresponding 5 µm × 5 µm AFM height images.

Fibrin(ogen) Adsorption on Surfaces in the Presence of Thrombin. Experimental surfaces were incubated with fibrinogen (at a final concentrations of 0.75 mg/mL), thrombin (at 1 NIH U/mL), and Alexa Fluor 647-conjugated fibrinogen (at a final concentration of 5 nM), in Tris-buffered saline (10 mM Tris, 150 mM NaCl, pH 7.4) with 5 mM CaCl$_2$, to activate thrombin at room temperature. TIRF microscopy of PEM$_{19}$, PEM+CS, and PEM+HEP at 30 minutes shows the onset of fibrin fiber formation on the surfaces. The PEM+PCN(CS-CHI) sample was incubated for two hours, under similar conditions. After a 2 hour incubation, there are still no apparent fibrin fibers or fibrin network formation on the PEM+PCN(CS-CHI) surface (Figure S.3).

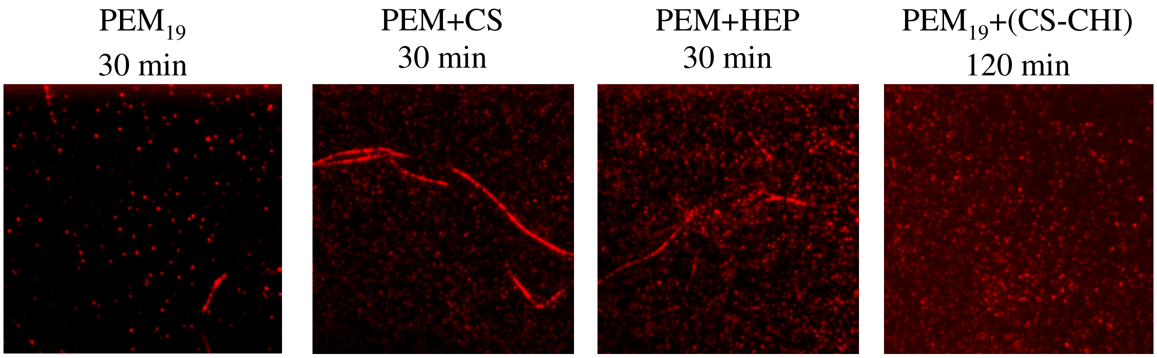

Figure S.3. TIRF microscopy images of fluorescently labeled fibron(ogen) after 30 minutes of incubation with thrombin on PEM$_{19}$, PEM$_{19}$+HEP, PEM$_{19}$+CS, and after 120 minutes of incubation on PEM$_{19}$+PCN(CS-CHI). These are the same fields of view shown at 40 minutes in Figure 5 of the main text. The PEM$_{19}$, PEM$_{19}$+HEP, PEM$_{19}$+CS show the onset of fibrin(ogen) fiber formation on the surfaces after only 30 minutes. However the PEM$_{19}$+PCN(CS-CHI) shows only single protein molecules with no fibrin(ogen) fiber formation after 120 minutes. Each image shows the average of 1500 frames from a microscopy video.

Video from Single-Molecule TIRF Microscopy of Thrombin and Fluorescently-Labeled Fibrin(ogen) on Glycocalyx Mimetic Surfaces. A video showing the formation of fibrin fibers and a fiber network on PEM, PEM+CS, and PEM+HEP, and showing no fiber or network formation on PEM+PCN(CS-CHI) and PEM+PCN(HEP-CHI) surfaces is available.